UNIVERSITY OF SOUTHAMPTON

FACULTY OF ENGINEERING AND THE ENVIRONMENT
Institute of Sound and Vibration Research

Modelling nonlinear interactions within the cochlea

by

Dario Vignali

Thesis for the degree of Doctor of Philosophy

June 2017

UNIVERSITY OF SOUTHAMPTON

ABSTRACT

FACULTY OF ENGINEERING AND THE ENVIRONMENT
Institute of Sound and Vibration Research

Doctor of Philosophy

MODELLING NONLINEAR INTERACTIONS WITHIN THE COCHLEA

by Dario Vignali

The auditory system has a wide dynamic range and remarkable selectivity, due partly to the nonlinear processing within the cochlea. Modelling the performance of the cochlea is a way to gain insight into how it operates and to better understand its mechanical structure, whose arrangement generates nonlinear phenomena. A box model with nonlinear micromechanics was simulated using the state space method and the quasi-linear method to understand nonlinear dynamic interactions within the cochlea. The results from the quasi-linear model were essential for obtaining cochlear compression curves, which were used to tune the saturation parameters of the nonlinear function incorporated into the state space model. The nonlinear state space model allows time domain simulations to be performed that can replicate spontaneous otoacoustic emissions (SOAEs); sounds that can be measured in the ear canal, which are generated inside the cochlea and are by-products of the nonlinear process of the cochlear amplifier. The time domain model was mathematically formulated to reduce the computational load, which has previously limited the number of results that could be obtained. A novel method of incorporating initial conditions into the state space model has also been developed. Time domain simulations illustrate how SOAEs are due to limit cycle oscillations, whose amplitude is controlled by the saturation of the cochlea's amplification process. The results support the standing wave theory, whereby the emissions are produced by the reflection from random perturbations along the length of the cochlear partition at one end and the stapes at the other. Simulations of the interaction between a SOAE and low frequency bias tones give results that are comparable with those produced experimentally, but allow a greater physical interpretation. Simulations are also performed of the interaction between a SOAE and other stimuli, such as a swept tone that sweeps through the frequency of the emission and a high-level, low-frequency tone.

Contents

List of Figures

List of Tables

Declaration of Authorship

I, Dario Vignali, declare that the thesis entitled *Modelling nonlinear interactions within the cochlea* and the work presented in the thesis are both my own, and have been generated by me as the result of my own original research. I confirm that:

- this work was done wholly or mainly while in candidature for a research degree at this University;
- where any part of this thesis has previously been submitted for a degree or any other qualification at this University or any other institution, this has been clearly stated;
- where I have consulted the published work of others, this is always clearly attributed;
- where I have quoted from the work of others, the source is always given. With the exception of such quotations, this thesis is entirely my own work;
- I have acknowledged all main sources of help;
- where the thesis is based on work done by myself jointly with others, I have made clear exactly what was done by others and what I have contributed myself;

Signed:..

Date:..

Acknowledgements

A very special thanks goes to my supervisors Prof Steve Elliott and Dr Ben Lineton. It was amazing working with you both, thank you for your immense support. In particular I would like to thank Prof Elliott, a person with great knowledge and skill, for all the interesting discussions we had together; it has been inspiring to work with you.

I would like to sincerely thank Eda, for always being very supportive and for all the enjoyable moments spent together. Teşekkürler!

Many many thanks to my parents (Antonio and Kay), my sister (Carla), brother in law (Nicola) and my little nephew (Fosco).

An enormous thanks goes out to all my friends that accompanied me through this journey, in particular, Giuseppe and Rich (our small musical journey was unforgettable) Luigi, Giulia, Michele I., Michele Z. and Cherith (a special thanks to you also for proof reading my thesis).

Abbreviations

AM	**A**mplitude **M**odulation
BM	**B**asilar **M**embrane
CA	**C**ochlear **A**mplifier
CEOAE	**C**lick **E**voked **O**to**A**coutic **E**mission
CF	**C**haracteristic **F**requency
DPOAE	**D**istortion **P**roduct **O**to**A**coustic **E**mission
FFT	**F**ast **F**ourier **T**ransform
FM	**F**requency **M**odulation
ICP	**I**ntra **C**ranial **P**ressure
IHC	**I**nner **H**air **C**ells
LSB	**L**ower **S**ide **B**and
ME	**M**iddle-**E**ar
MET	**M**echano-**E**lectrical **T**ransduction
OAE	**O**to**A**coustic **E**mission
ODE	**O**rdinary**D**ifferential **E**quation
OC	**O**rgan of **C**orti
OHC	**O**uter **H**air **C**ells
PMD	**P**referred **M**inimum **D**istance
PSD	**P**ower **S**pectral **D**ensity
RL	**R**eticular **L**amina
SFOAE	**S**timulus **F**requency **O**to**A**coustic **E**mission
SOAE	**S**pontaneous **O**to**A**coustic **E**mission
SPL	**S**ound **P**resssure **L**evel
TBOAE	**T**ransient **B**urst **O**to**A**coustic **E**mission
TEOAE	**T**ransient **E**voked **O**to**A**coustic **E**mission
TM	**T**ectorial **M**embrane
TW	**T**ravelling **W**ave
USB	**U**pper **S**ide **B**and

Symbols

SYMBOL	NAME	UNIT
$\frac{d}{dt}$	derivative with respect to time of a quantity	
∂	partial derivative operator	
$\lvert\,\rvert$	absolute value	
$\angle$	phase	
Σ	summation operator	
$\Re$	real part of a complex number	
$\Im$	imaginary part of a complex number	
A	amplitude of the driving force - Chapter 3.1	N
$\mathbf{A}$	(n x n) system matrix containing the coupled mechanics of the model	
$\mathbf{A}_E$	(n x n) system matrix containing the uncoupled mechanics of the model	
b	ratio of BM displacement to average BM displacement over radial cross section	
B	width of the flexible section of the BM	m
$\mathbf{B}$	(n x m) input matrix	
$\mathbf{B}_E$	(n x m) input matrix for the uncoupled state space equation	
c	wave speed of the travelling wave	ms^{-1}
$\mathbf{C}$	(p x n) output matrix	
$\mathbf{C}_E$	(p x n) output matrix for the uncoupled state space equation	
C_1, C_2, C_3, C_4	damping terms of the micromechanical element	Nsm^{-3}
C_h	damping term in the helicotrema boundary element	Nsm^{-3}
C_m	damping term in the middle ear boundary element	Nsm^{-3}
d	decay of the travelling wave	m

$\mathbf{D}$	(p x m) matrix that directly connects the input to the output	
e	Neper number	
$\mathbf{F}$	finite difference matrix	
f_{bias}	bias tone frequency	Hz
f_{ext}	external tone frequency	Hz
f_n	natural frequency at a specific location along the cochlea	Hz
f_0	natural frequency at the base of the cochlea	Hz
f_{SB}	side-band frequency	Hz
f_{SOAE}	SOAE frequency	Hz
$\overline{f_{SOAE}}$	geometric mean between two adjacent SOAE frequencies	Hz
H	height of the chambers above and below the cochlear partitions	m
$\mathbf{I}$	unit matrix	
j	complex number $\sqrt{-1}$	
$k(x,\omega)$	wavenumber of the travelling wave	m^{-1}
K_1, K_2, K_3, K_4	stiffness terms of the micromechanical element	Nm^{-3}
K_m	stiffness term in the middle ear boundary element	Nm^{-3}
L	length of the cochlea	m
l	characteristic length or cochlear length scale	mm
M_1, M_2	mass of the BM and the TM in the micromechanical element	kgm^{-2}
M_h	mass of the helicotrema boundary element	kgm^{-2}
M_m	mass of the middle ear boundary element	kgm^{-2}
N	number of micromechanical elements used along the length of the cochlea	
N_{SOAE}	ratio of SOAE frequency to the spacing	
n	index number of a specific micromechanical element	
$\mathbf{p}$	matrix of pressures	Pa
P_a	active pressure on micromechanical element	Pa
P_d	pressure difference acting on a micromechanical element	Pa
p	pressure difference along the cochlear partition	Pa
$\mathbf{q}$	vector of source terms	ms^{-2}
s	complex frequency variable $s = j\omega$	
t	time	s
$\mathbf{u}(t)$	(m x 1) input vector	

u	input of nonlinear function	m
v	output of nonlinear function	m
W	width of the BM	m
x	BM displacement(Van der Pol oscillator - Chapter 3.1)	m
x	distance along the length of the cochlea	m
$\mathbf{x}(t)$	(n x 1) state vector containing n state variables	
$[\dot{x}_1, x_1, \dot{x}_2, x_2]$	states of the n^{th} element in the cochlea	
x_{norm}	distance along the cochlea expressed as a proportion of its toal length	
$\mathbf{y}(t)$	(p x 1) output vector	
$Y_{BM}(x, \omega)$	BM admittance	$(\mathrm{Ns})^{-1}\mathrm{m}^3$
Z_1, Z_2, Z_3, Z_4	impedance terms of the micromechanical element	Nsm^{-3}
Z_{cp}	impedance of the cochlear partition	Nsm^{-3}
α	saturation point of nonlinear element	m
β	scales asymmetry of nonlinear element	
γ	feedback gain in the micromechanical element	
Δ	distance between two adjacent micromechanical elements	m
$\overline{\Delta f}_{SOAE}$	absolute value of the difference between two adjacent SOAE frequencies	Hz
$\overline{\Delta x}_{SOAE}$	average distance between resonant positions along the cochlea	m
ϵ	nonlinear damping term in the Van der Pol equation	Nsm^{-1}
λ	wavelength of the travelling wave	m
η	determines slope of nonlinear function	
λ_{peak}	peak wavelength of the travelling wave	m
ξ	acceleration of the cochlear partition	ms^{-2}
$\boldsymbol{\xi}$	vector of cochlear partition accelerations	ms^{-2}
ξ_p	average BM displacement over the radial cross section	m
ξ_{SO}	stapes displacement due to the external stimulus	m
ξ_{SR}	stapes displacement due to the loading by the internal pressure response in the cochlea	m
ξ_{st}	stapes displacement	m
π	irrational number 3.14...	
ρ	density of the cochlear fluids	kgm^{-3}
σ	real part of a pole	s^{-1}

ω	angular frequency of travelling wave	rads^{-1}
ω_{cp}	angular frequency of of a characteristic frequency	rads^{-1}
ω_d	driving angular frequency of a forced oscillation	rads^{-1}
ω_n	natural angular frequency of a SOAE	rads^{-1}

Chapter 1

Introduction

What are the benefits of modelling? What information does a model give us that we cannot obtain from experiments? Questions like these come naturally when trying to understand new features of an unknown system. However, the connection between modelling and reality is much deeper than it may seem at the surface. Scientific and technological achievements are generally reached through some kind of model, whether it be numerical, mechanical, electrical, etc.. It allows one to discard unimportant features in a system that may have very little influence at all or may be disregarded for the outcome one aims to achieve; in other words, one can make assumptions that simplify the model of a system. Therefore, modelling is of fundamental importance, whether it matches and confirms experimental results or allows for new numerical results that could not be achieved experimentally. Sometimes a model is necessary because physical experiments cannot be performed on certain systems due to their size, location, accessibility, etc.. A further important aspect about models that replicate physical processes is not necessarily whether they produce results that exactly fit the experimental data at hand, but rather the insight they bring regarding the system under study.

The system under scrutiny in this thesis is the human cochlea, which, not only is a very complex and active system, but one that is not easily accessible and whose active properties are hard to control and analyse under experimental conditions. Therefore, developing a numerical model of the cochlea is extremely beneficial for a greater understanding of its functioning. Assumptions can be made with regards to its properties that simplify its implementation and the model can be easily modified in order to compare its performance as a function of the parameters used to simulate this advanced biological system.

Nowadays, it is possible to create very large and complicated computer models thanks to software packages, such as MATLAB, that allow for fast simulations in the time domain. The mathematical model described in this thesis uses such a strategy to replicate the mechanics of the human cochlea and simulate cochlear phenomena, such as compression, self-suppression and the generation of otoacoustic emissions (OAE). The model incorporates micromechanical lumped elements that mimic the characteristics of radial slices of the cochlea. The basic micromechanical elements, which include nonlinear properties to model cochlear behaviour, are cast into a state space formulation, that allows for interaction between these individual slices and the fluid contained in the cochlea (Elliott et al., 2007). A macromechanical model of the coupled cochlea is therefore obtained, capable of performing both frequency and time domain simulations.

The strengths of the model are the capability of predicting its stability and of performing nonlinear time domain simulations. This provides great insight into the model's behaviour when stimulated by a virtual acoustic input signal. It is therefore possible, for example, to establish and predict the occurrence of certain OAEs.

Generally speaking, cochlear models operate either in the frequency domain, in the time domain, or both. A review of cochlear modelling efforts over the years is provided by de Boer (1996). Although frequency domain methods tend to be faster, analyses in this domain alone cannot take account of nonlinearities incorporated in the system. A strategy to partially overcome this problem is to implement a quasi-linear model to predict the response of the dynamics of the cochlear partitions in the frequency domain. This is possible because quasi-linear methods take into account, to a certain extent, nonlinearities incorporated in the system (Kanis and de Boer, 1993, 1994). Although it is not the main focus of this thesis, a model of this type was used in tandem with the time domain model to initially tune the nonlinear parameters and then to reduce the computational time.

The work undertaken here was a small part of a larger European project entitled "Semantic Infostructure interlinking an open source Finite Element tool and libraries with a model repository for the multi-scale Modelling and 3D visualization of the inner-ear" (SIFEM). The project's main aim was to address hearing loss, which is affecting an increasing number of people worldwide and hence to develop an inner-ear model that takes into account the anatomical details of the cochlea and therefore can help identify the mechanisms that trigger hearing loss (SIFEM, 2011).

The work presented in this thesis is a continuation of the work described in Elliott et al. (2007), where a cat's cochlea is modelled, and Dr. E. Ku's Ph.D. thesis (Ku, 2008), where a human cochlea is modelled. The work described in Elliott et al. (2007) and Ku (2008) introduces the state space model, demonstrating its efficiency in producing both frequency and time domain results.

The following sections of this chapter review the well known morphological aspects of the mammalian cochlea. This will also allow for a better understanding of the aims and contributions of the thesis, which are outlined at the end of this chapter. However, a more thorough review of the literature on the cochlear nonlinearity and how it has been modelled will be outlined in later chapters, particularly Chapters 2 and 3.

1.1 The mammalian cochlea

1.1.1 Historical developments in cochlear mechanics

The mammalian cochlea is an organ that has fascinated scientists for many years. Although its physiology and characteristics have been studied for a long time, numerous aspects of cochlear functioning are still not well understood, due to its inaccessibility and the difficulties associated with performing direct measurements on it. This intricate organ exhibits a variety of passive and active behaviours, which help us to perceive different sounds, and it is extremely sensitive to acoustical perturbations in time, frequency and intensity (Pickles, 2012). These incredible features make it an outstanding biological system from an engineering point of view. One of the first pioneering studies to be accomplished in this field was that undertaken by Georg von Békésy (von Békésy, 1949, 1960), who carried out experiments on cochleae in dead animals. His work shed light on the functioning of the cochlea despite the fact that, since the cochleae samples were procured from cadavers, Békésy could only predict the passive behaviour of the organ.

Thomas Gold suggested that an active process occurs in the living cochlea that fine tunes the perception of sound (Gold, 1948). His theories were confirmed many years later with the discovery of auditory responses, or more precisely emissions, measured from the ear canal with a small microphone that were observed when stimulating normal hearing ears with acoustic impulses near the threshold of audibility (Kemp, 1978). Later, these emissions would be termed otoacoustic emissions (OAE).

This active behaviour of the cochlea, and in general, cochlear mechanics, has also been studied using various modelling techniques (de Boer, 1996). These models require a number of assumptions, which have been necessary, either to overcome the lack of knowledge regarding the functioning of this organ and/or to simplify a model by disregarding properties considered negligible for the all-round functioning of the cochlea. It is, however, important that a model retains physiological plausibility if the results are to be understood in terms of the underlying processes within the cochlea.

1.1.2 Why model the mammalian cochlea?

Many models have been made of the human cochlea, ranging from mechanical structures, to electrical networks, to abstract mathematical representations (de Boer, 1996). But why are engineers and scientists obsessed with this minuscule organ? First of all, the cochlea is a unique organ that is characterised by some extremely interesting properties: it is a frequency analyser that divides incoming sounds into its various frequency components and its dynamic response varies over the range of intensities it perceives. All this is accomplished on a microscopic scale and by means of nonlinear phenomena.

From an engineering point of view, the phenomena that occur within the cochlea are complicated and only partly understood. To be able to simulate its properties with a model can be advantageous for the following reasons:

- Cochlea models are a way of better understanding and interpreting experimental results
- A better understanding of the cochlea would enable the production of more accurate hearing devices that would be extremely beneficial for the hearing impaired community
- Simulations that replicate the characteristics of specific ears may enable the diagnosis of certain causes of deafness and help understand what treatment is more suitable for individuals
- Smart structures and engineering sensors for real world applications could be designed that mimic the unique capabilities that distinguish the cochlea (Elliott and Shera, 2012)

1.1.3 Anatomy and properties of the cochlea

The ear, as shown in Figure 1.1, can be divided into the outer ear, the middle ear and the inner ear. As sound enters and travels through the ear canal, it encounters the ear drum, which can be considered the boundary between the outer ear and the middle ear. At this boundary, acoustical energy is transformed into mechanical energy and transferred to the inner ear via the three ossicles contained in the middle ear (malleus, incus and stapes). The middle ear acts as an impedance transformer that allows coupling between the air (low impedance) and the cochlear fluids (high impedance). The particular structure of the middle ear minimises transmission loss (Pickles, 2012).

The organ in the inner ear responsible for hearing is the cochlea, a snail shaped organ positioned inside the temporal bone in the skull. Sound is transmitted from the stapes to the oval window allowing the signal to enter the cochlea. This organ can be thought of as a frequency analyser that divides incoming acoustical pressure signals into their various frequency components in order to send appropriate neural impulses to the auditory cortex. Figure 1.1 shows the position of the cochlea in relation to the other parts of the ear, while Figure 1.2 shows a cross section of the cochlea of a guinea pig. Figure 1.2 illustrates the three chambers (or scalae) of the cochlea: the scala vestibuli, the scala media and the scala tympani.

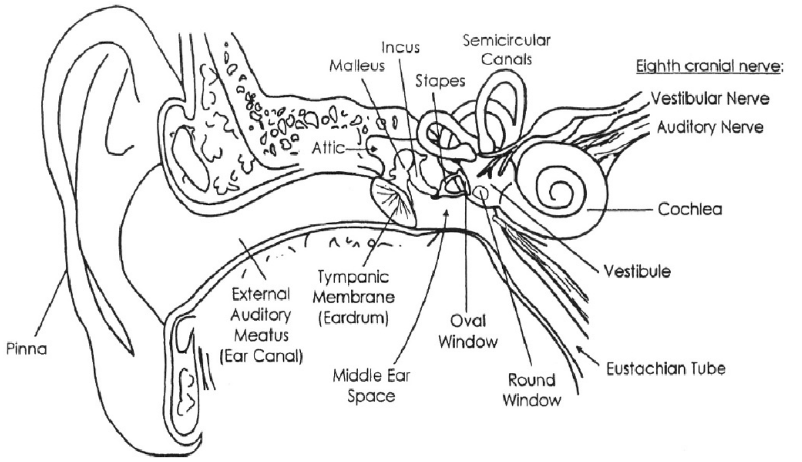

Figure 1.1: The peripheral auditory system. Reproduced from Gelfand and Levitt (1998). Permission requested.

The scalae spiral together from the base to the apex of the cochlea. The scala vestibuli and the scala tympani both contain a fluid called perilymph, and are joined together at the apex via the helicotrema, while the scala media forms an inner compartment containing a fluid called endolymph. Figure 1.3 shows an idealised representation of the uncoiled cochlea.

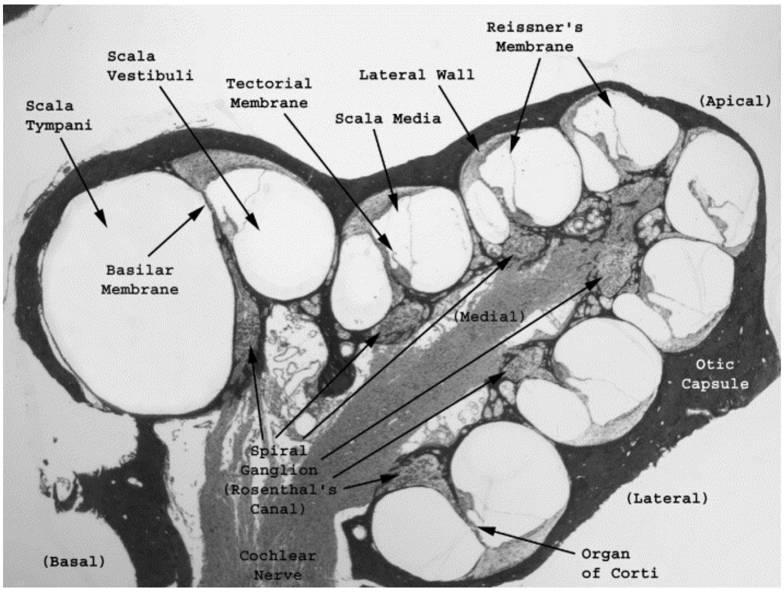

Figure 1.2: Cross section of the cochlea of the guinea pig. Reproduced with permission from Raphael and Altschuler (2003).

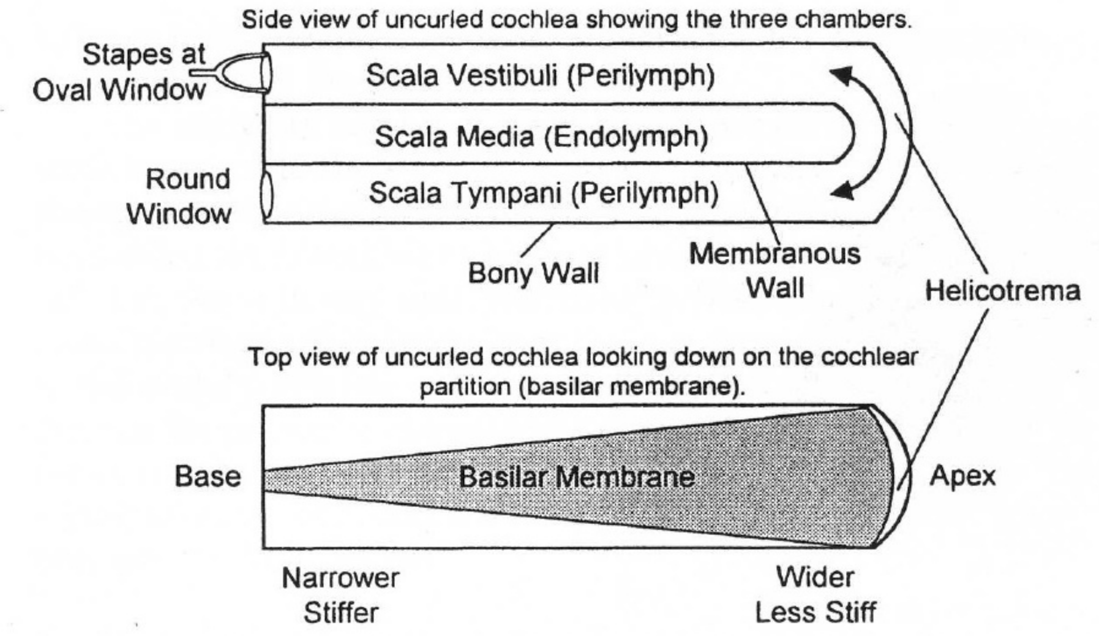

Figure 1.3: The uncoiled cochlea. Reproduced from Gelfand and Levitt (1998). Permission requested.

The oval window is at the base of the scala vestibuli and receives mechanical excitations from the stapes in the middle ear. This displaces the cochlear fluids, which in turn displace the round window at the basal end of the scala tympani, which acts as a pressure release boundary. The scala vestibuli and the scala media are separated by Reissner's membrane, which is generally considered acoustically transparent and assumed not to affect the mechanical properties of the cochlea (Dallos, 1996). The main function of Reissner's membrane is to separate endolymph from perilymph. The scala media and the scala tympani are separated by the basilar membrane (BM), which supports the organ of Corti (OC) and the hair cells responsible for the mechanical transduction process. The vibrations transmitted inside the cochlea by the stapes generate a wave-like displacement on the BM as it interacts with the cochlear fluid motion, as shown in Figure 1.4. It is this motion of the BM that displaces the tiny hair cells housed in the OC, that communicate directly to the auditory nerve fibres the information to be sent to the brainstem for the understanding of sound in the auditory cortex.

The lower section of Figure 1.3 shows how the BM changes its shape along the length of the cochlea: at the base it is narrower and stiffer, facilitating the detection of higher frequencies, while at the apex it is wider and less stiff, allowing it to be more easily stimulated by lower frequencies. This leads to what is known as a tonotopic frequency map of the cochlear membranes, where low and high frequency tones stimulate apical and basal locations respectively.

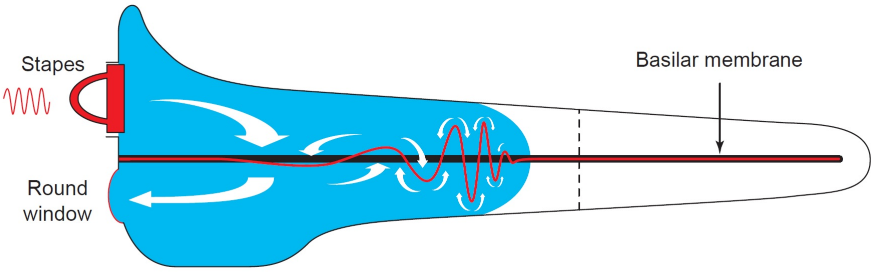

Figure 1.4: Travelling wave in the cochlea. The vibration of the stapes produces a travelling wave along the BM. Reproduced with permission from Nobili et al. (1998).

A representation of the cross section of a single turn inside the cochlea is shown in Figure 1.5. The OC sits on the BM and contains the receptor cells, inner hair cells (IHC), and outer hair cells (OHC), responsible for the transduction of pressure variations along the BM into electrical impulses. Generally speaking, both types of hair cells send and receive auditory information to and from the brain; however, IHCs mostly have afferent connections that convey auditory signals to the brainstem, whereas OHCs mostly have efferent connections that receive feedback signals from the brainstem and are involved in the cochlear amplification process (Pickles, 2012), as described below.

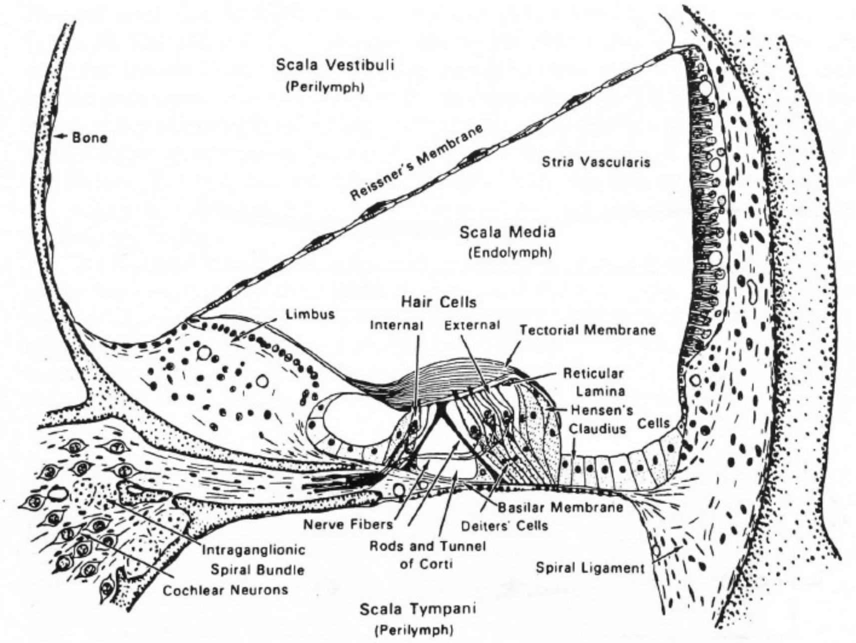

Figure 1.5: Cross section of the cochlea. Reproduced with permission from Davis (1962).

On top of the OC lies the Tectorial Membrane (TM), a gelatinous flap hinged along its inner edge and raised above the BM. Hence, the TM moves with a shear movement with respect to the BM (Pickles, 2012). Figure 1.6 shows in detail how the OC is arranged.

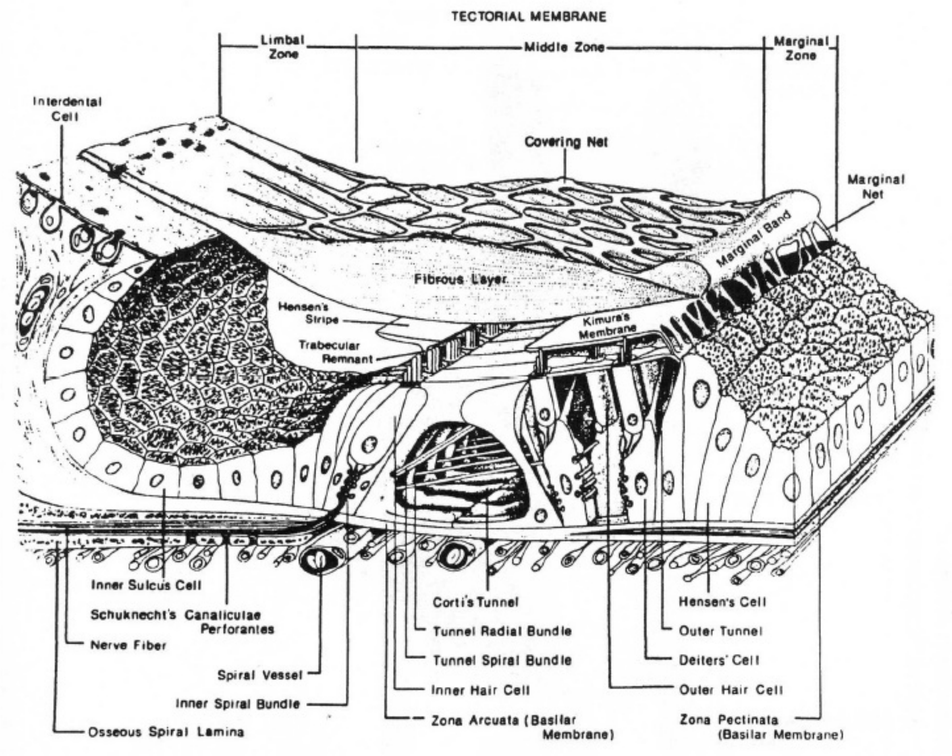

Figure 1.6: Cross section of the organ of Corti. Reproduced with permission from Lim (1986).

On the extremity of the hair cells are bundles of stereocilia, as shown in Figure 1.7, that are involved in the transduction process. The stereocilia are put into motion by the shear movement between the TM and the BM in response to a travelling wave. This process by the hair cells transduces the mechanical signal into an electrical one and is known as mechano-electrical transduction (MET) of the stereocilia (Pickles, 2012). The tallest stereocilium of the OHC is embedded in the TM.

The travelling wave that moves along the BM has an extremely important function and the pattern it generates on the BM depends on the complexity of the external acoustic stimulus. Frequency selectivity in the cochlea is very sharp, so that an acoustic stimulus at a single frequency will stimulate a specific narrow region on the BM (Pickles, 2012). It can be seen in Figure 1.8 that tones of different frequencies stimulating the ear generate displacement envelopes with peaks at different locations along the length of the cochlea, following the tonotopic mapping behaviour previously mentioned. These plots were originally obtained by G. von Bèkèsy, who used cochleae from cadavers where no active process was present.

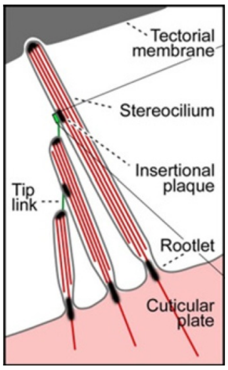

Figure 1.7: Stereocilia of an OHC. Stereocilia are hair-like organelles placed on IHCs and OHCs. They are connected to one another via tip links. The figure shows the case of an OHC, where the tallest stereocilium is embedded in the TM. Reproduced from LeMasurier and Gillespie (2005)

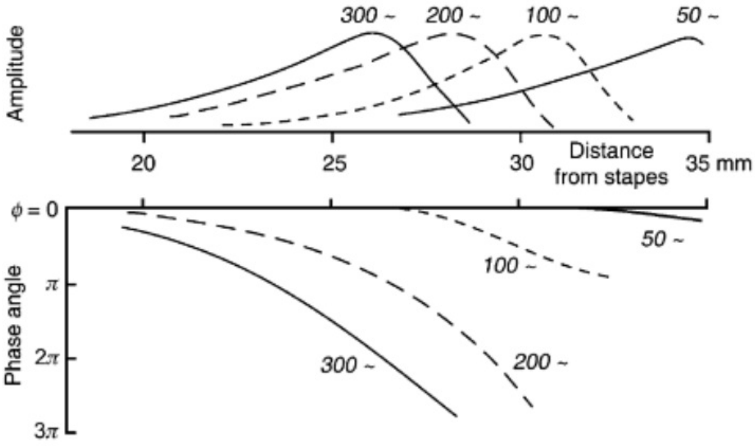

Figure 1.8: Amplitude and phase along the length of the cochlea due to travelling waves of different frequencies. Depending on the stimulus frequency, the displacement envelope peaks at specific regions of the cochlea. Reproduced with permission from Bekesy (1947).

In reality, live cochleae are characterised by a nonlinear active process that sharpens the frequency selectivity. The effect of this active nonlinear response of the cochlea on the BM motion is demonstrated in Figure 1.9. The plot shows the BM response at the position where the characteristic place along the tonotopic map is equivalent to 18 kHz in a guinea-pig. At different sound pressure levels (SPL) the response changes its form. At high excitation levels, the frequency response is broad. At low levels a sharp peak is generated at 18 kHz and a lower response at other frequencies. This amplification of the BM response at low levels is due to the active process and allows for great frequency selectivity (Pickles, 2012). In other words, as the SPL increases, the amplitude of the BM vibration also increases, but at a reduced rate, an effect that is known as self-suppression (Kanis and de Boer, 1993). Self-suppression is a result of the compressive nature of the cochlea. Compression is a remarkable aspect of the mammalian auditory system, as it allows us to perceive sounds over an extremely wide range of levels, approximately 120 dB for mid-frequency tones (Bacon, 2006; Johnstone et al., 1986; Robles et al., 1986), as shown in Figure 1.10, even though the sensory IHCs only operate over a dynamic range of about 30 to 40 dB (Bacon, 2006).

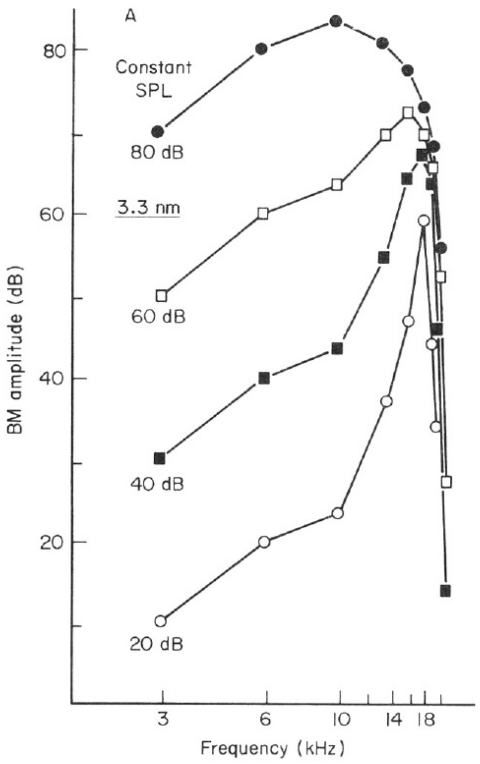

Figure 1.9: Compression of the BM response. The plot illustrates the BM response at the 18kHz point on the guinea-pig BM, against frequency. Connected points between specific curves indicate constant SPL of the stimulus at a particular frequency. Reproduced with permission from Johnstone et al. (1986).

The effect of compression along the BM can be seen more explicitly in Figure 1.11, where the response of the BM grows in a nonlinear fashion with respect to increasing external stimuli. Three stages can be observed: up until approximately 30 dB SPL the BM response is commonly thought of as being almost linear and active because of OHC amplification; saturation occurs between approximately 30 dB SPL and 90 dB SPL, resulting in compression of about $\frac{1}{3}\frac{\mathrm{dB}}{\mathrm{dB}}$, and finally, for higher levels of SPL, the system becomes once again linear, but totally passive, as the OHC activity is not sufficient to influence the dynamics (Pickles, 2012).

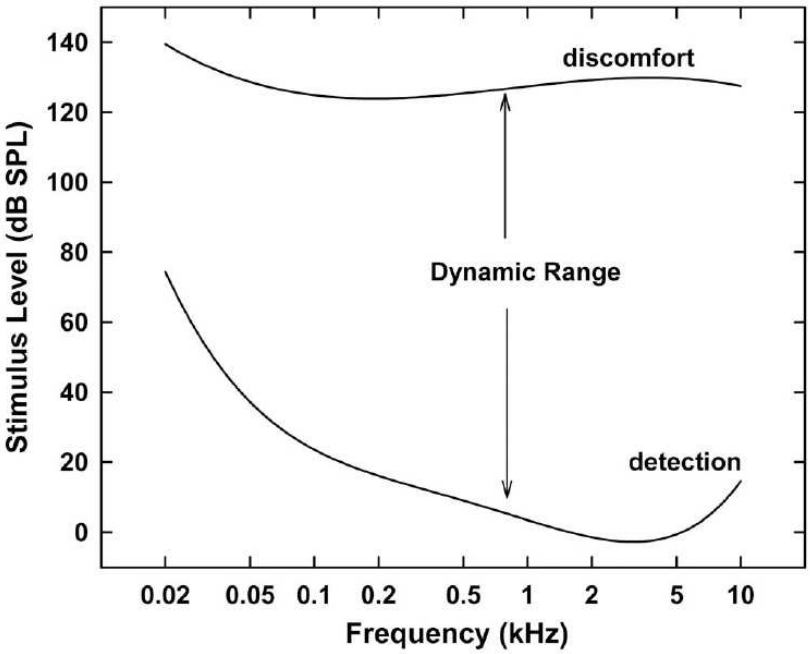

Figure 1.10: Dynamic range of the human auditory system. The bottom curve represents the threshold of hearing while the top curve represents the hearing levels that bring discomfort. The area between the two curves represents the dynamic range of human hearing across frequency. Reproduced from Bacon (2006).

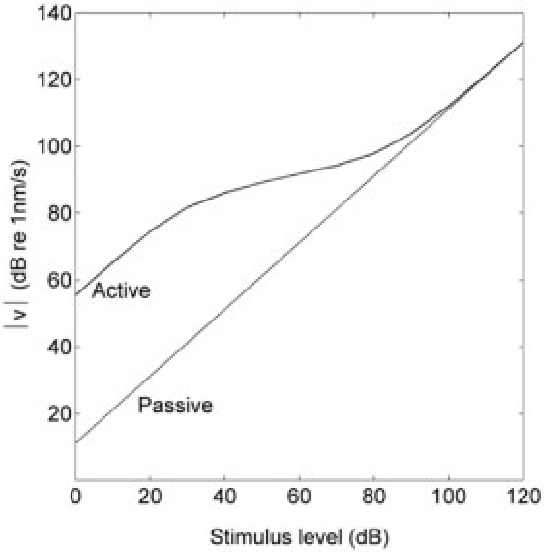

Figure 1.11: Compression in the human cochlea. The compression phenomenon due to cochlear amplification is illustrated in this plot, which is a combination of the linear passive mechanics and the saturating active mechanics. Reproduced from (Elliott and Shera, 2012).

Therefore, the cochlea has the capacity to act actively or passively. How does it achieve this? How are low level stimuli amplified, making them easier to perceive, while high level ones are not? The answer lies in a biological active feedback system situated within the inner ear that is referred to as the cochlear amplifier (CA). The CA can amplify the motion inside the inner ear by more than 40 dB at low excitation levels, but saturates at higher levels. This is because the transduction process performed by the OHCs that lead to cochlear amplification is highly nonlinear, as illustrated in Figure 1.12, which shows the input-output characteristics of a hair cell.

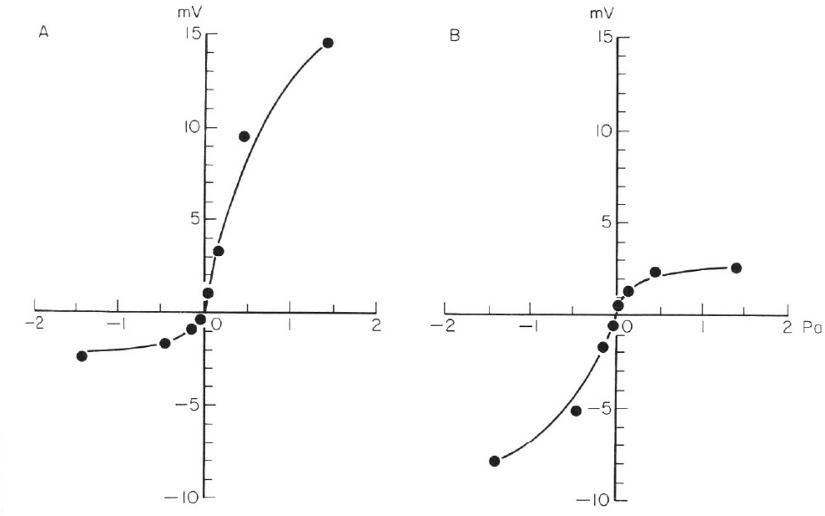

Figure 1.12: Transfer responses of IHCs and OHCs: intracellular voltage against the instantaneous pressure of a $600Hz$ tone stimulus. On the left is the transfer function of IHCs while the plot on the right shows the transfer function for OHCs. Reproduced with permission from Cody and Russell (1987).

It is important to understand how and where the nonlinear behaviour of the cochlea takes place. One of the origins of nonlinearity is without a doubt due to the MET process in the stereocilia and its effect on the CA (Guinan Jr. et al., 2012). With reference to Figure 1.13 (**A**) and (**B**), when the stereocilia are displaced towards the tallest row of the bundle due to the shear movement between the BM and the TM, tip links attached between adjacent stereocilia pull open channels on their apical end, allowing a flow of current into the hair cells. The tip links can be thought of as damper-spring mechanisms that when pulled with sufficient tension, cause the opening of the channels and therefore depend on both displacement and velocity of the shear motion between the BM and the TM. The mechanical opening of the channels generates a receptor current due to the endocochlear potential across the hair cells. This current causes a piezoelectric reaction in OHCs because of a motor protein named Prestin, as illustrated in Figure 1.13 (**C**). Prestin is unique to the mammalian auditory system, in that its piezoelectric capabilities allow motion at audio frequencies. In particular, depolarization of the hair cell produces OHC contraction and hyperpolarization causes OHC elongation, therefore generating a force on the cochlear partition (Guinan Jr. et al., 2012). This active mechanism works to its full potential with low level incoming sounds, which causes amplification of motion of the cochlear structures, i.e. amplification of the signal. However, when further elongation/contraction of the OHCs is no longer possible at higher SPLs, then saturation of system occurs, meaning that active amplification of the travelling wave will not take place.

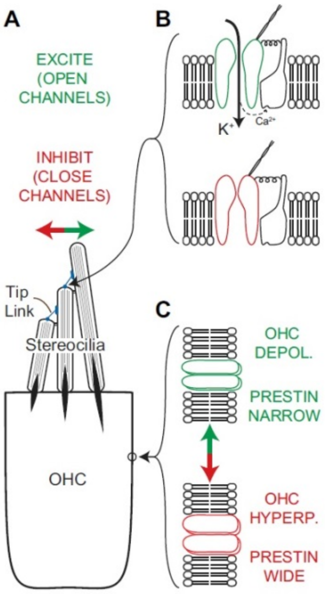

Figure 1.13: Mechanism of the stereocilia that provides OHC amplification. Reproduced with permission from Guinan Jr. et al. (2012).

The CA is thus crucial for a correct functioning of the auditory system and determines the sensitivity and selectivity of our sense of hearing. The nonlinearity of the active process is the cause of many features of the cochlear response that are discussed in the following chapters, in particular, compression, self-suppression and OAEs.

1.2 Objectives

This project involves investigating the effect of the nonlinearity of the CA and how it may play a role in the active processes in the cochlea. The properties of the nonlinearity are modified by active hair-bundle motility, which is a result of adaptational mechanisms in the hair-bundles, and can be studied using suitable cochlear models. This will allow the understanding of wave propagation within the inner ear and therefore of cochlear mechanics and cochlear amplification. Various mechanisms that occur in the human inner ear will be analysed in order to develop a cochlear model, which is cast in a state space formulation. It is then possible to predict the stability of the model and the motion of the cochlear structures, by performing frequency and time domain simulations. A quasi-linear model is also developed to predict self-suppression of the cochlea. Simulations give insight into nonlinear mechanisms that generate OAEs and the simulated emissions can then be compared to real experimental data. In summary, the main goals of this thesis are:

- To deduce a set of micromechanical parameters that can replicate the properties of the human cochlea, such as frequency tuning, dynamic range and the travelling wave (TW)
- To replicate a quasi-linear model based on Kanis and de Boer (1993, 1994) and a state space model based on Elliott et al. (2007) using the new human parameters
- To review previous work that has been performed on the suppressive properties of the cochlea and on OAEs, with particular attention to spontaneous OAEs (SOAEs)
- To simulate SOAEs using the state space model and replicate experiments performed on these emissions. This will help understand the underlying cause that generates SOAEs and other phenomena linked to the CA

1.3 Contributions

The following is a list of the main contributions of this doctoral research:

- The development and tuning of a nonlinear model of the human cochlea, validated against previous measured BM response data
- Significant reduction has been achieved in the calculation time of time domain simulations by pre-calculating initial conditions, which allows many sets of results to be calculated
- Simulations of the effects of low frequency bias tones on SOAEs have been performed in order to evaluate the nonlinear properties of the CA according to a method described in the literature by Bian and Watts (2008). Results were compared with experimental ones by Bian and Watts (2008), demonstrating that the method they describe does not measure accurately the characteristics of the nonlinearity of the CA
- Simulations of the effects of swept tones interfering with an SOAE were undertaken that were compared with experimental results by various authors (Bergevin and Salerno, 2015; Bergevin et al., 2015; Hansen et al., 2014). Simulation results demonstrate that nonlinear effects take place when such an experiment is performed, however, raise the question of whether entrainment or suppression or both phenomena are taking place

- Simulations of the effects of a high level low frequency tone interfering with an SOAE were performed; results show that the model does not account for nonlinear auditory effects reported during experiments on human subjects by Kugler et al. (2014)
- Simulations of click evoked otoacoustic emissions (CEOAEs) were performed; numerical results demonstrated that CEOAEs are strictly related to the threshold microstructure exhibited by the cochlear model, which has also been demonstrated experimentally
- The state space cochlear model was used to simulate other phenomena, i.e posture change and virtual bass, proving to be a valuable tool for understanding cochlear mechanics

The findings of the work presented in this thesis have been shared with the academic community through the following papers:

- Vignali, D., Elliott, S. j. and Lineton, B. (2015). 'Modelling the effect of low frequency bias tones on spontaneous otoacoustic emissions,' Proc. Int. Conf. Sound and Vibration (ICSV22), Florence, Italy.
- Shuokai, P., Elliott, S. J. and Vignali, D., (2015). 'Comparison of the nonlinear responses of a transmission-line and a filter cascade model of the human cochlea,' Applications of Signal Processing to Audio and Acoustics (WASPAA), 2015 IEEE Workshop on, New Paltz, NY, 2015, pp. 1-5.
- Vignali, D., Elliott, S. J. and Lineton, B. (2016), 'Modelling interactions between spontaneous otoacoustic emissions and external stimuli,' BSA Annual Conference, Poster Session.
- Vignali, D., Elliott, S. J. and Lineton, B. (2016), 'Modeling dynamic properties of spontaneous otoacoustic emissions: Low-frequency biasing and entrainment,' J. Acoust. Soc. Am. (171st Meeting Acoust. Soc. Am.), 139, 2074-2075

The research undertaken for the present thesis has resulted in the following awards:

- The Sir James Lighthill Prize in the Best Student Paper Competition at the 22nd International Congress on Sound and Vibration (ICSV22), Florence, Italy.
- Travel award for the Spring 2016, 171st meeting of the Acoustical Society of America, in Salt Lake City, Utah.
- Award for Best Overall Contribution First Prize at the Institute of Sound and Vibration Research (ISVR), Signal Processing and Control Group (SPCG), Away Day, 2016.

1.4 Thesis structure

The main goal of the work undertaken for this doctoral research was to model cochlear nonlinearities in the human auditory system. This study required background knowledge in the field of cochlear mechanics and cochlear modelling before delving into numerical models that replicate the dynamics of such organ. After the brief introduction to the anatomy of the mammalian cochlea in Chapter 1, Chapter 2 investigates the current thoughts in nonlinear cochlear mechanisms in the research community. An effort has been made to reproduce the most important notions found in the literature regarding the CA and OAEs, with particular attention to SOAEs. Chapter 3 reviews various cochlear models that exist in the literature and focuses on the ones used for the research presented in this thesis. Chapters 4 and 5 describe how the model was tuned in order to perform simulations that replicate the properties of the human cochlea. Chapter 6 shows the results from the simulations where the effects of low frequency bias tones on an SOAE were investigated: these results are compared with data from experimental findings on real cochleae, in order to give a better insight into its functioning. This comparison of results is of fundamental importance to understand the validity and reliability of the model. In Chapter 7, other nonlinear effects of the CA are investigated: a swept tone and a high level low frequency tone are used as stimuli to understand their effects on an SOAE, and a click stimulus is sent as an input to the model, in order to understand how the CA responds and how this response may be related to the internal microstructure of the cochlea. A small section is also dedicated to how changes in the middle ear may affect the CA. Chapter 8 summarises the findings of this research and suggests further work to be conducted.

Chapter 2

Nonlinear mechanisms in the cochlea

Developing a model of the human cochlea requires, on the one hand, inclusion of all the necessary details that are responsible for the correct functioning of this organ, and on the other hand, neglecting characteristics of the cochlea that do not play an essential role in its working. Making simplifications to the structure allows for an easier, but nonetheless efficient, computation of the model. This Chapter reviews the mechanisms present in the cochlea deemed necessary for a correct development of a cochlear model. It also discusses the active process that occurs in the peripheral auditory system, which produces OAEs as a by-product of its normal function. The assumptions made about the parameters of the cochlear model will be discussed in Chapters 3, 4 and 5. The second part of this chapter reviews the source, classification and properties of OAEs and different kinds of OAEs are then considered and explained. Finally, SOAEs are discussed in more detail, in order to understand how they occur and what experiments have been done to determine their properties, with the aim to cover what is most relevant for this project.

2.1 The active process of the peripheral auditory system

During Von Békésy's ground-breaking studies in the 1940s, many aspects of the cochlea were uncovered (von Békésy, 1949); one of his discoveries was the existence of travelling waves that excite the BM at a specific position according to the stimulus frequency, as shown in Figure 1.8. However, Békésy was working on dead specimens of the cochlea and therefore could not explain the extraordinary frequency resolution achieved by the BM, which would later be explained as an active process taking place in the inner ear and was no longer operational in dead specimens.

In 1948, an hypothesis of an active process occurring in the inner ear had already been proposed (Gold, 1948) that could explain the powerful self-tuning properties of the BM when responding to specific frequencies. According to Gold, an active element played a fundamental role when perceiving sounds that allowed the cochlea to be more sensitive to low level sounds and also more frequency selective. This theory, named the 'regeneration hypothesis', tried to explain how the viscous damping of the fluids in the cochlea is counteracted in order to perceive sounds correctly. Gold also mentions what he calls 'ringing' of the ear, which occurs when one of the active elements enters a state of self-oscillation and may result in "*the sensation of a single clear note of steady pitch*" (Gold, 1948). This 'ringing' may be thought of as a by-product of the 'regeneration hypothesis'. Hence, even before the first actual measurements of any form of OAE that occurred a few decades later, the theories postulated by Gold to explain the auditory system's great tuning capacities, already accounted for some kind of emission to occur.

What was clear at this point was that without some form of enhancement, the observed selectivity and the sensitivity of hearing could not be predicted from the BM measurements performed by Békésy. The main problem was trying to understand the source of what seemed to be a cochlear amplification process. The discovery and measurement of OAEs by Kemp in 1978 (Kemp, 1978) partially solved this dilemma, and helped to confirm the theory of a positive feedback mechanism that would enhance the BMs sensitivity and selectivity. The electro-motile response of the OHCs is now thought to be the driving force for the CA and hence to play an important role in OAE generation (Oghalai, 2004; LeMasurier and Gillespie, 2005; Kemp, 2009). This was experimentally proved by work performed on undamaged cochleae and further work on the functioning process of OHCs (Sellick et al., 1982; Brownell, 1990). Nevertheless, despite the numerous experiments undertaken to understand the nature of OAEs, it is not yet completely clear how this phenomenon is physically possible. What is clear is that a nonlinear active phenomenon does occur within the cochlea, which causes the BM to be sharply tuned (Johnstone et al., 1986) and that the emissions produced by the ear are considered to be by-products, or epiphenomena (Shera, 2003), of this active process. Since the CA is too difficult to observe directly, it may be that the properties of OAEs can be used to throw light on its operation.

As discussed in Section 1.1.3, the CA depends on the MET process of OHCs, and these hair cells behave nonlinearly, as demonstrated in Figure 1.11. The response of the cochlea varies according to the level of the external stimuli. Low level stimuli are boosted by the CA but as the level of a stimulus is increased the action of the CA decreases leading the latter's response to a saturation point and to what is known as self-suppression. The nonlinearity introduced by the OHCs defines the mechanics of motion of the cochlear structures and many studies have been performed to understand the nonlinear form of the OHC's transfer function (Nieder and Nieder, 1971; Bian and Watts, 2008; Brownell, 1990; Ospeck et al., 2003; Johnson et al., 2011; Zha et al., 2012).

Experiments on hair cells are often performed in vitro and may not faithfully reproduce OHC nonlinearity. However, Johnson et al. (2011) showed that if in vivo conditions are replicated in the environment where the OHCs are studied, then it is possible to obtain a more realistic transfer response from the OHC. The difference between the nonlinear properties of the OHC analysed in different environments are shown in Figure 2.1: (**E**) shows the estimated nonlinear function of OHCs in perilymph, which is an unrepresentative condition, while (**F**) shows the estimated nonlinear function of OHCs in endolymph, which is a more realistic condition.

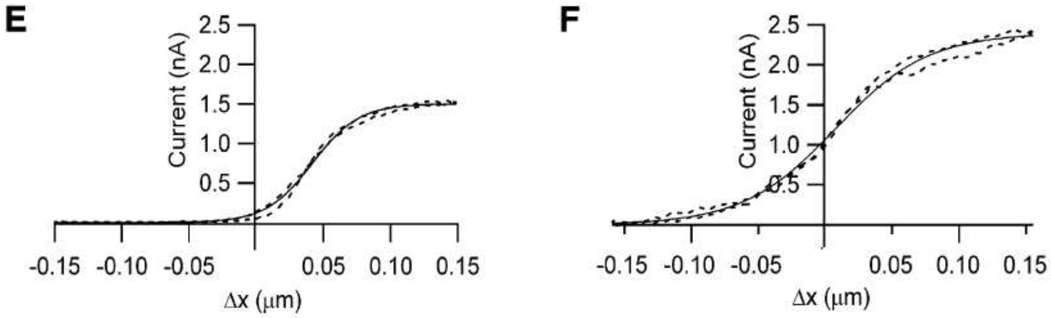

Figure 2.1: Transfer response of OHCs. Experiments performed on OHCs reveal their transfer response in terms of current vs. motion, when the cells are submerged in perilymph (**E**) and when they are submerged in endolymph (**F**). Reproduced from Johnson et al. (2011). No permission required.

In both scenarios, the transfer functions resemble that of a Boltzmann function. However, in the more realistic scenario in Figure 2.1(**F**), an increase in both the maximum current amplitude and the current activated by the OHC at rest are necessary conditions for a normal working OHC; these characteristics resemble a nonlinear Boltzmann function, whose asymmetrical features are very subtle. Moreover, this implies that the OHC channels have approximately a 0.5 probability of being open at rest, allowing a current of 1 nA to flow within the cell when there is no shear displacement between the BM and the TM. In the unrepresentative scenario shown in Figure 2.1(**F**), barely any current flows through the OHC when their is no shear displacement, and for maximum values of shear displacement the current reached, of approximately 1.5 nA, is not a realistic hypothesis when compared to the true nonlinearity represented in Figure 2.1(**E**). It will be shown later in Chapter 5 that these notions are fundamental for the correct development of a cochlear model.

In summary, sound-transduction performed by the peripheral auditory system is of fundamental importance for normal hearing and relies greatly on the nonlinearities of the system. In particular, the cochlea is an organ that involves nonlinear signal transformation that generates a number of important phenomena (Cooper, 1996), of which otoacoustic emissions is just one of them.

2.2 Otoacoustic emissions

Otoacoustic emissions are sounds that are detected in the ear canal (Hall, 2000) due to nonlinear interactions within the cochlea. The generation of OAEs is directly related to the electromotive action of OHCs, hence these emissions are carriers of important information residing in a microscopic and inaccessible area in the cochlea. OAEs vary from individual to individual and tend to remain very stable over time (Kemp, 2009). Therefore, OAEs are potentially an excellent way to monitor and probe the inner ear. Measurements of these sorts can be undertaken in vivo without compromising the cochlea's normal behaviour (Brownell, 1990; Shera and Guinan, 1999), which is otherwise vulnerable to more invasive measurements of BM motion. Differences can therefore be sought between healthy and unhealthy ears, since OHCs play an important role in the health of the peripheral auditory system. In fact, the production of OAEs following an acoustic stimulus through the ear canal is now considered such a good indication of healthy OHCs that it is common practice to use them to carry out screening tests on neonates in order to assess their hearing capabilities (Hall, 2000).

OAEs can be defined as sounds that are generated within the cochlea and escape the ear canal (Kemp, 2009). Their measurement was first reported in 1978 by Kemp (1978, 1979). He was able to measure emissions originating in the inner ear of human subjects when stimulating it with a low level stimulus. They were recorded by inserting a microphone probe into the auditory meatus while the latter was sealed. The emissions recorded by Kemp were found to be present in healthy human ears but not in ears affected by cochlear deafness. OAEs are now a well-established phenomena that have taken an important role in research within the auditory community. Their discovery had an enormous impact in the field of auditory sciences: first of all it was the beginning of a new topic to be investigated in more detail; secondly it supported the theory that the cochlea exhibits a nonlinear active behaviour.

The OHCs take part in the process that amplifies weak signals within the inner ear, known as the CA; these cells are capable of generating unique vibrations on the BM at specific frequencies depending on their position along the BM and on the intensity of the external acoustic stimulus. Weak stimulations are amplified, and the energy produced by the OHCs may escape from the inner ear, pass through the middle ear and reach the ear canal in the form of acoustical energy, therefore producing an OAE. However, OAEs generated at positions along the cochlea tuned to frequencies at and nearby the frequencies of high-level stimuli presented to the ear can be totally or partially suppressed (Long et al., 1990). Moreover, if the ear is presented with a pure tone stimulus, phenomena known as beating and entrainment, which shall be discussed later in this chapter, can occur depending on the intensity of the tone and its frequency with respect to the frequency of the OAE and in particular SOAEs (Long et al., 1990).

2.2.1 Importance of OAE

OAEs are invaluable tools for helping us understand the mechanics of the cochlea and therefore the mechanisms of a healthy, or unhealthy, ear. The fact that their measurement is non-invasive and performed on living subjects is very important, since it allows investigation of the properties of the CA without having to interfere with or dissect the cochlea, in which case it may totally or partially loose its active properties.

So why are OAEs so important? What makes them so interesting? It has already been mentioned that they are used to determine, non-invasively, potential hearing loss in new born babies (Hall, 2000). In fact, if OAEs are not present in an individual, whether a neonate or an adult, then the latter is probably affected by sensory transmissive hearing loss, i.e. "*poor transmission and frequency analysis of sound energy through the structures of the cochlea onto the sensory inner hair cells*" (Kemp, 2009). Appropriate treatment can then be given, whenever possible, to restore hearing to the individual.

The possibilities given by exploiting these emissions go further still; the properties of OAEs have been related to intracranial pressure (de Kleine et al., 2000; Voss et al., 2006). Abnormal intracranial pressure may occur for different reasons, for example head trauma, stroke, etc. and its variation has been associated with OAE frequency modulation. Hence, OAE analysis can potentially serve as a unique, non-invasive technique to monitor brain pressure and substitute other invasive methods (Voss et al., 2006).

Research has been undertaken to understand if OAEs can reveal certain hearing pathologies other than sensory transmissive hearing loss. Endolymphatic hydrops, i.e. an increase in pressure of the endolymph caused by an obstruction of the flow through the endolymphatic duct (Pickles, 2012), cause alterations to specific types of OAEs (Fetterman, 2001). It is also well-established that OAEs can be subject to changes in intensity if an individual is exposed to intense noise, especially if for long durations, ototoxic trauma or certain drugs (Kemp, 2009). In these cases, a modification of the emissions can be directly related to changes in the OHCs properties, and potentially OHC damage.

2.2.2 Types of OAE

OAEs are categorised depending on how they are generated. They are generally measured by inserting a probe into the external ear that seals the ear canal. The probe consists of an earphone that sends an appropriate stimulus to the ear and a microphone to detect the acoustic response, i.e. the OAE generated inside the cochlea. The acoustic stimulus sent to the ear determines the type of OAE detected by the microphone.

Different theories exist about OAE generation of which two are the most prominent: one is the mechanism-based taxonomy for OAEs suggested by Shera and Guinan (1999), where OAE generation is either due to linear reflections or to nonlinear distortions or a combination of these. Another theory supports the idea of local oscillators placed along the length of the cochlea that play an important role in the generation of OAEs. The work in this thesis supports the mechanism-based taxonomy for OAEs suggested by Shera and Guinan (1999).

Shera and Guinan (1999) hypothesize that "*evoked otoacoustic emissions arise by two fundamentally different mechanisms within the cochlea*". In other words, each type of OAE is the product of one, or a combination of two different mechanisms associated with the mechanics of the cochlea. These differences are due to the origin of the particular emission and are summarised schematically in Figure 2.2.

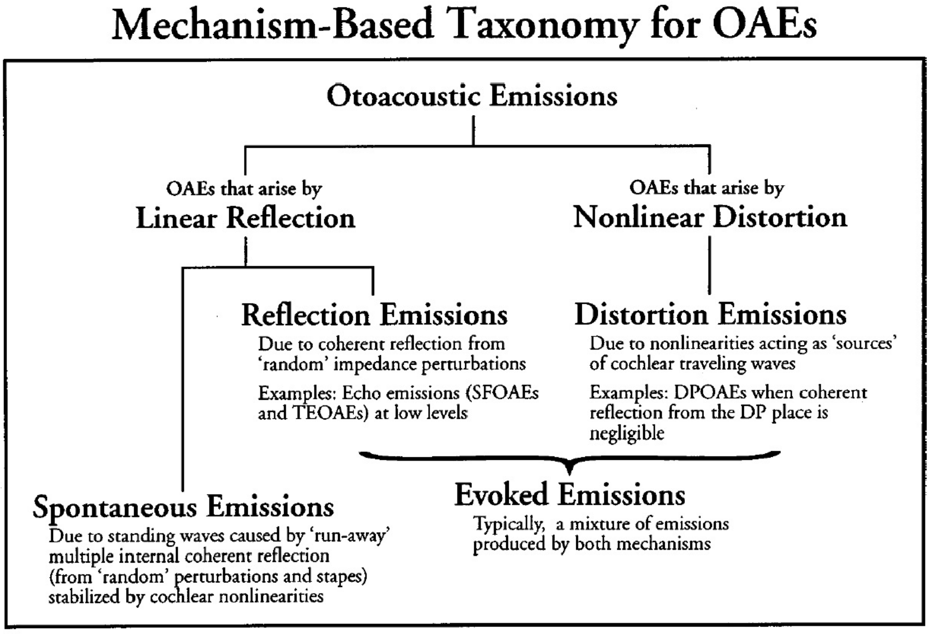

Figure 2.2: Taxonomy of otoacoustic emissions. Reproduced with permission from (Shera and Guinan, 1999).

Stimulus Frequency OAEs (SFOAEs), which include SOAEs and Transient Evoked OAEs (TEOAEs), are categorised as emissions that arise by linear reflection sources, while Distortion Product OAEs (DPOAEs) are regarded as emissions that arise by nonlinear distortion sources (Shera and Guinan, 1999, 2003; Shera, 2004).

Although spontaneous and reflection emissions arise from linear reflections, as shown in Figure 2.2, it can be argued that these types of OAEs are also affected by nonlinearity. Thus, in the case of SOAEs, linear reflections will undergo an amplification process because of the CA that will keep the travelling wave from decaying and therefore the SOAE stable, but the nonlinearity will limit their amplitude.

This mechanism-based taxonomy for OAEs is in contrast to a previous view of OAEs that can be found in the literature, for example in Kemp (1980), where all emissions are thought to be caused by nonlinear distortion possibly arising from the electromotive action of OHCs. Nevertheless, Kemp (1978) previously raised the possibility that the origin of the emissions could be attributed to a cochlear reflection hypothesis and, in a similar way, termed the mechanisms shown in Figure 2.2 as place-fixed, where a linear reflection due to irregularities along the cochlea is produced, and wave fixed, due to nonlinear distortions generated by the interference of stimuli of different frequencies and the activity of the CA (Kemp and Brown, 1983).

A further line of thought pursued by many researchers is that OAEs do not occur through backward travelling waves occurring on the BM, but that emissions escape the cochlea via other routes, such as 'fast wave' cochlear fluids (He and Ren, 2013). This hypothesis would obviously give far more importance to the interaction between fast and slow waves that propagate in the cochlea, but does not seem to be necessary to explain the results discussed in this thesis and so is not pursued further.

Transient evoked otoacoustic emissions (TEOAE)

TEOAEs are OAEs of the linear reflection family (Figure 2.2) that occur when stimulating the ear with a click sound (Kemp, 2009), or other short signals such as tone bursts. The interesting feature about stimulating the cochlea with a click is that the broad frequency spectrum of the stimulus can stimulate a large portion of the cochlea, therefore creating a travelling wave that runs across much of the BM, generating multiple emissions. An example of the response of a human cochlea to a click sound is shown in Figure 2.3. The time series of the TEOAE is shown in the left panel as a waveform that starts at approximately 3 ms and lasts approximately 20 ms. The inset figure in the left panel shows the click used as a stimulus and it can be seen that it has a duration of about 1 ms. Both signals are measured by the microphone in the probe, and can be distinguished in the time domain due to the delay between them, allowing them to be separated.

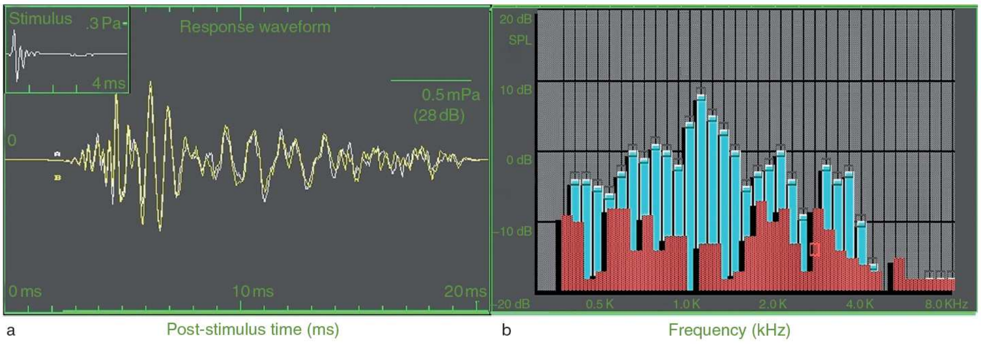

Figure 2.3: Response of a TEOAE evoked by a click. The time series in the left panel shows the emission where the click stimulus, shown in the inset, has been deleted. The right panel shows in blue the spectra of the emission in third octave bands, where the sound pressure level of each band represents otoacoustic emission content. Reproduced with permission from Kemp (2009).

The spectral content of the waveform, plotted with blue columns in the right panel, shows otoacoustic emission content within third octave bands. As shown in Figure 2.2, the development of TEOAEs is thought to be caused by reflection sites occurring irregularly along the cochlea that reflect the travelling wave back to the base of the cochlea. Energy is then transferred through the middle and outer ear, ultimately into an acoustic signal. Adding to this is the electro-motile action of the OHCs that amplify the stimulus at particular frequencies, feeding the reflected wave with enough energy to allow part of it to be emitted in the ear canal (Hall, 2000; Kemp, 2009).

A person affected by hearing impairment, in particular sensory hearing loss, is generally not able to hear sounds properly at frequencies at which an OAE cannot be emitted. Hence, performing a frequency analysis of TEOAEs can help understand whether the OHCs along the length of the cochlea are functioning or not. This said, the TEOAE technique is mainly valid in the frequency range between 1 to 4 kHz (Kemp, 2009), as can be seen also in Figure 2.3, partly due to the band-limiting transmission properties of the middle ear. TEOAEs vary from individual to individual but they tend to remain fairly constant over time, unless the ear undergoes trauma that modifies its behaviour.

Distortion Product Otoacoustic Emission (DPOAE)

DPOAEs are part of the family of nonlinear distortion emissions shown in Figure 2.2 and result from a nonlinear interaction amongst multiple tones. The principle behind the measurement of these emissions is that two pure tones presented to the ear will produce OAEs with frequencies equivalent to harmonic distortions of each tone and intermodulation distortion products between the two tones (Kemp, 2009). The tones used for such measurements are generally quite close in terms of frequency (one third of an octave apart). The stimulus and the DPOAEs are measured by the microphone and can be separated in the frequency domain in order to obtain a spectrum as the one shown in the left panel of Figure 2.4. The predominant DPOAEs are narrow-band pass filtered when recorded. Reichenbach et al. (2012) also emphasize that DPOAEs are generated by nonlinear distortion on the BM, but they suggest that these travel back towards the middle ear on both the BM and on Reissner's membrane.

The advantage of measuring DPOAEs is that the excitation frequencies and the distortion frequencies can be close; therefore, by stimulating a limited region of the cochlea, the sensory cells try to respond to the excitation tones individually and consequently create distortion. Hence, if the BM is stimulated by tones of frequencies f_1 and f_2, vibrations at new frequency components such as $2f_1 - f_2$ can arise. An example is shown in Figure 2.4, which illustrates the spectrum of the stimuli and of the distortion products; the right panel shows a DP-gram, which plots the SPL of the $2f_1 - f_2$ DPOAE against the frequency of f_2, where the ratio f_1/f_2 is kept constant. This can provide more detailed information about OHC motility up to a higher range of frequencies compared to a spectrogram of TEOAEs (Kemp, 2009).

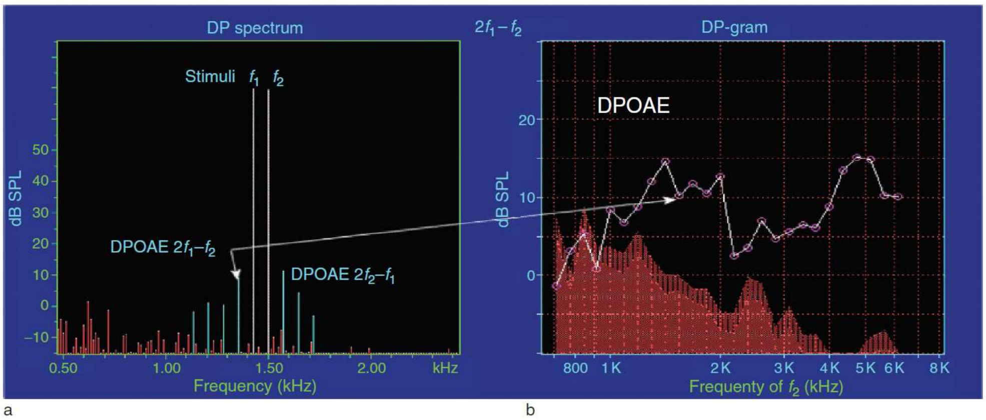

Figure 2.4: Response of a distortion product otoacoustic emissions (DPOAE). DPOAEs arise from intermodulation between two frequency components, in this case f_1 and f_2. The right panel shows a DP-gram, where the distortion product $2f_1 - f_2$ is plotted for increasing steps of f_1 and f_2 where the ratio f_1/f_2 is kept constant at 1.05. Reproduced from Kemp (2009). Permission requested.

Other types of OAEs

SFOAEs are OAEs of the linear reflection family that are measured when the cochlea is stimulated with a single tone; this method provides a way to analyse possible fluctuations over periods of time of OAEs generated at a specific position along the BM. It is also possible to use an acoustic stimulus that sweeps over a range of frequencies in order to ascertain OAEs produced over a wider portion of the BM (Kemp, 2009).

2.3 Spontaneous otoacoustic emissions (SOAE)

2.3.1 Importance of SOAE

SOAEs are one of the main topics under examination in this project. A brief introduction is given regarding their origin and some experiments concerning their properties are described.

Although it is shown in Figure 2.2 that SOAEs are emissions that are part of the linear reflection family, they occur spontaneously without any external acoustic stimulation. A reflection site along the cochlea, due to an irregularity, allows a forward travelling wave to be reflected and travel backwards to the middle ear where it is once again reflected, producing a forward travelling wave moving towards the irregularity. This back and forth motion of the travelling wave produces a standing wave. The active property of the CA plays a significant role in keeping the standing wave sustained. This is a result of the active process of the OHCs that overcome the loss of energy of the wave while travelling between the middle ear boundary and the site in the cochlea where the irregularity occurs (Shera, 2003). The compressive function of the nonlinearity prevents the amplitude of the emission from growing too large, therefore, producing a limit cycle (Shera, 2003; Ku, 2008). SOAEs are the product of unstable feedback loops present along the cochlea that can be considered as self-oscillatory sites along the BM located at specific positions (Shera, 2004; Ku, 2008). The phase accumulation in such a standing wave must be very precise, producing OAEs with a very narrow frequency band, typically of 1 Hz or less (Hall, 2000; Kemp, 2009).

Shera described SOAEs as a global collective phenomenon, "*necessarily involving the mechanics, hydrodynamics, and cellular physiology of the entire cochlea, as well as the mechanical and acoustical loads presented to it by the middle and external ears*" (Shera, 2003). Shera also proposes that a coherent reflection of waves is spanned over a region of the cochlea involving many hair cells, which is in contrast to a similar 'reflection theory' postulated by Kemp (Kemp, 1979), where reflection was thought to take place at specific points in the cochlea. The active global model takes account of the many properties of the cochlea that characterize spontaneous emissions. It explains that the dispersive nature of cochlear waves and the presence of distributed perturbations along the length of the cochlea allow for multiple emissions to be generated. Reflection occurs where the wave peaks, allowing for a round trip phase condition to be met, where the "*total phase change of the round trip wave travel is an integral number of cycles*" (Shera, 2003). Experimental observations on evoked OAEs have shown that in the frequency domain, emissions are arranged in an orderly pattern, "*consisting of regularly spaced, almost periodic peaks and valleys*" (Shera and Zweig, 1993). However, in the case of SOAEs, adequate amplification must occur to keep the wave from decaying, and since this will not be available throughout the whole length of the cochlea, SOAEs only occur at the various locations where the amplification criterion is met. The active global model predicts the characteristic minimum frequency spacing occurring between SOAEs, i.e. the minimum distance between neighbouring SOAEs, which is roughly (Shera, 2003)

$$\overline{\Delta x}_{SOAE} \approx \frac{1}{2}\lambda, \tag{2.1}$$

where λ is the wavelength of the travelling wave at its peak, but the spacing may be multiples of this. The ratio of the SOAE frequency to the spacing is given by

$$N_{SOAE} = \frac{\overline{f_{SOAE}}}{\Delta f_{SOAE}}, \tag{2.2}$$

where $\overline{f_{SOAE}}$ is the geometric mean between two adjacent SOAE frequencies and Δf_{SOAE} is the absolute value of the difference between the two frequencies. A histogram of the distribution of N_{SOAE} is shown in Figure 2.5 (Shera, 2003), using data of SOAE from Talmadge et al. (1993) and Burns et al. (1992). N_{SOAE} peaks at around 15, meaning that the SOAE spacing is approximately $\frac{1}{10}^{th}$ of an octave.

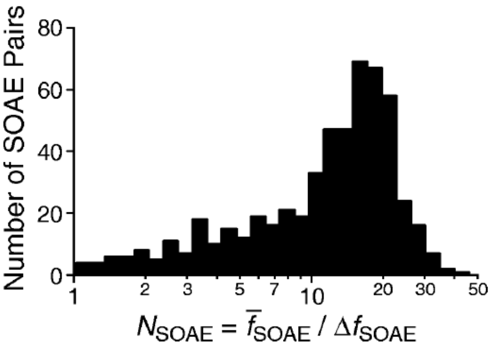

Figure 2.5: The histogram of N_{SOAE}. Reproduced with permission from (Shera, 2003).

It is possible to transform the SOAE signal into a complex phasor that can give useful information about the slowly varying amplitude and phase components of an SOAE. This is done by computing the Hilbert transform of the filtered waveform of the SOAE, which allows generating the imaginary part of the pressure from the measured real part (Shera, 2003). The probability distributions of an SOAE, which can be obtained by plotting the real part of the complex phasor of the SOAE against its imaginary part, has a very distinct shape (Shera, 2003), as shown in the left panel in Figure 2.6.

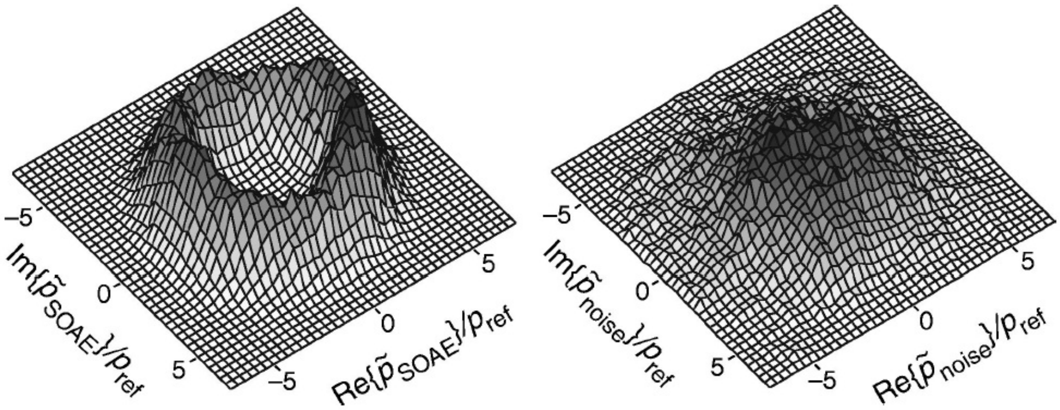

Figure 2.6: Probability distribution of a SOAE and of a noise signal. The plot on the left illustrates the statistical distribution of a SOAE and is compared with the plot on the right which is the distribution of noise filtered such that its power spectrum is equivalent to that of the SOAE. Reproduced with permission from (Shera, 2003).

The distribution takes the form of a ‘molerun’, demonstrating that SOAE amplitude fluctuations are very small, unlike SOAE phase, which is erratic over time. The plot in the panel on the right shows the probability distribution of a random noise signal that has been filtered such that its power spectrum is equal to that of the SOAE; the plot is characterised by a two-dimensional Gaussian distribution centred around the origin. The comparison between the two distributions with the same power spectra, shows that the statistical properties of SOAEs are very distinctive; similar results were previously obtained by Kemp (1984).

Although SOAEs are understood to be a ‘natural’ by-product of an important and necessary amplification process occurring in the ear, the literature seems to divide SOAEs in two categories: low frequency SOAEs, considered to be normally present in the majority of normal hearing people, and high frequency SOAEs, considered to be damage-related SOAEs caused by acoustic trauma, (Baiduc et al., 2014). In view of more recent studies conducted by Baiduc et al. (2014), it is still uncertain whether high frequency SOAEs, i.e. over 4.3 kHz, are attributable to cochlear pathologies.

One final categorization of SOAEs is necessary to avoid confusion regarding their origin: SOAEs can be divided into primary emissions, which are generated by cochlear instability, harmonic products, which are the harmonics of a primary emission, and distortion products, caused by the interaction between primary emissions. The cochlear model developed by Ku (2008) demonstrated that when many instabilities are present in the cochlea, these interact with one another in a complicated manner, generating different types of SOAEs.

2.3.2 Research on SOAEs

Roughness and fine structure of the mammalian cochlea

Before delving into experiments performed on SOAEs, it is necessary to understand two properties of the cochlea, known as cochlear roughness and threshold microstructure, which are thought to be highly related to the generation of SOAEs.

Experimental observations of the monkey cochlea have shown that it is not a smooth structure, but is characterised by irregularities along its length. Lonsbury-Martin et al. (1988), for example, obtained maps of the arrangement of OHCs in the rhesus monkey, shown in Figure 2.7, demonstrating that the cochlea presents what can be termed as cochlear roughness, an irregular alignment of OHC organisation that becomes more and more pronounced while moving towards the apex of the cochlea.

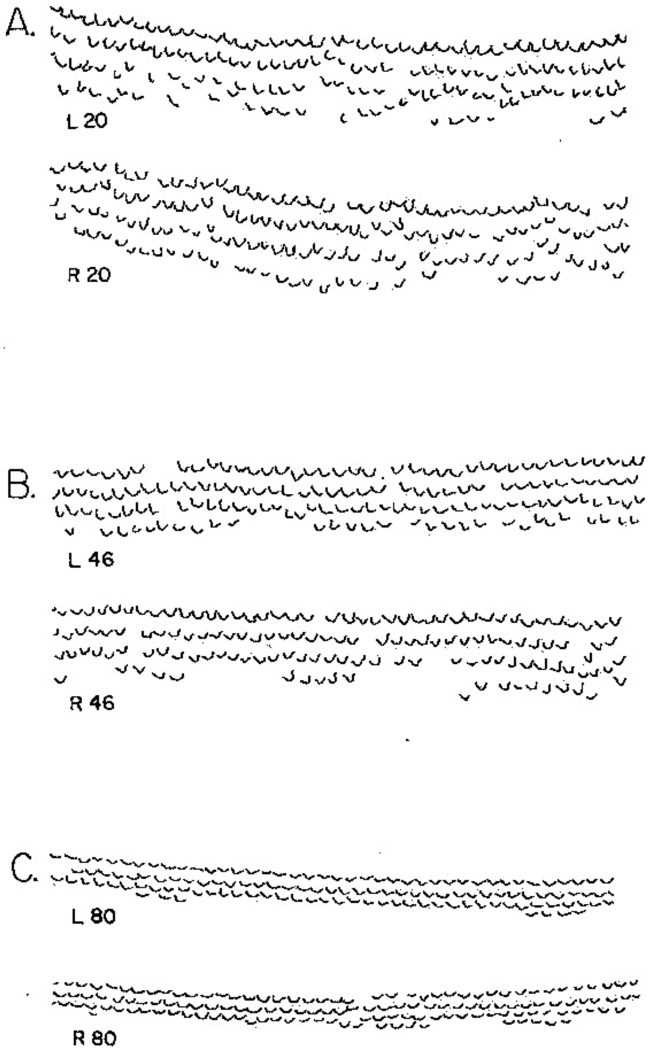

Figure 2.7: Detailed view of the organization of stereocilia bundles on OHCs at various sections along the length of the cochlea. They are taken from the left (L) and right (R) ears of rhesus monkeys having SOAEs; the numbers in the plots indicate the distance from the apex in percentage terms. A, B and C represent apical, middle and basal regions respectively. There is a striking difference between the patterns formed by the stereocilia that depends on the region along the cochlea where they are situated. Reproduced with permission from Lonsbury-Martin et al. (1988).

A striking difference appears in terms of organization and orientation of stereocilia bundles in different regions along the length of the OC. In the apical region that handles characteristic frequencies (CF) of approximately 500 Hz (20% distance from the apex) shown in Figure 2.7 (**A**), both stereocilia orientation and alignment are very irregular and disorganised; furthermore, four rows of OHCs are frequently seen. In Figure 2.7 (**B**), the middle region of the cochlea is shown, having CF of around 1.6 kHz (46% distance from the apex), where the bundles are slightly more organized and the fourth row is more intermittent. In the basal region that deals with frequencies around 16 kHz

(80% distance from the apex) shown in Figure 2.7 (**C**), stereocilia bundles are much more organized and the fourth row of OHC is nearly absent. Although the detailed relationship between the physical arrangement of the cochlea and SOAEs is difficult to understand, anomalies along the length of the cochlea are considered to be a feature of normal hearing ears in humans and primates, and their association with these types of emissions is a plausible hypothesis (Lonsbury-Martin et al., 1988; Hilger et al., 1995). In fact, it is highly plausible that cellular disorganization causes a gradual, but irregular, variation of impedance along the length of the cochlea, in particular moving towards the apex.

Elliott (1958) observed that when measuring thresholds in a human subject, sharp changes of sensitivity between frequencies that are very close to each other, in the order of tens of Hz, were present in the audiogram. These changes can be up to about 10 dB. The presence of ripples in the audiogram, as shown in Figure 2.8, is a universal phenomenon amongst humans and is known as threshold microstructure. This rippling effect has been associated with functional irregularities in the OC, i.e. cochlear roughness (Kemp, 1979).

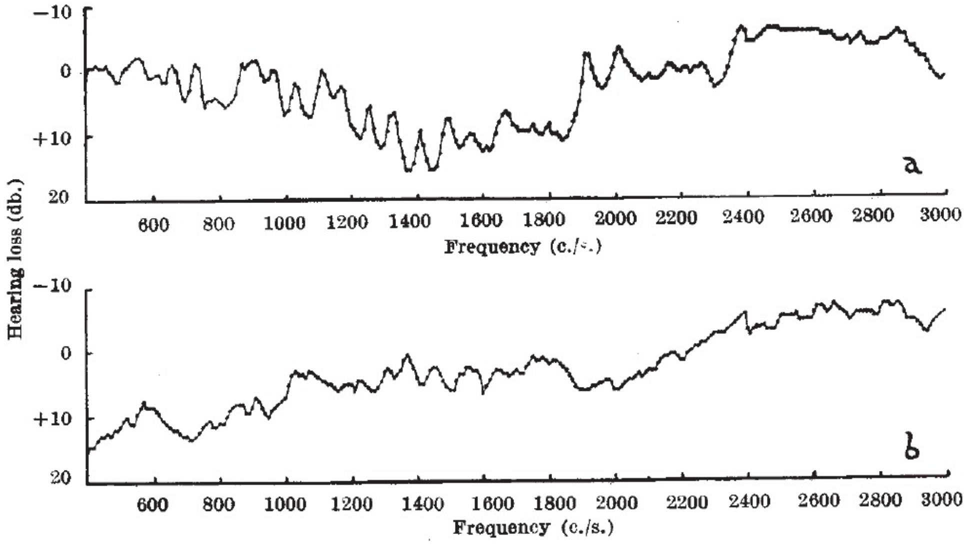

Figure 2.8: Audiograms of a typical threshold microstructure from two different subjects. Reproduced with permission from (Elliott, 1958).

Microstructure has been associated with the properties of specific types of OAEs, in particular reflection-source emissions (Shera and Guinan, 1999) i.e. SFOAEs (including SOAEs) and TEOAEs. Figure 2.9 shows the relationship between SOAEs and microstructure measured by Baiduc et al. (2014). It was experimentally shown that subjects with SOAEs also demonstrate microstructure pattern variation. In Figure 2.9, the black curves in the plots illustrate the spectra of SOAEs in 18 subjects, whose mean behavioural threshold, represented by the thick red curves, show a dip in the micrstructure of their thresholds in the vicinity of the frequency of the SOAE. These subjects were paired with other subjects having very similar behavioural thresholds in the frequency bands of interest, but no measurable SOAEs, and the microstructure of these subjects appeared to be more flat, as shown by the thick blue curves that represent the mean threshold of these subjects.

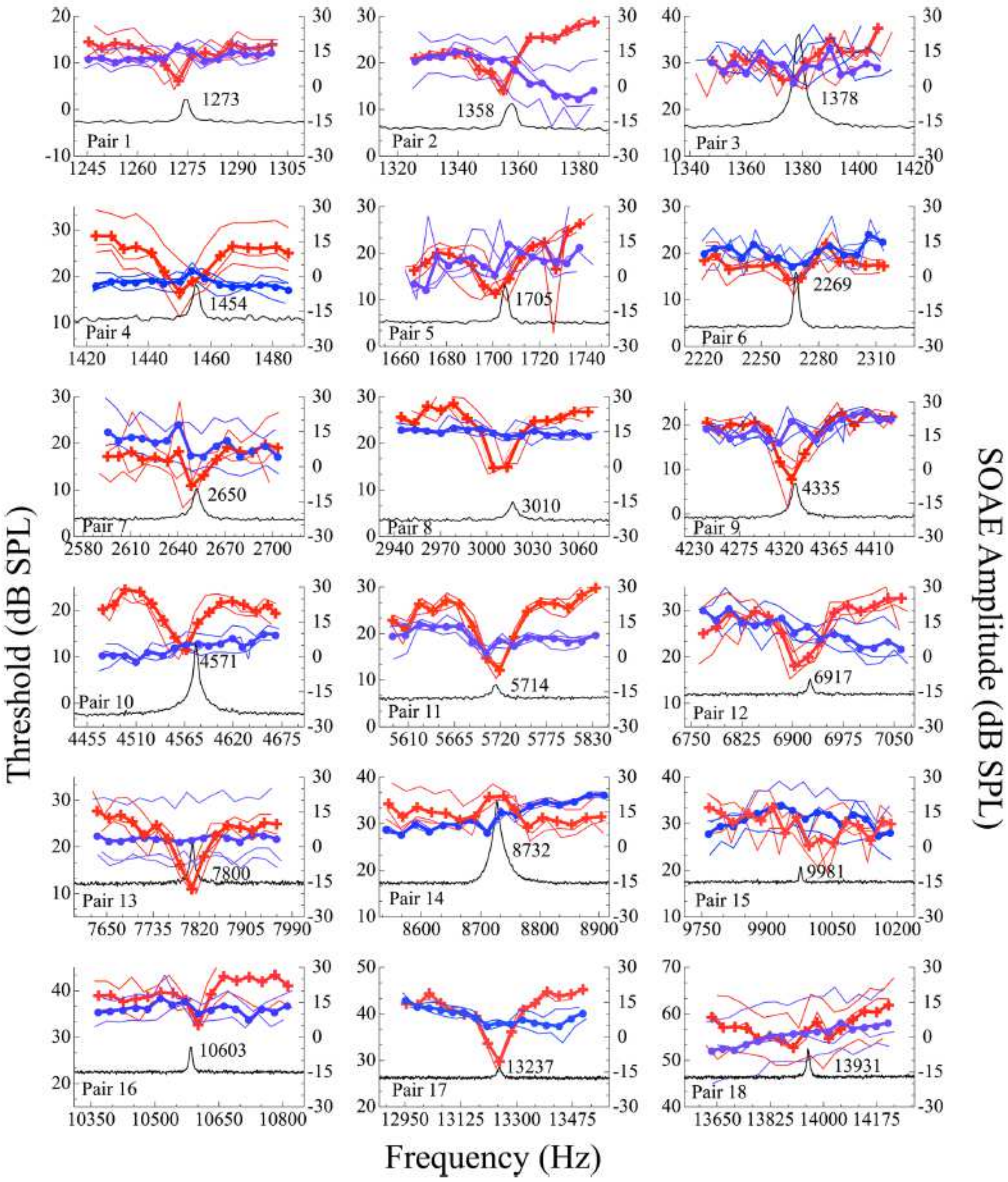

Figure 2.9: The 18 data-sets plotted are from 18 subject pairs, consisting of one subject having SOAEs matched to a subject with no measurable SOAE, but both subjects having similar threshold in certain frequency bands. The black curves show the spectra of an SOAE in the subject having emissions; the amplitude of the SOAE is shown in the ordinate on the right hand side of each plot. The red and blue curves show the behavioural thresholds in dB SPL, with the ordinate on the left hand side, of the subjects with and without the SOAE, respectively. The thin coloured lines represent the thresholds of a subject from three separate sessions, while the thick line is the mean of the three sessions. Reproduced with permission from Baiduc et al. (2014).

So very confined frequency bands with only one ripple in the audiogram, can be associated with an SOAE (Bright, 1985; Baiduc et al., 2014). Note that Figure 2.9 shows a few exceptions: subject 14, who has an SOAE, presents a trough rather than a dip in the microstructure, whereas subjects 15 and 18, both having an SOAE in the frequency band depicted, show a flat microstructure.

Furthermore, Brownell (1990); Long and Tubis (1988b) show that the consumption of aspirin has a short term deteriorating effect on SOAEs; SOAE suppression is accompanied by a 'flattening' of cochlear microstructure, as shown in Figure 2.10. This will be discussed further in the next section, regarding experiments on SOAE.

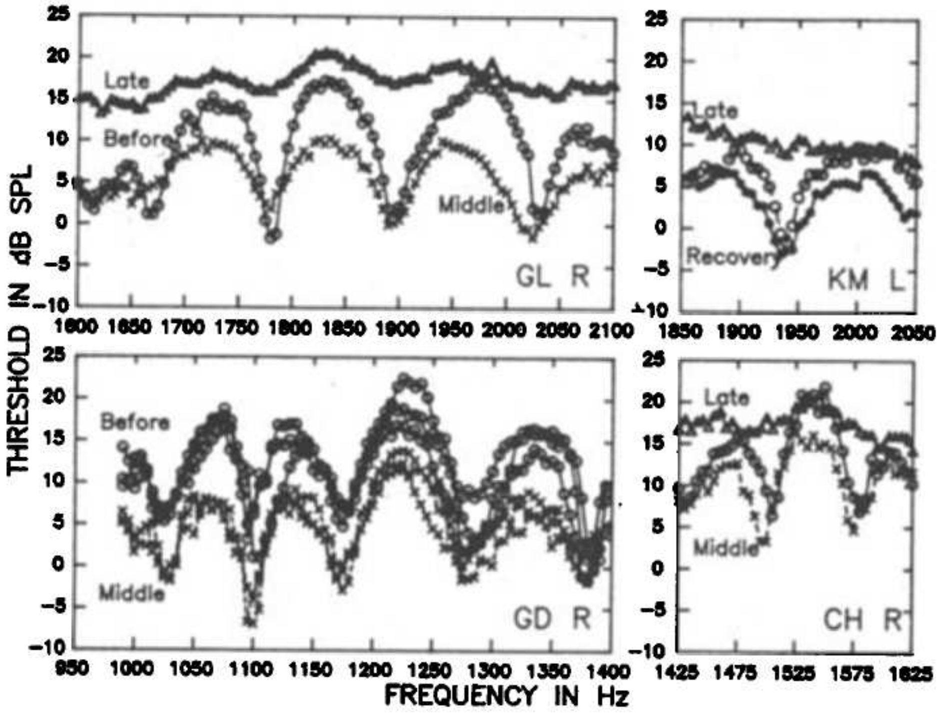

Figure 2.10: The four panels show the effect of aspirin on threshold microstructure in four different human subjects. The evolution undertaken by the threshold microstructure over time under the influence of aspirin is similar from subject to subject, and the top left panel, which is the most clear, is taken as an example: it can be seen that before aspirin consumption, the curve indicated by '*Before*' shows the typical threshold microstructure expected to be measured within a normal hearing subject; aspirin consumption then leads to an initial reduction of threshold microstructure, in particular at threshold maxima, accompanied therefore by increased auditory sensitivity, as shown by the curve indicated by '*Middle*'. After a certain amount of time has passed, a flattening of the threshold microstructure occurs, and therefore a decrease in sensitivity, as shown by the curve indicated by '*Late*'. Reproduced with permission from Long and Tubis (1988b)

2.3.3 Experiments

General aspects of SOAEs

SOAEs are present in most healthy ears, although they may be hard to measure without the correct equipment, given that isolation from noise floor is extremely important for their detection (Hall, 2000). SOAEs in human subjects seem to have a tendency to occur more in right ears and in greater quantity in female subjects (Burns et al., 1992). An impressive feature of SOAEs is there stability over time. Burns conducted a long term experiment by monitoring changes in SOAEs over a period of 19.5 years, noticing a slight linear change in their frequency of about $0.25\%/year$. On the contrary, level changes were quite unpredictable: changes did occur but were not consistent throughout subjects (Burns, 2009).

Experiments have demonstrated that SOAEs are not generated randomly along the length of the cochlea but instead their frequencies follow a pattern, as described in Section 2.3.1. Many theories have been suggested, demonstrating that the characteristic spacing between adjacent SOAEs increases in direct proportion to emission frequency (Braun, 1997; Shera, 2003) so that it is constant on a logarithmic scale, equivalent to a constant distance along the BM ($\approx 400\mu m$) or as a constant increase in fractions of an octave ($\approx \frac{1}{10}^{th}$ of an octave) (Braun, 1997). Braun argues that this pattern is only valid for two neighbouring emissions and that statistical analysis of SOAE data from many subjects shows no relation between system of multiples of the preferred minimum distance (PMD) and hence no spectral periodicity of SOAEs (Braun, 1997). On the contrary Shera confutes this prediction arguing that plotting the distribution of all SOAE pairs will inevitably provide weak relationships between emissions at multiples of the PMD. This relationship is foreseeable, however, if a first-order distribution is computed (Shera, 2003), as shown in Figure 2.5, where a peak occurs in the histogram at around 15, which would smear out if higher order distributions were calculated.

Various phenomena are known to affect the properties of SOAEs. Being aware of them is helpful to understand what physical circumstances are necessary to alter SOAEs and therefore inner ear properties such as cochlear fluid pressure, static displacement of cochlear membranes, etc.. Some interesting experiments from the literature that are known to affect SOAE are discussed below.

OAEs are affected by changes in cochlear fluid pressure. Pressure changes of the cochlear fluids are directly related to changes in intracranial pressure that can be caused by health related matters, such as a head trauma or a stroke. One method for inducing cochlear fluid pressure variations in a safe way is by subjecting human subjects to postural changes by using a reclining bed. OAEs measured in subjects affected by postural changes show that when the posture is such to increase the pressure of the cochlear fluids, OAEs are modulated in both amplitude and frequency (Voss et al., 2006; de Kleine et al., 2000, 2001). Figure 2.11 shows some examples of frequency modulation (FM) that occurs to an SOAE at 1065 Hz in a human subject when being tilted on the bed at specific angles.

The waterfall plot illustrates that after the subject is tilted to a recumbent position (head down 30 degrees) the SOAE centre frequency increased to 1090 Hz, the width of the peak increased and its height was decreased (de Kleine et al., 2000). It can also be seen that a new SOAE is generated at approximately 1170 Hz. The reason for these changes in emission properties is the increase in intracranial pressure and therefore of the cochlear fluids that press against the cochlear windows making them stiffer; this change will induce a modification of the overall impedance of the middle ear and consequently a change in its reflection properties.

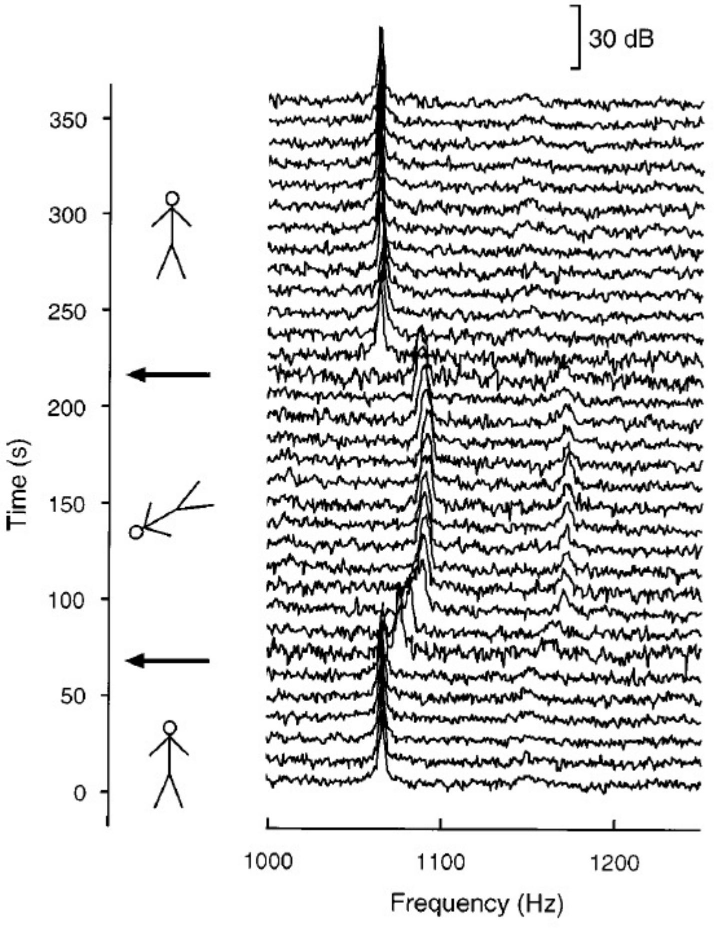

Figure 2.11: Frequency modulation of SOAEs during postural changes in human subjects. Reproduced with permission from (de Kleine et al., 2000).

Interaction between SOAEs and external low frequency tones

An interesting way to understand the properties of SOAEs is to observe how they interact with different external stimuli that induce changes in perilymphatic pressure. Bian and Watts (2008); Bian (2009) undertook experiments to observe the amplitude modulation (AM) and frequency modulation (FM) of SOAEs caused by low-frequency bias tones. Bian and Watts argued that by observing the relation between the AM and FM of a SOAE and a bias tone, the transducer function of OHCs could be obtained. The deduced nonlinear transducer characteristics resembled a 2^{nd} order Boltzmann function. OHC transfer functions were obtained, following Nieder and Nieder (1971), by performing what they term quasi-static analysis, where amplitude modulation of the SOAE was measured during the positive or negative half cycles of the low-frequency bias tone.

It was assumed that during the half cycles, OHC behaviour was quasi-static, i.e. a constant modulation of the amplitude of the SOAE. This experimental method relies on the fact that the frequencies of the bias tones are low enough to assume that the quasi-static behaviour is independent of bias tone frequency. SOAE amplitude is then plotted as a function of the peak level of the bias tone during its positive and negative half-cycles, as shown on the left of Figure 2.12, for many experiments with different levels of bias tone to give the individual data points shown. These points were fitted to bell shaped curves, obtained by taking the first derivative of second-order Boltzmann functions that are assumed to represent the cochlear transfer functions, which are then illustrated in the column on the right of Figure 2.12.

Although the bias tone frequencies change from plot to plot, the general bell shape of the curve is maintained; however, the higher the frequency of the bias tone the narrower is the width of the bell shaped curve, which does not fit well with the quasi-static assumption. One of the aims of this work was to replicate these experiments in a nonlinear numerical model of the cochlea. The exact form of the nonlinearity in such a model is known, so the nonlinear function derived using Bian's method can be directly compared with this to test the validity of the approach.

High level bias tones are able to reduce and eventually suppress the amplitude of the SOAE while producing side bands. The generation and subsequent suppression of side bands as a function of bias tone level, as observed by Bian and Watts (2008), is shown in Figure 2.13. The effect was greater for higher levels of the biasing tone, until total suppression of the emission occurred. The side bands occur at frequencies equal to $f_{SB} = f_{SOAE} \pm f_{bias}$. The low frequency bias tone is able to shift the cochlear partition, affecting the nonlinear dynamics of the OHCs that produce SOAEs, thus supporting the hypothesis that the SOAEs are by-products of the CA (Bian and Watts, 2008).

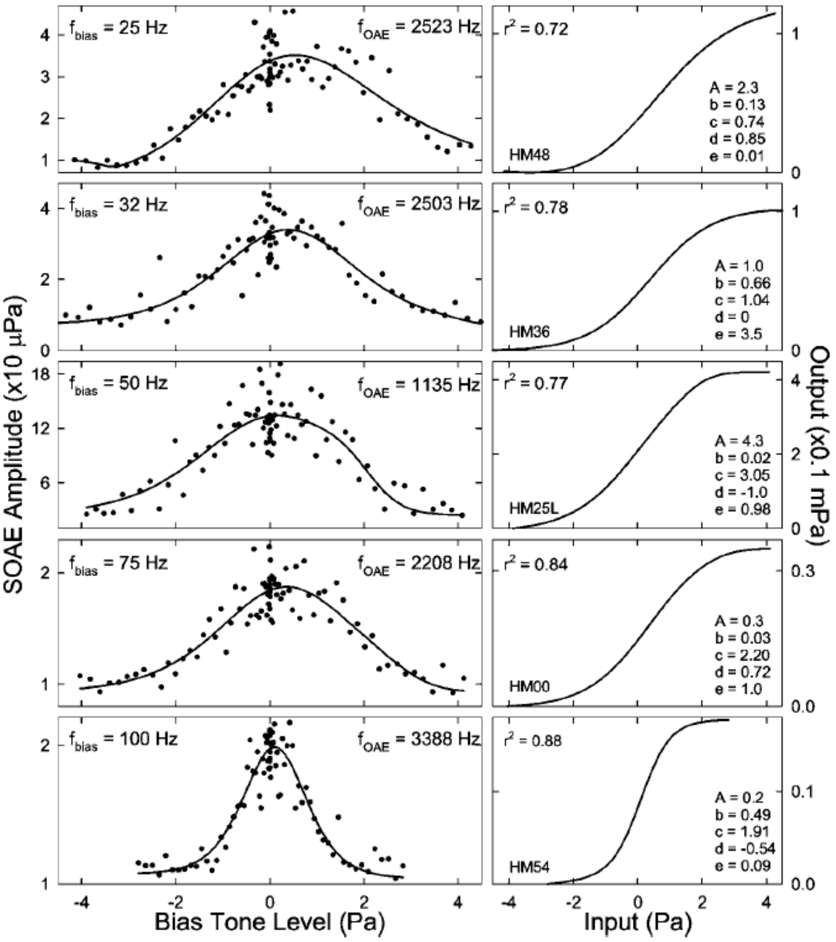

Figure 2.12: Variation of SOAE amplitude as a function of peak bias tone amplitude. The bell shaped curves shown in the left side columns are derived and fit to the scattered points in the plots by taking the derivative of the assumed nonlinearity of the CA, shown in the right hand column. Reproduced with permission from (Bian and Watts, 2008).

Bian and Watts (2008) also measured the effect of the external bias tone over one period in time on the amplitude envelope of the SOAEs. Their results, given in Figure 2.14, show that for high level bias tones, the modulation patterns present two peaks, as shown by the the lower traces in each panel. By decreasing the level of the bias tone, the two peaks merge with each other, generating a single peak within a period of the bias tone.

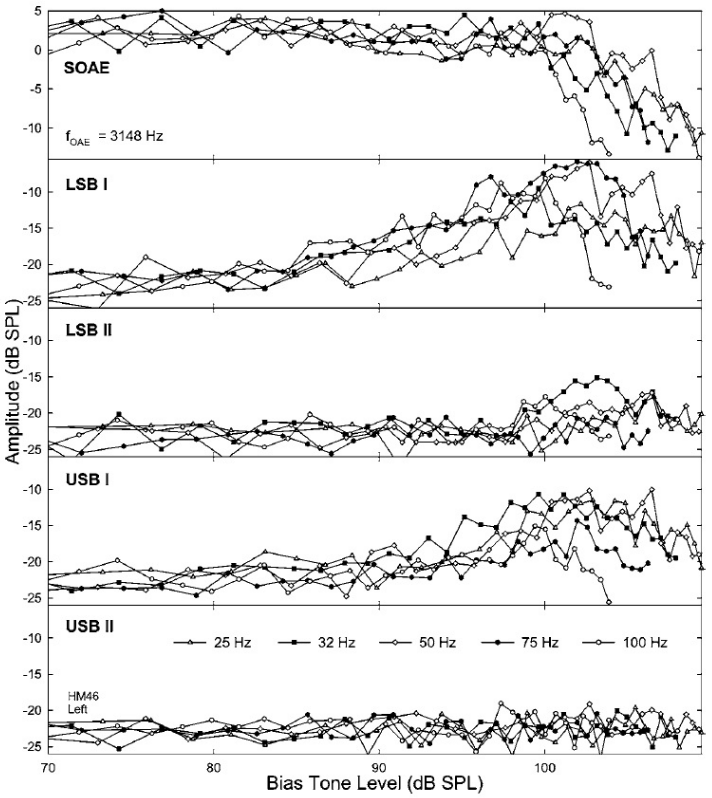

Figure 2.13: Measured variation of an SOAE and its side-bands amplitude as a function of bias tone level. Reproduced with permission from (Bian and Watts, 2008).

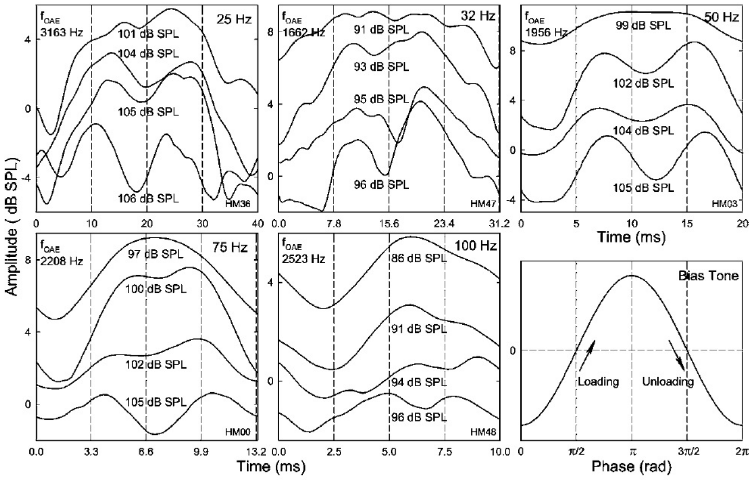

Figure 2.14: Modulation patterns of SOAEs, produced over a single period of the bias tone. Results are shown for different bias tone frequencies in the different boxes and for different bias tone levels within each box. When the level of the external bias tone is higher, the patterns obtained show two peaks in the SOAE during the period of the bias tone. However, as the level of the bias tone decreases, the amplitude of the SOAE increases and these two peaks merge into a single peak. Reproduced with permission from (Bian and Watts, 2008).

Changes in perilymphatic pressure can occur due to low frequency biasing tones which affect the CA. Wind turbines can generate high levels of low frequency sound and it has been hypothesised that they can affect the normal operation of the peripheral auditory system. It is a well known fact that wind turbines generate infrasound, which is commonly thought to not disrupt the auditory system in humans since it is outside the audible frequency range. However, more recent studies on the subject have shown that this may not be the case since infrasound does stimulate OHCs and varies the cochlear fluid pressure, therefore varying the perception of audible sounds that are modulated by the superimposed infrasound (Salt and Lichtenhan, 2014). People that reside near wind turbines often feel discomfort due to dizziness and nausea; infrasound generated by the wind turbine might be the reason, although this is a contentious issue and research is still being undertaken in this area (Salt and Lichtenhan, 2014).

Further experiments, where low-frequency bias tones were used to modulate the mechanical properties of the ear were undertaken by Kugler et al. (2014, 2015), in which human subjects were exposed to high-level low-frequency sounds that are generally considered to be harmless for the auditory system. The experiments demonstrated that after low frequency sound exposure, human hearing does in fact respond quite dramatically to such sounds producing amplitude and frequency shifts to SOAEs together with the formation of new SOAEs for lengthy periods of time, of the order of 100 seconds, as shown in Figure 2.15. There is reasonable evidence to support the hypothesis that AM and FM of the SOAEs, together with the formation of new emissions, is caused by OHC calcium homoeostasis (Kugler et al., 2015). Hence, although these low frequency sounds may be perceptually unobtrusive, they may in fact have a deteriorating effect on the mechanical properties of the cochlea when over-stimulation occurs, inducing oscillating variations in cochlear gain.

Interaction between SOAEs and other stimuli

The interaction of external tonal stimuli with SOAEs is a widely studied area. Phenomena such as synchronization, frequency locking, suppression and frequency shift of a SOAE due to an external tone has been observed in many experiments, for example Wilson and Sutton (1981); Kemp (1979); Long (1998); Bergevin et al. (2015); Bergevin and Salerno (2015); Manley and van Dijk (2016). Generally speaking, these consist of interactions between the emission and external stimuli, which demonstrate the nonlinear nature of the CA. Although these measurements have been published in a number of papers, the bigger question is what is happening to the cochlear structures to allow such phenomena to occur and how is the CA affected? These questions are extremely hard to answer without physical access to an active cochlea.

Frequency-locking of an SOAE to an external tone is an interesting phenomenon: it depends on the level, frequency and phase of the tone. Wilson and Sutton (1981) made successful attempts in synchronising SOAEs with short tone bursts of different frequencies. A tone burst of sufficient level is capable of synchronising a spontaneous emission, regardless of the phase. However, by lowering the level of the tone burst to a critical level, the phase then becomes important as there will be a push-pull effect between the emission and the tone burst; the SOAE is phase locked in certain instances but returns to its natural frequency in others (Wilson and Sutton, 1981).

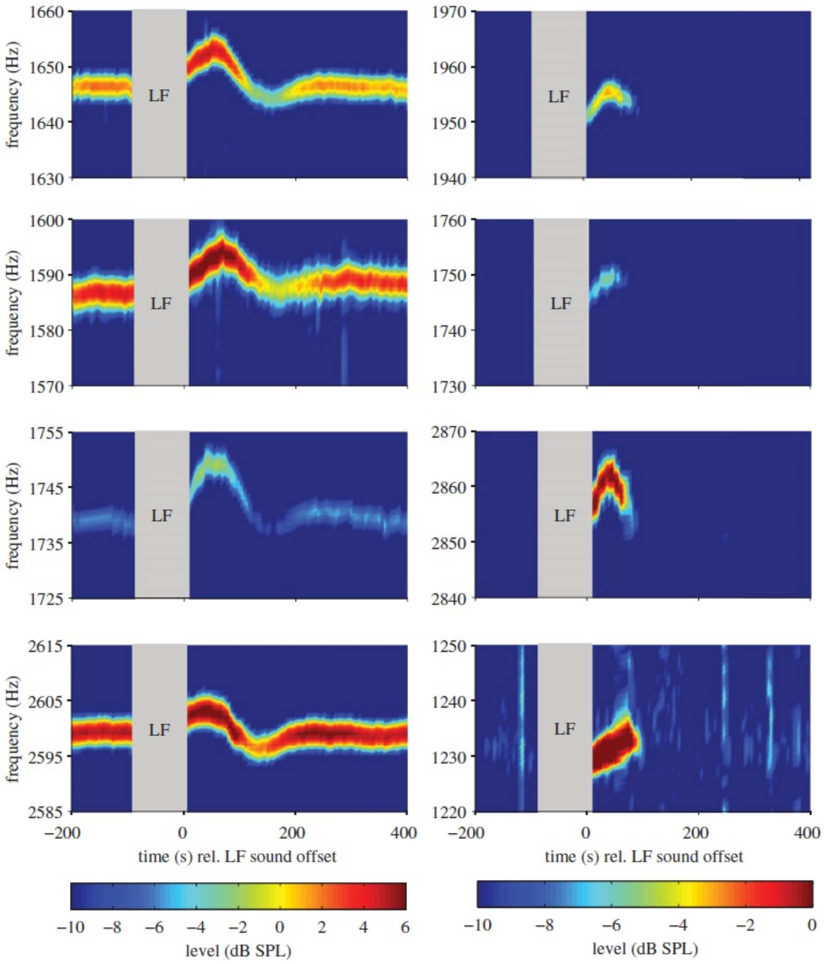

Figure 2.15: Amplitude and Frequency Modulation of SOAEs measured after exposure to high level low frequency sounds. It can be seen in the plots in the left column that after an exposure to high level low frequency sounds, delineated by the grey areas, the SOAE is modulated in both amplitude and frequency for approximately 100s, before returning to its natural state. Furthermore, the plots in the right column show the formation of new SOAEs after exposure to low frequency, which then eventually die out. Reproduced from (Kugler et al., 2014). No permission required.

An example of a frequency-locking tuning-curve is shown in Figure 2.16 (Wilson and Sutton, 1981), where the sound spectra has been recorded in the sealed ear, at first without any external stimulation (lower curve), then with an external stimuli of tonal bursts at various levels, shown by the numbers next to the curves, and frequencies. It can be seen that for the lower level stimuli at -7 dB and 3 dB, the emission component and its bandwidth are unaffected, indicating that there is no interaction going on, although a rise in baseline level occurs. At higher levels the emission begins to synchronise itself over a range of frequencies delineated by the triangles with the external tone bursts.

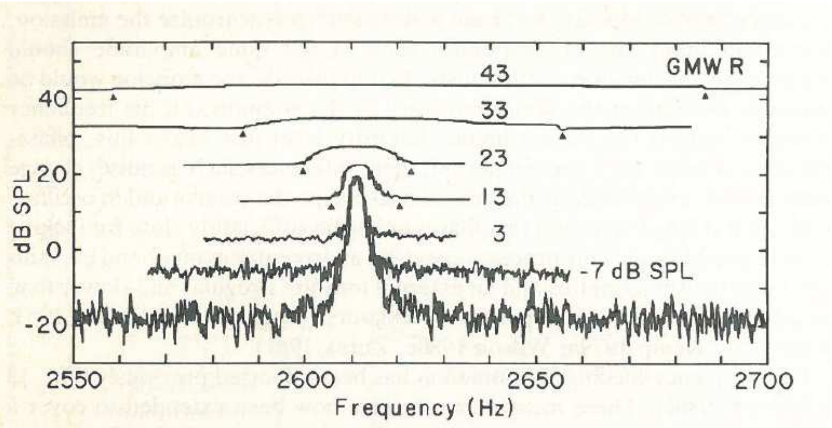

Figure 2.16: Frequency locking tuning curves showing the amplitude of the pressure recorded in the ear. The curves are obtained experimentally by stimulating the ear with tones of various level, having frequencies near to that of an SOAE. Low level tones do not affect the SOAE, while higher level tones interact with the emission, allowing it to synchronise with the external stimulus between the frequencies indicated by the triangles. Reproduced with permission from Wilson and Sutton (1981).

Results similar to these, where the external stimulus is a sweeping tone, have been reported in other experiments (Long, 1998; Hansen et al., 2014) and their results are shown in Figure 2.17. The curves in Figure 2.17 show the interaction between an SOAE and the continuous external tone that sweeps in frequency over that of the emission, allowing one to distinguish between regions of beating and entrainment. Note that the frequency range covered in Figure 2.16 is much narrower in Figure 2.17 and interaction between the two components is always occurring. At first, when the sweeping tone has a frequency, f_{ext}, that is lower than that of the SOAE, f_{SOAE}, but they are close enough, beating will occur at $f_{SOAE} - f_{ext}$. Secondly, when f_{ext} is sufficiently close to f_{SOAE}, a region of entrainment begins, where f_{SOAE} is locked to the tone for a certain frequency range. In the third and final stage, the SOAE will unlock itself from the external tone and beating will occur once again as f_{ext} increases further at $f_{ext} - f_{SOAE}$.

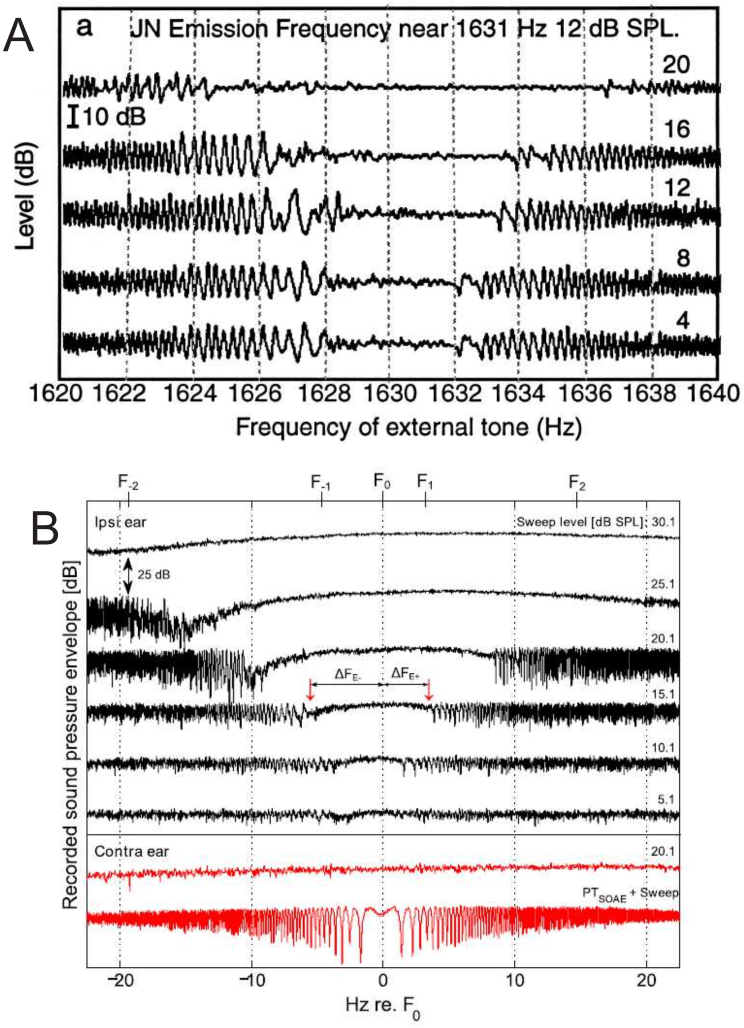

Figure 2.17: Examples of entrainment results showing the pressure level recorded in the ear canal obtained experimentally for different levels of swept tone. Areas of beating occur between the external tone and an SOAE occur before a region of entrainment and suppression of the emission due to the external tone. In both examples, it can be seen that entrainment depends on the level of the external swept tone and that it has an asymmetrical aspect. Upper plot reproduced with permission from Long (1998) and lower plot reproduced with permission from Hansen et al. (2014).

Zwicker and Schloth (1984) obtained similar results when they found that spontaneous emissions could be synchronised, or frequency-locked, with external stimuli of neighbouring frequencies, and that this property depended on the level of the external tone. Before synchronisation occurs, they mention that there is a region which gives rise to deviations due to both beating and partial synchronisation of the two components as seen in Figure 2.18. Interestingly, the dashed line has the properties of a sharp tuning curve. Furthermore, they show that as the external stimulus sweeps across the SOAE frequency, it does not necessarily enhance the amplitude of the SOAE, but in some cases reduces the amplitude of the sound pressure measured in the sealed ear canal.

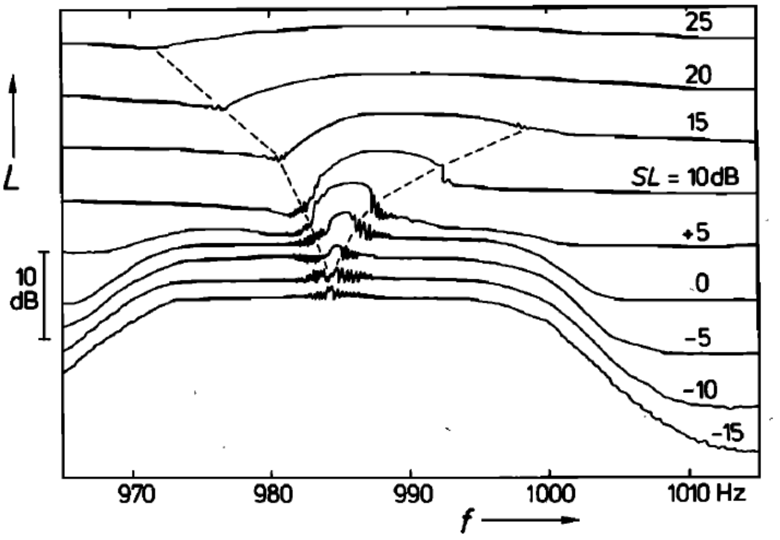

Figure 2.18: Plot of the level, L, of the sound pressure in the sealed ear canal against frequency of the stimulating pure tone for different sensation levels, SL. Frequency locking of a SOAE is illustrated with external stimuli of neighbouring frequencies and of various levels. Note that the dashed line resembles the properties of a sharp tuning curve. Reproduced with permission from Zwicker and Schloth (1984).

It has been reported that when subjects with spontaneous emissions are presented with an external tone, they perceive interaction between two tones, although they do not perceive the emission on its own (Kemp, 1979; Zwicker and Schloth, 1984; Long and Tubis, 1988a). This phenomenon has been identified as monaural diplacusis and it has been proven that the perception of the tone changes in accordance with the level of the external stimulus. For low level stimuli, two simultaneous tones were perceived by most of the subjects, while at higher levels beating would start to occur. Increasing the level further would decrease the beat rate until a limit is reached where beating would disappear. Suppressing the SOAE by administrating aspirin to the subjects would eliminate the monaural diplacusis (Long, 1998). As discussed in Section 2.3.2, aspirin consumption can reduce and/or abolish the production of SOAEs while also affecting threshold microstructure: initially, there is an increase in sensitivity followed by a decrease in sensitivity and flattening of the microstructure. It is plausible that the initial reduction of maxima in the threshold microstructure, i.e. increased sensitivity, is due to the abolishment of SOAEs, and therefore their masking effect on frequencies in the vicinity of the regions that are affected by SOAEs. In fact, the aspirin appears to affect OHC physiology before affecting the physiological aspects of the cochlea related to its microstructure. SOAE abolishment can be related to the weakening of the OHCs hydraulic skeleton, hence, their ability to generate the mechanical force involved in the production of a spontaneous emission (Brownell, 1990; Long and Tubis, 1988a). It should also be mentioned that other than aspirin, many other drugs cause changes in the properties of the peripheral auditory system and consequently to SOAEs, such as cisplastin, certain antibiotics, quinine, etc. (Whitehead et al., 1996).

SOAEs are found in many animals across different species, regardless of the large anatomical differences in their auditory systems. Bergevin and Salerno (2015) performed a study where a comparison was made between SOAE characteristics of a human, a barn owl and a lizard (anolis carolinensis). For the purposes of this thesis, only the properties of SOAEs from human subjects are discussed, but generally speaking, SOAEs from human cochleae tend to be more stable over time and produce spectra with distinctive peaks, whereas other species, especially lizards, tend to have spectra where the peaks are broader. This is thought to be because SOAEs in lizards seem to turn on and turn off over time. Bergevin and Salerno (2015) show how SOAEs in humans resemble the characteristics of a relatively stable sinusoid as shown in the top row in Figure 2.19. Figure 2.19(**A**) shows the spectra obtained from a measurement of the ear canal pressure, where typical peaks of SOAEs are observed. The stability of the emissions over time is illustrated in Figure 2.19(**B**): an individual SOAE takes on the appearance of a stable sinusoidal signal, giving it its characteristic ringing sound when measured in the ear canal. Furthermore, its time series of the calculated envelope, shown in Figure 2.19(**C**), is quite stable. These features of human SOAEs are not found in all animals, for example, the response is more dominated by noise in barn owls and lizards, as shown in the second and third rows of Figure 2.19. In particular, these animals do not appear to have SOAEs that are stable in both amplitude and frequency over time.

Bergevin and Salerno (2015); Bergevin et al. (2015) also obtained entrainment patterns using tone bursts of increasing centre frequency in a similar way to Wilson and Sutton (1981), as shown in Figure 2.20, where a comparison is again made between a human (top row of plots) and a lizard (bottom row of plots). These results are obtained by stimulating the ear with tone bursts of increasing frequency over time. The spectrogram is then calculated as shown in Figures 2.20(**A**) and (**D**), while Figures 2.20(**B**) and (**E**) show the variation in level of the SOAE over time, given the time events of the tone burst onset. It is shown that as the frequency of the tone burst approaches that of the SOAE, the latter becomes more and more entrained. In particular, two time constants are considered and shown in Figures 2.20(**C**) and (**F**): when the tone burst is sufficiently near the emission there is an entrainment time coefficient and a second one when the emission returns to steady state. Bergevin refers to these as the entrainment time coefficient when the emission is going into the suppressed state, and the relaxation time coefficient when the emission returns to its steady state. Interestingly, these two time coefficients differ from each other, meaning that the actual dynamics of the system that generate the emission play a role in determining these time intervals. This phenomenon is significantly different than that shown in Figure 2.15, where the level of the external tone was much higher and the SOAE took a greater amount of time to regenerate.

Bergevin mentions that when stimulating the cochlea with a swept tone, in particular one made up of tone bursts, the shape of the bursts may affect entrainment.

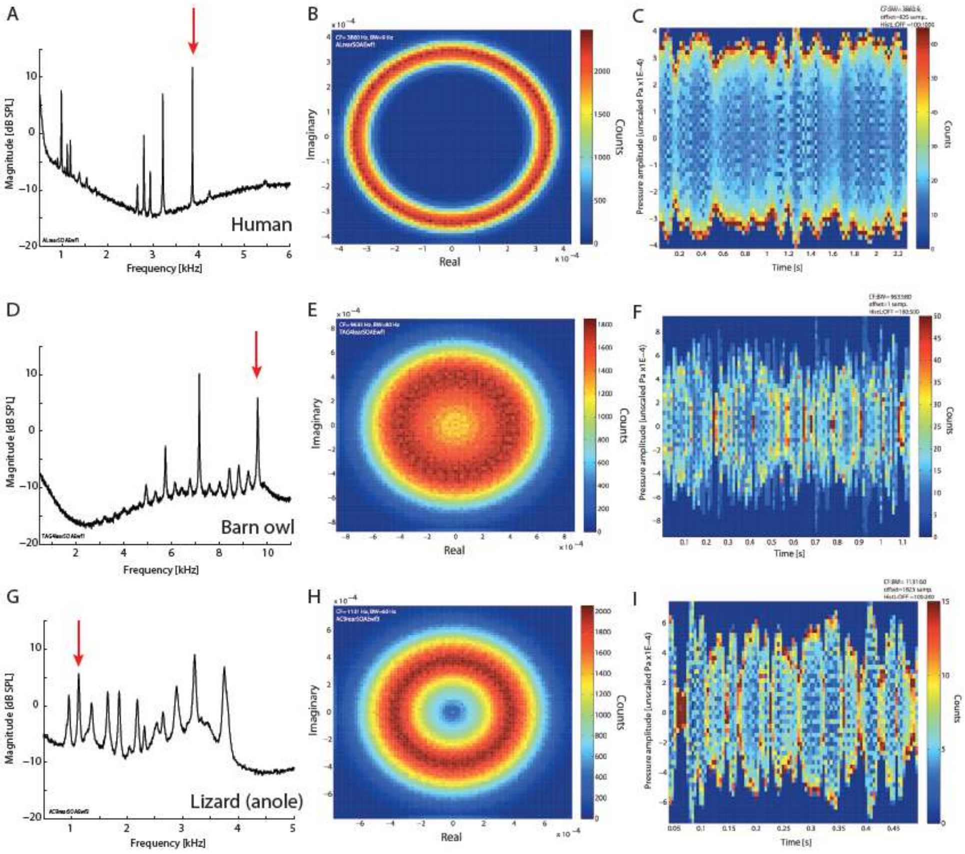

Figure 2.19: Spectra, phase plots and envelope functions illustrating how SOAEs from different species appear to have different properties. The top row of plots were measured from a human subject, the middle row from a barn owl at the bottom row from a lizard. Plots **A**, **D** and **G** show the spectra of the SOAE. Plots **B**, **E** and **H** are obtained by taking the Hilbert transform and thereafter, plotting the real part against the imaginary part. Plots **C**, **F** and **I** show the envelope of the SOAEs over time. Reproduced with permission from Bergevin and Salerno (2015).

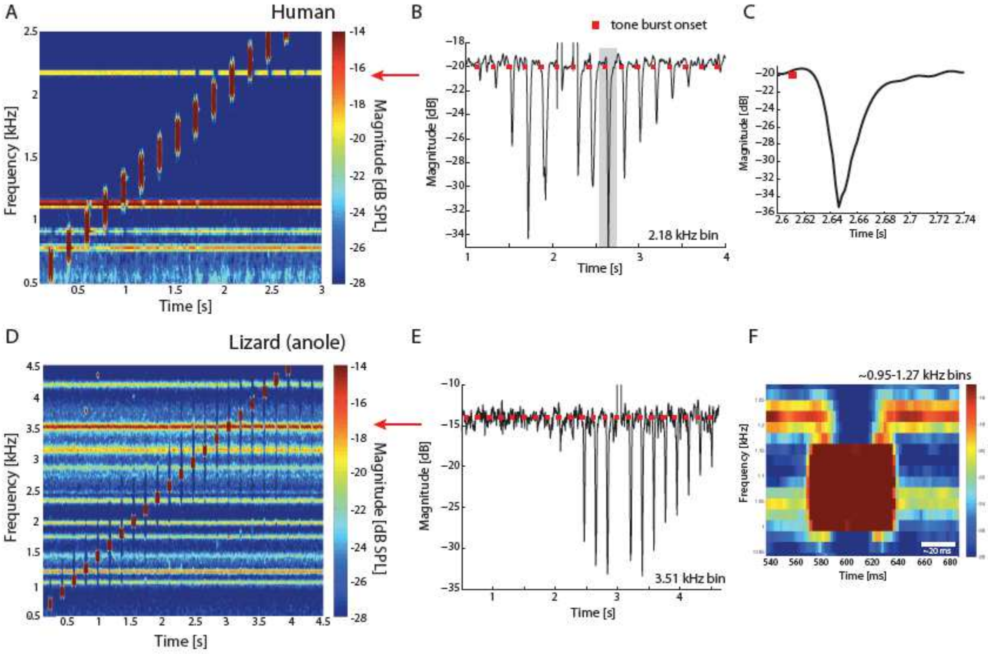

Figure 2.20: Comparison between the properties of SOAEs of a human subject (top row) and of a lizard (bottom row). Plots **A** and **D** show the spectrograms of the SOAE when the ear is stimulated by tone bursts of varying centre frequency. Plots **B** and **E** show SOAE amplitude over time together with the time events of the tone burst onset. Plots **C** and **F**, although plotted in two different ways, show SOAE amplitude over time in relation to one specific time burst, in order to investigate the different time constants that develop from the interaction. Reproduced with permission from Bergevin and Salerno (2015).

Other entrainment patterns are shown in Figure 2.21, obtained by taking spectrograms of the response in the ear canal of an SOAE to a swept tone presented to the ear as a stimulus (Bergevin and Salerno, 2015). SOAEs appear as horizontal lines, while the swept tone appears as a diagonal line. These examples show that as the swept tone passes through the frequency of a SOAE, the latter will be suppressed. The expanded plot on the right was said to demonstrate the entrainment effect, where the frequency of the SOAE is pulled towards the frequency of the swept tone as it is passing by, although this is not particularly clear.

In summary, interaction between the stimulus and the emissions show that the following events are taking place:

- As the swept tone approaches and leaves the frequency of the spontaneous emission, it tends to push or pull the frequency of the emission towards or away from itself;
- When the swept tone is near enough in frequency to the SOAE, beating will occur that depends on the level of the swept tone;

- When the swept tone is even closer to the SOAE frequency, it will act as a masker towards the SOAE and supress/frequency lock it;
- Subharmonic distortion patterns are generated due to the interaction;
- Facilitation, i.e. regions where an increase of magnitude the SOAE, occurs.

Bergevin notes that by changing the sweep rate or the direction of the stimulus had little effect on the entrainment patterns.

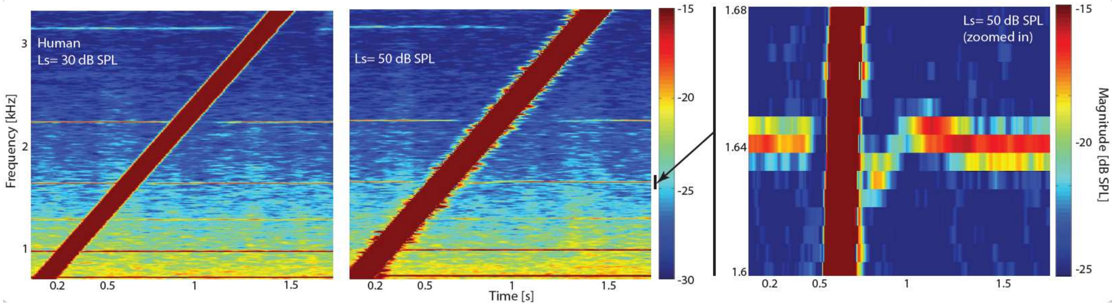

Figure 2.21: Entrainment patterns obtained from experimental results on a human subject: horizontal lines represent SOAEs, while the diagonal line is the swept tone. The left and middle plots show areas of suppression, while the plot on the right, shows the entrainment effect, where the SOAE frequency is pulled towards the frequency of the external stimulus. Reproduced from Bergevin and Salerno (2015). Permission requested.

2.4 Summary

This chapter has provided a review of the literature that covers many aspects about OAEs and experiments performed on them. A review of some of the types of OAEs was given, followed by an in depth discussion about SOAEs, how they originate and how they may be linked to threshold microstructure. Many experiments have been performed on SOAEs and how these emissions interact with external stimuli, in particular low frequency bias tones and swept tones. External low frequency bias tones have been used to estimate the nonlinear properties of the transducer function of the CA (Bian and Watts, 2008). External swept tones have shown to generate a number of phenomena on SOAEs, i.e. entrainment, beating and suppression, which if studied appropriately, may reveal other aspects cochlear functioning.

Chapter 3

Cochlear modelling

A cochlear model can be a very helpful tool to help understand how the cochlea works and, if possible, also make predictions, about OAE generation in the inner ear for example. The advantage of obtaining results through a model rather than experimentally is that it is possible to test predictions about how different parts of it affect the generation of OAEs. Many mechanical models have been formulated over the years to simulate the cochlea's behaviour and various models exist that mimic SOAE generation. There is still some debate as to whether spontaneous emissions are the product of local oscillators along the length of the cochlea or if they are generated by a number of global and interrelated properties of the cochlea. Some of the models in the literature, which are the most relevant for the present thesis, are described in the following sections of this chapter. Local models, in which only the localised behaviour of a SOAE generation site is modelled, should be distinguished from global models of the whole cochlea, in which SOAEs emerge as an instability due to multiple reflections.

3.1 Models using Van der Pol oscillators

A particular local model of SOAEs, used for example by Talmadge et al. (1998), takes advantage of a Van der Pol oscillator.

The dynamic properties of a nonlinear dissipative oscillator like the Van der Pol oscillator are very attractive when modelling a biological complex system such as the cochlea. In fact, it produces nonlinear limit cycle oscillations, i.e. oscillations of a fixed amplitude and period, without the need of an external stimulus (Slotine and Li, 1991), which closely resemble the properties of SOAEs. The Van der Pol equation incorporates a single degree of freedom system with nonlinear damping; the forced and normalised form of the equation can be expressed as the following:

$$\ddot{x} + \epsilon(\mid x^2 \mid -1)\dot{x} + \omega_n^2 x = A \cdot \cos(\omega_d t) \tag{3.1}$$

Where:

- x is a nondimensional displacement at the site of an SOAE
- ω_n is the natural angular frequency of the SOAE
- ω_d is the driving frequency of the forced oscillation
- ϵ is the nonlinear damping term that has a value greater than 0
- A is the amplitude of the driving force

Forced oscillations applied to such a system can produce frequency locking when the frequency of the forced oscillation approaches the natural frequency of the system (Hanggi and Riseborough, 1983).

If a mass spring damper system is associated with this equation, it can be said that it contains a damping coefficient $\epsilon(\mid x^2 \mid -1)$ that, assuming no driving force is acting on the system, depends on the amplitude of x. For large values of x the damping coefficient is positive, so the system loses energy and x will decrease to the amplitude of the limit cycle. If x is smaller than the amplitude of the limit cycle, the damping coefficient becomes negative, hence energy is added to the system and x increases, until once again, the amplitude of the limit cycle is reached. Therefore, regardless of the initial state of the system, it will always converge to a limit cycle when the system is not perturbed. Figure 3.1 shows a section of a time domain simulation performed on a Van der Pol oscillator by the author of this thesis: it can be seen that the dynamics of the system tend to stabilise and generate a limit cycle. The properties of a Van der Pol oscillator make it an interesting tool for modelling SOAEs because the limit cycle generated can be tuned to resemble a spontaneous emission when the oscillator is not forced.

Assuming the validity of such an oscillator for this application, perturbing the oscillator with an external force having amplitude A, and driving frequency ω_d, is a possible method to understand interactions between a SOAE and an external stimulus. Correct tuning of the parameters of the Van der Pol equation will lead to suppression and entrainment of the natural frequency of the limit cycle across a “basin of entrainment”.

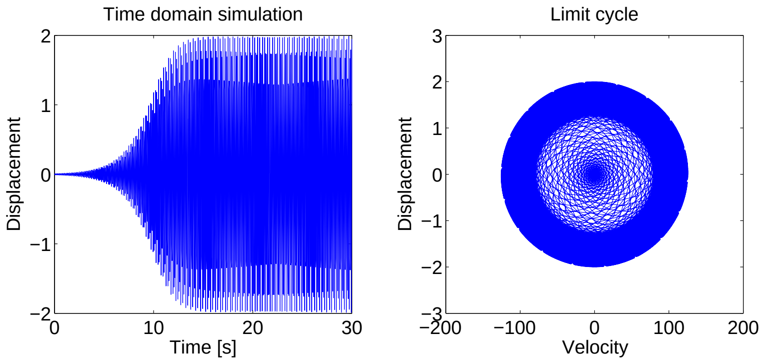

Figure 3.1: The plot on the left shows a time domain simulation of a Van der Pol oscillator reaching steady state and producing a limit cycle. The plot on the right shows a phase plot, demonstrating the convergence of the dynamic variables to stability, therefore generating a limit cycle.

A number of simulations were performed as part of this thesis using a Van der Pol oscillator, where a forced component was used to interact with the limit cycle, the latter having a natural frequency of 10 Hz. Figure 3.2 shows two examples where the external force applied has an amplitude of A corresponding to 40 dB in the top panel and to 50 dB in the lower panel. In both cases, the frequency of the external force is varying between 9 Hz and 11 Hz. Note that the tone is not swept across this range of frequencies, instead, individual time domain simulations were performed for external forces in this range of frequencies. A swept tone does not have the time to let the system reach steady state and also it would be computationally expensive to perform such a simulation.

The results of the simulations using a Van der Pol oscillator can be summarised as follows: the properties of the driving force alter the system; higher amplitudes lead to a widening of the basin of entrainment, meaning that an external force will suppress or partially suppress the limit cycle within a greater range of frequencies, ω_d around the natural frequency, ω_n. The values of A and ω_d will determine the "pull-out amplitude", which, for a fixed value of ω_d, determines the boundary between moderate to high driving levels that will trigger the suppression of the limit cycle at ω_n (Ku, 2008). The pull-out amplitude is a function of ω_d.

The amplitude of the signal at the limit cycle frequency and that of the driving tone are calculated from a Fourier transform of the steady state time history. The drawback of a Van der Pol model is that it cannot easily produce an asymmetrical basin of attraction at frequencies close to the oscillator's natural frequency. In reality, frequency locking of an SOAE has an asymmetrical shape when a low-level tone is swept at frequencies close to the region of an SOAE (refer to Chapter 2.3.3, Figures 2.18 and 2.20), unlike the results shown in Figure 3.2, where the frequencies that delineate the basin of entrainment are at similar distances from ω_n. In addition, as the suppressor frequency, ω_d, approaches the natural frequency, ω_n, of the Van der Pol oscillator, the latter does not move away, a phenomenon known as frequency pushing that is seen in SOAEs. These two disadvantages are also discussed by Long et al. (1990).

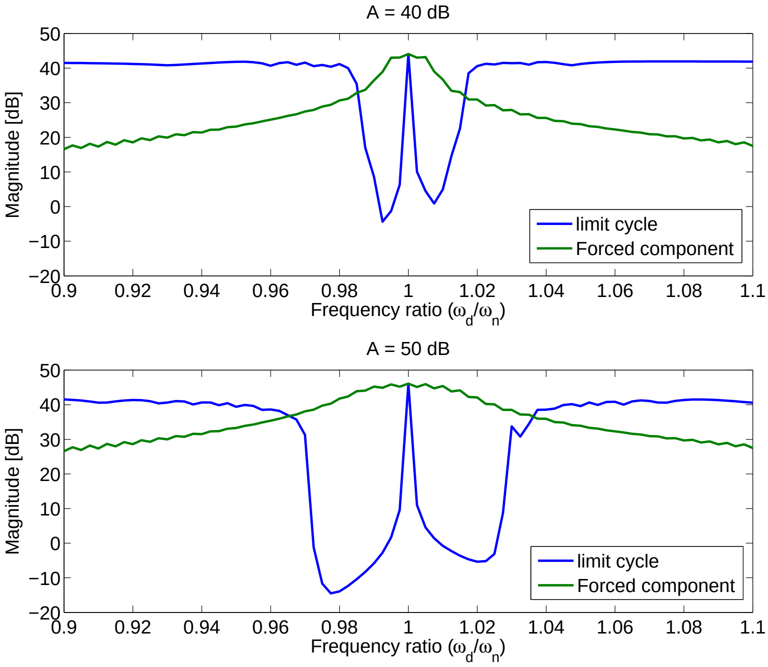

Figure 3.2: Simulations illustrating the basin of entrainment produced from a Van der Pol oscillator when driven by external forces of different magnitudes. Greater amplitudes of the external force generate a larger basin of entrainment and vice-versa.

Experiments on human subjects have proven that SOAE amplitudes and frequencies fluctuate over time, either naturally (van Dijk and Wit, 1990), or when perturbed by external stimuli (Bian and Watts, 2008; Bian, 2009). Comparing these results with a SOAE modelled by a second order Van der Pol oscillator with nonlinear damping shows that the analytical results are not compatible with experimental ones because the SOAE does not present any kind of fluctuation in amplitude and frequency over time. Van Dijk and Wit discuss that this can be obviated by using alternative oscillators with nonlinear stiffness terms driven by narrow band noise and that analytical studies have proven that nonlinear stiffness must be small for the emission generator to function correctly.

The Van der Pol oscillator model was widely used in the work by Long and Tubis (Long and Tubis, 1988b; Long et al., 1990). This also included variations to the model that could mimic SOAE changes due to drug consumption, such as aspirin. The evolution undertaken by an SOAE under the effect of aspirin consumption can be directly associated with the changes occurring to threshold-microstructure in the vicinity of the same SOAE, as shown in Figure 2.10. As discussed in Section 2.3.3, both features undergo alterations; in particular there is an initial increase in sensitivity, followed by a decrease in sensitivty and flattening of the microstructure. Analytically speaking, Long and Tubis (1988b) modelled this effect using a Van der Pol oscillator and proved that the latter may indeed be tuned to reduce threshold microstructure when the amplitude of the SOAE in question is reduced.

Summarising the results of local oscillator models such as those using Van der Pol oscillators, it can be said that the biggest disadvantage is the requirement of fine tuning of the individual oscillators, which therefore act independently. According to Shera's global standing-wave model for SOAE generation (Shera, 2003), in which the cochlea resembles a laser oscillator, there is a strict dependency between the overall cochlear structures and SOAE properties, and this therefore excludes the idea of secluded and independent oscillators along the cochlea.

3.2 Coupled model of the cochlea

A coupled model of the cochlear mechanics must include both the fluid coupling in the chambers and the dynamics of an array of micromechanical models of the OC along the length of the cochlea. The state space formulation of the mechanics of the cochlea developed by Elliott et al. (2007) uses the micromechanical element by Neely and Kim (1986) as its basic building block. Neely and Kim's micromechanical element represents an individual radial slice of the cochlea and uses a mechanical formulation that simulates the behaviour of the OC. Figure 3.3 illustrates the details of this element, which is comprised of two masses, M_1 and M_2, three springs, K_1, K_2 and K_3, and three dampers, C_1, C_2 and C_3. M_1 and M_2 can be interpreted as the masses of the BM and of the TM respectively and are coupled by means of K_3 i.e. the stiffness of the OHC and stereocilia (Ku, 2008). Neely and Kim (1986) define the impedances of the micromechanical element as follows:

$$Z_1 = \frac{K_1}{s} + C_1 + sM_1 \tag{3.2}$$

$$Z_2 = \frac{K_2}{s} + C_2 + sM_2 \tag{3.3}$$

$$Z_3 = \frac{K_3}{s} + C_3 \tag{3.4}$$

$$Z_4 = \frac{K_4}{s} + C_4 \tag{3.5}$$

where

$$s = j\omega. \tag{3.6}$$

Z_1 is the impedance associated with the BM, Z_2 with the TM, Z_3 couples together the BM and the TM, and can be associated with the passive part of the OHC impedance, while the active part is represented by Z_4.

Each element is driven by the pressure difference, P_d, that acts on M_1. The element has two resonant frequencies, one where the motion of the two masses is in phase, and one where they are out of phase. It is the out of phase motion between the two masses that drives the CA.

The cochlear element offers an interpretation of the CA. It hypothesises that active elements, such as the one shown in Figure 3.3, which are spatially distributed along the length of the cochlea, are capable of replicating the peripheral auditory system's frequency resolution and sensitivity. It assumes that the OHC impedance is formed of an active part, Z_4, and a passive part, Z_3. While the element in Figure 3.3 provides a plausible mechanical model of the micromechanics of the inner ear, its limitation is that it is physically unrealistic, in that no reacting force exists to counteract the active pressure, P_a, pushing against the mass, M_1, of the BM, and so it cannot be said to be an accurate representation of the detailed dynamics.

The model by Elliott et al. (2007) introduces nonlinearities in the micromechanical elements, which are able to suppress excessive values of relative motion between the BM and the TM, leading to saturation of the dynamical system. Figure 3.4 shows the micromechanical element with the nonlinear component applied. In previous work on the model by Elliott et al. (2007); Ku (2008); Ku et al. (2009), the nonlinearity has been modelled either as a hyperbolic tangent function, $tanh$, or by a Boltzmann function. The nonlinearity is the reason why, under certain circumstances, the system can saturate and produce a limit cycle comparable to the behaviour of OAEs (Ku et al., 2009). The state space model demonstrates that SOAEs are a by-product of the active elements when driven by high values of gain and that they are comparable to limit cycles attributed to unstable linear coherent reflections inside the cochlea that produce standing waves and that are stabilised due to the saturation of the nonlinear active transducer function of the CA; therefore, the model supports the global standing wave theory of the cochlea.

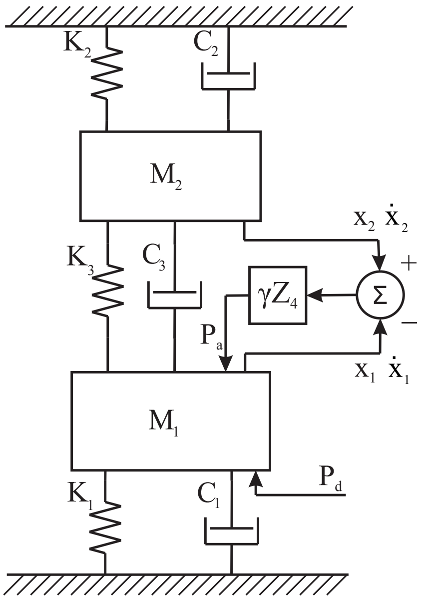

Figure 3.3: Micromechanical element of the cochlea by Neely and Kim (1986).

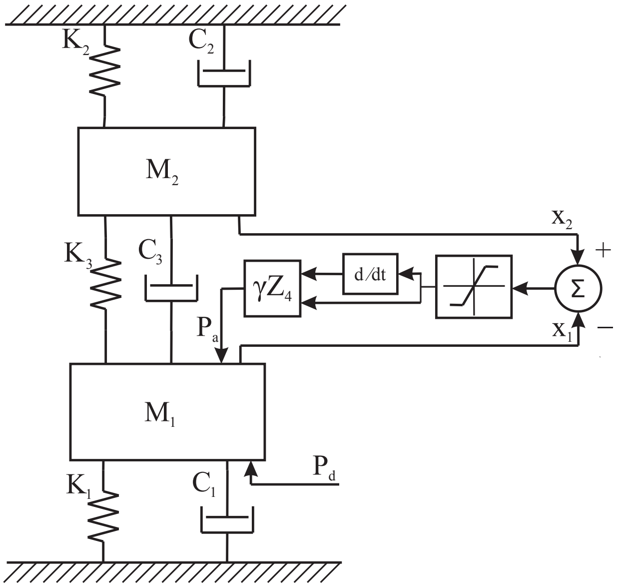

Figure 3.4: Neely & Kim's micromechanical element of the cochlea with the addition of the nonlinearity.

Most of the results presented in this thesis use the state space formulation of the cochlear model, which is outlined in Appendix A. The standard notation for the state space formulation is as follows:

$$\dot{\mathbf{x}}(t) = \mathbf{A}\mathbf{x}(t) + \mathbf{B}\mathbf{u}(t) \tag{3.7}$$

$$\mathbf{y}(t) = \mathbf{C}\mathbf{x}(t) + \mathbf{D}\mathbf{u}(t), \tag{3.8}$$

where bold lower case symbols represent vectors and bold upper case symbols represent matrices (Friedmand, 2005); in particular:

- $\mathbf{x}(t)$ is the $(n$ x $1)$ state vector containing n state variables
- $\mathbf{A}$ is the $(n$ x $n)$ system matrix containing the mechanics of the model
- $\mathbf{B}$ is the $(n$ x $m)$ input matrix that relates the input $\mathbf{u}(t)$ to the model
- $\mathbf{u}(t)$ is the $(m$ x $1)$ input vector
- $\mathbf{y}(t)$ is the $(p$ x $1)$ output vector
- $\mathbf{C}$ is the $(p$ x $n)$ output matrix
- $\mathbf{D}$ is the $(p$ x $m)$ matrix that directly connects the input to the output

It is shown in Appendix A that the state space formulation is applied first to describe all the micromechanical elements, and secondly, to couple all of the individual elements through fluid coupling, in order to obtain the macromechanical model of the cochlea. The major advantages of the state space model formulation are that it is possible to easily check the system's stability and also to perform time domain simulations whilst including nonlinearities in the system.

The micromechanical element used for the simulations presented in later chapters, is one that contains a nonlinear component, shown in Figure 3.4, and will be discussed in more detail in Chapter 4. By supplying the element with a nonlinear component, the system matrix $\mathbf{A}_n$ in Equation A.6, Appendix A, can be divided into two separate matrices, one including the active part that undergoes a nonlinear transformation, and the other including the passive part. This is shown in Equation 3.9.

$$\mathbf{A}_n = \mathbf{A}active_n + \mathbf{A}passive_n =$$

$$\begin{bmatrix} \frac{g\gamma C_4}{M_1} & \frac{g\gamma K_4}{M_1} & \frac{-\gamma C_4}{M_1} & \frac{-\gamma K_4}{M_1} \\ 0 & 0 & 0 & 0 \\ 0 & 0 & 0 & 0 \\ 0 & 0 & 0 & 0 \end{bmatrix}_n + \begin{bmatrix} -\frac{(C_1+C_3)}{M_1} & -\frac{(K_1+K_3)}{M_1} & \frac{C_3}{M_1} & \frac{K_3}{M_1} \\ 1 & 0 & 0 & 0 \\ \frac{C_3}{M_2} & \frac{K_3}{M_2} & -\frac{(C_2+C_3)}{M_2} & -\frac{(K_2+K_3)}{M_2} \\ 0 & 0 & 1 & 0 \end{bmatrix}_n . \tag{3.9}$$

Assuming, at this stage, linearity of the system and given an initial estimate of the coupled state vector $\mathbf{x}_n(t)$, either from the initial conditions or from previous iterations during a simulation, the active pressure P_a at a particular element n acting on M_1 in Figure 3.4 can then be calculated using the active matrix $\mathbf{A}active_n$ as follows:

$$P_a = M_1 \mathbf{A}active_n \mathbf{x}_n(t) = M_1 \begin{bmatrix} \frac{g\gamma C_4}{M_1} & \frac{g\gamma K_4}{M_1} & \frac{-\gamma C_4}{M_1} & \frac{-\gamma K_4}{M_1} \\ 0 & 0 & 0 & 0 \\ 0 & 0 & 0 & 0 \\ 0 & 0 & 0 & 0 \end{bmatrix}_n \begin{bmatrix} \dot{x}_1 \\ x_1 \\ \dot{x}_2 \\ x_2 \end{bmatrix}_n \tag{3.10}$$

In the nonlinear case, the state vector $\mathbf{x}_n(t)$ may undergo compression depending on the relative displacement and velocity between the BM and TM, which are subject to nonlinear compression as follows:

$$NL_{function}\{\Delta\dot{x}\} = NL_{function}\{\dot{x}_2 - \dot{x}_1\} \tag{3.11}$$

and

$$NL_{function}\{\Delta x\} = NL_{function}\{x_2 - x_1\}, \tag{3.12}$$

where $NL_{function}$ may assume a number of sigmoid nonlinear functions, as will be shown in Chapter 5. Therefore, the nonlinearity will suppress large values of $\Delta\dot{x}$ and Δx.

The value of the feedback gain, γ, determines the performance of the active impedance Z_4 that will amplify the BM displacement and velocity. Therefore, it determines the total performance of OHC impedance given by Z_4 in Figure 3.4. Z_4 will remain fully active for very low incoming sound levels. However, for high levels of sound, the nonlinearity compresses $\Delta\dot{x}$ and Δx to the extent that the effect of Z_4 is de-activated, resulting in a totally passive system.

The macromechanical model of the cochlea is constructed by coupling together, through fluid coupling, the individual radial slices represented by the micromechanical elements. There is still a debate as to whether it is important to account for the fact that adjacent elements of the cochlea are mechanically coupled in the longitudinal direction. Naidu and Mountain (2001) describe longitudinal coupling as a key feature to the overall response of the cochlea, whereas Robles and Ruggero (2001) claim that the basilar membrane exhibits negligible longitudinal coupling. The work presented in the present thesis follows the suggestions from Robles and Ruggero, where longitudinal coupling along the BM is considered negligible. Figure 3.5 shows how all the micromechanical elements are aligned next to one another to form the overall discrete macromechanical model of the cochlea. The elements for the cochlear partition go from 2 to $N-1$, while element 1 describes the dynamics of the middle ear and element N those of the helicotrema. The distance between two adjacent micromechanical elements, n and $n+1$, is termed Δ.

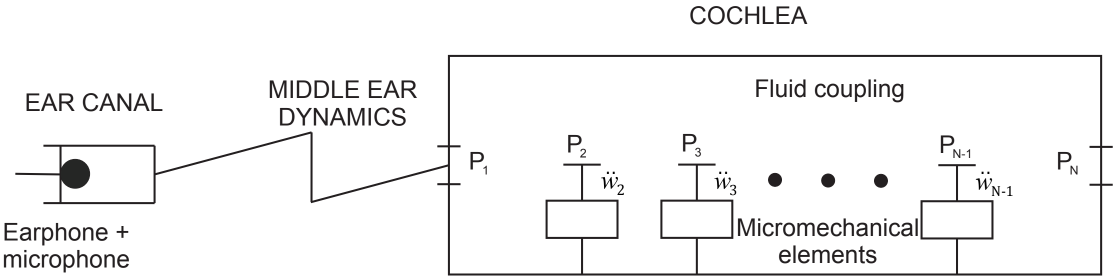

Figure 3.5: Discrete model of the cochlea showing the disposition of the micromechanical elements coupled to one another by the cochlear fluids.

Appendix A details the mathematical formulation of the macromechanical cochlear model. The state space formulation for the fluid-coupled model with included boundary conditions can be written as:

$$\dot{\mathbf{x}}(t) = \mathbf{A}\mathbf{x}(t) + \mathbf{B}\mathbf{u}(t) \tag{3.13}$$

where

$$\mathbf{A} = [\mathbf{I} - \mathbf{B}_E\mathbf{F}^{-1}\mathbf{C}_E]^{-1}\mathbf{A}_E, \tag{3.14}$$

$$\mathbf{B} = [\mathbf{I} - \mathbf{B}_E\mathbf{F}^{-1}\mathbf{C}_E]^{-1}\mathbf{B}_E, \tag{3.15}$$

and

$$\mathbf{u} = \mathbf{F}^{-1}\mathbf{q}. \tag{3.16}$$

The details of Equations 3.14, 3.15 and 3.16 are the following:

- $\mathbf{A}_E$ is the system matrix containing the uncoupled mechanics of the model
- $\mathbf{B}_E$ is the input matrix for the uncoupled state space equation
- $\mathbf{C}_E$ is the output matrix for the uncoupled state space equation
- $\mathbf{I}$ is a unit matrix
- $\mathbf{F}$ is the finite difference matrix
- $\mathbf{q}$ is the vector of source terms

Equations 3.14, 3.15 and 3.16 are derived by taking into consideration the coupled response due to the cochlear fluids, described in detail in Appendix A. The state space equation for the coupled response of the model can then be derived, as shown in Equation 3.13, where the state vector, $\mathbf{x}$, contains the displacements and velocities of the BM and TM of each micromechanical element.

Matrix $\mathbf{A}$ is termed the system matrix. Calculating the eigenvalues of such a matrix determines the poles of the system's transfer function and therefore its stability. The system is stable when all poles have a negative real part (Elliott et al., 2007).

If the nonlinearity is ignored and the system matrix $\mathbf{A}$ is independent of $\mathbf{x}(t)$, then Equations 3.7 and 3.8 can be solved in the Laplace domain, assuming all waveforms are proportional to e^{st}, to give

$$\mathbf{Y}_p(s) = [\mathbf{D} + \mathbf{C}(s\mathbf{I} - \mathbf{A})^{-1}\mathbf{B}]\mathbf{U}(s). \tag{3.17}$$

To run time domain simulations, an alternative formulation of the above equations is used that increases computational efficiency and speed (Pan et al., 2014). Its derivation is discussed in Appendix B. The final equation that gives the displacements and velocities of the cochlear partition when using this alternative formulation is

$$\dot{\mathbf{x}} = \mathbf{A}_E(x) + \mathbf{B}_E(\mathbf{F} - \mathbf{C}_E\mathbf{B}_E)^{-1}\mathbf{C}_E\mathbf{A}_E(x) + \mathbf{B}_E(\mathbf{F} - \mathbf{C}_E\mathbf{B}_E)^{-1}\mathbf{q}. \tag{3.18}$$

Equation 3.18 has the advantage of using tridiagonal matrices that can be inverted very rapidly. In addition, putting $\mathbf{A}_E$, $\mathbf{B}_E$, $\mathbf{C}_E$, $\mathbf{F}$ and $(\mathbf{F} - \mathbf{C}_E\mathbf{B}_E)$ into sparse form greatly increases simulation speeds.

3.3 Quasi-linear model

One of the drawbacks of linear simulations using the state space formulation in the frequency domain is that it cannot automatically account for nonlinearities in the system. A possible solution to this is to use a quasi-linear method which considers the effect that nonlinearities have on the model. This approach has previously been used, for example, by Kanis and de Boer (1993, 1994); Young (2011).

The aim of the quasi-linear method is to simulate cochlear nonlinearity in the frequency domain (Kanis and de Boer, 1993), taking into consideration the nonlinear properties of OHCs that depend on the level of the incoming stimulus. Figure 3.6 (**a**) shows the case of the linear micromechanical model where the active component is always present, regardless of the level of the input. However, Figure 3.6 (**b**) introduces a sigmoid nonlinear function that scales the difference in velocity and displacement between the

BM $(x_1, \dot{x}_1)$ and the TM $(x_2, \dot{x}_2)$ that are then used to calculate, through Z_4, the quasi linear outer hair cell pressure, p_{OHC}^{QL}, which is equivalent to p_a in Figure 3.6 **(b)**. Higher levels of input increase the difference in displacement and velocity between the BM and the TM, which will saturate after a certain limit due to the nonlinear function making the system level dependent. As will be shown in later chapters, different nonlinear functions can be used to simulate OHC nonlinearity.

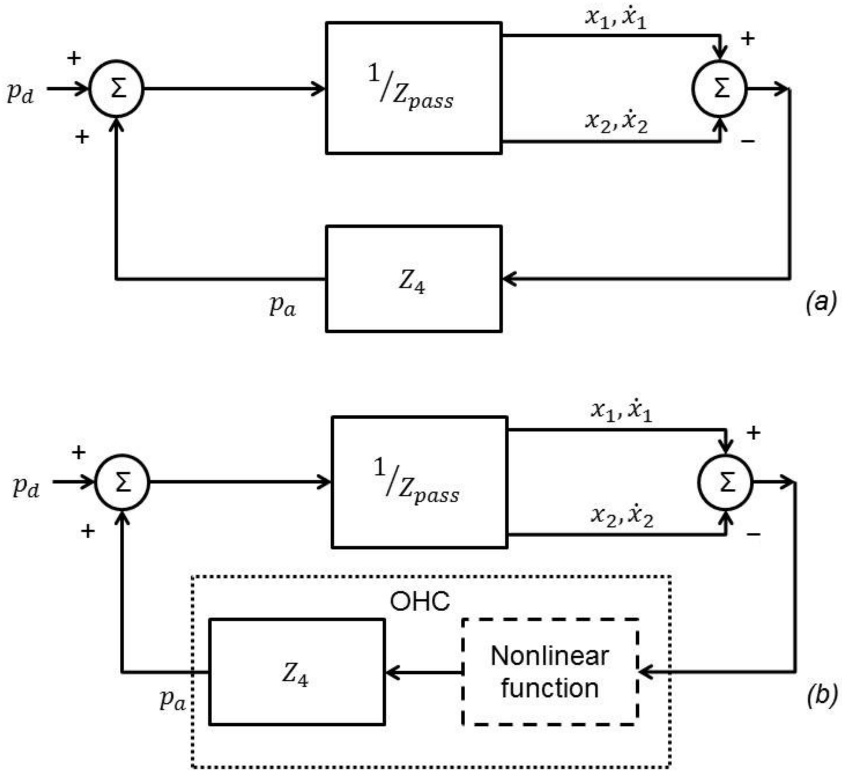

Figure 3.6: The upper diagram represents the linear micromechanical element. The lower diagram has a nonlinearity introduced into it and represents the basic functioning of the quasi-linear model.

An obvious consequence of the nonlinearity is the generation of harmonics at its output that will influence the response of the BM motion. This is illustrated in Figure 3.7: considering, for example, a Boltzmann function, when the input is low compared to the saturation point, the output will be similar to the input and the spectra of both input and output are equivalent. When the input is high compared to the saturation point of the nonlinearity, the output will saturate, and, depending on the parameters of the Boltzmann function, the output will resemble a square wave. What is important is the difference between the spectrum of the input and that of the output, the latter having extra harmonics, as shown in the bottom right plot in Figure 3.7.

The aim of the quasi-linear method is that, even when the output produces harmonics, to consider only the fundamental component as the output of the nonlinear function, while discarding higher order harmonics. This is reasonable if the primary component is dominant with respect to the higher harmonics. At this point, since the 'new' output of the nonlinear function is a sinusoid, the system may be regarded as linear and analysis in the frequency domain may be performed.

The procedure used to obtain the output of the nonlinear function requires the input to be transformed from the frequency domain to the time domain; this is done by constructing a time vector of, typically, $N_t = 24$ samples per period (Kanis and de Boer, 1993), although the number of samples, N_t, may be incremented if necessary to reduce overall error. The output can then be converted back to the frequency domain for analysis.

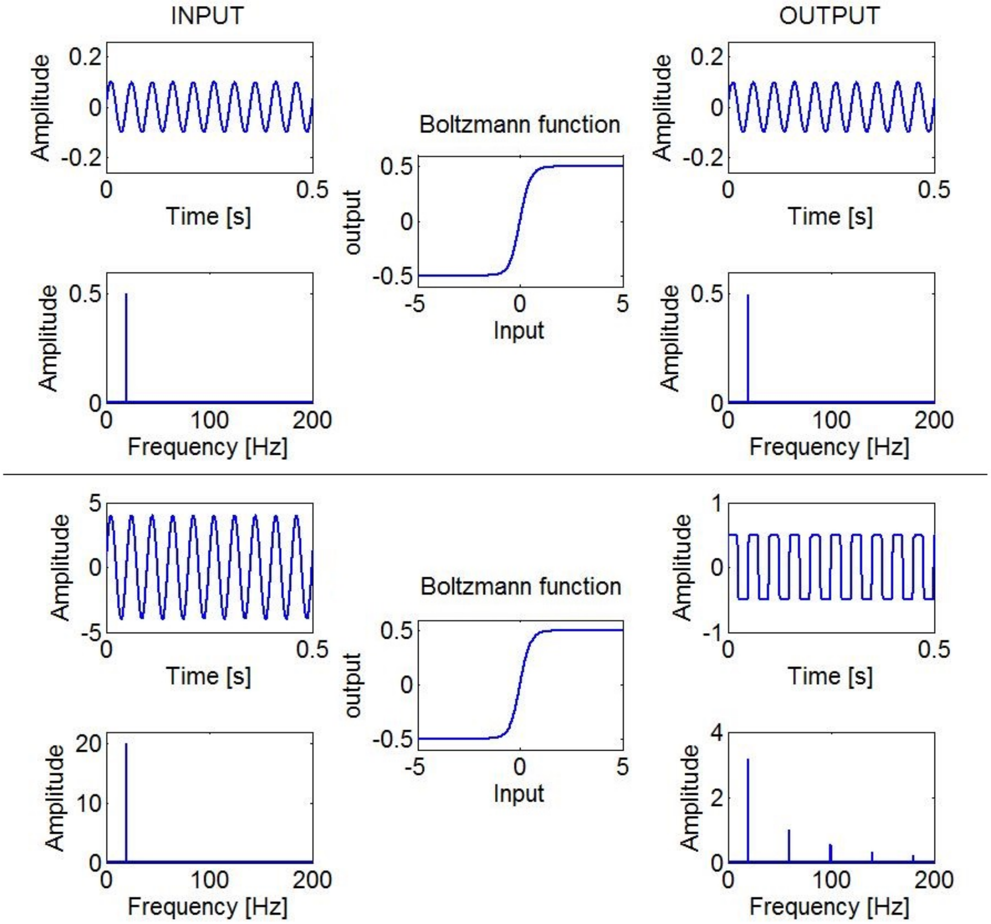

Figure 3.7: Example of the response of the system containing the nonlinearity, in both time and frequency domains, to a low level input with respect to the saturation point of the nonlinearity (top five graphs) and to high level input with respect to the saturation point of the nonlinearity (bottom five graphs).

Although Kanis and de Boer (1993); Young (2011) use single degree of freedom micromechanical elements to develop the quasi-linear model, for this doctoral project, the two degree of freedom element, shown in Figure 3.4, is used, in order to be consistent with the micromechanics of the state space model. This allows us to use the two models in tandem for obtaining different results. As with the original state space model, 512 of these elements are spatially aligned to form the cochlear partition and coupled together via the cochlear fluid. Appendix C provides the detailed mathematical formulation of the quasi-linear model, which has been kept out of the main body of the thesis, since the results obtained from this model are not the main focus of the project.

3.4 Summary

This chapter has reviewed some of the models that can be used to model cochlear mechanics. First, Van der Pol oscillators were introduced, showing how they are used to simulate local effects inside the cochlea, including SOAE generation and entrainment. Secondly, the micromechanical model by Neely and Kim was introduced, and it was shown how it can be used as the basic building block to construct a macromechanical model of the cochlea using the state space formulation. Individual micromechanical elements are coupled through fluid coupling. The state space formulation has the advantage of allowing nonlinear time domain simulations to be easily performed. In the last section of this chapter, the quasi-linear model of the cochlea was introduced, which allows computing simulations of the cochlear model containing nonlinear elements in the frequency domain.

Chapter 4

Development of the linear properties of the cochlear model

A cochlear model is based on assumptions and simplifications that allow components that do not contribute significantly to the functioning of the cochlea to be neglected. The modeller must choose which parameters are most important for it to operate correctly and select values for these parameters. A theoretical model of the cochlea must be tuned in order to obtain results that can be compared to experimental measurements. It is therefore very important to understand the processes, both linear and nonlinear, inside the cochlea and how they can produce by-products such as OAEs that can be measured for experimental purposes. The primary cochlear model used here is the state space model introduced in Chapter 3, which is composed of a series of sharply tuned active micromechanical elements, as shown in Figure 3.3, spatially distributed along the length of the cochlea. These are coupled through cochlear fluid coupling, using the state space formulation.

The present chapter will explain the details of the model, including the reasons behind the choice of the parameters assigned to the micromechanics of a human cochlea. The parameters were obtained by converting those from the cochlea of a cat used by Neely and Kim (1986). Furthermore, the sensitivity of the model has been adjusted to match as well as possible the enhancement properties of the human cochlea and considerations have been made regarding the influence on the cochlear fluids and their impact on the frequency response curves.

4.1 Tuning the model to replicate a human cochlea

4.1.1 Frequency tuning and response

The parameters used in the Neely & Kim model were selected to represent the biomechanical properties of the cochlea of a cat, according to physiological measurements and experiments (Neely and Kim, 1986). The frequency range used for the original model was from approximately 200 Hz to 60 kHz. Neely and Kim originally compared their results with the experimental data of neural tuning in a cat from Liberman (1982). Figure 4.1 shows the frequency to place map obtained when using the state space formulation implemented here with Neely & Kim's parameters of the cat's cochlea, which is compared with Greenwood's function (Greenwood, 1990), given by the following:

$$CF = 418 \cdot (10^{2.1x_{norm}} - 0.8), \tag{4.1}$$

where x_{norm} is expressed as a proportion of length along the cochlea, with the apex = 0 and the base = 1. The characteristic frequency (CF) curve obtained from the state space model fits well within a range of frequencies with Greenwood's function. Problems arise at low frequencies, at the apical end of the cochlea, where the results from the state space model tend to continue to decrease logarithmically, while the Greenwood function decreases rapidly covering a wider range of low frequencies. Nonetheless, the CF results from the state space model are a good approximation of the frequency mapping in the cochlea of a cat.

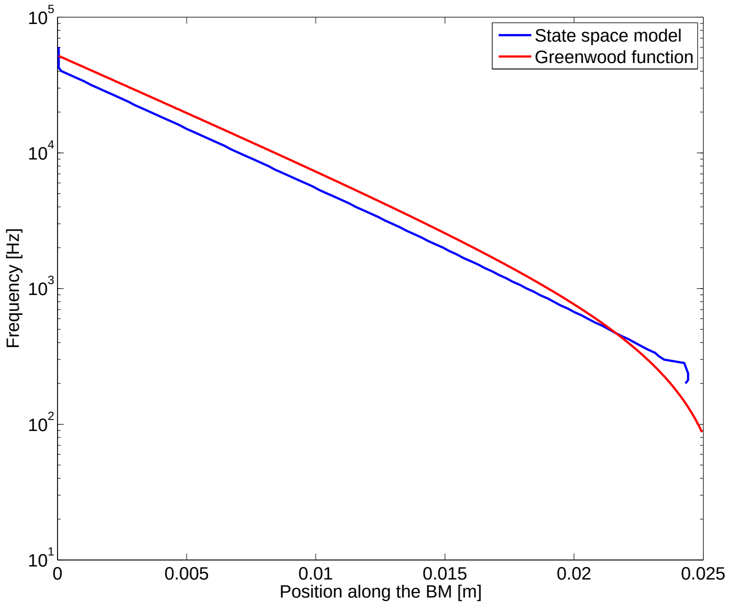

Figure 4.1: Frequency to place map of the state space model using Neely & Kim cat parameters (blue curve) compared with Greenwood's function (red curve).

Tuning the Neely & Kim parameters to be more appropriate for a human cochlea was achieved by equating those at the base of the cochlea to those in the 20 kHz region in Neely & Kim's model of the cat's cochlea. The stiffness parameters along the cochlea were then tuned to provide a range of natural frequencies from 20 kHz at the base, to 200 Hz at the apex, stretched over a length of 35 mm, i.e. the length of the human cochlea. The damping terms were scaled to give Q factors for each micromechanical element that are in reasonable agreement with those in the original Neely & Kim model.

The red dashed curve in Figure 4.2 shows the Greenwood function for the human cochlea, which is given by the following equation:

$$CF = 165.4 \cdot (10^{2.1x_{norm}} - 0.8). \tag{4.2}$$

In order to match this trend, amendments were made to the exponential decay of the new set of human stiffness and damping parameters over the length of the cochlea. This allowed for a correct assignment of the natural frequencies to each micromechanical element. The solid black line in Figure 4.2 shows the frequency to place mapping of the human parameters obtained. The slope of this curve and that of the Greenwood function are very similar, although a slight discrepancy still exists in the apical end from approximately 25 mm upwards; after this point the Greenwood function tends to decrease more rapidly although there is no certain evidence of the cochlear mapping at the apical end of the inner ear.

Also plotted is the curve obtained from the commonly used approximation $f_n = f_0 e^{-x/l}$, where f_0 is the natural frequency at the base of the cochlea, showing the distribution of natural frequencies that is exponential and assumes a characteristic length of the frequency distribution of $l = 7$ mm. The characteristic length, or cochlear length-scale, l, can be defined as the distance over the length of the cochlea by which the characteristic frequency varies by a factor of e (Shera, 2003). The value assigned to the length scale is strictly linked to other cochlear properties such as the minimum wavelength and the preferred minimum distance (PMD) and therefore spacing between adjacent SOAEs. These properties will be dealt with further on in this chapter. The correct assignment of the length scale l, which in this case is 7 mm for the properties of human cochleae, provides a distribution of natural frequencies along the cochlea which is very similar to the distribution of frequencies obtained from the Greenwood Function and is also comparable to the mapping derived from the cochlear model, as shown in Figure 4.2.

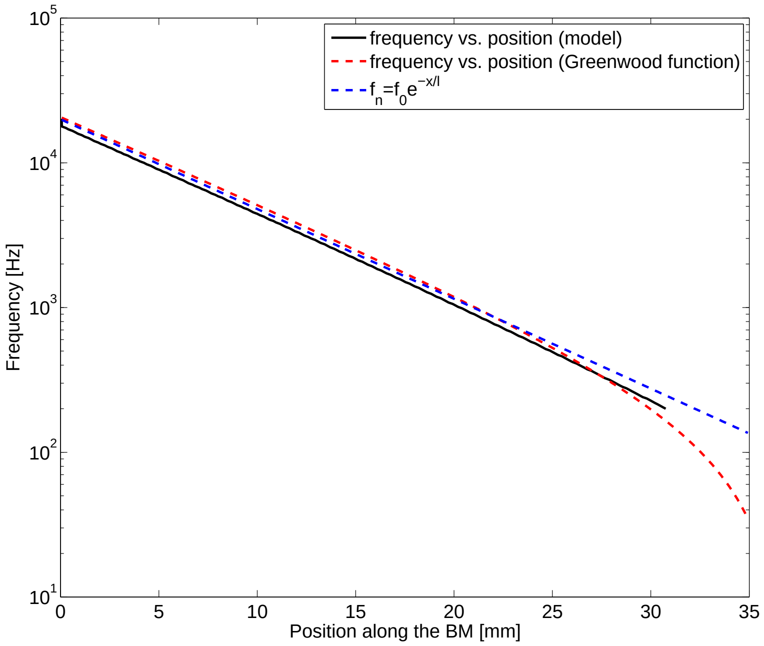

Figure 4.2: Frequency to place map of the state space model using human parameters derived from Neely & Kim's cat parameters (black curve) compared with Greenwood's function (red curve). Also plotted is the distribution of natural frequencies along the cochlea assuming exponential variation and a characteristic length-scale of $l = 7$ mm.

The new set of modified parameters to be used in the model for the human cochlea is listed in Table 4.1, together with their revised formulation. The mass of the BM was chosen to be the same as that in Neely and Kim (1986), and the effect of this mass on the form of the coupled response is further discussed in Appendix D. Table 4.1 also shows the variations that were applied to the helicotrema and middle ear boundary conditions of the model. In particular, the apex of the cochlea was modelled by allowing a minimum amount of damping to occur in this region that would reduce reflectivity and therefore affecting only the lower frequencies (Ku et al., 2008c). The middle ear parameters at the basal end were changed to match the characteristics of the human cochlea and are modelled based on measurements by Puria (2003) and later on revised for the state space model by Ku (2008).

Table 4.1: Parameters of the modified micromechanical model for the human cochlea

Quantity	**Symbol**	**Formula (SI)**	**Units**
Stiffness of BM	$k_1(x)$	$2.25 \cdot 10^9 e^{-276.14x}$	Nm^{-3}
Damping term of BM	$c_1(x)$	$200 + 6.79 \cdot 10^3 e^{-138.07x}$	Nsm^{-3}
Mass of BM	$m_1(x)$	$3 \cdot 10^{-2}$	kgm^{-2}
Stiffness of TM	$k_2(x)$	$1.25 \cdot 10^7 e^{-300.68x}$	Nm^{-3}
Damping term of TM	$c_2(x)$	$42.19 e^{-150.34x}$	Nsm^{-3}
Mass of TM	$m_2(x)$	$5 \cdot 10^{-3}$	kgm^{-2}
Stiffness of passive OHC impedance	$k_3(x)$	$2.05 \cdot 10^7 e^{-276.14x}$	Nm^{-3}
Damping term of passive OHC impedance	$c_3(x)$	$13.82 e^{-64.43x}$	Nsm^{-3}
Stiffness of active OHC impedance (Z_4)	$k_4(x)$	$1.26 \cdot 10^9 e^{-276.14x}$	Nm^{-3}
Damping term of active OHC impedance (Z_4)	$c_4(x)$	$4.71 \cdot 10^3 e^{-138.07x}$	Nsm^{-3}
Micromechanical feedback gain	γ	0.745	–
BM to inner hair cell (IHC) lever gain	g	1	–
Ratio of BM displacement to average BM displacement over radial cross section	b	0.4	–
Length of the cochlea	L	35	mm
Height of the cochlea	H	1	mm
Stiffness of middle ear boundary element	k_m	$2.63 \cdot 10^8$	Nm^{-3}
Damping term of middle ear boundary element	c_m	$2.8 \cdot 10^4$	Nsm^{-3}
Mass of middle ear boundary element	$m_m(x)$	$2.96 \cdot 10^{-2}$	kgm^{-2}
Damping term of helicotrema	c_h	210	Nsm^{-3}
Mass of helicotrema	$m_h(x)$	$1.35 \cdot 10^{-2}$	kgm^{-2}
Cochlear fluid density	ρ	1000	kgm^{-3}
Number of cochlear elements	N	512	–
Characteristic length scale	l	7	mm

The frequency response of the linear model can be calculated using Equation 3.17 in both the passive case, with $\gamma = 0$, and in the fully active case, with $\gamma = 0.745$. The derivation of this particular value assigned to γ will be explained later on in this chapter. Examples of the frequency response of the cochlear model are shown in Figure 4.3. The response along the cochlea due to pure tone inputs at three different frequencies (0.8 kHz, 3.2 kHz and 12.8 kHz) are shown for both the active case and the passive case, represented by the solid lines and the dashed lines respectively.

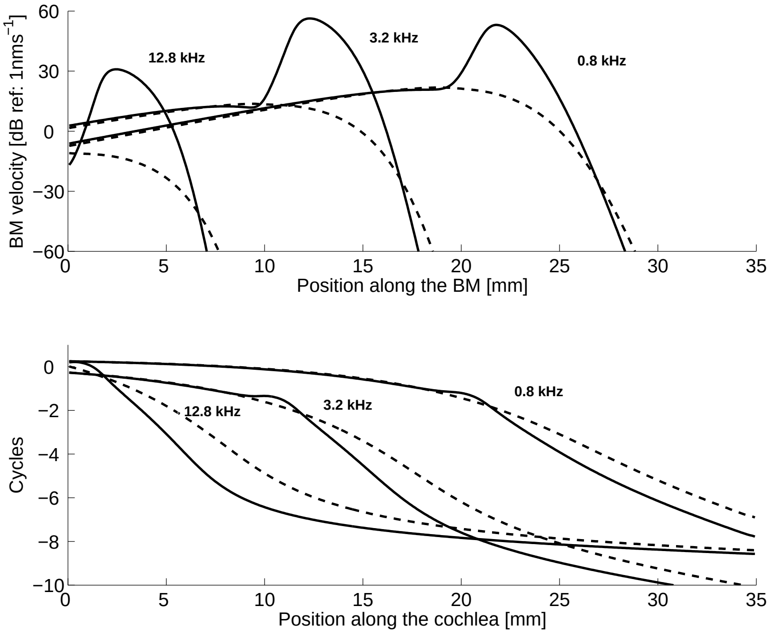

Figure 4.3: Predicted amplitude and phase of the BM velocity responses along the cochlea produced by the linear state space model at 0.8 kHz, 3.2 kHz and 12.8 kHz. The solid line represents the response of the active cochlea, where $\gamma = 0.745$, and the dashed line represents the response of the passive cochlea, where $\gamma = 0$.

These responses show the typical transition seen in experimental measurements, (Robles and Ruggero, 2001), between the well damped peak when passive, to the "broad and tall" peak, with a half octave shift in the best frequency, when active.

4.2 Modelling cochlear amplification

The amplification process of the CA occurring in the cochlea is fully active for low level stimuli where maximum enhancement takes place. The feedback gain, γ, shown in Table 4.1, can be thought of as a parameter that allows full activation of the CA, and therefore maximum enhancement. When this parameter is zero, the active impedance of the OHCs, Z_4, also becomes zero, and the model becomes completely passive. When γ is greater than zero, the active impedance adds what has come to be known as "negative damping" to the system. An upper limit value has to be given to γ, which will be used for a fully active model, when stimulated by low level stimuli. The value assigned to γ also determines the stability of the model. For a constant value of γ equal to 1.016 along the whole length of the cochlea, it was found that the model became unstable. It is therefore important to understand how much enhancement occurs over the frequency range of interest when the model is fully active and stimulated by low level sounds by assigning the correct value to γ.

Enhancement curves were produced from the simulated frequency responses, in order to understand the value to assign to γ, which show the difference in peak values of the BM response for specific values of γ set along the length of the BM. Figure 4.4 shows several such curves, with values of γ between 0.2 and 0.8. The final value selected was $\gamma = 0.745$, which allowed for a maximum enhancement of approximately 45 dB at the base of the cochlea and of 20 dB at the apex, which is in reasonable agreement with measured enhancements in rodents (Robles and Ruggero, 2001), although there is some debate about whether the maximum enhancement in humans is somewhat higher (Shera et al., 2002).

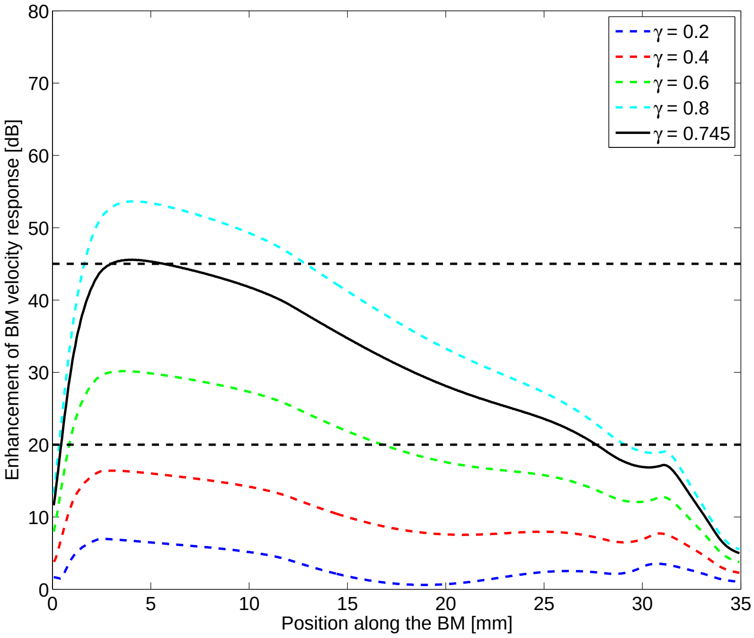

Figure 4.4: Enhancement of the state space model of the human cochlea using various levels of γ. A value to γ of 0.745 provides a maximum enhancement of approximately 45 dB at the base of the cochlea and of 20 dB at the apex, which are levels indicated by the black dashed lines.

4.3 Sharpness of the cochlear model tuning curves

The validity of the parameters shown in Table 4.1 were also verified by calculating the sharpness of the tuning curves, which depends on the amount of damping in the system. This was assessed using the following formula:

$$Q_{10dB} = \frac{f_{centre}}{\Delta f_{10dB}}, \tag{4.3}$$

where f_{centre} is the natural frequency at a specific location along the BM, and Δf_{10dB} is the interval between the frequencies of the response that has fallen by 10 dB on either side of f_{centre}. An example of how this was performed for one of the responses in the frequency domain is shown in Figure 4.5. The overall sharpness of tuning obtained for the human parameters in Table 4.1 used here and the cat cochlea, using Neely and Kim's original parameters, are shown in Figure 4.6. It can immediately be seen that the human cochlear model shows a greater selectivity than that of the cat. This is in agreement with studies conducted by Joris et al. (2011) that demonstrate, by means of both non-invasive and invasive experimental methods, that the cochlea of macaque monkeys, which are considered to be phylogenetically closer to humans, is more selective than that of other species, in particular cats, guinea pigs and chinchillas. The values of Q_{10dB} obtained from the human model here are, however, somewhat less than the psychophysical tuning measurements reported by Yoon et al. (2011) at higher frequencies. Yoon also reports a smoother increase of Q_{10dB} with CF.

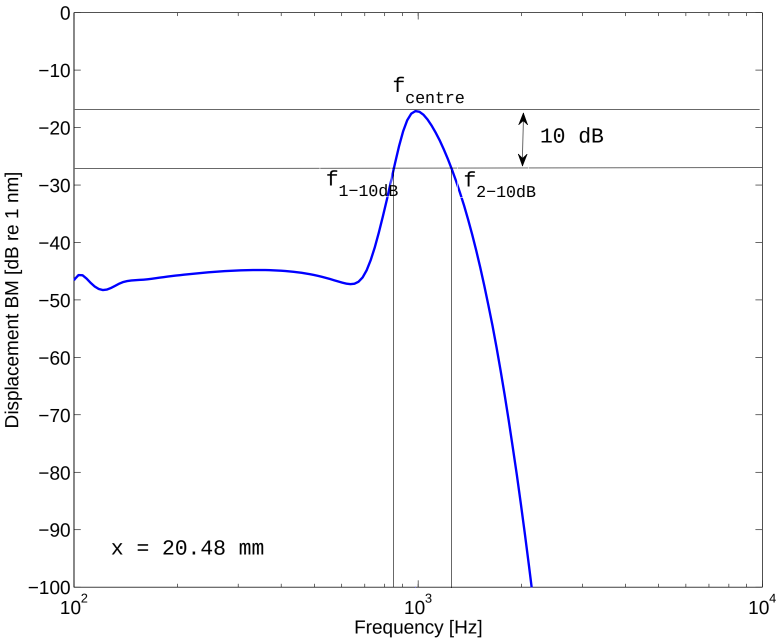

Figure 4.5: Frequency response of the BM at 20.48 mm. The figure shows values of frequencies to be used to obtain the sharpness of tuning of the curve.

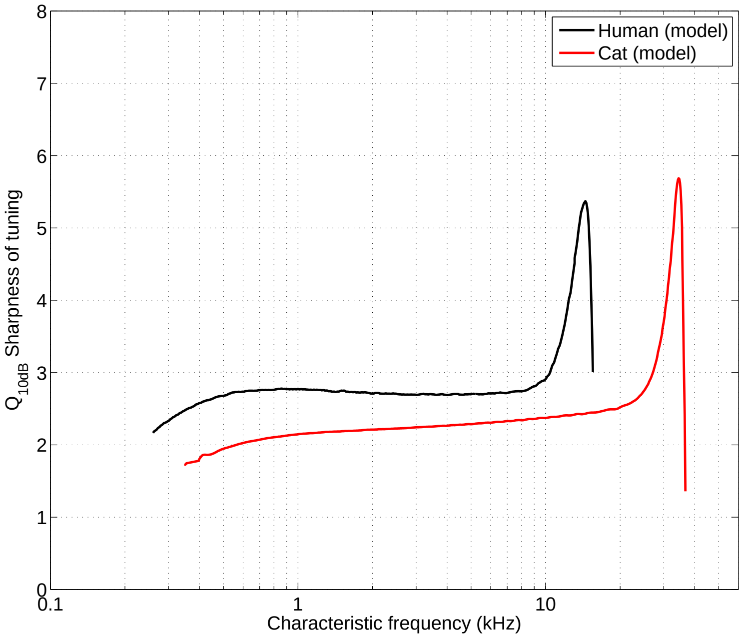

Figure 4.6: Modelled sharpness of tuning of the BM as calculated with the current active model for the human and using the original Neely and Kim parameters in the model for the cat.

Although the sharpness of the tuning curves from the model show a flatter trend with respect to frequency than the experimental results by Yoon et al. (2011), for example, the values assumed by the model are in reasonable agreement with measured ones and are considered acceptable, given the ability of the model to simulate to a good degree other properties of the human cochlea.

4.4 SOAE spacing

An SOAE is generated by a standing wave produced between the middle ear boundary and a reflection site along the BM; the phase change of the wave undergoes an integral number of cycles during its round trip and is kept sustained by the CA (Shera, 2003). How the state space model can replicate this phenomenon and generate SOAEs will be explained in Chapter 5 . However, it is possible at this stage to make predictions of the spacing between adjacent SOAEs. Shera and Zweig (1993) hypothesised that the average distance between resonant positions along the cochlea that take part in SOAE generation is:

$$\Delta S_{SOAE} \hat{\approx} \frac{1}{2}\lambda_{peak}. \tag{4.4}$$

This equation assumes a dependency between the distance between sources of generation of SOAEs and the peak wavelength, λ_{peak}. λ_{peak} is calculated by means of the impedance of the cochlear partition, Z_{cp}, which is evaluated at each position along the cochlea and is dependent on the characteristic frequency at that specific location:

$$\lambda_{peak} = maximum\ of\ \Re\Big\{\sqrt{\frac{HZ_{cp}(x_{cf},\omega_{cf})}{-2i\omega_{cf}\rho}}2\pi\Big\}, \tag{4.5}$$

where H and ρ are defined in Table 4.1. The peak wavelength is plotted as a function of position in the top plot of Figure 4.7, for different values of feedback gain. When $\gamma = 0$, the peak wavelength, λ_{peak}, is about twice that for $\gamma = 0.745$, and in both cases this increases somewhat at higher values of CF. Assuming the validity of the active cochlear model, the average distance between resonant positions of SOAEs, ΔS_{SOAE}, along the cochlea, obtained from Eq. 4.4, is approximately equal to 0.6 mm at the base. This is in acceptable agreement with findings by Talmadge et al. (1993), where the characteristic frequency separation between adjacent independent emissions within an ear corresponded to approximately 0.4 mm, while for adjacent emissions with larger separation the distance tends to be a multiple of 0.4 mm.

Shera (2003) shows that Equation 4.4 is related to the more common method for obtaining spontaneous emission separation given by

$$\frac{f}{\Delta f} = \frac{2l}{\lambda_{peak}}. \tag{4.6}$$

It was previously shown in Figure 2.5 that the measured value of $f/\Delta f$ peaks at about 15. Results from the cochlea model in Figure 4.7 show that in the active case, where $\lambda_{peak} \approx 1$ mm, values of $f/\Delta f$ vary between a range of 5 and 11. This variation is plausible, although N_{SOAE} was, in practice, shown to increase with SOAE frequency (Shera, 2003) rather than fall as in Figure 4.7. However, the active cochlear model predicts a value for $f/\Delta f$ of about 11 at the base, which is in reasonable agreement with what is expected.

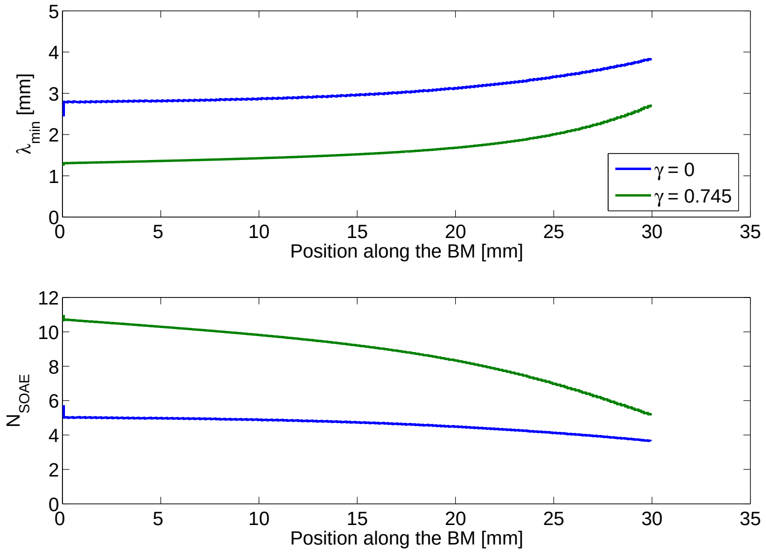

Figure 4.7: The top plot shows the variation in minimum wavelength that the travelling wave undergoes at different locations along the length of the cochlea in the present model. The bottom plot shows the variation in PMD along the length of the cochlea, as calculated using Eq. 4.6.

4.5 Cochlear irregularity

The parameters in Table 4.1 have a smooth variation along the cochlea. In reality, the mammalian cochlea, particularly in primates, is characterised by random irregularities, or roughness, of the parameters between the base and the apex, as discussed in Chapter 2. The constant values of feedback gain were thus superimposed with a random Gaussian distribution that could take account of the perturbations along the cochlear length with a smaller variation at the base, where the cochlea is more sensitive than at the apex. The random variations of the feedback gain will allow for an unstable cochlea model, i.e. the generation of positive poles when calculating the eigenvalues of the system matrix **A** in Equation 3.14 that initiate the generation of spontaneous emissions (Elliott et al., 2007; Ku, 2008). It is therefore possible to generate a cochlear model that produces a statistically plausible number of SOAEs by changing the characteristics of the random perturbation (Ku et al., 2008c). Talmadge et al. (1993) showed that emissions were present in 72% of the subjects and in 56% of the ears under examination in their study. Furthermore, studies from a number of authors, summarised in Table 4.2, show that the mean number of SOAEs measured is between 3.0 and 6.9 and the median number is between 2.0 and 5.0, where these numbers depend to some extent on the instrumentation and methodologies used and the variation in the backward middle ear transfer function. There is also a difference between genders, with prevalence and average numbers of SOAEs being slightly higher in women than in men.

Table 4.2: Results from various experiments involving SOAE measurement in humans using different methods. The second column shows the average number of people with SOAEs across all subjects in %. The mean number and the median number of SOAEs per emitting ear are also shown.

Study	**All [%]**	**Mean**	**Median**
Penner et al. (1993)	66	3.0	2.0
Talmadge et al. (1993)	72	6.9	5.0
Penner and Zhang (1997)	62	3.4	2.0
Zhang and Penner (1998)	75	3.6	3.0

As discussed in Chapter 2, a natural variability of the irregularities exists along the length of the cochlea, with the base being more smooth and regular with respect to the apex, where there is a more chaotic arrangement of OHC organization. It is assumed that this is a further reason to believe that spontaneous emissions are predominant in the lower frequency hearing range, i.e. between 0.5 and 6 kHz with the highest number ranging between 1 and 2 kHz (Probst et al., 1991). It is desirable to include these properties in the cochlear model to understand their influence on the way the cochlea operates. The potential number of SOAEs that a model can generate can be calculated by considering the number of unstable eigenvalues of matrix **A** in Equation 3.14, although not all of these potential instabilities grow into distinct SOAEs due to their interaction with each other (Ku, 2008; Ku et al., 2008c, 2009). The form of the irregularity used here was:

$$\gamma(x) = \gamma_0 + \delta(x), \tag{4.7}$$

where $\gamma_0 = 0.745$, as estimated previously from the enhancement curves in Figure 4.4, and

$$\delta(x) = D(x)r(x), \tag{4.8}$$

where $D(x)$ varies smoothly from 0 to 1 between $x = 0$ mm to $x = 35$ mm along the length of the cochlea, and $r(x)$ is a Gaussian random function with unit variation. Random variations of the feedback gain that generate statistically plausible numbers of SOAEs in the model were generated. Amongst a large set of random variations obtained through simulations, the ones that generate only one unstable pole, and therefore one SOAE in a certain frequency range, were chosen as possible candidate variations for running further simulations. The reasoning behind this choice is simplicity: assuming the variation is a plausible example of the irregularities in the human cochlea, it will initially be easier to understand how a single SOAE interacts with external tones without being interfered by other instabilities along the length of the cochlea.

The feedback gain of the cochlea, γ, was set at 0.745, as shown in Equation 4.7, and was used as the mean value of the generated Gaussian random variation. The roughness function, $r(x)$, was generated by passing a Gaussian white noise signal through a 5^{th} order Butterworth band pass filter (Ku et al., 2008c). The high cut-off wavelength was chosen such that the wavelengths do not exceed the actual length of the cochlea (35 mm). The low cut-off wavelength was chosen above the scale of the cochlear discretization (0.0684 mm); despite this limit, various values were evaluated for the lower cut-off wavelength. The vertical dashed line shown in the Figure 4.8 represents half the wavelength of the travelling wave at its peak; the pass-band spectrum shown includes this value since this allows the travelling wave to encounter irregularities at correct distances along the length of the cochlea. A comparison of the results using various wavelength spectra and peak-to-peak amplitudes for gain variation is shown in Table 4.3. The lower cut-off frequency chosen is $\lambda_{cut-off} = 0.19$ mm and gives what Ku describes as a feedback gain with a densely spaced random variation (Ku et al., 2008c). This allows for a more rapid spatial variation that generates instabilities in the lower part of the frequency spectrum, i.e. below 2 kHz. The choice of cut-off wavelengths is also consistent with Shera's view that the generation of SOAE in human cochleae is due to dense, random inhomogeneities along its length (Shera and Zweig, 1993). In particular, the values of cut-off frequency allow for enough spectral content in the inhomogeneities at half the peak wavelength, (λ_{peak}).

Various peak-to-peak amplitudes (standard deviations) were also tested for evaluating the most plausible results. The chosen statistical parameters to apply to the random vector are those shown in red in Table 4.3. The chosen standard deviation for the random vector predicted an ensemble of cochleae models with a mean number of primary SOAEs equal to 3.18 and a median value of 3. By running a total of 400 simulations, 13.25% of these produced random feedback gains that would generate one unstable pole, with 5.5% of these having an unstable pole below 6 kHz.

Table 4.3: Results of 400 numerical simulations of models with irregularity in the gain with different statistical parameters. The percentage of simulations with a single SOAE are shown, together with an SOAE below 6 kHz, the mean and median number of SOAEs per ear.

Cut-off wavelength [mm]	**peak-to-peak amplitude** [%]	**Simulations with one SOAE** [%]	**Simulations with one SOAE** <= 6 **kHz** [%]	**mean number of SOAEs per ear**	**median number of SOAEs per ear**
0.48	5	27.75	4.75	1.13	1
0.48	10	0.50	0.25	6.82	7
0.3	5	23.75	4.00	0.61	0
0.3	10	1.75	0.50	5.53	5.50
0.19	5	9.5	1.25	0.17	0
0.19	10	13.25	5.50	3.18	3
0.14	5	2.50	0.00	0.04	0
0.14	10	21.75	5.25	1.96	2

Figure 4.8 shows how the chosen parameters assigned to produce random variations of feedback gain affect the model in terms of SOAE generation. The plot on the top left shows the spectra of the various filters used using a $\lambda_{cut-off} = 0.19$ mm. Different $\lambda_{cut-off}$ allowed the amount of irregularity of the feedback gain to be varied. The vertical dashed line shows the position of half the wavelength of the travelling wave at its peak (λ_{min}). The plot on the top right shows the ensemble of values obtained for the parameter $f/\Delta f$ for 400 realizations of the random variation, most of them assuming a value around 11 (dashed black line), as also predicted in the lower plot in Figure 4.7. The bottom left plot of Figure 4.8 shows a histogram of the ensemble of unstable frequencies. Most unstable poles occur between approximately 2 and 15 kHz. The bottom right plot shows a histogram of normalised spacings per cochlea, again showing a peak around 11.

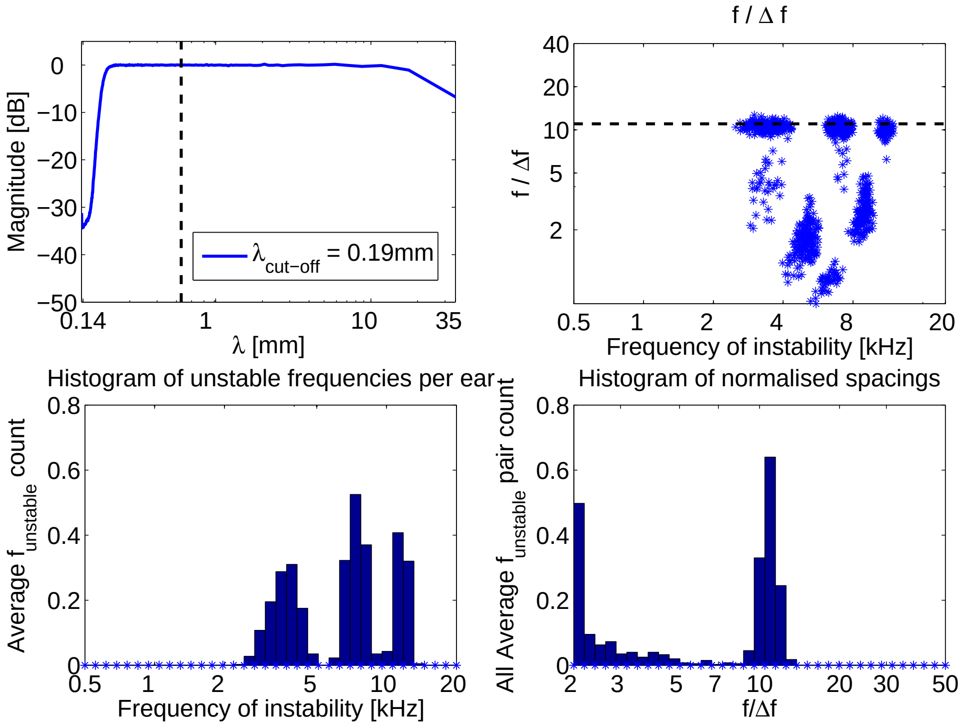

Figure 4.8: Results obtained from the simulations that tested the suitability of a random variation with specific statistic parameters. The plot on the top left shows the spectrum of the filter used when $\lambda_{cut-off} = 0.19$ mm. Different $\lambda_{cut-off}$ were tested, which allowed varying the amount of irregularity of the feedback gain. The vertical dashed line shows the position of half the wavelength of the travelling wave at its peak (λ_{min}). The plot on the top right shows the values obtained for the parameter $f/\Delta f$, most of them assuming a value around 11 (dashed black line). The bottom left plot shows a histogram of the unstable frequencies across the ensemble of simulated cochleae. The bottom right plot shows a histogram of normalised spacings per cochlea, also across the ensemble of simulated cochleae.

With respect to previous work performed on the state space cochlea model in Ku et al. (2008c), the overall value of $f/\Delta f$ is lower, being approximately 15 in Ku's case and 11 in the present study. The reason behind this involves the value assigned to the feedback gain. Although it is possible to increase the $f/\Delta f$ to a more desirable value by increasing the average level of feedback gain, this would not be feasible since the enhancement given by the model would be too high and unrealistic. Therefore, a compromise has been made by leaving the mean value of the feedback gain at 0.745, in order to have acceptable values of enhancement, peak wavelength and $f/\Delta f$.

Amongst the many cases that gave the results shown in Figure 4.8, one specific pattern of random feedback gain along the cochlea was chosen. The aim was to use a pattern that would lead to a stability plot with only one unstable pole. Figure 4.9 shows the stability plot for the random gain variation used for the simulations shown in the following chapters of this thesis, where σ is the real part of the eigenvector of $\mathbf{A}$, which is positive if the pole is unstable, that do include only one SOAE. The zoomed-in section shows the location of the unstable pole, having a frequency of approximately 2.6 kHz. The SOAE produced by running time domain simulations for this model has a frequency of 2665 Hz at a level of -17 dB SPL in the ear canal. The inset in Figure 4.9 shows the chosen feedback gain distribution along the length of the cochlea.

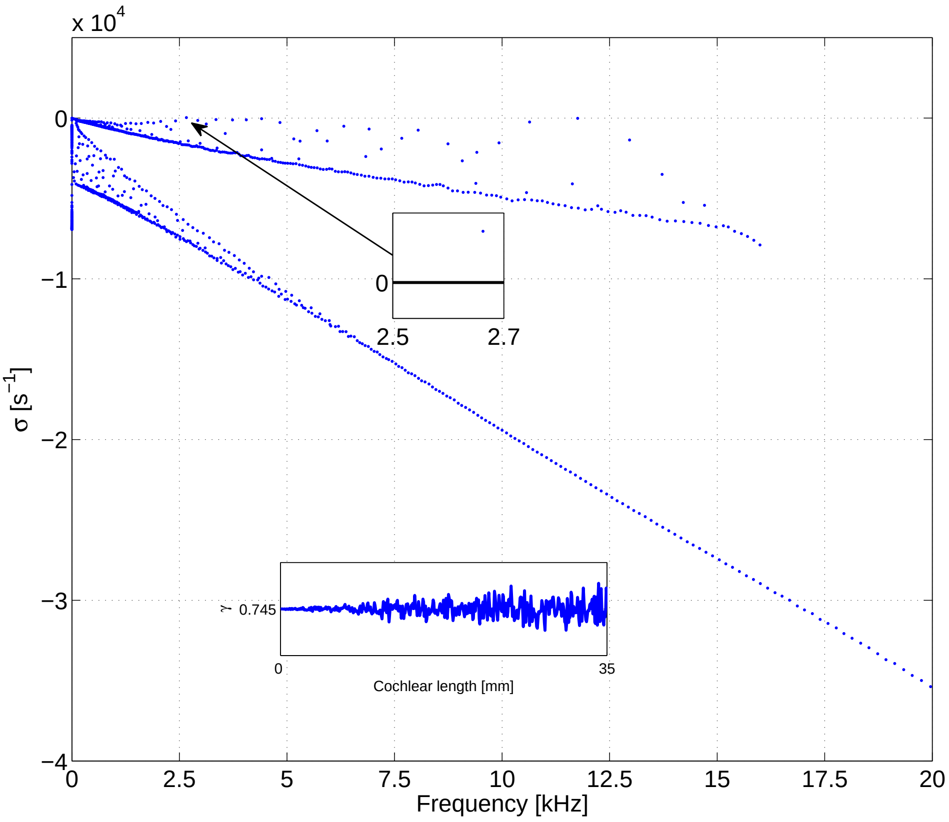

Figure 4.9: Example of the stability plot together with the random variation in the feedback gain that produces it. The zoomed in section shows the location of the unstable pole having a frequency of approximately 2.6 kHz. This random feedback gain will be used for further simulations in the following chapters of the thesis.

4.6 Summary

In this chapter, the development of the linear properties of the state space cochlear model have been presented. The estimated parameters for the model were derived by modifying those used by Neely and Kim (1986) and were tested in order to validate their suitability for replicating the characteristics of a human cochlea, including frequency to place mapping, sharpness of the tuning curves and enhancement. Simulations were performed on the model to predict SOAE spacing; Ku (Ku, 2008; Ku et al., 2008c,b,a), has shown that the state space model predicts with reasonable accuracy the normalised spacing between SOAE as predicted by Shera (2003). A neat periodicity in the spectrum of SOAEs appears when a number of unstable poles are present in the model, where the spacing between emissions depends on the phase of the travelling waves that generate them and undergo integral round trip phase changes. The fact that the model predicts this periodicity improves its credibility, since no fine tuning of emission location is required, unlike mathematical models that use Van der Pol oscillators as SOAE generators (van Dijk and Wit, 1990; Long et al., 1990; van Dijk et al., 1994). The latter usually rely on oscillators whose parameters are finely tuned to obtain oscillations that reproduce the periodic properties of SOAEs. The frequency of the generated SOAE in the state space model is such that its response undergoes an integral number of cycles of phase change while travelling between the middle ear boundary and the reflection site inside the cochlea. There must also be sufficient gain close to the site where the travelling wave peaks to overcome the reflection losses and viscous damping and sustain the travelling wave. In fact, pole instability means that this standing wave will be sustained by negative damping. However, if the numerical results are compared to experimental ones such as those by Probst et al. (1991); Talmadge et al. (1993); Zhang and Penner (1998), it is plausible that both microphone restrictions and middle ear reverse transfer function properties could explain why the state space cochlear model is likely to have instabilities, and therefore spontaneous emissions over a larger range, i.e. up to 15 kHz, in contrast with experimental results that tend to not measure SOAEs above 9 kHz if not less. In a realistic scenario, multiple travelling waves of various frequencies will interfere constructively across multiple reflection sites, generating a number of primary and secondary SOAEs.

The state space cochlea model reflects reasonably well what is assumed to happen in the cochlea. However, modelling the irregular structure of the human cochlea is open to debate and the random feedback gain chosen to replicate it here is not necessarily the best reproduction of what occurs in reality, although the results shown in this thesis reproduce reasonably well what has been measured experimentally.

Chapter 5

Modelling cochlear nonlinearity

5.1 Introduction

In Chapter 2, it was noted that the CA is inherently nonlinear and provides a reduction in the active contribution of the cochlea as the input signal is increased, i.e. self-suppression (Kanis and de Boer, 1993). This nonlinearity is also important in the generation of OAEs. In modelling the cochlea, it is important to take into account these nonlinear characteristics. The nonlinear mechanism can be replicated in a numerical model using various functions to mimic OHC behaviour. This chapter will focus on the nonlinear functions used to model CA nonlinearity and on how these can be adjusted to obtain results that compare favourably to experimental measurements. As discussed in Chapter 3, the assumed position of the nonlinear element in the feedback loop of the micromechanical model used here is before the active impedance (Z_4); the latter acts according to the displacement and velocity caused by the shear motion between the BM and the TM. Although some models, such as Kanis and de Boer (1993), locate the nonlinearity after the active impedance, it can be argued from a physiological point of view that the order of events that produce an active force on the cochlear partition is such that the active pressure is a consequence of the nonlinear OHC impedance. A further reason for placing the nonlinear function before the active impedance is because this configuration allows for a more suitable comparison with those found experimentally (Young, 2011; How et al., 2010).

5.2 Assumed form of the nonlinearity

With the nonlinearity positioned before the active impedance it was possible to compare the results of the simulations using two forms of nonlinearities: a symmetric hyperbolic tangent function

$$v(u) = \frac{\alpha}{2} \tanh \frac{2u}{\alpha}, \tag{5.1}$$

and a first order Boltzmann function

$$v(u) = \frac{\alpha}{1 + \beta e^{-\frac{u}{\eta}}} - \frac{\alpha}{1 + \beta}, \tag{5.2}$$

where, v is the displacement output, u is the displacement input, α is the saturation point having units of displacement, which is a function of position along the cochlea, β is dimensionless and scales the amount of asymmetry of the Boltzmann function, and η determines the slope of the function. In order to ensure that the function has a slope of unity for low level inputs, η is constrained, given α and β. In particular,

$$\frac{dv(u)}{du}|_{u=0} = 1 \tag{5.3}$$

so that

$$\eta = \frac{\alpha\beta}{(1+\beta)^2}. \tag{5.4}$$

The stereocilia are assumed to be affected by both the shear displacement and velocity between the BM and the TM. Figure 3.4 illustrates that both the output of the nonlinear function used, and its derivative, velocity, are inputs to the the block, γZ_4.

Experiments have shown that emissions generated by the mammalian cochlea, in response to a pure tone, contain both even and odd harmonics. This initial consideration, makes the asymmetric Boltzmann function a more suitable candidate than the tanh function. Its input-output characteristic also appears to be a good approximation of those of OHCs, shown, for example, in Figures 1.12 and 2.1 (Cody and Russell, 1987; Kros et al., 1992; Dallos, 1996; Kros, 1996; Johnson et al., 2011). One of the biggest unknowns is the degree of asymmetry that it should provide, as the literature is inconclusive on this point (Johnson et al., 2011).

The saturation levels of the nonlinear function will depend on the specific location of an element along the length of the cochlea, and hence, the saturation point, α is a function of position. The tonotopic map of the cochlea also implies that the micromechanical elements at the base, which have greater values of stiffness, will saturate differently compared to the elements at the apical end, which have lower values of stiffness and hence, greater magnitudes of displacement. Figure 5.1 shows examples of how the Boltzmann function varies as a function of α. In this particular case, where β is set to 1, the

Boltzmann functions take the same symmetrical form of a tanh functions. The parameter β controls the amount of even and odd components in the output by altering the asymmetry of the function. Higher values of β allow for greater amplitudes of even harmonics relative to the odd harmonics. Figure 5.2 shows examples of how the Boltzmann function varies as a function of β, while keeping α fixed at a 1.

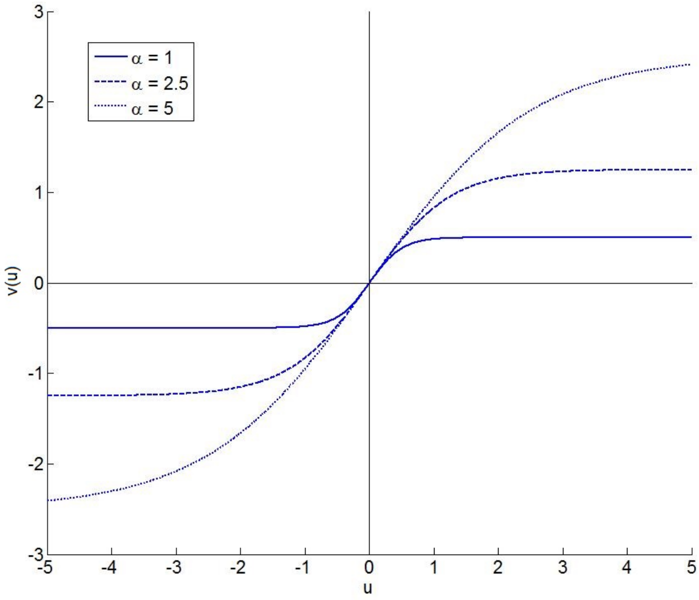

Figure 5.1: Variation of the input-output characteristics of the Boltzmann function when varying the parameter α. β is set to 1.

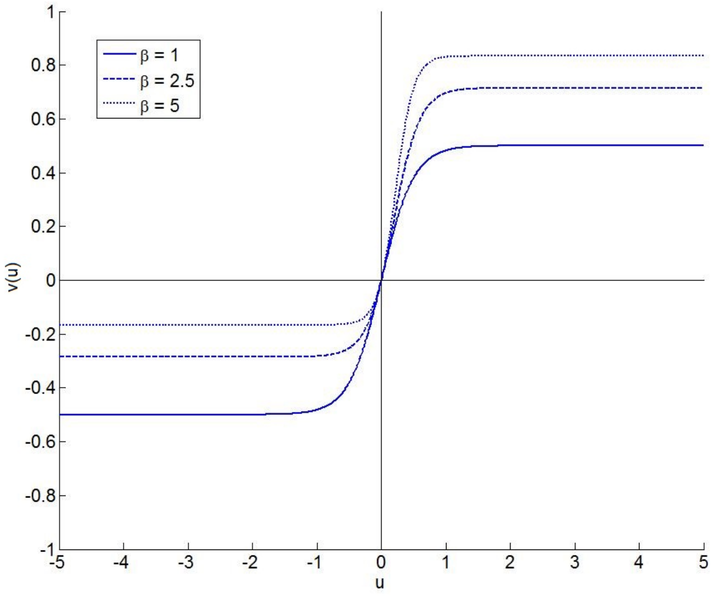

Figure 5.2: Variation of the input-output characteristics of the Boltzmann function when varying the parameter β. α is set to 1.

5.3 Choice of parameters

By comparing results using the hyperbolic tangent function with the Boltzmann function, it is possible to gain insight into the effect of the symmetrical properties of the nonlinearities on the results from the model. Physiological data that can help to set the parameters, α and β, is not attainable in vivo, as many of the measurements are from in vitro experiments, making it hard to predict the actual properties of the nonlinear phenomenon occurring in the CA. Furthermore, the cochlear model includes a nonlinearity whose output has the same dimensions as the input. This is not the case during experimental data, where the input is usually a SPL and the output is an electrical signal, i.e. the electrical potential generated in OHCs. To evaluate the values for α that would simulate the correct level of cochlear self-suppression at different positions along the cochlea, the quasi-linear model introduced in Section 3.3 was implemented, based on the one by Kanis and de Boer (1993), but using the same parameters as the state space model, which allowed the effective gain of the nonlinearity to be calculated for various driving amplitudes, at various frequencies between 200 Hz and 20 kHz. The α parameter of the two nonlinearities was adjusted to ensure that compression of the response began for input SPLs in the ear canal of about 30 dB, below which the response is assumed to be almost linear. It is difficult to know whether this is a feature of the cochlea over the whole frequency range. In fact, compression is certainly a characteristic of cochlear mechanics at high and mid frequencies, but there is little evidence to suggest that compression, and in particular mechanical nonlinearity, occurs in the lower frequency range below approximately 500 Hz (Cooper and Yates, 1994). However, it has been assumed that 30 dB is the starting point for compression at all frequencies. Between about 30 dB and 80 dB, self-suppression becomes increasingly effective, generating a compression curve with a slope between $1/5^{th}$ and $1/3^{rd}$ of a dB per dB (Robles and Ruggero, 2001). Above inputs of about 80 dB SPL, the system is assumed to again become linear, but is now passive. Figure 5.3 shows examples of level curves for excitation at characteristic frequencies of 0.2 kHz, 0.8 kHz, 3.2 kHz and 12.8 kHz, for the model incorporating either the tanh (left panel) or the Boltzmann functions (right panel). Both cases are very similar, which demonstrates that it is difficult to deduce the form of the nonlinearity, and particularly its degree of asymmetry, from these level curves alone.

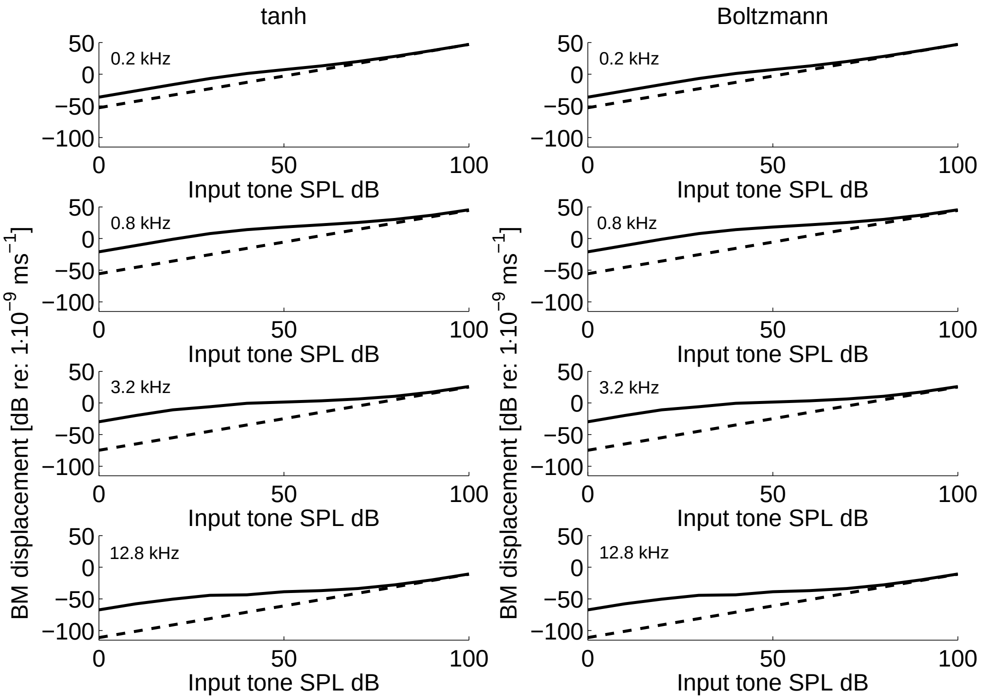

Figure 5.3: Compression curves for the state space cochlear model, obtained from the quasi-linear method, illustrating how the parameter α is tuned so that compression commences at approximately 30 dB until around 80 dB, where the model becomes nearly entirely passive. Compression is shown for input tones of 0.8 kHz, 3.2 kHz and 12.8 kHz for levels that vary between 0 dB and 100 dB. The solid line represents the response of the active cochlea where $\gamma = 0.745$ and the dashed line represents the response of the passive cochlea where $\gamma = 0$. Results are shown for the cochlear model containing both the tanh and the Boltzmann functions, but the results are indistinguishable on this scale.

Even order harmonics arise as a consequence of the asymmetry in the CA's nonlinearity. The assignment of an appropriate value to β in the Boltzmann function can thus be determined from the measured amplitude of the 2^{nd} harmonic in measurements of the nonlinear BM response (Cooper, 1998). Young (2011) assigns a value of 1.2 to β. Young (2011) and How et al. (2010) explain that the simulated DPOAEs change less than 1 dB when increasing this parameter from 1.3 to 3 and that its value does not notably affect the amplitude of predicted DPOAEs. On the basis of these results, β has again been assigned the value of 1.2.

Setting the parameter α as a function of position along the cochlea, also requires considering the following details of the ear model and of experimental data:

- Experimental findings show that saturation values of BM nonlinearity do not vary significantly in terms of input SPL over the audible frequency range

- Middle ear mechanics will influence the overall response given its frequency dependence
- Cochlear micromechanics vary in stiffness along the length of the cochlear partition making it stiffer at the base and less stiff at the apex; consequently, when moving from base to apex, if the parameter α is set to a constant value, then the saturation point would increase from base to apex

After running a number of quasi-linear simulations, it was possible to obtain reasonable values for α along the length of the cochlea by trial and error, and these are plotted as a function of position in Figure 5.4. This choice of values for α allows compression to commence at approximately 30 dB and to end at around 80 dB, where the model becomes nearly entirely passive for all excitation frequencies. The variation of α with position is somewhat different from results obtained by Ku (2008) and Young (2011). It can be seen in Figure 5.3 that to maintain compression from 30 dB to 80 dB, the saturation values given by α need to decrease after around 20 mm, as shown by the solid curve in Figure 5.4. If α is kept constant at the apical end, as in the work by Ku (2008) and Young (2011), then compression for the lower frequency range starts at a SPL that is too high.

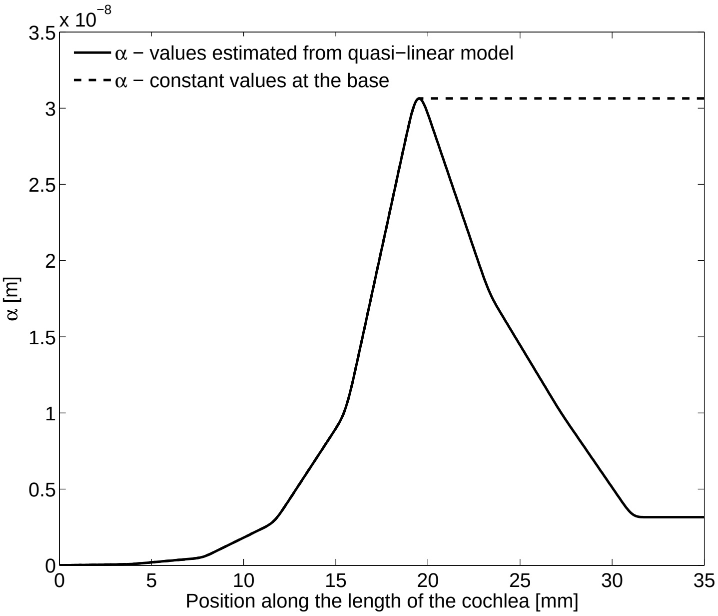

Figure 5.4: Saturation values, α, of the Boltzmann function incorporated into the micromechanical elements plotted as a function of position. The solid curve shows the calculated values while the dashed curve shows an example similar to those used by Ku (2008) and Young (2011).

A comparison of the two functions used in the model 15 mm along its length is illustrated, together with their slopes, in Figure 5.5. The differences in the symmetry of the functions are seen in the top panel of Figure 5.5, where the Boltzmann function is shifted upwards on the ordinate for larger positive and negative inputs with respect to the tanh function. The slopes of the different functions indicate the gain of the system and are shown in the lower panel of Figure 5.5. Unlike the hyperbolic tangent function, which is symmetrical with respect to the ordinate at 0 input, the slope of the Boltzmann function is asymmetrical, and initially increases for positive input values, adding gain to the output as it grows higher than 1. Both functions are defined to have unity gain for low level excitation. Figure 5.5 illustrates that the difference between the two functions is very subtle, demonstrating that the asymmetry introduced by the Bolzmann function is minimal, in accordance with experiments that resemble in vivo studies of OHCs (Johnson et al., 2011) as discussed in Section 2.1.

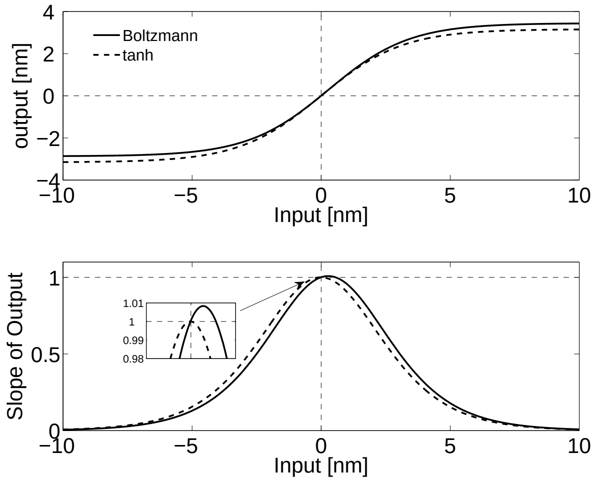

Figure 5.5: Comparison of the nonlinear characteristics of a tanh function and a Boltzmann function with $\beta = 1.2$. The top plot shows the output vs. input. The bottom plot shows the slope of the output vs. input for both functions. The parameters of the nonlinear functions are those used 15 mm along the cochlea, close to the position where the SOAE is generated.

5.4 Self-suppression using the quasi-linear model

One reason for using the quasi-linear cochlear model was to determine the values of α that could then be used in the state space cochlear model. The quasi-linear model was also used to find initial conditions from which to start time domain simulations of the state space model, as described in Section 6.4. An example of the results from the quasi-linear model is given in Figure 5.6; it can be seen that increasing stimulation levels decreases the activity of the system and reduces cochlear amplification. For higher input levels the response becomes less sharp and more broad. This is clearly shown in the top left plot of Figure 5.6, where at the characteristic place along the length of the cochlea, the magnitude does not increase as much for increasing levels of input as it does at the base of the cochlea. The lower left plot shows the real part of the cochlear partition impedance. This has a negative part, which provides negative damping, and hence, amplifies the cochlear wave when the input level is below about 60 dB SPL. This shows that for lower input levels, an active component is acting on the cochlear partition, while at higher level inputs, the cochlear partition is totally passive, leading to a dampening of the cochlear structures. The lower right plot shows how γ varies along the cochlea for different input levels: for lower input levels it assumes its maximum value of 0.745 along the whole length of the cochlea, but as the input level increases, γ decreases, particularly at the best position corresponding to the frequency of the input signal. Note that γ also decreases in a region at the base of the cochlea, which is far away from the characteristic place. As previously discussed, the values of α in this region have been tuned for high frequency input tones, however, significant motion is occurring in this region even for inputs of lower frequencies.

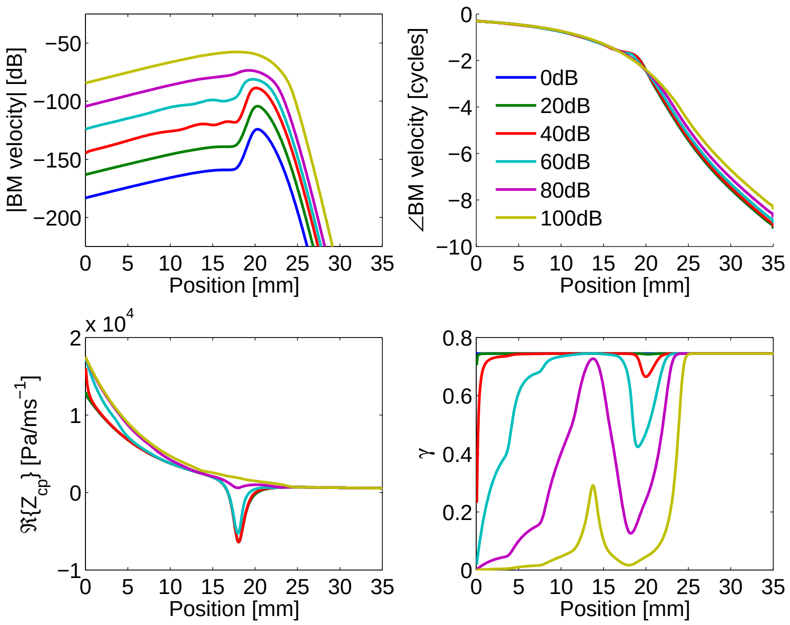

Figure 5.6: Self-suppression of a 1 kHz tone simulated using the quasi-linear method. The top plots show the magnitude of the BM velocity on the left and the phase of the BM velocity on the right, both as a function of position and it can be seen that increasing input levels lead to greater compression, but little change in the phase. The lower left plot shows the real part of the cochlear partition impedance, which has a negative part (negative damping) for lower input levels, indicating that an active component is acting on the cochlear partition, while for higher level inputs the cochlea is passive, leading to a dampening of the cochlear structures. The lower right plot shows how γ varies according to different input levels: for lower input levels it assumes its maximum value of 0.745 along the whole length of the cochlea, but as the input level increases, γ also decreases in particular at the position of the frequency of the input signal, but also at the base.

5.5 Two-tone suppression using the quasi-linear model

The quasi-linear model can also be used to predict two-tone suppression (Kanis and de Boer, 1994). In this case two sinusoidal signals, a probe tone kept at a constant SPL and a suppressor tone, whose SPL is varied, are simultaneously applied to the nonlinearity and its response is analysed to give the quasi-linear gain at the two frequencies. An example of the two-tone suppression results that were produced using the quasi-linear model here is shown in Figure 5.7; in this example, the probe tone is at 2 kHz and the suppressor tone is at 2.4 kHz, and it can be seen that increasing the level of the suppressor compresses the response of the probe tone. The frequency of the suppressor tone will affect the way it suppresses the probe.

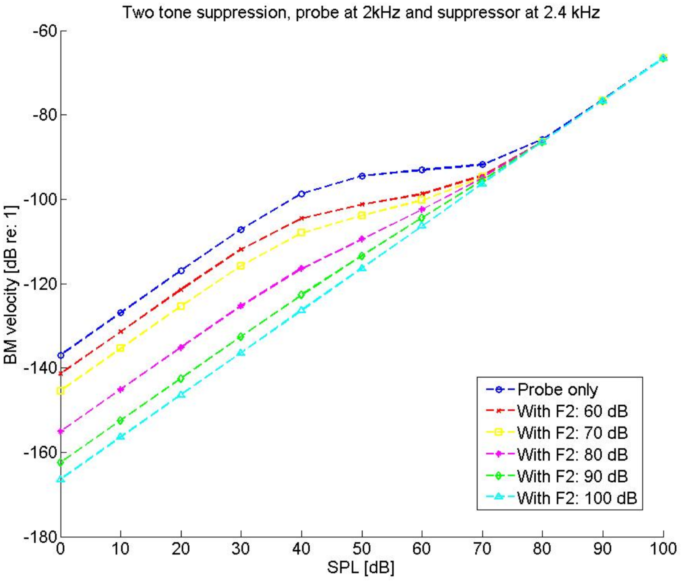

Figure 5.7: The BM simulated velocity at the probe tone is a function of the SPL at this frequency, for different levels of suppressor tone, illustrating two-tone suppression where the probe tone is 2 kHz and the suppressor tone is 2.4 kHz.

Similar results to the ones shown in Figures 5.6 and 5.7 were used to make comparisons between this state space model and a filter cascade model by Pan et al. (2015b), who also compared the prediction with measurements of two tone suppression measured in the cochlea by Cooper (1996).

5.6 Summary

In this chapter a symmetrical and an asymmetrical nonlinear function are introduced as possible models for that in the CA. The parameters of these functions have been set to reproduce the saturation curves measured in the cochlea, using the results from a quasi-linear model. The use of the quasi-linear model to model self-suppression, as well as two-tone suppression, is also described.

Chapter 6

Modelling SOAEs and the effect of low frequency bias tones

6.1 Introduction

This chapter describes numerical simulations of SOAEs performed using the cochlear models, with the aim of gaining a better insight into the possible causes behind cochlear nonlinearity and OAEs. The best way to validate a model is by replicating real experiments in order to obtain similar results. It is then possible to help understand the nature of the results by modifying parts of the model and making comparisons between the results from the alterations made. This strategy also allows understanding of whether certain results from real experiments are due to the mechanics of the cochlea and are replicable by the model, or if they are due to other effects, for example, neural, electrochemical or cellular that are not contained in the model. The state space model includes the presence of a nonlinear CA and can be used to simulate the generation of OAEs, and these are the focus of the results in the following sections.

First, a discussion regarding the stability of the state space model is outlined, then the results obtained from its time domain response are illustrated and compared with experimental data. Simulations of the variation in SOAE frequency and amplitude over time when affected by low-frequency external tones, i.e. bias tones, are then discussed and the results compared with experimental studies by Bian (2009). An ear canal and middle ear model are used in conjunction with the cochlear model to obtain input and output SPLs from the ear canal in a similar fashion to real experiments, as described in Appendix F.

6.2 Stability of the state space model

One of the great advantages of the state space method is the ease with which one can determine the system's stability. By calculating the eigenvalues of the state matrix **A** in Equation 3.7 it is possible to obtain the poles of the system. A system is classified as stable when its transfer function contains only poles having negative real parts. If this is not true, the linear system becomes unstable making its response grow exponentially. The second great advantage of this formulations, is that the state matrix **A** can include nonlinear functions when running time domain simulations of the cochlea; these nonlinearities will limit the exponential growth of motion of the system when it contains one or more unstable poles, generating the limit cycles that give rise to SOAEs.

As explained in Section 3.2, the macromechanical model consists of 512 micromechanical elements that resemble slices of the BM. Adjacent elements are coupled to one another through fluid coupling. The feedback gain, γ, is represented by a vector equal in length to the number of micromechanical elements, excluding the middle ear (the first element) and the helicotrema (the last element); the latter two elements represent the boundary conditions of the system. Therefore, each element is associated with a particular value of γ.

Figure 6.1 shows the poles of the system for four different sets of values associated to the feedback gain, γ; in each plot there are 2048 poles and so the individual poles appear to form lines. Note that the imaginary part of the poles has been divided by 2π to give units of Hz and plotted on the abscissa for notational clarity. The two upper plots show examples of when γ is constant along the whole length of the cochlear partition, where γ is equal to 0.745 on the left and to 1.02 on the right. For $\gamma = 0.745$, the system is completely stable as all poles have a negative σ; but when $\gamma = 1.02$, a number of poles become unstable. The frequencies of the unstable poles shown on the imaginary axis correspond to the frequencies of generated SOAEs. These emissions can also combine with one another, generating new SOAE frequencies that are not necessarily associated with an unstable pole (Ku, 2008). The plot on the bottom left shows a step variation introduced in the feedback gain, γ, that results in a single unstable pole of the system, as shown in the zoomed in portion of the plot. In the bottom right plot, γ resembles a more realistic condition of the cochlea, with the random distribution of the feedback gain at each location described in Section 4.5, which also has a single unstable pole that generates an SOAE at approximately 2.6 kHz.

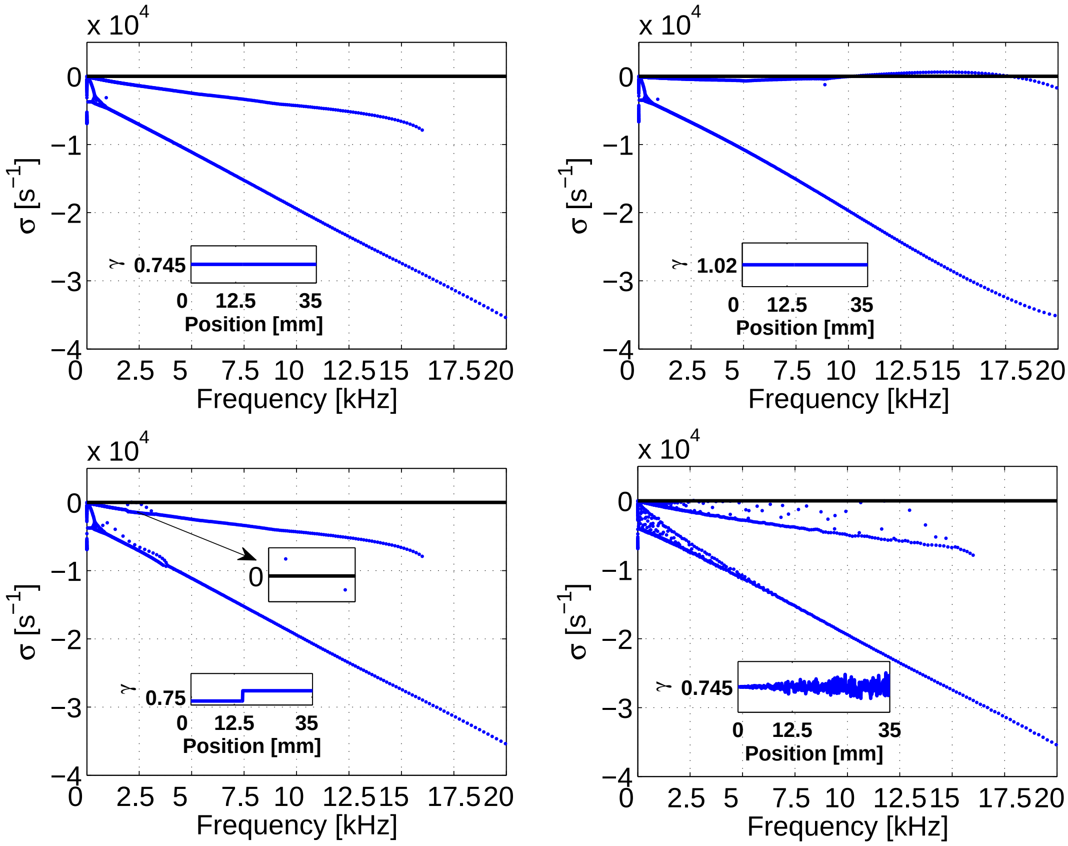

Figure 6.1: Stability plots for the coupled cochlear model with various gain distributions. Top left panel, $\gamma = 0.745$, system is stable; top right panel, $\gamma = 1.02$, system is unstable; bottom left panel, γ includes a step variation, system contains one unstable pole; bottom right panel, γ resembles a random gain distribution as described in 4.5, system contains one unstable pole.

6.3 Time domain simulations

A strength of the state space formulation of the cochlea model is the ease with which it can perform nonlinear time domain simulations, using a 4^{th} order Runge-Kutta ordinary differential equation (ODE) solver as implemented in MATLAB, ODE45, for coupled ODEs. The sampling rate of the model was set to be 96 kHz in these simulations. The time domain results obtained are extremely useful to show how the cochlear partition is affected by incoming sound and how the travelling wave actually moves along the cochlea. Simulations were run using two different nonlinear functions: a hyperbolic tangent function, tanh, and a first order Boltzmann function. The results are compared to understand their effects on the results.

6.3.1 Speeding up the simulations

The numerical implementation of the time domain simulations using the ODE45 solver for the modified state space model has been modified to be much faster than the original implementation by Elliott et al. (2007). Improvements have been made to the numerical implementation of the state space algorithm to produce much faster time domain simulations (Pan et al., 2015a). When compared with the computational efficiency of the simulations in Elliott et al. (2007), these are now more than 140 times faster, and reach steady-state conditions very quickly when specific initial conditions are given by the user.

Specifically, numerical implementation of the state space model was coded so that the formulation included tri-diagonal matrices, whose inverse and product with a vector may be calculated very rapidly, greatly aiding the algorithm in delivering faster simulations. Another factor that optimized simulation time was matrix sparsity. By converting large matrices containing vast numbers of zeros into sparse form, computational efficiency was increased.

Most of the results presented in this paper were obtained from the simulations once the system dynamics had reached steady-state. By forcing the correct initial conditions in the dynamics of the system, steady-state can be reached very quickly compared with starting from zero initial conditions (Vignali et al., 2015). The strategy developed to set the initial conditions of the system are discussed later on in this chapter.

6.3.2 Modelling an SOAE

To initiate the SOAE for the initial tests, the model is stimulated by an impulse, and the response is left to die away until the SOAE reaches steady-state. The results of this are illustrated in Figure 6.2, which shows a colour plot of the instantaneous BM velocity amplitude at each position along the cochlea as a function of time. As the initial impulse dies away over time, which is similar to that seen in the stable cochlea, a limit cycle develops at approximately 15 mm along the cochlea. Even though the BM amplitude is small at the base and most of the backward travelling wave is reflected at the stapes, the pressure is large enough for part of the wave energy to escape into the middle ear, travelling through to the ear canal and generating the SOAE. Given the dispersive nature of the system, the wave speed of the travelling wave varies while moving from the stapes to the location of the characteristic frequency, as explained in Appendix D. This leads to a variation in wave amplitude along the cochlea, which complicates the interpretation of the travelling wave produced by the limit cycle shown in Figure 6.2. A clearer representation of the forward and backward travelling waves is depicted in the steady state condition of the limit cycle shown in Figure 6.3, where a comparison is also made between the two nonlinearities used. Here, the instantaneous waveform of the BM response along the cochlea is shown on a logarithmic scale, in contrast to the linear scale in Figure 6.2, to show more detail. The level of positive velocities is now shown in red and those of negative velocities is now shown in blue, so that the transition at 0 dB is somewhat artificial. The reference value used for converting the velocity into logarithmic scale was $v_{ref} = 1$ nm.

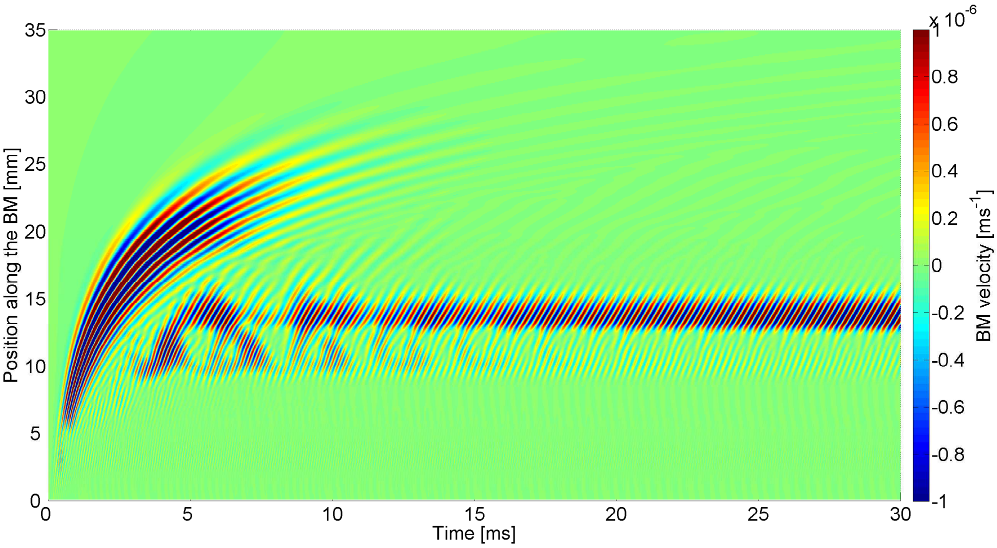

Figure 6.2: Illustration of the time domain simulation, showing the velocity along the BM when stimulated by a low amplitude click that sets into motion all the elements. The instability leads to the generation of the SOAE at 15 mm from the base. It can be seen that the limit cycle reaches steady-state conditions after about 20 ms, while the linear response to the impulse is still dying away.

The forward-travelling nature of the limit cycle that generates the SOAE, as it is amplified at positions close to 15 mm from the base of the cochlea, is seen as diagonal lines with a positive slope. In contrast, the pressure due to the limit cycle at more basal positions is characterised by the backward-travelling wave on its way to the middle ear, which also appear as diagonal lines of constant phase, but with a negative slope. The micromechanical elements at around 15 mm possess negative damping, aiding the generation of the limit cycle, and the constant oscillation of the stapes footplate due to the backward travelling wave, sets into motion the middle ear ossicles and the ear drum, generating an SOAE in the ear canal. The results in Figure 6.3 lead to the possibility of the travelling wave that generates the SOAE to be classified as a standing wave with boundaries at the stapes and at the location of the irregularity, i.e. the limit cycle. This would be in agreement with the theory suggested by Shera (2003), which states that SOAEs result from standing waves generated within the cochlea. Interestingly, simulation results obtained from the state space model also show that if the middle ear stiffness is changed, then the reflection at the stapes is affected and unstable poles at different frequencies are generated.

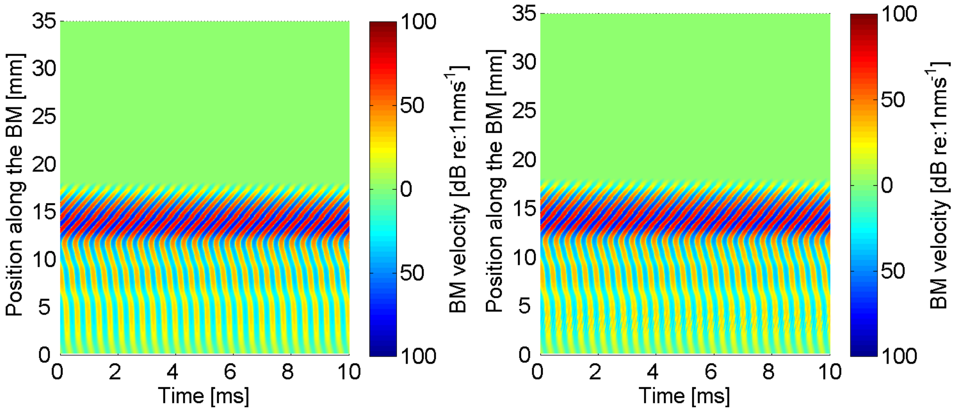

Figure 6.3: Representation of the results from the time domain simulation of the limit cycle when the model is in steady state. The plot on the left shows the case where the nonlinearity is a hyperbolic tangent function while the one on the right shows the case where it is a Boltzmann function.

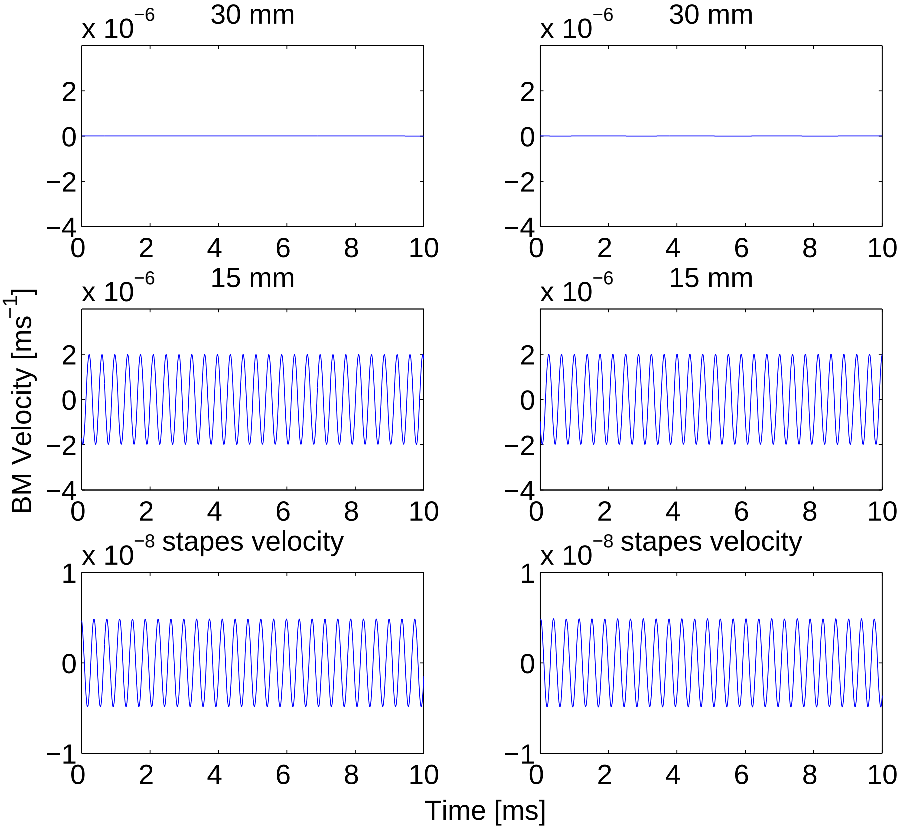

Figure 6.4: Results from the time domain simulation at specific points along the BM when the model is in steady state with no stimulation occurring. The column on the left shows the cases where the nonlinearity is a hyperbolic tangent function while the one on the right shows the cases where it is a Boltzmann function.

Therefore, the location of the limit cycle changes together with SOAE frequency. These results are shown in Appendix E and are discussed more in detail in Chapter 7; however, variation of SOAE frequency due to changes in middle ear stiffness indicate that the middle ear behaves as a boundary that reflects the travelling wave, thus playing an important role in generating the standing wave between itself and the irregularity at the height of the limit cycle.

Figure 6.4 shows individual waveforms of the BM motion at various locations, together with the stapes velocity for the cochlea model with a limit cycle oscillation at 15 mm from the base. Ultimately, it is the stapes motion that generates sound in the ear canal as explained through experiments, for example, by Kemp (2007).

Figures 6.3 and 6.4 do not appear to show any significant difference between the results obtained using the tanh function and those obtained using the Boltzmann function.

6.4 Pre-establishing initial conditions from the frequency domain

Running time domain simulations of complex models can be very time consuming; however, if suitable initial conditions are applied to the model that allow the results to reach steady state very quickly, then the duration of the simulations can be shortened. Initial conditions can be obtained by pre-calculating the waveforms of the state variables for the SOAE and for the bias tone individually, which are then superimposed before being applied to the ODE solver. Although the steady state responses of the SOAE and the bias tones will be slightly different from those obtained individually, they are close enough to allow the time domain simulations to converge rapidly to an overall steady state solution. Initial conditions for the SOAE are obtained from previous nonlinear simulations in which an impulse is left to decay until the SOAE reaches stable conditions, as shown in Fig. 6.3. These conditions can then be used for future simulations involving this SOAE generated by specific feedback gains. The steady-state conditions for the bias tone are obtained by calculating the frequency response of the cochlear model when applying the bias tone as the only input of the system as calculated using Equation 3.17, which is re-written here

$$\Re\{\mathbf{Y}_p(i\omega)\} = \Re\{[\mathbf{D} + \mathbf{C}(i\omega\mathbf{I} - \mathbf{A})^{-1}\mathbf{B}]\mathbf{U}(i\omega)\}. \tag{6.1}$$

An example of pre-calculated initial conditions for both the SOAE and the bias tone is shown in Figure 6.5.

The frequency response that leads to $\Re\{\mathbf{Y}_p(i\omega)\}$ is obtainable either from a linear or from a quasi-linear cochlear model. One of the advantages of the latter is that it allows initial conditions to be obtained for high level input signals that undergo self-suppression (Kanis and de Boer, 1993).

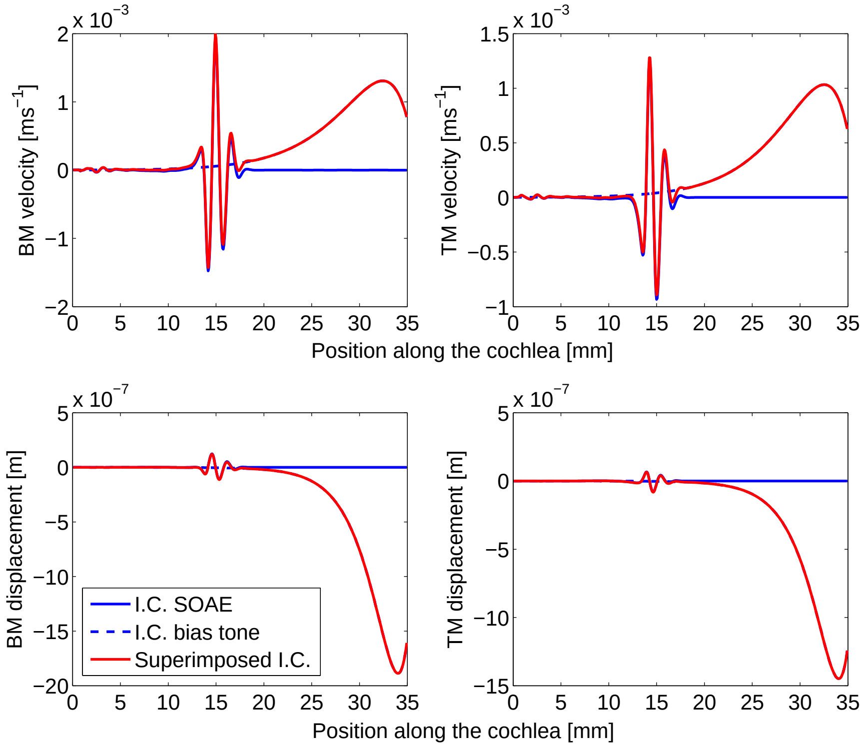

Figure 6.5: Initial conditions applied to the ODE45 solver (red solid line), which are made up of the sum of the initial conditions for the SOAE (blue solid line) and initial conditions for the bias tone (blue dashed line).

6.5 Simulating the effect on an SOAE of a low-frequency bias tone

Low frequency bias tones were used as input driving pressures to the ear canal of the cochlear model in order to understand the interaction between the SOAE and the bias tone. The frequencies of the bias tones were varied between 10 Hz and 100 Hz in steps of 10 Hz. For each frequency, a simulation was performed for varying amplitudes: typically, the lower level limit assigned to the bias tone was -10 dB, where no modulation of the SOAE occurs. The upper limit depended on the level required for total suppression of the emission for specific bias tone frequencies and are shown in Table 6.1. The suppression levels shown in Table 6.1 were obtained by stimulating the model with bias tones for each frequency that would produce a displacement of approximately 2.4 nm on the BM at the location of the limit cycle. This BM displacement would be entirely due to the bias tone, enabling total suppression of the BM displacement due to the limit cycle. For each bias tone frequency, 40 equal steps in level were assumed between the lower and upper limits. Each step involved a simulation 0.6 seconds long with the initial conditions as described in Section 6.4. This method allowed for immediate interaction between the SOAE and bias tone. SOAE spectral features were obtained by high-pass filtering the computed ear canal pressure at 500 Hz to eliminate the low frequency bias component. Spectral information of the SOAE peak amplitude, its upper side bands (USB) and lower side bands (LSB), were retrieved from the last 0.3 second sections of each simulation.

Table 6.1: The bias tone level, at different frequencies, found to give suppression of the SOAE.

Bias tone frequency $[Hz]$	**Suppression level** $[dB]$
10	100
20	88
30	100
40	94
50	91
60	94
70	91
80	91
90	91
100	91

Quasi-static properties were also obtained, as described in Bian and Watts (2008), with only the last period of the bias tone considered for analysis after high-pass filtering the computed ear canal pressure at 500 Hz. After extracting sections of the time series from both the positive and negative half cycles of the bias tone pressure in the ear canal, Fast Fourier Transforms (FFT) of these sections were taken and the amplitudes of the SOAE plotted as a function of the positive and negative peak pressures in the bias tone. These results, addressed in Section 6.6, show how the amplitude of the SOAE depends on bias tone level and frequency.

A comparison of the results in the time domain was made between cochlear models using either a tanh function or the Boltzmann function and the results are shown in Figures 6.6 to 6.9 for low-frequency bias tones of 10 Hz and 100 Hz, respectively. Similar results are shown for all other bias tones used from 20 Hz to 90 Hz, as shown in Appendix F. Again, the velocity in the contour maps shown are plotted with a dB scale with $v_{ref} = 1$ nm, for both positive and negative phases. It should be noted that in some of the contour plots, the time frame used is such that it causes the SOAE waveform to be aliased down to a lower apparent frequency due to under-sampling, although the features of the figures are still accurate. All the results have been plotted so that the bias tones of different frequencies go through two cycles. Also, the velocity in the waveform plots have been scaled differently in each case for clarity; however, each row of plots representing the same locations along the length of the cochlea are scaled equally.

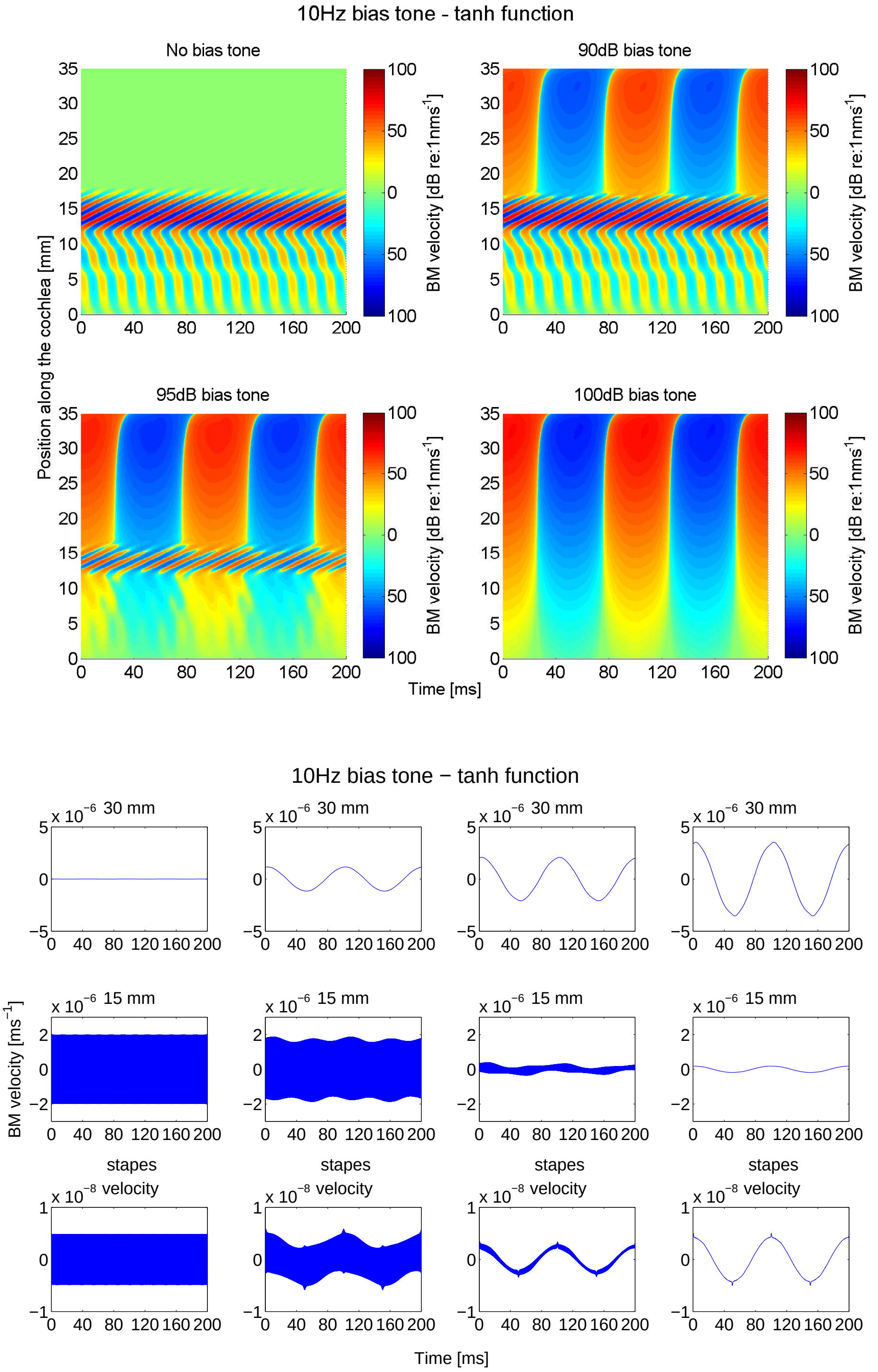

Figure 6.6: The results from the time domain simulations in terms of the level of the BM velocity when the model containing tanh nonlinearities is stimulated by a 10 Hz biasing tone of various levels. The contour plots show the response at different positions and times: top left panel, no bias tone present, top right panel, 90 dB, bottom left panel, 95 dB and bottom right panel, 100 dB. The waveform plots show the BM velocity at different times and specific locations: far left panel, no bias tone present, centre-left panel, 90 dB, centre-right panel, 95 dB and far right panel, 100 dB. The plots show how the SOAE is affected by the bias tone at different levels: at first, the emission is unaffected, but higher levels of biasing tone modulate its characteristics until it is suppressed at even higher levels.

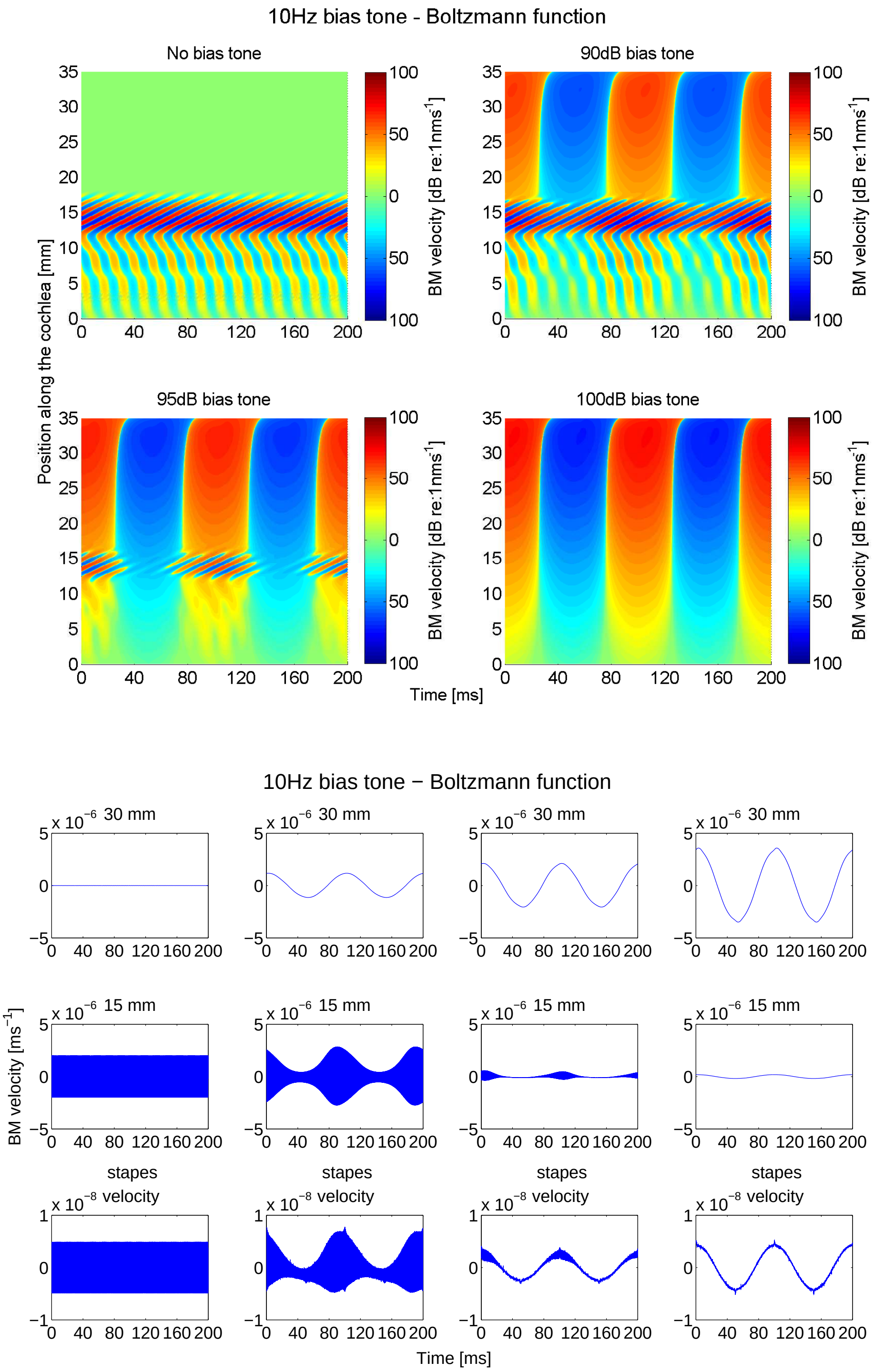

Figure 6.7: The results from the time domain simulations in terms of the level of the BM velocity when the model containing Boltzmann nonlinearities is stimulated by a 10 Hz biasing tone of various levels. The contour plots show the response at different positions and times: top left panel, no bias tone present, top right panel, 90 dB, bottom left panel, 95 dB and bottom right panel, 100 dB. The waveform plots show the BM velocity at different times and specific locations: far left panel, no bias tone present, centre-left panel, 90 dB, centre-right panel, 95 dB and far right panel, 100 dB. The plots show how the SOAE is affected by the bias tone at different levels: at first, the emission is unaffected, but higher levels of biasing tone modulate its characteristics until it is suppressed at even higher levels.

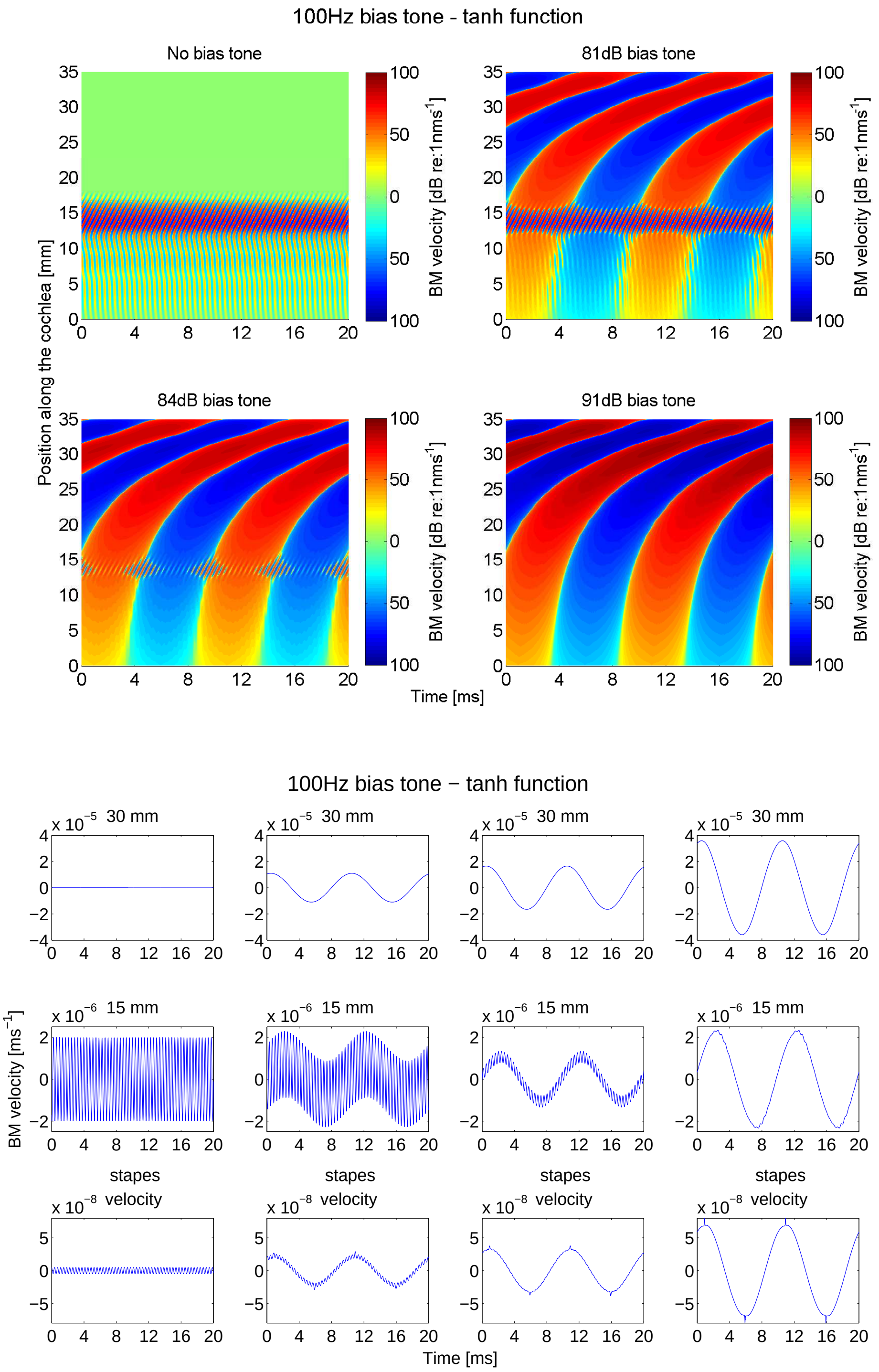

Figure 6.8: The results from the time domain simulations in terms of the level of the BM velocity when the model containing tanh nonlinearities is stimulated by a 100 Hz biasing tone of various levels. The contour plots show the response at different positions and times: top left panel, no bias tone present, top right panel, 81 dB, bottom left panel, 84 dB and bottom right panel, 91 dB. The waveform plots show the BM velocity at different times and specific locations: far left panel, no bias tone present, centre-left panel, 81 dB, centre-right panel, 84 dB and far right panel, 91 dB. The plots show how the SOAE is affected by the bias tone at different levels: at first, the emission is unaffected, but higher levels of biasing tone modulate its characteristics until it is suppressed at even higher levels.

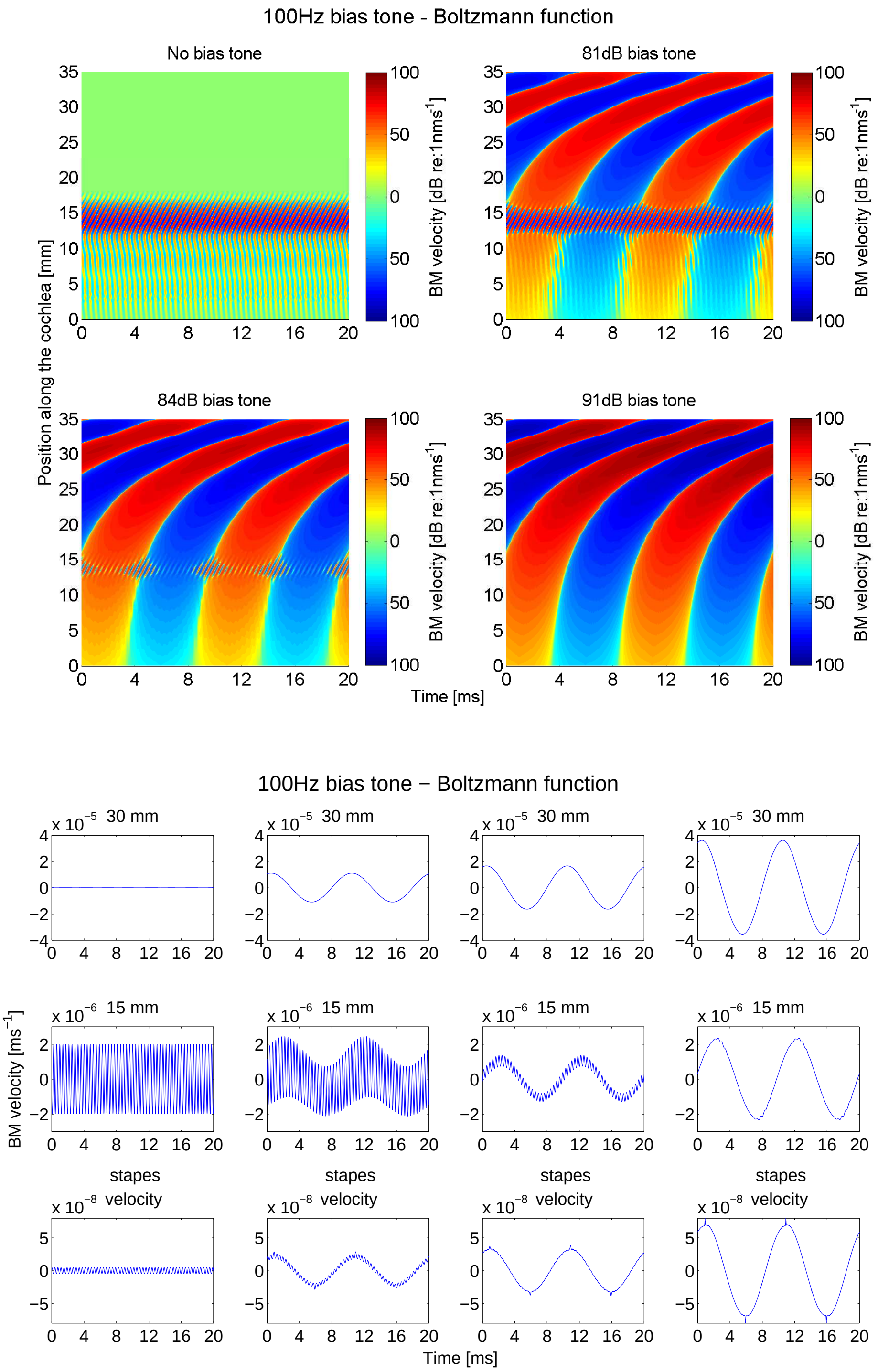

Figure 6.9: The results from the time domain simulations in terms of the level of the BM velocity when the model containing Boltzmann nonlinearities is stimulated by a 100 Hz biasing tone of various levels. The contour plots show the response at different positions and times: top left panel, no bias tone present, top right panel, 81 dB, bottom left panel, 84 dB and bottom right panel, 91 dB. The waveform plots show the BM velocity at different times and specific locations: far left panel, no bias tone present, centre-left panel, 81 dB, centre-right panel, 84 dB and far right panel, 91 dB. The plots show how the SOAE is affected by the bias tone at different levels: at first, the emission is unaffected, but higher levels of biasing tone modulate its characteristics until it is suppressed at even higher levels.

When the cochlea is stimulated by high-level low-frequency bias tones, interaction occurs between these tones and the SOAE, as can be seen in Figures 6.6 through 6.9. Regardless of the frequency, increasing levels of bias tone initially modulate the level of the emission but then at higher levels it is totally suppressed for both types of nonlinearities. However, the results show that one can differentiate between "very-low-frequency" bias tones, up to approximately 50 Hz, and "low-frequency" bias tones, between 60 and 100 Hz for the cases shown. The model containing the tanh function appears to modulate the emission in a similar way during positive and negative cycles of the bias tone for all the bias tone frequencies, as shown most clearly in the bottom left panel of the contour plots in Figures 6.6 and 6.8. Whereas, in the case of the Boltzmann function, for "very-low-frequency" bias tones, the emission is modulated differently by positive cycles and negative cycles of the bias tone, as shown in the bottom left panel of the contour plots in Figure 6.7, and as shown in Appendix F up to a bias tone of about 50 Hz. However, when the bias tones have frequencies of approximately 60 Hz and above, the model containing Boltzmann nonlinearities behaves similarly to the model containing tanh nonlinearities. In these cases, the emission is modulated in a similar way during positive and negative cycles of the bias tone, as shown in Figure 6.9, and as shown in Appendix F for bias tone frequencies of and above 60 Hz.

For very low frequency bias tones of 10 and 20 Hz, as shown in Figures 6.6 and 6.7, the BM moves in phase along almost the entirety of its length. For higher frequency bias tones, equal to 30 Hz and above, the travelling wave caused by the bias tone appears to curve, and therefore slows down in speed, as soon as it reaches the location of the characteristic frequency, as shown, for example, in Figures 6.8 and 6.9.

6.5.1 Harmonic generation

With no bias tone, the spectrum of the SOAE, as shown in the top two panels in Figure 6.10, nearly resembles that of a pure tone. Figure 6.10 also demonstrates that increasing the level of a 10 Hz bias tone leads to the formation of lower side bands, LSBs, and upper side bands, USBs, in the spectrum of the emission, where there is now a significant difference between the results given by the model using the hyperbolic tangent function and that using the Boltzmann function. The former, shown in the left column of Figure 6.10, shows a diminution of the fundamental peak of the emission as bias tone level is increased, with little formation of side bands. The most prominent side bands that do occur are at $f_{SOAE} \pm 2f_{bias}$, and this is due to the symmetrical nature of the tanh function that generates distortion products at $f_{SOAE} \pm 2nf_{bias}$, where $n = 1, 2$. In the case of the asymmetric Boltzmann function, shown in the right-side column of Figure 6.10, the side bands are larger and appear at $f_{SOAE} \pm nf_{bias}$, where $n = 1, 2$. Emission energy is therefore spread across a greater frequency range.

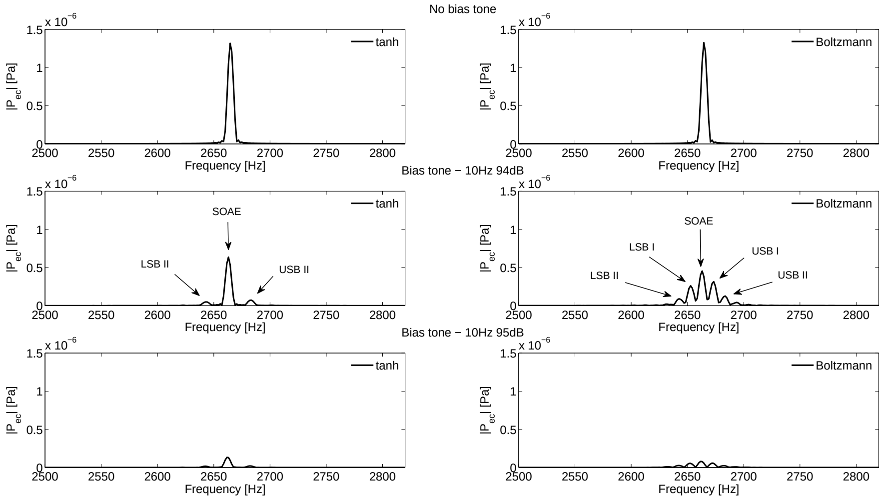

Figure 6.10: The spectrum of the simulated SOAE for different levels of 10 Hz external bias tone when using the hyperbolic tangent function (left column) and the Boltzmann function (right column). The top panels show the spectra of the SOAE when no bias tone is presented to the ear canal. The middle row shows SOAE variations due to a 10 Hz, 92 dB bias tone. The formation of LSBs and USBs at $f_{SOAE} \pm n f_{bias}$, where $n = 1, 2$, can be seen very clearly in the case of the model using the Boltzmann function, while this effect is less prominent for the model using the tanh function. In the latter case, the level of the fundamental frequency of the SOAE is still quite high and contains most of the emissions energy, and part of the remaining energy is distributed to $f_{SOAE} \pm 2f_{bias}$. The bottom row shows substantial suppression of the SOAE, due to high levels of external bias tones.

For the sake of brevity only three examples are shown, in Figures 6.11, 6.12 and 6.13, that are sufficient to describe how different bias tone levels and frequencies generate LSBs and USBs. In every case, the model containing the Boltzmann function generates side-bands at $f_{SOAE} \pm n f_{bias}$, where $n = 1, 2$, while the model containing the tanh function only generates side-bands at $f_{SOAE} \pm 2f_{bias}$.

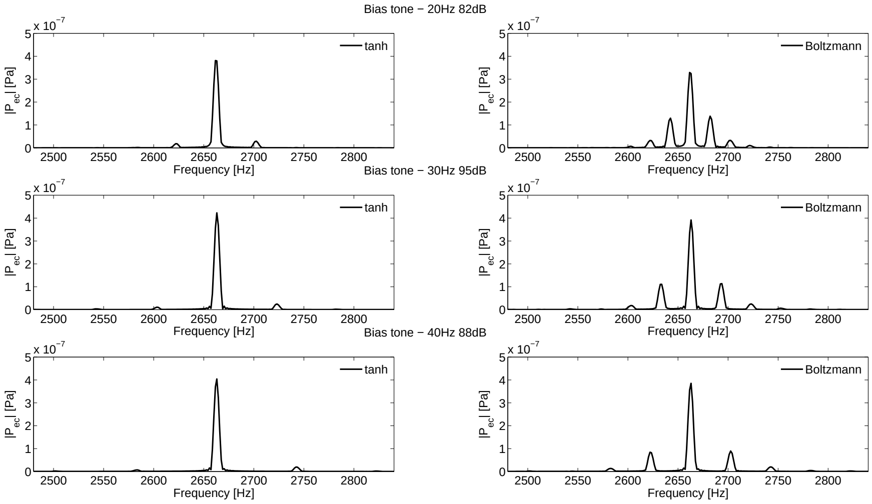

Figure 6.11: Spectrum of the SOAE for different levels and frequencies of the external bias tone when using the hyperbolic tangent function (left column) and the Boltzmann function (right column). Each row of panels show SOAE variations due to a bias tone of a specific frequency and level. The formation of LSBs and USBs at $f_{SOAE} \pm nf_{bias}$, where $n = 1, 2$, can be seen very clearly in the case of the model using the Boltzmann function, while this effect is less prominent for the model using the tanh function. In the latter case, the level of the fundamental frequency of the SOAE is still quite high and contains most of the emissions energy, and part of the remaining energy is distributed to $f_{SOAE} \pm 2f_{bias}$.

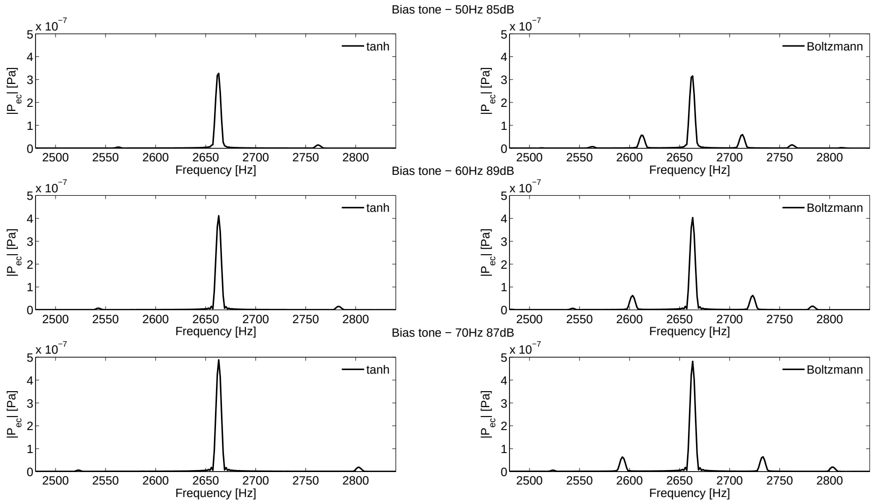

Figure 6.12: Spectrum of the SOAE for different levels and frequencies of the external bias tone when using the hyperbolic tangent function (left column) and the Boltzmann function (right column). Each row of panels show SOAE variations due to a bias tone of a specific frequency and level. The formation of LSBs and USBs at $f_{SOAE} \pm n f_{bias}$, where $n = 1, 2$, can be seen very clearly in the case of the model using the Boltzmann function, while this effect is less prominent for the model using the tanh function. In the latter case, the level of the fundamental frequency of the SOAE is still quite high and contains most of the emissions energy, and part of the remaining energy is distributed to $f_{SOAE} \pm 2f_{bias}$.

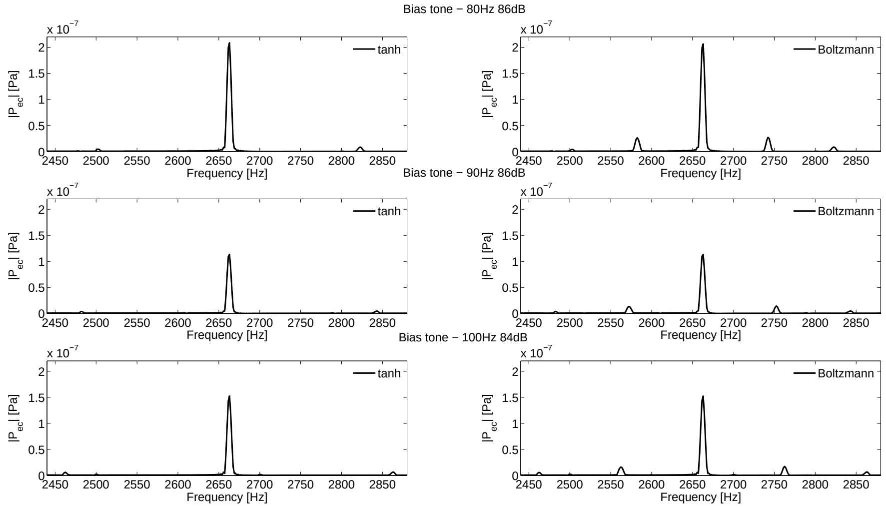

Figure 6.13: Spectrum of the SOAE for different levels and frequencies of the external bias tone when using the hyperbolic tangent function (left column) and the Boltzmann function (right column). Each row of panels show SOAE variations due to a bias tone of a specific frequency and level. The formation of LSBs and USBs at $f_{SOAE} \pm nf_{bias}$, where $n = 1, 2$, can be seen very clearly in the case of the model using the Boltzmann function, while this effect is less prominent for the model using the tanh function. In the latter case, the level of the fundamental frequency of the SOAE is still quite high and contains most of the emissions energy, and part of the remaining energy is distributed to $f_{SOAE} \pm 2f_{bias}$.

Figure 6.14 shows how the SOAE amplitude and the amplitude of some of the side-bands vary with bias tone level. In both cases there are similar variations of the fundamental amplitude of the SOAE for different bias tone frequencies. Bian and Watts (2008) show experimental data that is similar to these cases, but where the rate of decline of the SOAE also depends on f_{bias}. In Figure 6.14, the rate of decline of the SOAE is almost constant for every case and appears to be independent of f_{bias}. Aside from this feature, the gradual suppression of the fundamental component of the SOAE resembles the measured results of Bian and Watts (2008), shown in Figure 2.13, for both the tanh and Boltzmann nonlinearities.

The most striking aspect of the plots in Figure 6.14, however, is the difference in LSB and USB generation between the two forms of nonlinearity. These show USB I and LSB I at $f_{SOAE} \pm f_{bias}$ and USB II and LSB II at $f_{SOAE} \pm 2f_{bias}$. In the case of the tanh function, the nonlinearity is symmetrical, and the saturation of a high level bias tone superimposed with the SOAE, leads to the generation of an output having equal positive and negative cycles. The left hand column of panels in Figure 6.14 shows that intermodulation between the two components generates prominent harmonics around the emission at $f_{SOAE} \pm 2f_{bias}$. The right hand column of panels show that the asymmetry of the Boltzmann function, on the other hand, generates distortion products at $f_{SOAE} \pm f_{bias}$ and $f_{SOAE} \pm 2f_{bias}$.

The simulation results with the Boltzmann function give a much better prediction of the measured results of Bian and Watts (2008) than those with the tanh function, indicating that even the rather subtle degree of asymmetry seen in Figure 5.5 can have a large influence on the generation of these side-bands.

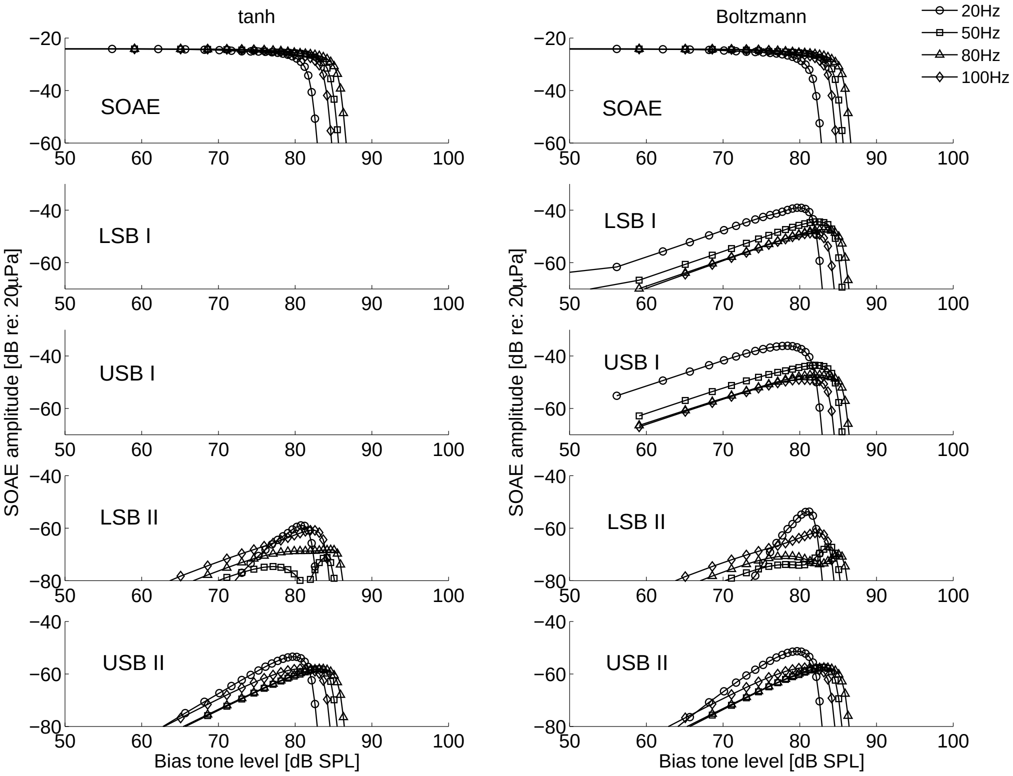

Figure 6.14: Variation of the fundamental amplitude, LSBs and USBs of the SOAE with bias tones of varying frequency and level. The column on the left shows the results obtained when the nonlinearity used is the hyperbolic tangent function while the plots in the column on the right show the ones obtained when using the Boltzmann function. The fundamental amplitude appears to vary in a similar way in both cases; the variation of the amplitudes of both LSBs and UBs is significantly different from one case to another.

6.6 Quasi-static analysis of the biased SOAE

Figures 6.7 and 6.9 show that for the model using the Boltzmann function, the level of the SOAE is modulated differently for the positive or negative parts of the cycle of the external bias tone. Analysing differences between change in SOAE level between these parts of the cycle, as with the quasi-static analysis of Bian and Watts (2008) described in Section 2.3.3, helps to understand the effect of the bias tone on the SOAE and in particular, the effect of different nonlinear functions embedded in the model. Figure 6.15 shows the average amplitude of the SOAE in the positive and negative half cycles of the bias tone, calculated as per the method described in the beginning of Section 6.5, plotted against the peak BM displacement due to the bias tone at the location of the SOAE. An advantage of the model is that it allows the peak BM motion due to the bias tone to be evaluated in the different cases and thus provides a more direct representation of the quasi-static results than is possible with experimental results. In Figure 2.12, taken from Bian and Watts (2008), for example, only the average SOAE amplitude is plotted as a function of the bias tone pressure. The curves in Figure 6.15 are symmetrical for all biasing frequencies when the tanh function is used as expected, but with the asymmetrical Boltzmann function, the SOAE is affected differently for positive and negative cycles of bias tone frequencies below approximately 40 Hz. At higher bias tone frequencies a more symmetrical bell shaped curve is observed even with the Boltzmann nonlinearity. This suggests that the SOAE amplitudes only approach the quasi-static value when the period of the bias tone is large enough to allow the SOAE to settle down to a steady-state. Although the SOAE appears to have reached a steady state about 20 ms after the transient excitation shown in Figure 6.2, it in fact takes much longer to achieve its final amplitude, and this time depends on the form of the transient excitation and its amplitude. To a first approximation, however, this 20 ms settling time gives a good prediction of the period of the highest bias tone that would behave quasi-statically, which corresponds to a frequency of 50 Hz.

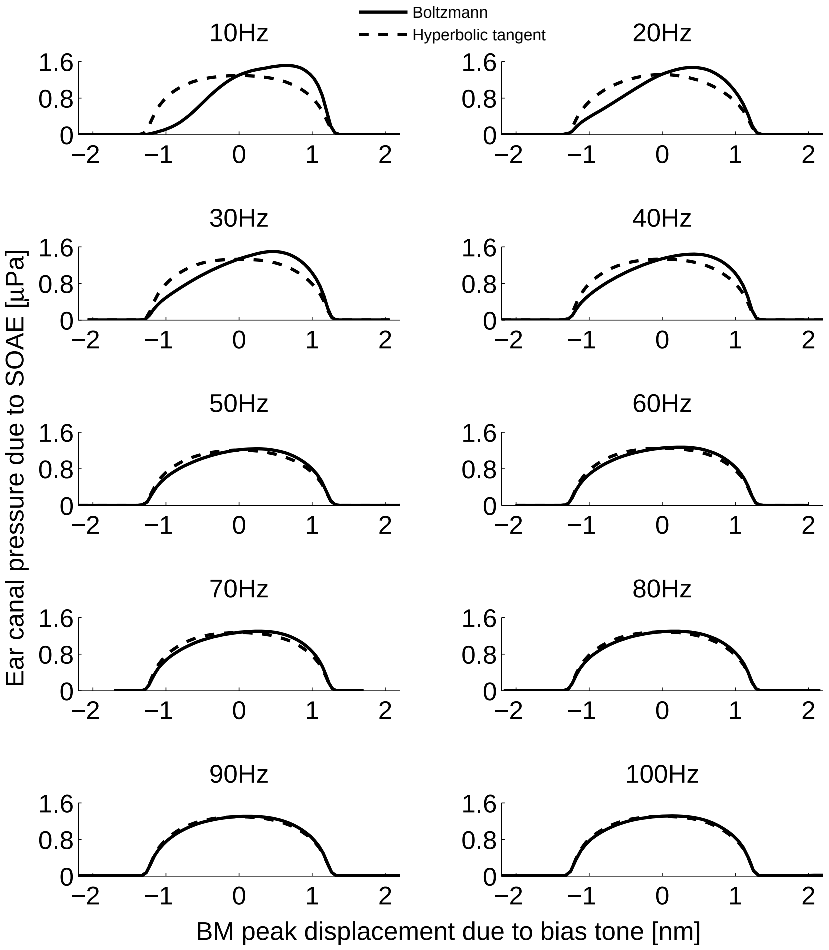

Figure 6.15: The average amplitude of the SOAE in the positive and negative half cycles of the bias tone is plotted against the peak BM displacement due to the bias tone in the simulations of the quasi-static method. Simulations were performed for different bias tone frequencies of varying level for models containing either the tanh function or the Boltzmann function. For very low bias tone frequencies, in particular 10 Hz, 20 Hz, 30 Hz and 40 Hz, the Boltzmann function affects the cochlear model by inducing an asymmetrical shape in the curves, but for the higher bias tone frequencies, the bell shape curves are symmetrical; however, when the tanh function is employed in the model, symmetry of the bell shape curves occurs at all bias tone frequencies.

Interestingly, when the model employing the Boltzmann function is stimulated by very low bias tone frequencies (below 40 Hz), the amplitude of the emission is slightly increased during the positive cycle of the bias tone, as may be expected from the increase in the gain of the Boltzmann function for slightly positive inputs seen in Figure 5.5.

The results shown in Figure 6.15 are similar to those obtained by Bian and Watts (2008) shown in Figure 2.12. However, Bian and Watts plot the bell-shaped curves as a function of bias tone pressure rather than BM displacement, using bias tone frequencies of 25, 32, 50, 75 and 100 Hz. As described in Section 2.3.3, Bian and Watts (2008) fit the bell-shaped curves to the scattered data from the derivative of what they assume to be the nonlinearity that describes the CA. In particular, they model the nonlinear hair cell transfer function as a second-order Boltzmann function, whose parameters change according to the bell-shaped curve that will be obtained from its derivative, as shown in Figure 2.12 (Bian and Watts, 2008; Bian et al., 2002). The derived bell-shaped curves in their analysis are more symmetrical for higher frequency bias tones than for those at lower frequencies, as found in the simulations using the state space model.

A reverse strategy was undertaken in this thesis compared to that used by Bian and Watts (2008); the nonlinear function describing the CA was modelled from the integral of the bell-shaped curves obtained from the simulations. This was possible since the simulations allowed obtaining directly the bell-shaped curves, unlike in the experiments performed by Bian and Watts, where the curves had to be inferred from the scattered data obtained from the measurements.

Therefore, by calculating the integral of the bell-shaped curves in Figure 6.15, it is possible to derive the nonlinear functions that are assumed for the CA by Bian and Watts (2008), as shown in the right column in Figure 2.12. These nonlinear functions should thus be similar to the nonlinear curves actually used for the CA simulations, as shown in the top panel of Figure 5.5, if the assumptions of Bian and Watts (2008) are correct. The results obtained by taking the integral of the curves in Figure 6.15 are shown in Figure 6.16, where the left panel shows the derived function for the simulations using the tanh nonlinearity, and the right panel shows the derived function for the simulations using the Boltzmann function. These integrals have been normalized to have a slope of unity at the origin so that they can be directly compared with the nonlinearites shown in Figure 5.5.

The first thing to note from these results is that the nonlinear function derived from the results of the model with the tanh function are symmetric, as expected, but also almost independent of bias tone frequency. In contrast, the nonlinear function derived from the quasi-static results from the model with the Boltzmann function does depend on bias tone frequency and is only asymmetric for bias tone frequencies below about 40 Hz, for which the period is large enough for the SOAE to settle towards a steady-state condition.

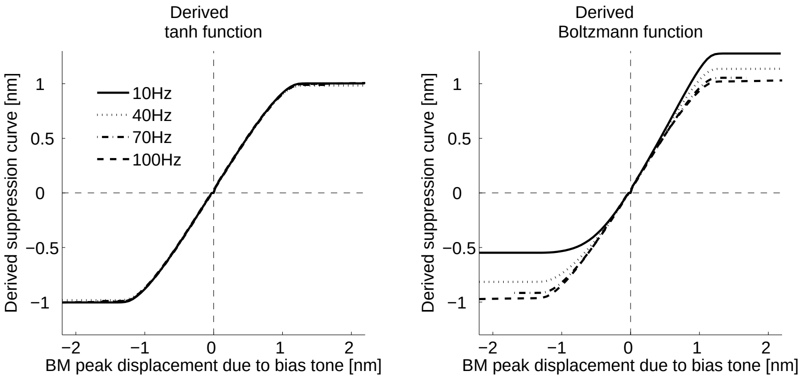

Figure 6.16: The derived nonlinear functions obtained from the bell shaped curves shown in Fig. 13 for the cochlear models that used either the tanh nonlinearity (left) or the Boltzmann nonlinearity (Right).

On closer inspection, however, the scale of the derived nonlinear functions are significantly different from those used to generate them, in Figure 5.5, and the asymmetry in the derived Boltzmann function is much greater than the Boltzmann function used in the micromechanical model.

These results thus indicate that, although the analysis of the quasi-static measurements suggested by Bian and Watts (2008) does give an indication of whether the nonlinear function generating the SOAE is symmetrical or not, provided the bias tone frequency is sufficiently low, it does not accurately reproduce the actual form of the nonlinearity. This may be partly due to the procedure whereby the quasi-static responses are calculated, with the average SOAE amplitudes calculated for the whole of the positive and negative half-cycles of the bias tone. It may also reflect an over-simplified view of the generation mechanism, since in practice the OHC nonlinearity is a function of stereocilia shear displacement, rather than the BM displacement, and these two displacements are not linearly proportional to each other because of the nonlinear action of the CA. It is also clear that instead of the SOAE amplitude gradually decreasing for higher levels of bias tone, it becomes completely suppressed, which is not accounted for in the quasi-static view.

6.7 Temporal features of the biased SOAE

The modulation properties of the SOAE when exposed to low frequency bias tones were also studied by band pass filtering the ear canal pressure, p_{ec}, between 1.5 kHz and 4 kHz and then applying the Hilbert transform. The output was then low pass filtered at 200 Hz to obtain the slowly varying temporal features of the biased SOAE. This allowed amplitude modulation (AM) and frequency modulation (FM) patterns to be obtained that gave a description of the instantaneous variation of SOAE amplitude and frequency during a cycle of the external bias tone.

This method of extracting the envelope differed from that used by Bian and Watts (2008), where temporal features were extracted from the inverse Fourier transform of the rectangular windowed spectrum of specific SOAEs with their side-bands. When the method of envelope extraction used by Bian and Watts (2008) was applied to the signals obtained from the simulations, curves similar to their results for the measured data were found, but these were different from those obtained using the Hilbert transform. It is possible that there are difficulties applying the Hilbert transform to noisy experimental data, however, for the clean simulated data shown here, the Hilbert transform method appears to be the best way of calculating the envelope.

Figure 6.17 shows the envelope function of the SOAE when exposed to bias tones of different frequencies and levels. The symmetrical tanh function generates SOAE envelopes that oscillate at twice the frequency of the bias tone, and the amplitude never rises above the unperturbed level of the SOAE. The minimum amplitude in the temporal pattern occurs twice during the period of the bias tone, first caused by the lowest pressure of the bias tone and secondly caused by its highest pressure. The Boltzmann function behaves differently because of its asymmetry, so that the saturation of the cochlear structures is different depending on the direction in which they are biased by the external tone. Amplitude variations then occur at the same frequency of the bias tone, and an increase in SOAE amplitude, over the steady-state level, can be seen at some parts of the cycle.

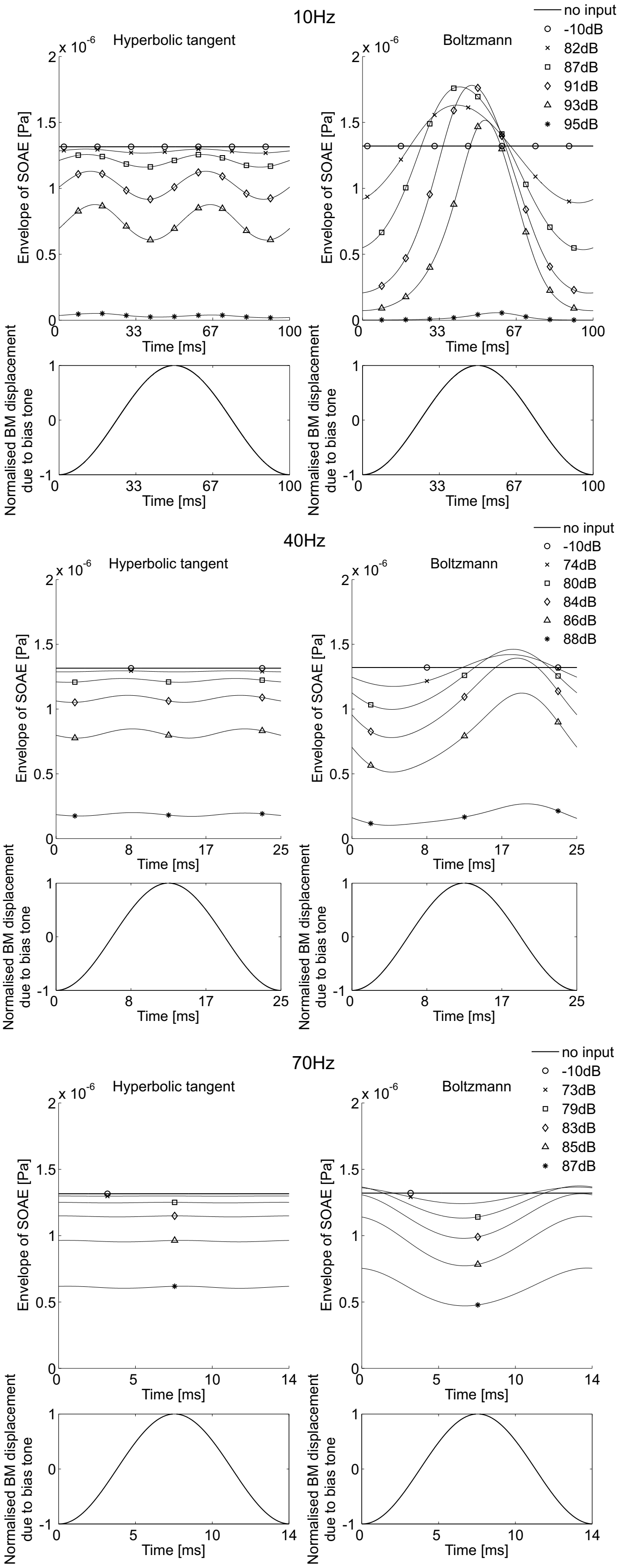

Figure 6.17: Temporal patterns of p_{ec} obtained from taking the AM patterns from the Hilbert transform of the signal. Temporal patterns are shown from simulations using different bias tone frequencies, from top to bottom, 10 Hz, 40 Hz and 70 Hz. Each plot shows multiple curves that indicate different levels assumed by the bias tones. A comparison is made between the model using the Boltzmann function and the model using the tanh function.

It is interesting to note that even for very low bias tone frequencies, the position of the peak SOAE amplitude changes significantly with level. This is shown in Figure 6.17 for the case of the model using the Boltzmann function stimulated by a 10 Hz bias tone. Plotting instantaneous SOAE amplitude against instantaneous BM displacement thus results in a series of open loops, as shown in Figure 6.18, rather than a single-valued function, which do not accurately describe the underlying nonlinearity of the CA. However, once again, these curves highlight the symmetrical difference between the two nonlinearities. The model including the tanh function modulates the SOAE in the same way during positive or negative half-cycles of the external bias tone, whereas the model including the Boltzmann function modulates the SOAE differently.

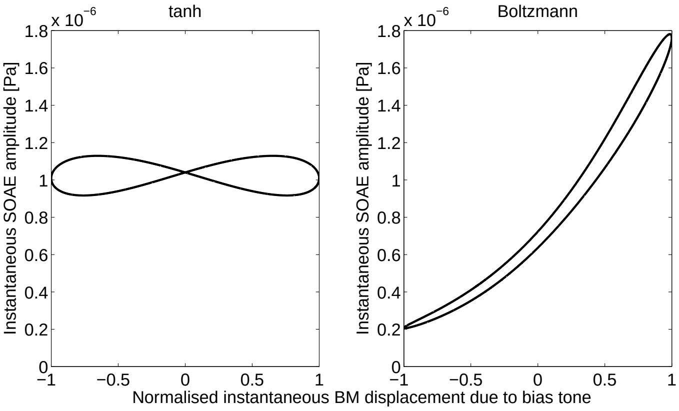

Figure 6.18: Open loops obtained by plotting the instantaneous SOAE amplitude of the pressure in the ear canal against the normalised instantaneous pressure in the ear canal due to the bias tone. The curves show an example of when the model is stimulated by an external bias tone of 10 Hz and 91 dB when using different nonlinear functions.

With regards to the frequency modulation of the SOAE by the bias tones, the results of which are shown in Figure 6.19, similar considerations can be made about the temporal features for the two forms of nonlinearity. In this case, the symmetrical tanh function generates a variation in frequency of the SOAE that oscillates at twice the frequency of the bias tone, as in the case for AM. The variation in frequency modulation does not oscillate symmetrically around f_{SOAE}, which is approximately 2665 Hz. In fact, when the 10 Hz bias tone is introduced into the system, the f_{SOAE} decreases and oscillates at values that range between about 2660 Hz and 2665 Hz. Figure 6.19 shows that f_{SOAE} becomes greater than its unperturbed value of about 2665 Hz for a short period of time, but only for frequencies of bias tones above 40 Hz. The Boltzmann function behaves differently because of its asymmetry, and already at 10 Hz the SOAE frequency oscillates between higher and lower frequencies of the unperturbed value of 2665 Hz. FM variations occur at the same frequency of the bias tone, and an increase in SOAE frequency over the steady-state level can be seen at some parts of the cycle.

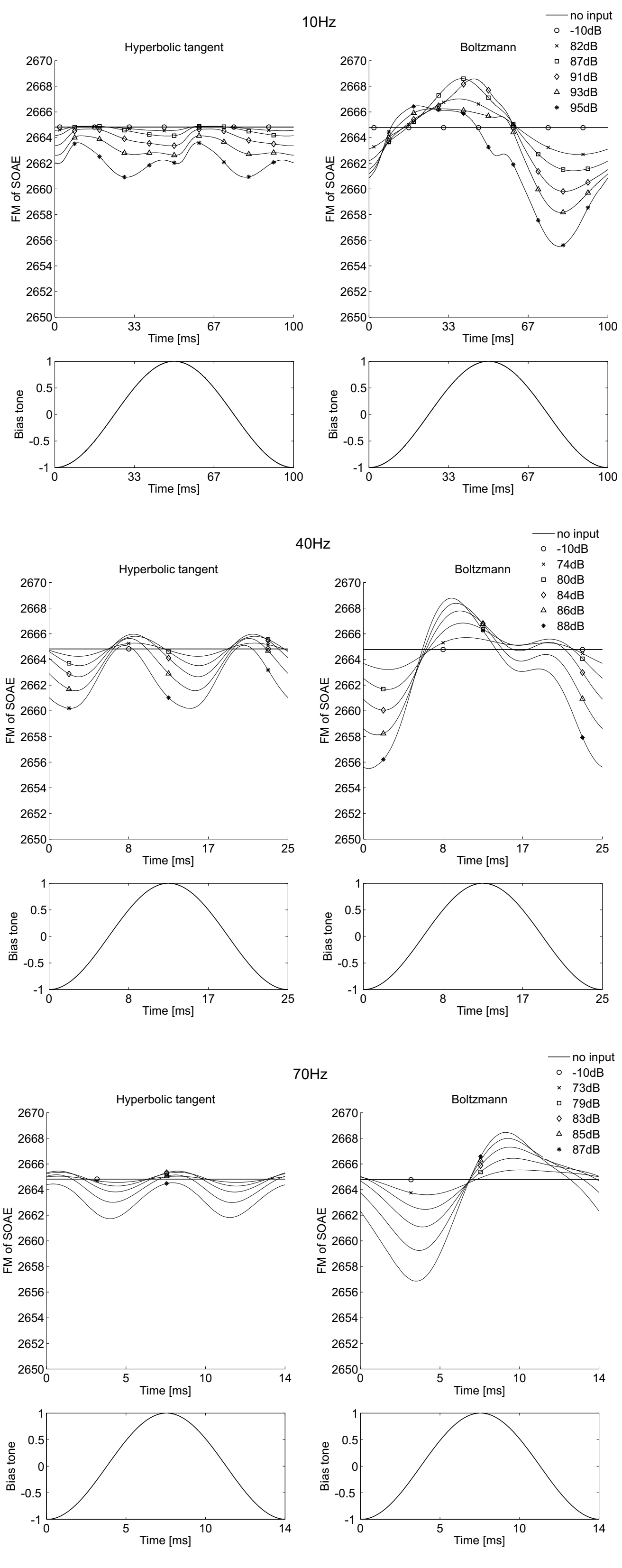

Figure 6.19: Temporal patterns of p_{ec} obtained from taking the FM patterns from the Hilbert transform of the signal. Temporal patterns are shown from simulations using different bias tone frequencies, from top to bottom, 10 Hz, 40 Hz and 70 Hz. Each plot shows multiple curves that indicate different levels assumed by the bias tones. A comparison is made between the model using the Boltzmann function and the model using the tanh function.

6.8 Summary

In this chapter, time domain simulations of the nonlinear state space model of the cochlea have been used to investigate the nature of an isolated SOAE and its interaction with a low frequency bias tone. The initial simulations clearly illustrate the forward and backward going waves that generate the SOAE. The simulations also suggest that it takes about 20 ms for the SOAE to become established after a transient excitation, which ties in reasonably well with the frequency below which quasi-static features of the low frequency modulation are independent of bias tone frequency, which is also about 50 Hz.

Although the form of the assumed nonlinearity in the model did not significantly affect the way in which it was suppressed by bias tones of increasing level, the side-bands of the SOAE were very different in the two cases. The rather mild asymmetry assumed in the Boltzmann function had a large effect on some of these side-bands and gave predicted results that were similar to those that have been measured.

The quasi-static analysis of Bian and Watts (2008) has also been applied to the simulated SOAE in order to compare the nonlinear function deduced using this method with that actually used in the model of the CA. Even if very low frequency bias tones are used, it is found that the assumptions of the Bian and Watts analysis are not valid and rather different nonlinear functions are predicted from the quasi-static analysis than those used in the CA model.

Finally, the amplitude modulation and frequency modulation of the simulated SOAE due to a low frequency bias tone are analysed using the Hilbert transform. This analysis is different to perform on experimental data, presumably due to noise problems, but generates some interesting predictions, particularly for frequency modulation, that it may be possible to validate experimentally.

Chapter 7

Modelling other nonlinear effects in the cochlea

7.1 Introduction

In this chapter, various other nonlinear effects in the cochlea are discussed. A section replicating results from SOAEs interacting with an external swept tone is included for comparison with the measured results in the literature. Other simulations were performed to understand the interaction between an SOAE and a very high level, low frequency tone. A small section is also dedicated to the simulation of microstructure and its relationship with SOAEs and CEOAEs. Also, tests were performed to understand what would happen to the modelled SOAE when the middle ear stiffness was changed, in order to replicate posture changes experiments. Further simulations were also performed to understand whether the model could predict the generation of low frequency distortion products that can explain the phenomenon known as virtual bass.

7.2 Simulating the interaction between an SOAE and a swept tone

In this section, results are shown from the model when it is stimulated by a swept tone that passes through f_{SOAE}, which is approximately 2660 Hz for the simulations discussed above. Experiments using swept tones have been performed by a number of researchers, for example Bergevin and Salerno (2015); Bergevin et al. (2015); Hansen et al. (2014); Long (1998). Some of the results from these authors were shown in Figures 2.17 and 2.21. By performing numerical simulations that replicate these measurements using the model, it may be possible to understand what is happening from a mechanical point of view on the cochlear structures.

A series of simulations were performed using swept tones of different levels and sweeping frequencies, while other simulations used individual tones as the input to the model, having a frequency in proximity to f_{SOAE}. The model used was the one containing the Boltzmann function in its mechanics, since from the results in the previous chapter this appeared most realistic. It should be noted that each of these simulations took about 12 hours on a desktop computer, with a 3.1 GHz Core i5 processor, 4GB RAM, and would not have been practical without the improvements in simulation time described in Appendix B.

Figure 7.1 shows three examples of the spectrograms of the pressure at the ear canal obtained when slowly sweeping a tone between 2610 Hz and 2710 Hz. It can be seen in each case that as the frequency of the swept tone passes through that of the emission, f_{SOAE}, the stimulus interacts with the SOAE. These spectrograms are similar to those obtained experimentally in Bergevin et al. (2015), and they show that an interaction is taking place that involves the nonlinear features of cochlear mechanics. However, they do not provide clear evidence of whether the SOAE is entrained by the stimulus or if the emission is simply suppressed by the incoming swept tone.

A feature that stands out from these results is the generation of distortion products at frequencies equal to $2f_{SOAE} - f_{swepttone}$ and $2f_{swepttone} - f_{SOAE}$. These are a by-product of the nonlinearity introduced in the CA of the model and, to the knowledge of the author, have not been measured or detected in real experiments.

To understand more fully when entrainment and/or suppression occurs, the ear canal pressure was bandpass filtered with centre-frequency at the emission frequency, i.e. 2660 Hz, and a bandwidth of 15 Hz. The waveform obtained was full-wave rectified and sent through a further bandpass filter that could extrapolate the low-frequency beating patterns given by the difference over time between the frequencies of the swept tone and the emission, as used by Hansen et al. (2014). The latter filter had a low cut-off frequency of 0.4 Hz and a high-cut-off frequency at 20 Hz. The results from the analysis are shown in Figure 7.2 and it can be seen that, starting from $t = 0$ s, beating occurs between the stimulus and the SOAE as the frequency of the former approaches that of the latter. For a certain frequency difference, which depends on the level of the stimulus, the waveform smooths out. This creates a region of entrainment and/or suppression, where the frequency of the emission appears to either lock on to that of the stimulus, or the SOAE is abolished by the incoming stimulus. Note that for higher level stimuli, the smooth regions occur over larger bands of time. Simulated results of the patterns shown in Figure 7.2 are in reasonable agreement with those obtained from experimental analysis of real data, as shown by Hansen et al. (2014) and Long and Tubis (1988a) in Figure 2.17.

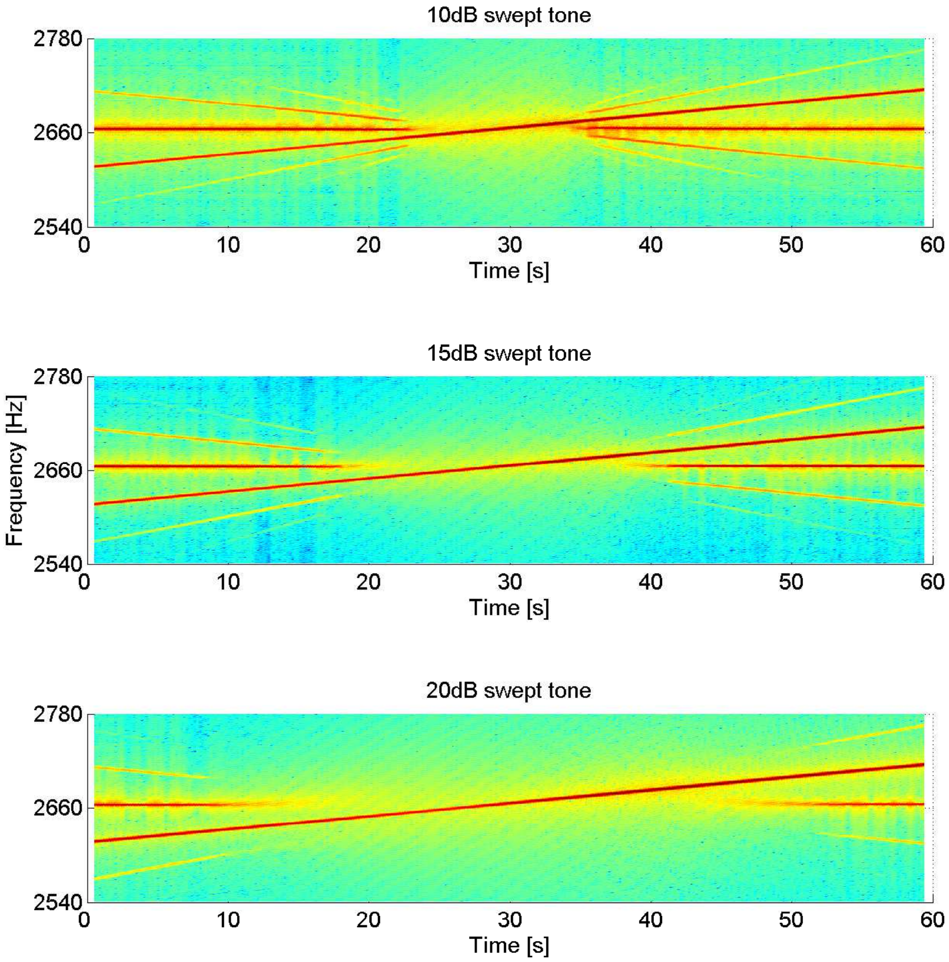

Figure 7.1: Spectrograms of the predicted pressure in the ear canal during the simulated interaction between a SOAE and a swept tone of different levels. The left column shows spectrograms of the pressure at the ear canl where it can clearly be seen that as the swept tone passes by the SOAE frequency, the emission is abolished. There appears to be a slight deviation from f_{SOAE} of the SOAE just before and after it is suppressed, which may suggest entrainment.

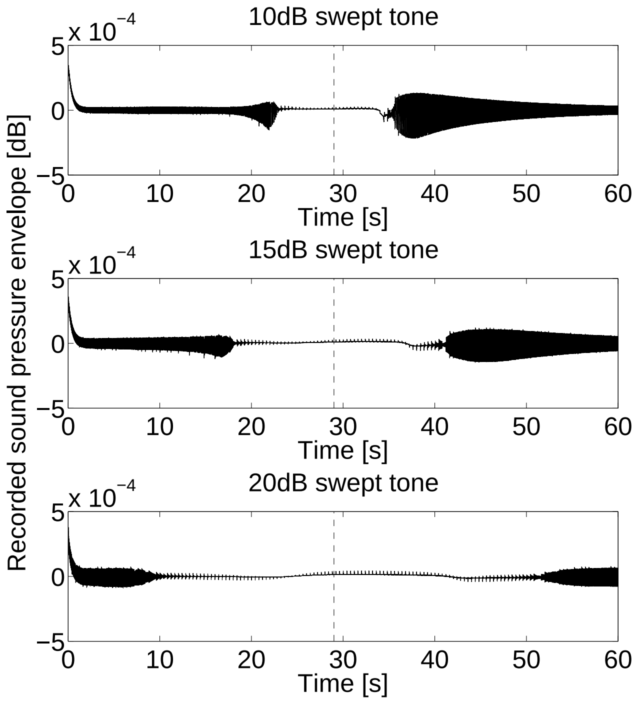

Figure 7.2: Level curves of the narrow-band pressure in the ear canal during the simulated interaction between an SOAE and a swept tones of different levels. Areas of rough beating and of smooth entrainment or suppression between the stimulus and the SOAE can be seen. $f_{swepttone}$ is equal to f_{SOAE} at $29s$ in these simulations, as shown by the dashed line.

An expanded detail of Figure 7.1, between 35 and 45 seconds, is shown in Figure 7.3. In this region of interaction between the two components, the SOAE is starting up again, after having been suppressed by the external swept tone. Before completely restabilising at around 2665 Hz, it appears to take on slightly higher frequencies, as if it were entrained by the swept tone. Although this phenomenon is pronounced more in this figure than in the other results, it does show an event that can be likened to entrainment, although the evidence is not strong.

To understand whether entrainment or just suppression is occurring, individual tones were fed into the model that have frequencies very close to f_{SOAE}. By leaving the system to reach steady state, it was possible to investigate the interaction occurring between the components in more detail. Figure 7.4 shows the power spectral density (PSD) of the pressure at the stapes when the model is not stimulated by the external tone; therefore, the peak of the PSD falls approximately at 2665 Hz.

Figure 7.5 shows how the PSD of the pressure at the stapes changes when the model is stimulated by 15 dB tones of different frequencies; the frequency of the external tone is shown in each individual panel. The top left plot shows that when the external tone's frequency is in proximity to the frequency of the SOAE, extra components are present in the spectra due to the nonlinear interaction between the SOAE and the stimulus. These components are equivalent to the diagonal lines that emerged in the spectrograms in Figure 7.1. The top right plot shows that as the frequency of the external tone gets closer to f_{SOAE}, the frequency of the SOAE does not change, but the power content in the frequency band between the two components due to distortion products, i.e. between 2648 Hz and 2665 Hz, has increased. This may explain the entrainment effect shown in Figure 7.3, where there is an increase in power across a broader frequency band. Thereafter, higher frequencies of the input tone suppress totally the SOAE, until it reaches a frequency of approximately 2680 Hz, as shown in the fourth panel in Figure 7.5. At 2688 Hz and 2691 Hz, the SOAE has been restored and again, the power content in spectra between f_{SOAE} and the input frequency show higher values that resemble entrainment. In the final panel, the SOAE appears to be restored and is interacting with the input stimulus to generate harmonics at other frequencies in their proximity. The steady state portions of the simulated waveforms used in this frequency analysis were 0.2 seconds long and the window size on the FFT used was also 0.2 seconds, so that the frequency resolution was about 5 Hz.

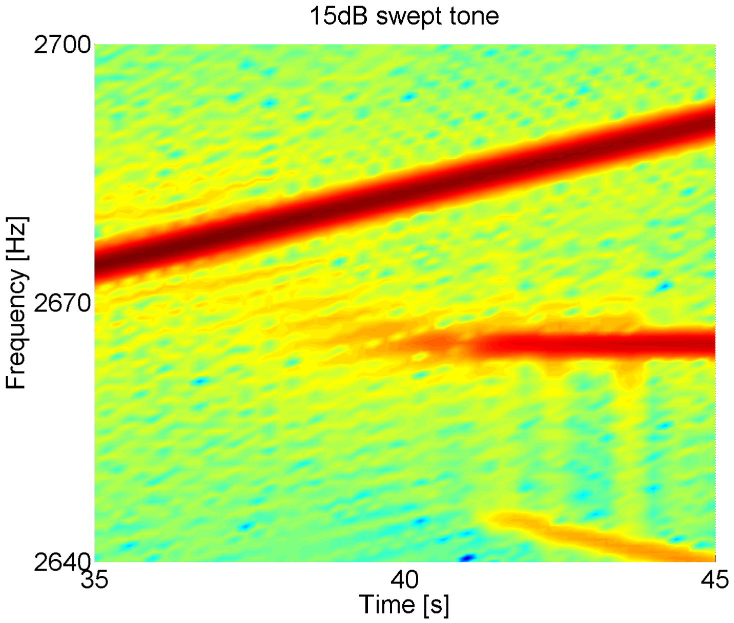

Figure 7.3: Analysis of the SOAE using a 15 dB swept tone. What is shown is a detail from Figure 7.1, between 35s and 45s. In this period of time the SOAE is being regenerated and appears to increase very slightly over time in frequency as it was entrained by the swept tone.

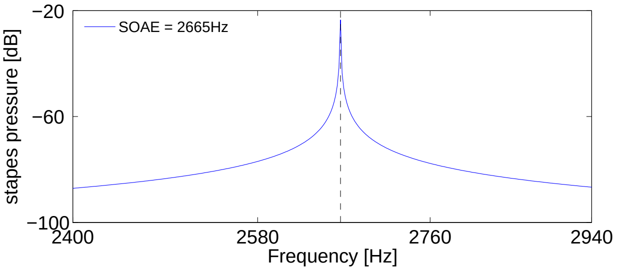

Figure 7.4: Power spectral density of the pressure at the stapes when no input is presented to the ear. The response resembles that of a quasi-pure tone at 2665 Hz, as shown by the dashed line.

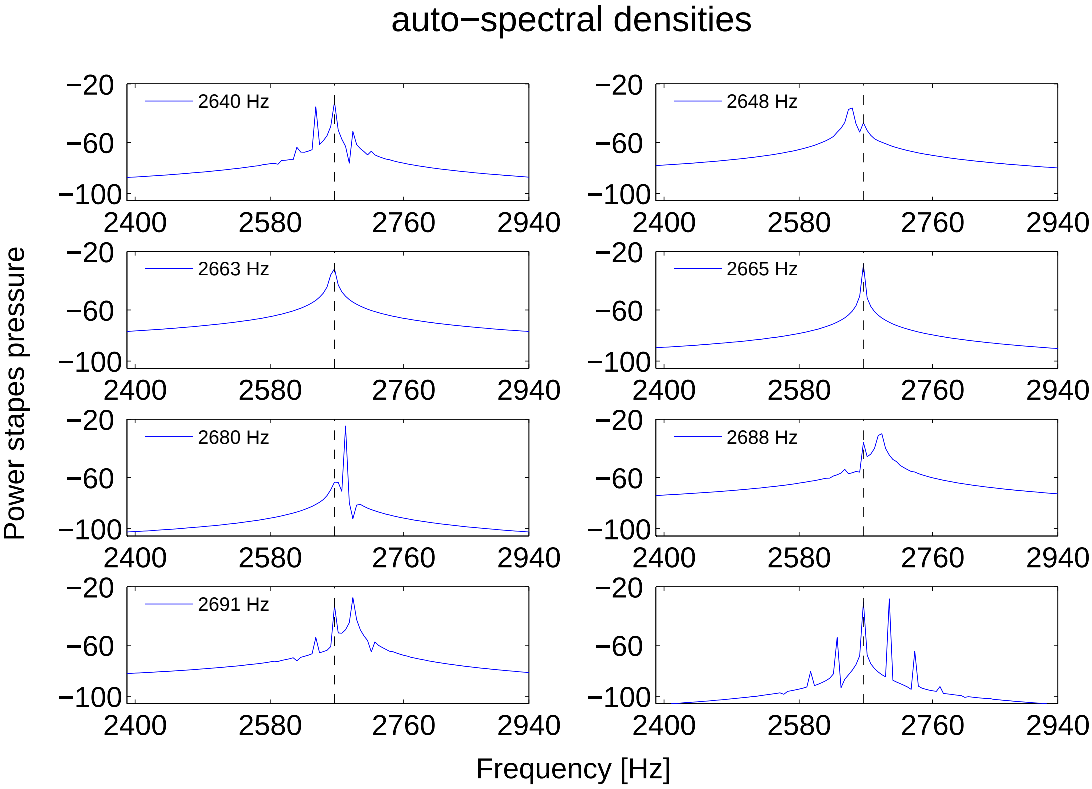

Figure 7.5: Power spectral density of the pressure at the stapes when various pure tone inputs are used to drive the simulations that generate a single SOAE. The frequency of the input tone is increasing from the top left panel to the lower right panel and interacts with the SOAE, while the unperturbed frequency is indicated by the dashed line.

In order to further test whether the entrainment and suppression phenomena shown in Figure 7.1 were occurring because of the modelled nonlinearity of the CA, a simulation was performed with the cochlear model where the random perturbations in the feedback gain generated only stable poles. Such a model produces no SOAE; but in this case, apart from the swept tone, the simulation consisted of a continuous stimulus that was also used to drive the model at 2665 Hz, which replicated the SOAE. The model was then stimulated by a second input swept tone, as used to generate in Figure 7.1. The aim was to understand whether nonlinear interactions within the cochlear model would also lead in this case to entrainment and/or suppression of either component. The result is shown in Figure 7.6, which is rather different in form to those in Figure 7.1, in that neither entrainment, nor suppression occurs and that there is no generation of distortion products. The two components only produce a beating pattern with one another, throughout the whole duration in time of the swept tone, as shown in Figure 7.7.

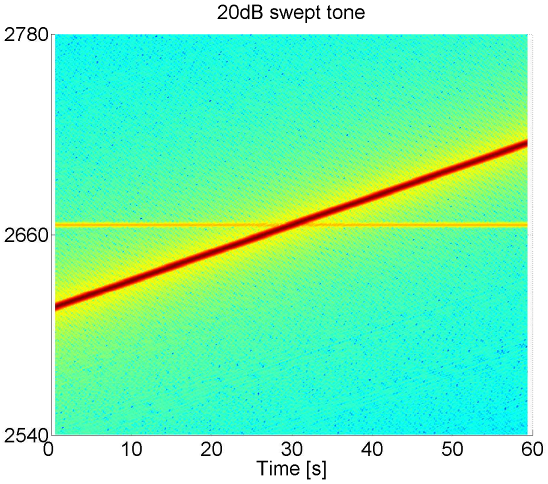

Figure 7.6: Analysis of the interaction between a swept tone and a pure tone both driving the ear canal in a model where no SOAE is present. No interaction exists between the two components in this case.

Although the results from the simulations give great insight into the functioning of the cochlear model, and possibly the functioning of the real cochlea, the entrainment effect appears to be somewhat weak. It is difficult to find unambiguous evidence for entrainment in measurements on human subjects. Also, it appears that confusion exists in the literature between SOAE entrainment and SOAE suppression due to an external tone. A proper distinction should be made between these two phenomena since they involve different alterations of SOAE properties.

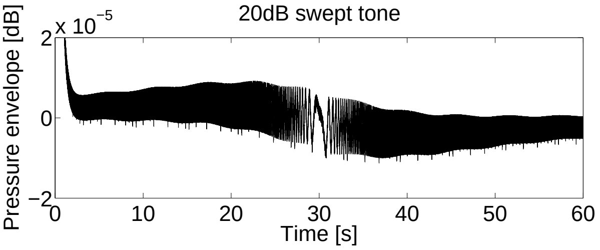

Figure 7.7: Analysis of the interaction between a swept tone and a pure tone both driving the ear canal in a model where no SOAE is present. Beating occurs between the two components for the whole duration of the swept tone, meaning that the components are never suppressed or entrained.

7.3 Modelled SOAE response after exposure to high level low frequency bias tone

Kugler et al. (2014) demonstrated experimentally that the human auditory system responded to high level low frequency tones that would modulate SOAEs for periods of approximately $100s$ after the bias tone was cut off and could also generate new SOAEs as reproduced in Figure 2.15. The same test was performed on the state space model to investigate whether it would produce any amplitude and/or frequency modulations on the limit cycle (and consequently on the SOAE) if the model was stimulated by a high level low frequency tone that was suddenly turned off. The results are shown in Figure 7.8, where it can be seen that there is very little resemblance to the results by Kugler et al. (2014), since the SOAE recovers within about $0.5s$ with no amplitude or phase modulation. The long term modulation effects observed by Kugler et al. (2014) are presumably a consequence of homoeostasis in the auditory cells, which is not replicated in this model.

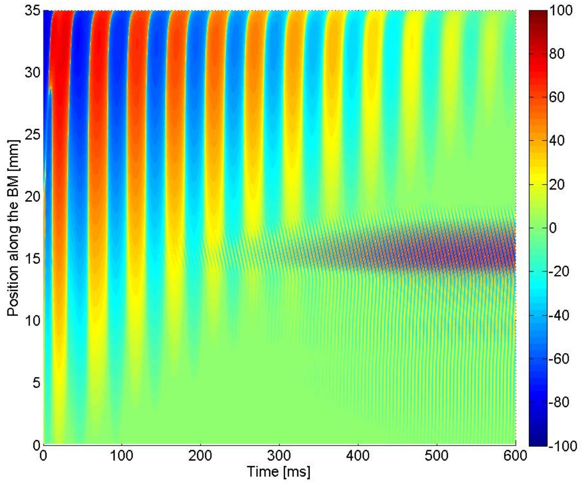

Figure 7.8: Response of the limit cycle when a high level 30 Hz tone is suddenly switched off at $t = 0s$. It can be seen that the limit cycle that produces the SOAE regenerates itself without any kind of FM or AM modulation as shown experimentally by Kugler et al. (2014).

7.4 Modelling microstructure and its relation to OAEs

Both OAE microstructure and threshold microstructure are quasi-periodic features that are indications of roughness in the physical structure of the cochlea (Talmadge et al., 1998; Shera, 2003). Epp et al. (2010) assumes that threshold stimulation of the cochlear membranes requires a given BM velocity. So in order to investigate microstructure here, simulations were performed, where the threshold microstructure was measured in a cochlear model. This was achieved by feeding input tones at various levels and frequencies, which would generate the same velocities along the BM at the characteristic place stimulated by each frequency. Two models were used, one of which generates an SOAE and one which did not. However, both models are characterised by random feedback gain with the same statistical properties. The threshold microstructure of the two models is seen in the top panels of Figures 7.9 and 7.10. The bottom panels in these figures, show spectrograms of the stapes pressure, when the cochlear model was stimulated with a click to generate click evoked otoacoustic emissions (CEOAE). These have specific frequency components that fade away over time, which can be seen in the spectrogram in Figure 7.9 as red peaks that decay away after about 0.03 or 0.04 seconds.

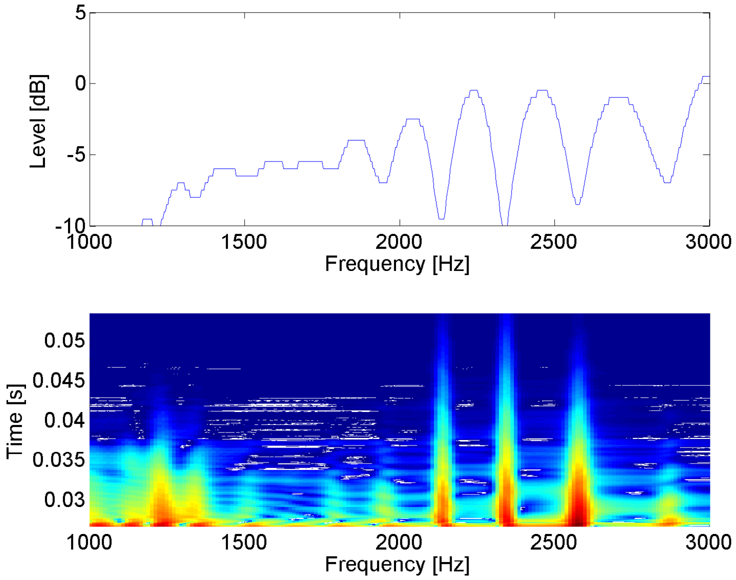

Figure 7.9: Illustration of threshold microstructure (top panel) and of CEOAEs (lower panel) from simulations of a stable cochlear model having random feedback gain. It can be seen that the CEOAEs generated after the click coincide with the troughs in the threshold microstructure.

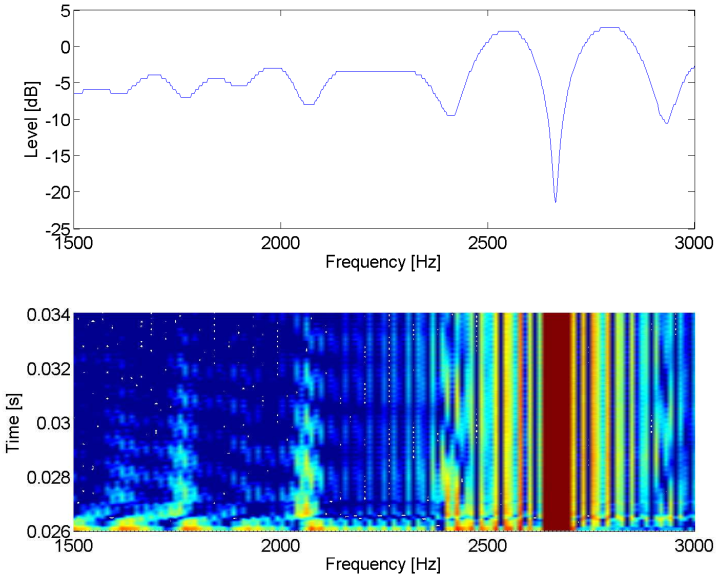

Figure 7.10: Illustration of threshold microstructure (top panel) and of CEOAEs (lower panel) from simulations of an unstable cochlear model having random feedback gain, which produces an SOAE at approximately 2.6 kHz. It can be seen that the CEOAEs generated after the click coincide with the troughs in the threshold microstructure. However, the biggest trough in the microstructure coincides with the frequency of the SOAE.

A striking resemblance exists between the upper and lower panels in Figures 7.9 and 7.10, where it can be seen that the spectral peaks in the CEOAEs coincide with the troughs in the threshold microstructure. These results agree with experimental findings of Long and Tubis (1988b).

Figure 7.10 shows the results from the cochlear model that generated a SOAE. In this case the equivalent trough in the threshold microstructure is lower than other troughs. Baiduc et al. (2014) performed experiments, showing that SOAEs appear to be associated with troughs in the threshold microstructure, as shown in Figure 2.9. The cochlear model demonstrates that a plausible explanation for this phenomenon is that the negative damping that generates the SOAE, leads the BM to reach a given velocity for lower level inputs when this location of the cochlea is stimulated.

These simulations have shown that the principle behind the generation of SOAEs and CEOAEs in the cochlear model are similar, the fundamental difference being the stability of the poles. The SOAE is generated by a pole, which is always unstable. However, when the model is stimulated by a click, some of the stable poles give rise to resonant responses for a short period of time, leading to the generation of CEOAEs.

7.5 Simulating posture change with the state space cochlear model

It was noted in Chapter 2 that postural changes can affect SOAE properties in human subjects. This is shown clearly in Figure 2.11, where both the amplitude and the frequency of the SOAE are subject to change when a subject's posture is changed, together with the formation of the new SOAEs. It is believed that this phenomenon is due to the change in the stiffness of the middle ear (ME) ossicles, due to variations in cochlear fluid pressure, and this hypothesis was tested in some preliminary simulations here.

It was assumed that by changing the value of the ME stiffness in the cochlear model, it would be possible to replicate this event. The original value of ME stiffness used during all previous simulations is $k_{ME} = 2.63 \cdot 10^8 Nm^{-3}$. A comparison was made between the SOAE results with this value of stiffness and those with k_{ME} that is 100 times larger or 100 times smaller than $2.63 \cdot 10^8 Nm^{-3}$. These assumed values of stiffness are not based on any measurement and therefore do not replicate the actual variation of ME stiffness when a subject undergoes a change in posture, but were chosen to investigate their effect. Figure 7.11 shows the envelope of the absolute value of BM velocity plotted against position along the cochlea from simulations of the cochlea that produced a SOAE with the nominal ME stiffness.

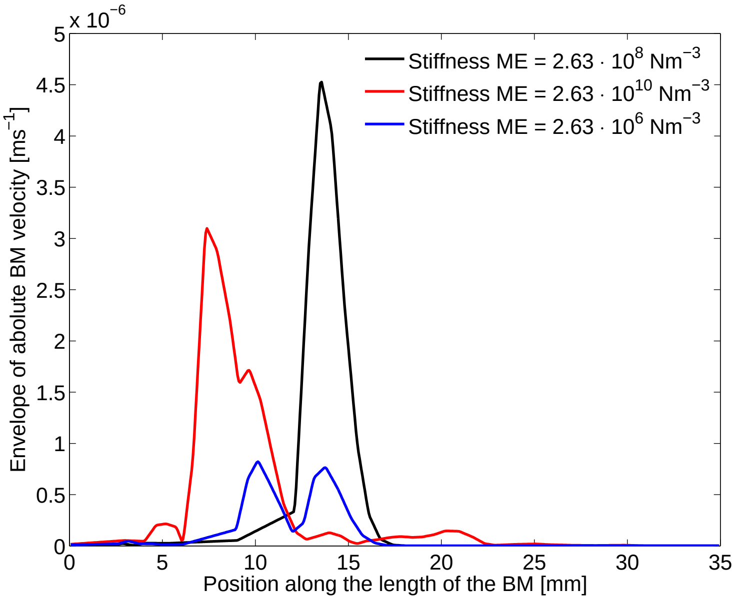

Figure 7.11: Variations in the properties of the limit cycles that generate the SOAEs in the cochlear model as a function of ME stiffness. The curves represent the envelope of the absolute BM velocity plotted against cochlear length.

With the original ME stiffness the model develops an SOAE at around 15 mm from the base, which has a higher amplitude with respect to the other cases. In the case of increased ME stiffness, the amplitude of the limit cycle's envelope decreases, and its frequency increases. This is demonstrated by the location of the limit cycle, which is closer to the base. In the third scenario, where the ME stiffness is decreased, the amplitude is very low with respect to the other two cases. Furthermore, two limit cycles appear to now be generated, which would lead to the transmission of two SOAEs in the ear canal. These results have similar characteristics to the measurements of de Kleine et al. (2000), shown in Figure 2.11. These results depend on the roughness introduced in the cochlear model, since this is what determines the stability of the poles of the model. This can be likened to the differences between cochlear properties of different individuals.

7.6 Can the cochlear model generate virtual bass?

Many studies have shown that the auditory system has the capability to generate the missing fundamental component of complex signals. This principle is taken advantage of in the audio industry to compensate for the poor low frequency response of loudspeakers (Gan and Oo, 2010; H. Mu and Tan, 2015). The virtual bass effect is most probably due to psychoacoustics and perhaps to the neural pathways involved in the auditory system. Nevertheless, an attempt was made in this thesis to understand whether there may also be a mechanical explanation to this phenomenon, which can be demonstrated with the cochlear model, due to its nonlinear properties. Simulations were performed by driving the model with signals containing multiple harmonics, such as a square wave and a saw-tooth wave, with and without their fundamental harmonic. An example is shown in Figure 7.12, where the top panel shows a 100 Hz saw-tooth wave, and the lower panel shows the same wave without its fundamental.

The BM velocity was calculated from the cochlear model when driven by these two waveforms, and Figures 7.13 and 7.14 show the BM velocity at specific locations along the length of the cochlea. The responses in the panels on the left show the variation of the velocity of the BM in the time domain at 35 mm, 32.5 mm and 30 mm from the base of the cochlea, while the equivalent responses in the frequency domain are shown in the panels on the right and have a resolution of 25 Hz. The most interesting location shown in Figures 7.13 and 7.14 is the one at 35 mm, for which the characteristic frequency is 100 Hz, which is the fundamental component of the saw-tooth waveform. A clear response is seen at this position in both time and frequency domains when the fundamental is included to the saw-tooth wave, but no response is seen if the fundamental is removed. Changes also occur between the two cases at the other locations of 32.5 mm and 30 mm, where the characteristic frequencies correspond to approximately 200 Hz and 300 Hz.

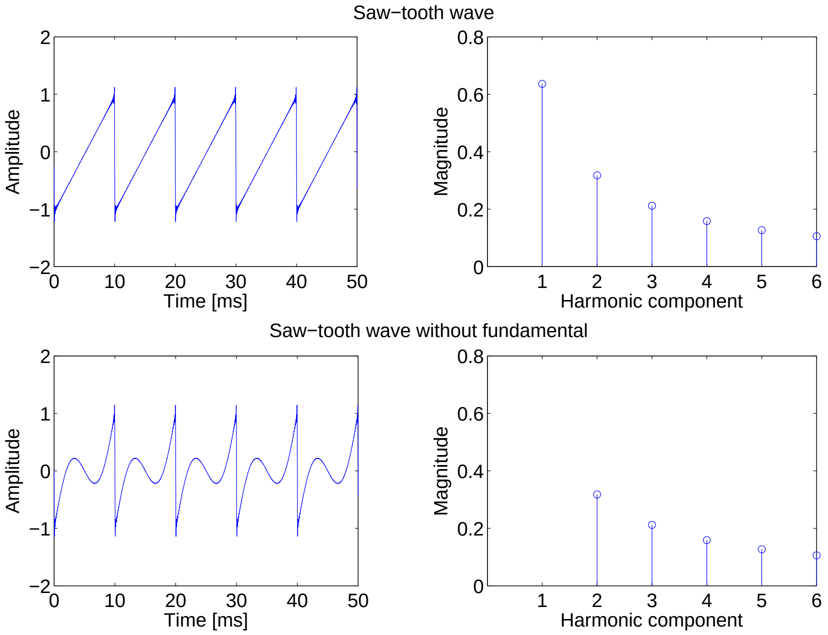

Figure 7.12: An example of a saw-tooth wave illustrated with its fundamental component in the top panel, and without the fundamental component in the lower panel.

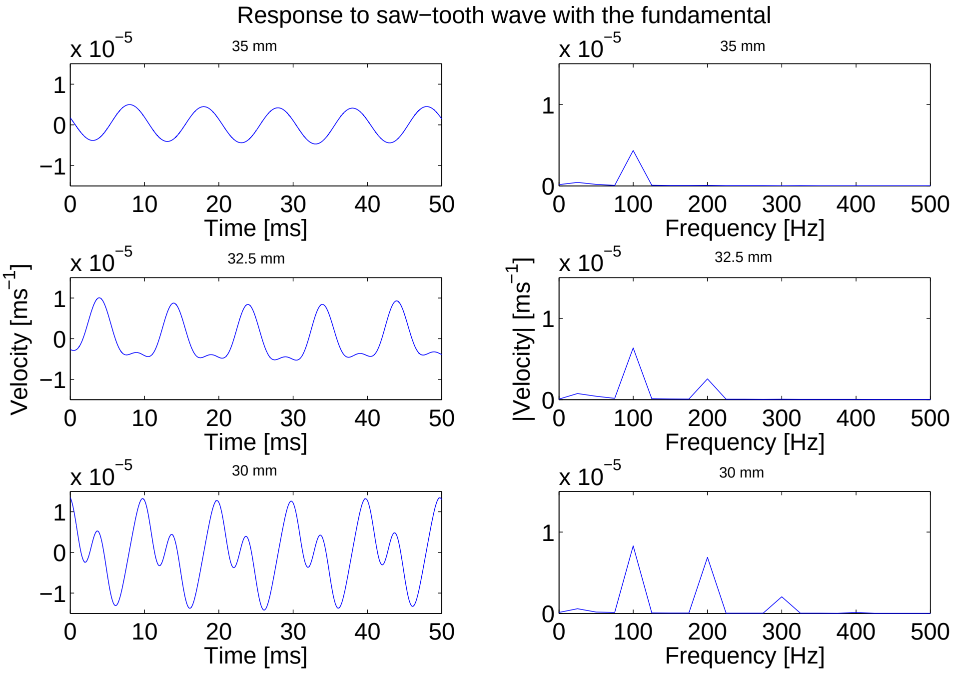

Figure 7.13: The response in the time domain (left panels) and in the frequency domain (right panels) at different positions along the BM to a 100 Hz saw-tooth wave with its fundamental component. The positions chosen correspond to characteristic frequencies of approximately 100 Hz, 200 Hz and 300 Hz.

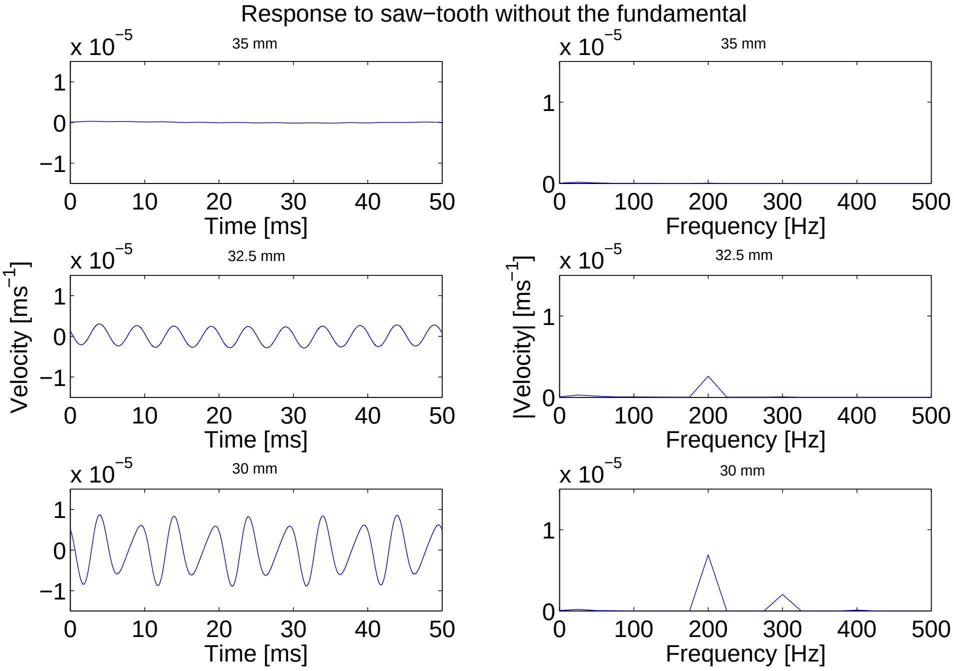

Figure 7.14: The response in the time domain (left panels) and in the frequency domain (right panels) at different positions along the BM to a 100 Hz saw-tooth wave without its fundamental component. The positions chosen correspond to characteristic frequencies of approximately 100 Hz, 200 Hz and 300 Hz.

The presence or absence of the fundamental component causes differences in the waveforms of the BM response at thus locations, presumably due to the presence or absence of the biasing effect due to the lower frequency 100 Hz component. So although the missing fundamental is not explicitly generated by the nonlinearity in the cochlear mechanics, this does have an effect on the BM waveforms at the higher harmonics.

7.7 Summary

In this chapter, time domain simulations of the nonlinear state space model of the cochlea have been used to investigate various nonlinear effects in the cochlea. Simulations of the interaction between an SOAE and a swept tone were first performed, where the results clearly illustrated the generation of distortion products and suppression of the SOAE when the frequency of the swept tone was close to that of the emission. When the SOAE was not suppressed, beating amongst the two signal occurred. The evidence for entrainment does not appear to be very strong from the results of those simulations.

When the same effect was investigated in a cochlear model with no SOAE, but with an extra stimulus that replicated the SOAE, no suppression and/or entrainment effects were observed. This confirms that when suppression does occur in the model that produces a SOAE, it is due to nonlinear effects of the CA.

Further simulations were undertaken of the modelled SOAE response after exposure to a high-level low-frequency bias tone. Kugler et al. (2014) observed through experiments that such an exposure would suppress SOAEs for lengthy periods of time and that new SOAEs would appear. However, the model failed to reproduce this phenomenon, as it is presumably due to homoeostasis within the auditory cells, which is not replicated in the model.

Cochlear microstructure was replicated and its relation to OAEs was investigated. Results from the model confirmed what was demonstrated experimentally by Long and Tubis (1988b) and Baiduc et al. (2014), showing that spectral peaks in the CEOAEs signal coincided with troughs in the threshold microstructure. Furthermore, very deep troughs could be associated with SOAEs.

Finally, simulations of the nonlinear cochlear mechanics were performed to investigate whether the cochlear model could replicate the effect of virtual bass. The simulations performed did not generate the missing fundamental, which is heard in these systems, although the nonlinearity did affect the cochlear response at other harmonics. This confirms that the main mechanism for this effect is psychoacoustic rather than being directly caused by the cochlear nonlinearity.

Chapter 8

Conclusions and suggestions for further work

It is fascinating how the mechanics of the cochlea are so precise in delivering appropriate stimuli to the auditory nerve, and the scale at which these actions are performed. Nonlinear interactions in the cochlea are crucial for the correct functioning of the ear as a whole and have been the focus of the work presented in this thesis. This Chapter outlines the conclusions of the work performed in the thesis: a general discussion of the state space model of the cochlea is summarised, where its strengths and weaknesses are reviewed, followed by a summary of the most important findings. The later sections of this chapter deal with suggestions for further work and outline what can be done to improve the state space model, including what simulations would be useful.

8.1 The cochlear state space model and modelling SOAEs

A nonlinear state space model of the cochlea, based on previous work from Elliott et al. (2007), has been developed to simulate the generation of a single SOAE and how it interacts with various external stimuli. It has the capability of linking together cochlear mechanisms that occur both on a microscopic level, due to OHCs, and on a macroscopic level, where coupling between the micromechanics is made possible. The model was modified here to replicate the properties of the human cochlea, including the generation of SOAEs. The results demonstrate how the generation of an SOAE is due to the combination of forward and backward waves that travel along the BM, in accordance with the multiple reflection theory of Zweig and Shera (1995). The state space formulation adopted has the benefit of easily performing time domain simulations so that comparisons can be made of the results when changing different parameters in the model. It also allows simulation of the effect of unstable poles on the results, by introducing roughness in the parameters, which can be stabilized using nonlinear functions to mimic compression of the CA in the real cochlea. Numerical experiments were performed, where one unstable pole was generated in the model that would generate a limit cycle. The limit cycle generated along the BM is directly linked to the SOAE measured in the ear canal. OHC activity has previously been shown to be highly nonlinear (e.g. Cody and Russell (1987)), but the direct measurement of such nonlinearity in vivo is challenging. The present model can readily incorporate and test various forms of nonlinearities in the CA and the results can then be compared with experimental data in order to demonstrate the plausibility of different forms of nonlinear functions. Two types of nonlinearities were used in the micromechanical elements of the model, i.e. a hyperbolic tangent function and a first order Boltzmann function.

8.2 The quasi-linear model

A quasi-linear version of the same cochlear model has been developed, based on previous work (Kanis and de Boer, 1993, 1994; Young, 2011). The model gives insight into self-suppression, which is a phenomenon due to nonlinear activity of the cochlear structures. This model has been used to predict input/output compression response curves of the cochlea and for modelling saturation levels of the nonlinear function used in the micromechanical elements.

The quasi-linear model was also used to predict initial conditions for time domain simulations in the state space model.

8.3 Low frequency biasing of the cochlear structures and estimation of cochlear nonlinearity

A large proportion of the thesis has dealt with the response of the cochlear model to external low frequency bias tones and how they interact with an SOAE. It has been shown how these stimuli are valuable in helping to determine nonlinear properties of the cochlea. The simulations show that biasing the cochlear structures with an external low-frequency bias tone influences the behaviour of the limit cycle and therefore that of the SOAE. Interesting features are demonstrated when different nonlinear functions are included in the cochlear micromechanics, influencing the modulation of the SOAE. The simulations show that a SOAE can be partly or totally suppressed by external low frequency bias tones, and also generates side-bands in the process, as measured experimentally (Zwicker and Schloth, 1984; Bian and Watts, 2008). However, the simulation results change according to the nonlinearity used in the cochlear micromechanics. The symmetrical hyperbolic tangent function biases the structures in the same way during positive and negative half cycles of the low frequency stimulus, while an asymmetrical Boltzmann function included in the CA biases the cochlear structures differently during positive and negative half-cycles of the bias tone.

Bian and Watts (2008) refers to the measurements made during these half-cycles as quasi-static measurements. The simulations have shown that the asymmetrical Boltzmann function produces more similar results to the experiments than the hyperbolic tangent function. It is shown that excessive motion of the BM and TM is compressed due to external bias tones, and that the limit cycle is compressed differently according to the nonlinear function embedded into the mechanics.

For the Boltzmann function there is an added gain for small positive inputs. Quasi-static results are then “inflated” for positive half cycles and “deflated” for negative half-cycles, especially for the cases when the bias tone frequency is lower than approximately 40 Hz. Bian and Watts (2008) assumed that the details of the nonlinearity featured in the CA may be reconstructed from the modulated response of SOAEs to the low frequency bias tones. But simulations show that, although similar features to the measured quasi-static responses are generated when using an asymmetric nonlinearity, the details of the reconstructed nonlinearity do not match those of that used in the cochlear model. This is thought to be due to assumptions inherent in the quasi-static analysis method and also because the nonlinearity of the CA depends on the shear motion of the OHC, rather than just the displacement of the BM.

The instantaneous amplitude and frequency of the simulated SOAE modulated by an external tone has also been obtained using the Hilbert transform, in order to illustrate temporal modulation patterns. Again, this shows significant differences for symmetrical and asymmetrical nonlinearities in the modelled CA. The amplitude and the frequency of the bias tone greatly affected the modulation of the emissions.

Using different frequencies for the biasing tone has led to the conclusion that quasi-static modulation, as defined by Bian and Watts (2008), only occurs for bias tones below about 10 Hz. When the bias tone is greater than 10 Hz, the situation is really due to dynamic modulations, since the SOAE does not appear to reach steady state at these modulating frequencies. The upper frequency of the quasi-static behaviour is related to the settling time observed to establish the steady state behaviour of the SOAE. The model demonstrates that quasi-static measurements, as performed by Bian and Watts (2008), can be misleading and do not fully take account of the nonlinear properties of the cochlea. This is due to the failure of the limit cycle to sustain itself when the gain of the CA is lowered, a result of the bias tone affecting the dynamics of the system.

8.4 Nonlinear properties of the cochlear model

Interaction between an SOAE and a swept tone

Chapter 7 was dedicated to simulating a number of other nonlinear phenomena that occur in the cochlea. Various experiments described in the literature have shown that SOAEs interact with external swept tones, which cross their frequency, and that this leads to suppression and entrainment. Although suppression effects are relatively easy to quantify in experiments, entrainment effects, where the SOAE frequency is pulled towards and eventually merged with the swept tone at some critical frequency, have not been demonstrated as clearly as it has been with animal subjects, in particular barn owls and lizards Bergevin and Salerno (2015). The model can easily predict suppression of an SOAE as the frequency of the swept tone enters the vicinity of the emission, but entrainment is harder to demonstrate. There was some evidence from the simulations that the SOAE is pulled and pushed away from the stimulus, but these results are complicated by distortion product generation.

Interaction between an SOAE and a very high, low frequency tone

The response of the SOAE in the model to a transient of the very high, low frequency tone gave results that differed greatly from recent experiments. This suggests that the experimental results, that extend over time-scales of 100s of seconds, are dominated by cell homoeostasis behaviour, which is not included in the cochlear model.

The relationship between threshold microstructure and CEOAEs according to the cochlear model

The literature suggests a relationship between CEOAEs and SOAEs and threshold microstructure. This was clearly demonstrated through simulations, where the frequencies of CEOAEs and of an SOAE coincided with troughs in the threshold microstructure. It can be concluded that reflection emissions are generated at locations along the cochlea that are more sensitive to external sounds. In fact, these locations are characterised by weaker values of damping, close to instability in the locations where CEOAEs are generated, and unstable for locations of negative damping that generate SOAEs.

Simulating the effect on postural changes on the cochlea

Initial work was undertaken to understand the effects of postural changes on the cochlea. Postural changes were implemented in the model by varying the value of middle ear stiffness. These variations lead to changes in SOAE properties in both amplitude and frequency, and also to the generation of new SOAEs, which are phenomena that have been documented in the literature (de Kleine et al., 2000).

Can the cochlear model predict virtual bass effects?

Simulations to understand whether virtual bass is caused by cochlear mechanics were performed, demonstrating that the model did not account for this phenomenon and that, as stated in the literature, this effect is more likely to be a consequence of psychoacoustic effects further up the neural pathway.

8.5 Future work

In the following sections, an effort has been made to summarise what the author believes to be the most interesting, useful and relevant modelling experiments to be performed in light of the results shown in the present thesis.

Refining the model and expanding its capabilities

When modelling a system such as the cochlea, whose physical properties are extremely hard to measure, one has to deduce from experimental measurements what mechanical parameters to use, as was done in this project. The cochlear parameters used in this thesis, could be used in future work, but the micromechanical model used here may not be entirely realistic, and new micromechanical models need to be developed as more of the actual physical properties of the cochlea are measured. In fact, a great advantage of working on a numerical model such as this one, is the possibility to modify its structure and parameters and understanding how such a modification affects the system. The aim of the model is not necessarily to perfectly match real existing data, but to convey greater insight into the functioning of the system. Moreover, future work is necessary to understand if asymmetrical nonlinear functions, other than the Boltzmann function, may be more suitable for the model.

It was found towards the later stages of the project, that the frequency response of the cochlea to very low frequencies gave inaccurate results, where, for example, the response would contain multiple resonances and anti-resonances as well as the resonance expected at the characteristic frequency of a particular location. An example of the frequency response measured at one position, 15 mm, along the cochlea is given in Figure 8.1, where the highest peak occurs at around 2 kHz. This is due to the expected resonance of the cochlea's characteristic frequency for this location, but other resonances also occur, for example, at around 20 Hz and 50 Hz. Similar resonances, but of a lower magnitude, have recently been observed by Marquardt and Hensel (2013). These effects are thought to be due to reflections at the helicotrema, which do not seem to be accurately modelled by the boundary condition in the current model, but were discovered at a stage during the project where it would have been inconvenient to modify the model. However, further work is required to understand this effect more fully.

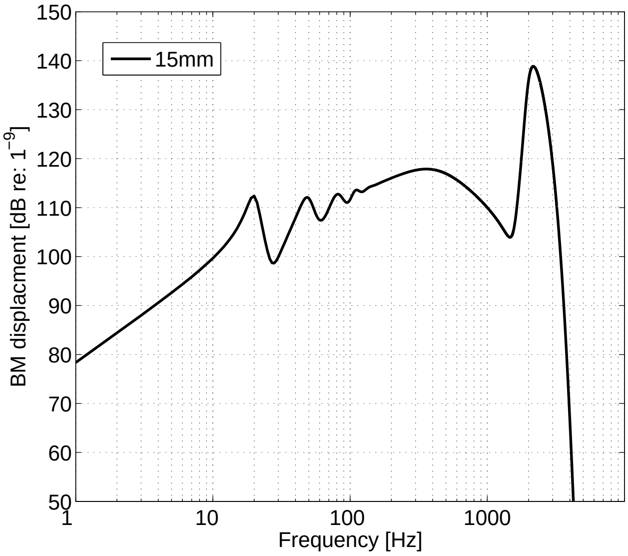

Figure 8.1: Illustration of the model's response at 15 mm from the base to low frequency.

Many efforts were made to make time domain simulations faster. Increased speed was achieved through a number of mathematical and coding strategies. However, it is desirable to make the model even more efficient. A possible solution is to code the model with alternative programming languages, such as Python or C++, whose coding efficiencies may allow for faster simulations, while still remaining fairly easy languages to use.

It was discovered that, when the model was stimulated by a very high level, low frequency tone, its response differed from real experimental data. It was concluded that the response of real cochleae are influenced by cell homoeostasis, which was not modelled into the mechanics of the state space model. A future model may be developed to include such mechanisms.

The ultimate goal of a model is to replicate as accurately as possible the system under scrutiny. Work has been undertaken to use linear finite element models to predict the individual responses from acoustic pressure and OHC activity to BM vibration and hair bundle shear, and then combine these together with a nonlinear OHC model to predict the active response of a single slice of the cochlea (Ni et al., 2015). One method of simulating the coupled response of the cochlea from these results, would be to use a modified form of the state space model above. The fluid coupling, calculated for the base model in $\mathbf{F}^{-1}$ in the *Macromechanical model* section in Chapter 4, may need to be modified to account for the 3D geometry of the model and the two degree of freedom model in Figure 3.3 could be replaced with one based on the low-order model behaviour of the finite element model. In this way the parameters of a tractable nonlinear model of the nonlinear cochlea could be generated from a number of more detailed finite element models, and this model then used to predict the coupled response of the cochlea, potentially including the OAEs.

Further interesting simulations

Results from the simulations have led to the conclusion that a bias tone with a low enough frequency will modulate the SOAE slowly enough to avoid interactions with the dynamics of the SOAE initiation process that occurs within the cochlea. This was performed using bias tones down to 10 Hz, but it would be better if it could be proved in a future study involving the use of bias tones of frequencies down to 1 Hz. The problem with such a simulation is that it requires a lot of computer memory, due to the length in time of a 1 Hz tone, and was not achievable during this project.

CEOAEs and their relation to microstructure were briefly analysed with the model, giving some very interesting results. There is still some debate on the existence of roughness along the cochlear structures, hence, further exploration of this would be very beneficial to better understand the properties of cochlear roughness, how and if it affects hearing, and whether it is linked to the generation of OAEs or not.

It was shown in Chapter 7 that variations to the middle ear stiffness changed the properties of the cochlea, in particular of the limit cycle generated along the length of the BM. Simulations like these should be further pursued, in order to match real experimental results, and to understand the relationship between posture, OAEs and intracranial pressure. These findings could be very helpful for determining to what extent OAEs vary with intracranial pressure (ICP) variations, and ultimately lead to the creation of alternative non-invasive methods to measure ICP, which is currently measured using invasive methods.

Other interesting simulations would involve the interaction between multiple primary SOAEs and the generations of distortion products amongst these emissions.

Other cochlear models

A state space model using 3dof lumped micromechanical elements

Future work could compare the proposed state space model used here with other models, involving three degrees of freedom micromechanical elements, which are documented in the literature (Galvez and Elliott, 2014). These aim to increase the reliability and precision of a cochlear model. Figure 8.2 (a) shows a slice of the cross section of the OC; this can be transformed into a lumped parameter model with three degrees of freedom, shown in Figure 8.2 (b). Unlike the micromechanical element shown in Figure 3.3, this model takes into consideration the motion of the reticular lamina (RL), a stiff membrane lying between the hair cells and the TM.

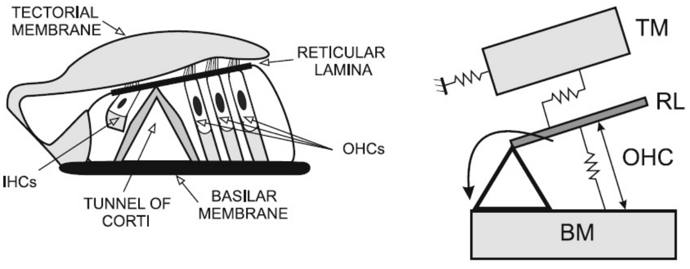

(a) (b)

Figure 8.2: Representation of a cross section of the organ of corti (a) and its equivalent three degree of freedom lumped parameter model (b). Reproduced from Galvez and Elliott (2014).

Figure 8.3 (a) illustrates how the element tends to move in two directions; this can be simplified by adjusting the structures such that motion occurs along a single axes, as shown in Figure 8.3 (b). The overall macromechanical model incorporates a number of micromechanical elements coupled through fluid coupling.

A disadvantage of the current implementation of this model is that it is not capable of predicting appropriate levels of the feedback gain. By using a quasi-linear method it may be possible to obtain a more realistic distribution of feedback gain along the cochlea.

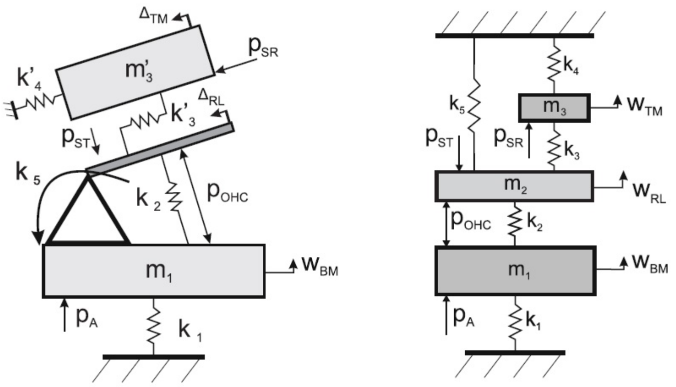

(a) Shear and transversal motion. (b) With motion in only one axis.

Figure 8.3: Lumped parameter model of the organ of Corti having motion in two axis (a) and its transformation into a micromechanical model having motion on a single axis (b). Reproduced from Galvez and Elliott (2014).

A state space model using Van der Pol oscillators

A further model that would be of great interest is a state space model with Van der Pol oscillators as micromechanical elements. Van der Pol oscillators have been used to understand local effects in the cochlea by, for example, Talmadge et al. (1998) and a brief analysis of their behaviour was also described in this thesis in Chapter 3.1. By modelling the entire length of the cochlea using many of these oscillators, which can be coupled together using a state space formulation, it may be possible to understand other cochlear phenomena and also to compare results obtained from the state space model used in this thesis.

Translational research - from simulations to real experiments

One of the ultimate goals of cochlear modelling is to promote translational research and help our understanding of hearing loss. The closer a cochlear model can replicate the properties of a real cochlea, the greater are its possibilities to replicate various forms of hearing loss. However, one needs to distinguish between various forms of hearing loss. Given the mechanical structure of the state space model used in this thesis, it may be suitable in future applications to understand sensory transmissive hearing loss, but further work is still required to reach this stage.

This thesis has concentrated on obtaining results that replicate experiments performed on human subjects. Morphological differences exist between the cochleae of humans and other animals, which lead to differences in SOAE properties. For this reason, SOAEs should be classified according to the animal/species and a separate analysis has to be done before comparing SOAEs between species. For this reason, the state space model developed cannot simulate features that arise in the cochleae of other species that may have a different anatomy, and further development is required in this area.

Appendix A

State space formulation of the cochlear model

A.1 State space formulation of the micromechanical model

The following sections describe how the state space model is developed. The reader should refer to Elliott et al. (2007) for further details on the theoretical background regarding the application of the state space formulation to the cochlear model. In particular, the micromechanical model from Neely and Kim (1986) will be introduced here, followed by its application to the state space model in order to obtain the coupled macromechanical model.

With reference to Figure 3.3 and to Equations 3.7 and 3.8, the BM and TM displacements and velocities are represented in the state space formulation as follows:

- $\dot{x}_1(t) \equiv$ BM velocity
- $x_1(t) \equiv$ BM displacement
- $\dot{x}_2(t) \equiv$ TM velocity
- $x_2(t) \equiv$ TM displacement

The differential equation describing the dynamics of the micromechanical element, as shown in Elliott et al. (2007), can be written as follows:

$$\begin{aligned} \ddot{x}_1 = \frac{1}{M_1}\{p_d(t) + g\gamma[C_4(\dot{x}_2(t) - \dot{x}_1(t)) + K_4(x_2(t) - x_1(t))] \\ - \dot{x}_1(t)(C_1 + C_3) - x_1(t)(K_1 + K_3) + \dot{x}_2(t)C_3 + x_2(t)K_3\} \end{aligned} \tag{A.1}$$

and

$$\ddot{x}_2 = \frac{1}{M_2}\{-\dot{x}_2(t)(C_2 + C_3) - x_2(t)(K_2 + K_3) + \dot{x}_1(t)C_3 + x_1(t)K_3\} \tag{A.2}$$

Note that equations A.1 and A.2 are written in terms of $x_1(t)$ and $x_2(t)$ and incorporate the active feedback term, γ. The state vector can be written as follows:

$$\mathbf{x}_n = \begin{bmatrix} \dot{x}_1(t) \\ x_1(t) \\ \dot{x}_2(t) \\ x_2(t) \end{bmatrix}_n , \tag{A.3}$$

where n refers to the index number of the element. The derivative of Equation A.3 is:

$$\dot{\mathbf{x}}_n = \begin{bmatrix} \ddot{x}_1(t) \\ \dot{x}_1(t) \\ \ddot{x}_2(t) \\ \dot{x}_2(t) \end{bmatrix}_n . \tag{A.4}$$

The mechanics of the single element can now be expressed in state space form as follows:

$$\dot{\mathbf{x}}_n(t) = \mathbf{A}_n\mathbf{x}_n(t) + \mathbf{B}_n p_n(t), \tag{A.5}$$

where

$$\mathbf{A}_n = \begin{bmatrix} -\frac{(C_1+C_3-g\gamma C_4)}{M_1} & -\frac{(K_1+K_3-g\gamma K_4)}{M_1} & \frac{(C_3-\gamma C_4)}{M_1} & \frac{(K_3-\gamma K_4)}{M_1} \\ 1 & 0 & 0 & 0 \\ \frac{C_3}{M_2} & \frac{K_3}{M_2} & -\frac{(C_2+C_3)}{M_2} & -\frac{(K_2+K_3)}{M_2} \\ 0 & 0 & 1 & 0 \end{bmatrix}_n \tag{A.6}$$

$$\mathbf{B}_n = \begin{bmatrix} \frac{1}{M_1} \\ 0 \\ 0 \\ 0 \end{bmatrix}_n \tag{A.7}$$

The output given by Equation 3.8 becomes

$$\dot{x}_{n_1}(t) = \mathbf{C}_n\mathbf{x}_n(t) + \mathbf{D}_n p_{d_n}(t), \tag{A.8}$$

where

$$\mathbf{C}_n = \begin{bmatrix} b & 0 & 0 & 0 \end{bmatrix} \tag{A.9}$$

and

$$\mathbf{D}_n = 0. \tag{A.10}$$

The term b in Equation A.9 selects the desired output, which in this case is the BM velocity of the n^{th} element, although one can choose to modify matrix **C** to obtain one of the other state variables. Neely and Kim (1986) use the following differential equation to describe the dynamics of the middle ear:

$$p_1(t) = M_m \ddot{x}_1(t) + C_m \dot{x}_1(t) + K_m x_1(t) \tag{A.11}$$

where M_m, C_m and K_m are the lumped mass, damper and stiffness terms of the middle ear and x_1 is the displacement of the middle ear element. This can be cast into the state space formulation for the first element as:

$$\dot{\mathbf{x}}_1(t) = \mathbf{A}_1 \mathbf{x}_1(t) + \mathbf{B}_1 p_1(t), \tag{A.12}$$

where

$$\mathbf{x}_1(t) = \begin{bmatrix} \dot{x}_1 \\ x_1, \end{bmatrix} \tag{A.13}$$

$$\mathbf{A}_1 = \begin{bmatrix} \frac{-C_m}{M_m} & \frac{-K_m}{M_m} \\ 1 & 0 \end{bmatrix}, \tag{A.14}$$

and

$$\mathbf{B}_1 = \begin{bmatrix} \frac{1}{M_m} \\ 0 \end{bmatrix}. \tag{A.15}$$

The boundary conditions at the helicotrema, as shown in Ku et al. (2008c), are the following:

$$p_N(t) = M_H \ddot{x}_N(t) + C_H \dot{x}_N(t), \tag{A.16}$$

where M_H and C_H are the lumped mass and damper of the helicotrema and x_N is the displacement of the helicotrema. This can be cast into the state space formulation for the last element as:

$$\dot{\mathbf{x}}_N(t) = \mathbf{A}_N \mathbf{x}_N(t) + \mathbf{B}_N p_N(t), \tag{A.17}$$

where

$$\mathbf{x}_N(t) = \begin{bmatrix} \dot{x}_N \\ x_N \end{bmatrix}, \tag{A.18}$$

$$\mathbf{A}_N = \begin{bmatrix} \frac{-C_H}{M_H} & 0 \\ 1 & 0 \end{bmatrix}, \tag{A.19}$$

and

$$\mathbf{B}_1 = \begin{bmatrix} \frac{1}{M_H} \\ 0 \end{bmatrix}. \tag{A.20}$$

Given that the micromechanical element is a linear system and given that $\mathbf{A}_n$ is independent of $\mathbf{x}_n(t)$, the admittance of an isolated micromechanical element can be solved in the Laplace domain from Equations A.5 and A.8 and written as:

$$\mathbf{y}_{pn}(s) = [\mathbf{D}_n + \mathbf{C}_n(s\mathbf{I} - \mathbf{A}_n)^{-1}\mathbf{B}_n]\mathbf{p}_n(s), \tag{A.21}$$

where $s = \sigma + j\omega$.

A.2 State space formulation of the macromechanical model

The one-dimensional wave equation describing the dynamics of the cochlear partition in terms of the radially averaged acceleration is the following (Elliott et al., 2007):

$$\frac{\partial^2 p(t)}{\partial x^2} - \frac{2\rho}{H}\ddot{\xi}_p(t) = 0, \tag{A.22}$$

where ξ_p is the average BM displacement over the radial cross section, ρ is the density of the cochlear fluids and H is the height of the chambers above and below the cochlear partition. Note that, as in the box model described by de Boer (1996), the model takes into account only two chambers of the cochlea by neglecting the effect of Reissner's membrane. The dependence of $p(t)$ and $\ddot{\xi}_p(t)$ on the variable x is suppressed for notational convenience. The boundary condition at the base of the cochlea in conjunction with the middle ear can be written in terms of the stapes acceleration, $\ddot{\xi}_{st}(t)$, as follows:

$$\left.\frac{\partial p(t)}{\partial x}\right|_{x=0} = 2\rho\ddot{\xi}_{st}(t). \tag{A.23}$$

$\ddot{\xi}_{st}(t)$ can be written as the sum of two linearly superposing components $\ddot{\xi}_{st}(t) = \ddot{\xi}_{SO}(t) + \ddot{\xi}_{SR}(t)$, i.e. the sum of the acceleration due to an external stimulus, $\ddot{\xi}_{SO}(t)$, and the acceleration due to the loading by the internal pressure response in the cochlea at $x = 0$, $\ddot{\xi}_{SO}(t)$. Therefore, equation A.23 can be written as:

$$\left.\frac{\partial p(t)}{\partial x}\right|_{x=0} - 2\rho\ddot{\xi}_{SR}(t) = 2\rho\ddot{\xi}_{SO}(t). \tag{A.24}$$

The boundary condition at the apical end of the cochlea is described by the following equation (Ku et al., 2008c):

$$\left.\frac{\partial p(t)}{\partial x}\right|_{x=L} \approx \frac{p_{N-1} - p_N}{\Delta} = 2\rho\ddot{\xi}_N + \frac{1}{H}p_N. \tag{A.25}$$

Equations A.22, A.23 and A.25 can be defined using a finite difference approximations method, allowing them to be used in the state space formulation. The finite difference wave equation used to approximate the pressure difference and the acceleration of the n^{th} element of the cochlear partition, as shown in Equation A.22, is the following:

$$\frac{p_{n-1}(t) - 2p_n(t) + p_{n+1}(t)}{\Delta^2} - \frac{2\rho}{H}\ddot{\xi}_n(t) = 0, \tag{A.26}$$

while boundary condition at the basal end of the cochlea, shown in Equation A.23, becomes:

$$\frac{p_2(t) - p_1(t)}{\Delta} - 2\rho\ddot{\xi}_{SR}(t) = 2\rho\ddot{\xi}_{SO}(t) \tag{A.27}$$

and at the apical end, shown in Equation A.25, becomes:

$$p_N(t) = \frac{H}{\Delta^2}\left[\frac{\Delta}{H}p_{N-1}(t) - \left(\frac{\Delta}{H} - \frac{\Delta^2}{H^2}\right)p_N(t)\right] = 2\rho\ddot{\xi}_N. \tag{A.28}$$

Equations A.26, A.27 and A.28 can be represented in matrix form (Neely, 1981):

$$\frac{H}{\rho\Delta^2}\begin{bmatrix} -\frac{\Delta}{2H} & \frac{\Delta}{2H} & & & & & 0 \\ 1 & -2 & 1 & & & & \\ 0 & 1 & -2 & 1 & & & \\ & & \ddots & \ddots & \ddots & & 0 \\ & & & 1 & -2 & 1 & 0 \\ & & & & 1 & -2 & 1 \\ 0 & & & & & \frac{\Delta}{-(\frac{\Delta}{H}+\frac{\Delta^2}{H^2})} & -\frac{\rho\Delta^2}{H} \end{bmatrix}\begin{bmatrix} p_1(t) \\ p_2(t) \\ \\ \vdots \\ \\ p_{N-1}(t) \\ p_N(t) \end{bmatrix} - \begin{bmatrix} \ddot{\xi}_{SR}(t) \\ \ddot{\xi}_2(t) \\ \\ \vdots \\ \\ \ddot{\xi}_{N-1}(t) \\ \ddot{\xi}_N(t) \end{bmatrix} = \begin{bmatrix} \ddot{\xi}_{SO}(t) \\ 0 \\ \\ \vdots \\ \\ 0 \\ 0 \end{bmatrix}. \tag{A.29}$$

This can be written as:

$$\mathbf{F}\mathbf{p}(t) - \ddot{\boldsymbol{\xi}}(t) = \mathbf{q}, \tag{A.30}$$

where:

- $\mathbf{F}$ is the finite different matrix
- $\mathbf{p}$ is the vector of pressure differences
- $\ddot{\boldsymbol{\xi}}$ is the vector of cochlear partition accelerations
- $\mathbf{q}$ is the vector of source terms

The uncoupled micromechanical elements are all gathered and combined into matrix form:

$$\dot{\mathbf{x}}(t) = \mathbf{A}_E\mathbf{x}(t) + \mathbf{B}_E\mathbf{p}(t) \tag{A.31}$$

and

$$\dot{\xi}_p(t) = \mathbf{C}_E\mathbf{x}(t), \tag{A.32}$$

where the vectors are defined as

$$\mathbf{x}^T(t) = [\mathbf{x}_1^T(t)\mathbf{x}_2^T(t)\ldots\mathbf{x}_{N-1}^T(t)\mathbf{x}_N^T(t)], \tag{A.33}$$

$$\dot{\xi}_p^T(t) = [\dot{\xi}_1(t)\dot{\xi}_2(t)\ldots\dot{\xi}_{N-1}(t)\dot{\xi}_N(t)], \tag{A.34}$$

and

$$\mathbf{p}^T(t) = [p_1(t)p_2(t)\dots p_{N-1}(t)p_N(t)], \tag{A.35}$$

and the block diagonal matrices are:

$$\mathbf{A}_E = \begin{bmatrix} \mathbf{A}_1 & 0 & \cdots & & \\ 0 & \mathbf{A}_2 & & & \\ \vdots & & \ddots & & \vdots \\ & & & \mathbf{A}_{N-1} & 0 \\ & & \cdots & 0 & \mathbf{A}_N \end{bmatrix}, \tag{A.36}$$

$$\mathbf{B}_E = \begin{bmatrix} \mathbf{B}_1 & 0 & \cdots & & \\ 0 & \mathbf{B}_2 & & & \\ \vdots & & \ddots & & \vdots \\ & & & \mathbf{B}_{N-1} & 0 \\ & & \cdots & 0 & \mathbf{B}_N \end{bmatrix}, \tag{A.37}$$

and

$$\mathbf{C}_E = \begin{bmatrix} \mathbf{C}_1 & 0 & \cdots & & \\ 0 & \mathbf{C}_2 & & & \\ \vdots & & \ddots & & \vdots \\ & & & \mathbf{C}_{N-1} & 0 \\ & & \cdots & 0 & \mathbf{C}_N \end{bmatrix}. \tag{A.38}$$

The nomenclature '**T**' means that the vector or matrix is transposed. Solving Equation A.30 for **p** gives:

$$\mathbf{p}(t) = \mathbf{F}^{-1}\ddot{\boldsymbol{\xi}}(t) + \mathbf{F}^{-1}\mathbf{q}(t) \tag{A.39}$$

and given that $\ddot{\xi}_p(t) = \mathbf{C}_E\dot{\mathbf{x}}(t)$ the following is obtained:

$$\mathbf{p}(t) = \mathbf{F}^{-1}\mathbf{C}_E\dot{\mathbf{x}}(t) + \mathbf{F}^{-1}\mathbf{q}(t) \tag{A.40}$$

The state space formulation for the fluid-coupled model with included boundary conditions can now be written as:

$$\dot{\mathbf{x}}(t) = \mathbf{A}\mathbf{x}(t) + \mathbf{B}\mathbf{u}(t) \tag{A.41}$$

where

$$\mathbf{A} = [\mathbf{I} - \mathbf{B}_E\mathbf{F}^{-1}\mathbf{C}_E]^{-1}\mathbf{A}_E, \tag{A.42}$$

$$\mathbf{B} = [\mathbf{I} - \mathbf{B}_E\mathbf{F}^{-1}\mathbf{C}_E]^{-1}\mathbf{B}_E, \tag{A.43}$$

and

$$\mathbf{u} = \mathbf{F}^{-1}\mathbf{q}. \tag{A.44}$$

As previously shown for the case of the micromechanical element, if the nonlinearity is ignored and the system matrix $\mathbf{A}$ is independent of $\mathbf{x}(t)$, then Equations A.42 and A.43 can be solved in the Laplace domain, assuming all waveforms are proportional to $e^{j\omega t}$, to give

$$\mathbf{Y}_p(s) = [\mathbf{D} + \mathbf{C}(s\mathbf{I} - \mathbf{A})^{-1}\mathbf{B}]\mathbf{U}(s). \tag{A.45}$$

Appendix B

Speeding up the state space model - alternative formulation

One of the main problems of the state space model was its simulation speed. In the original formulation by Elliott et al. (2007), running times would approach approximately 8 hours to simulate 0.1 seconds of data. The main factors involved with the speed of the algorithm are related to matrix size, inversion and sparsity, but also the inclusion of nonlinear elements. Dr. Teal, from the School of Engineering and Computer Science at the Victoria University of Wellington New Zealand (no reference available), devised a formulation that greatly increased the speed of the time domain simulations. This method relies on the fact that the formulation includes a tridiagonal matrix, i.e. $(\mathbf{F} - \mathbf{C}_E\mathbf{B}_E)$, whose inverse and product with a vector may be calculated very rapidly. The original formulation of the state space model does not include such a matrix since the state matrix is obtained by other means.

$\dot{x}$ can be eliminated by combining Equations A.31 and A.32. Combining also with A.30 the following is obtained:

$$\ddot{\xi} = \mathbf{C}_E\dot{x} = \mathbf{C}_E\mathbf{A}_E(x) + \mathbf{C}_E\mathbf{B}_E\mathbf{p} = \mathbf{F}\mathbf{p} - \mathbf{q} \tag{B.1}$$

which can be rearranged as:

$$(\mathbf{F} - \mathbf{C}_E\mathbf{B}_E)\mathbf{p} = \mathbf{C}_E\mathbf{A}_E(x) + \mathbf{q} \tag{B.2}$$

$$\mathbf{p} = (\mathbf{F} - \mathbf{C}_E\mathbf{B}_E)^{-1}\mathbf{C}_E\mathbf{A}_E(x) + (\mathbf{F} - \mathbf{C}_E\mathbf{B}_E)^{-1}\mathbf{q} \tag{B.3}$$

where $\ddot{\xi}$ is eliminated.

Substituting Equation B.3 into Equation A.31 gives the following equation:

$$\dot{\mathbf{x}} = \mathbf{A}_E(x) + \mathbf{B}_E(\mathbf{F} - \mathbf{C}_E\mathbf{B}_E)^{-1}\mathbf{C}_E\mathbf{A}_E(x) + \mathbf{B}_E(\mathbf{F} - \mathbf{C}_E\mathbf{B}_E)^{-1}\mathbf{q}, \tag{B.4}$$

which is much faster to compute than the method utilised by Ku (2008), also shown in Appendix A. Also note that the term **q** in Equation B.4 can be computed before calling the ODE45 solver in MATLAB:

$$\mathbf{q'} = \mathbf{B}_E(\mathbf{F} - \mathbf{C}_E\mathbf{B}_E)^{-1}\mathbf{q} \tag{B.5}$$

Note that the matrix $(\mathbf{F} - \mathbf{C}_E\mathbf{B}_E)$ is tridiagonal, meaning that the inverse of such a matrix multiplied by a vector can be computed very fast and efficiently using appropriate algorithms. It is important also to keep this matrix in sparse form for speed improvements.

Matrix sparsity can also greatly optimize simulation time. In fact, matrices $\mathbf{A}_E$, $\mathbf{B}_E$, $\mathbf{C}_E$ and **F** have all been modified into sparse form, therefore, increasing computational efficiency of the simulations (Pan et al., 2014). In summary, it can be said that a matrix should be made sparse depending on the amount of nonzero values it has; if these elements are far less than the zero elements then it is generally convenient to make a matrix sparse.

The computational efficiency of the time domain simulations has been much improved when compared to previous simulations performed by Ku (2008), as shown in Table B.1.

Table B.1: Parameters of the modified model for the human cochlea.

Study	**Computer**	**Simulation Time**	**Running Time**
Ku (2008), linear simulation	Desktop computer, 3.4 GHz Pentium 4 processor, 2 GB RAM	100 ms	8 hours
Present study, nonlinear simulation	Desktop computer, 3.1 GHz Core i5 processor, 4 GB RAM	100 ms	3 minutes 21 seconds

Table B.1 shows that when running similar simulations with the same absolute and relative tolerances, set at 10^{-15} and 10^{-13} respectively, and the same sampling rate (50 kHz), the present study is much more efficient being approximately 143 times faster. This has allowed to compute much longer simulations in acceptable amounts of time that can be compared to experiments that are performed over lengthy periods of time. Furthermore, very long time domain simulations were able to be computed; these were set to run for 60 seconds to test entrainment properties of the nonlinear state space formulation of the cochlear model by using a swept tone as the input signal that would interfere with SOAE. These simulations require great amounts of physical storage space; this was overcome by adopting the “matfile” function in MATLAB, which allows saving variables without having to load and/or clear them; in fact, the latter operation is both time consuming, ineffective for storing variables and very inefficient from a computational point of view.

Appendix C

Quasi-linear method

The formulation of the quasi-linear method is shown below; the impedances of a micromechanical element will have the following notation for the analyses shown:

$$Z_1(x,\omega) \equiv Z_{BM}(x,\omega) \tag{C.1}$$

$$Z_2(x,\omega) \equiv Z_{TM}(x,\omega) \tag{C.2}$$

$$Z_3(x,\omega) \equiv Z_{OHC}^{passive}(x,\omega) \tag{C.3}$$

$$Z_4(x,\omega) \equiv Z_{OHC}^{active}(x,\omega) \tag{C.4}$$

The total active impedance of an isolated micromechanical element of the cochlear partition is the following:

$$Z_{CP}^{active}(x,\omega) = \frac{g}{b}\frac{Z_{BM}(x,\omega)(Z_{TM}(x,\omega)+Z_{OHC}^{passive}(x,\omega))+Z_{TM}(x,\omega)(Z_{OHC}^{passive}(x,\omega)-\gamma Z_{OHC}^{active}(x,\omega))}{Z_{TM}(x,\omega)+Z_{OHC}^{passive}(x,\omega)} \tag{C.5}$$

where:

$$Z_{BM}(x,\omega) = \frac{K_1(x)}{j\omega} + C_1(x) + j\omega M_1(x) \tag{C.6}$$

$$Z_{TM}(x,\omega) = \frac{K_2(x)}{j\omega} + C_2(x) + j\omega M_2(x) \tag{C.7}$$

$$Z_{OHC}^{passive}(x,\omega) = \frac{K_3(x)}{j\omega} + C_3(x) \tag{C.8}$$

$$Z_{OHC}^{active}(x,\omega) = \frac{K_4(x)}{j\omega} + C_4(x) \tag{C.9}$$

The quasi-linear algorithm is applied for a number of iterations depending on how accurately the result converges to a stable value; the number of the iterations depends on the precision of the results. The first iteration takes into account a fully active cochlea. In the case shown in this example the fully active cochlea assumes that the active gain (γ) is equal to 0.745 for every micromechanical element along the whole length of the cochlea. At every iteration the value of γ of each micromechanical element will be reduced to certain values until it is stable, at which point the iterative process stops.

At the beginning of each iterative stage, the BM displacements (x_{BM}) and velocities ($\dot{x}_{BM}$) and the TM displacements (x_{TM}) and velocities ($\dot{x}_{TM}$) are calculated at each location along the cochlear partition; this is done in the frequency domain by implementing numerically the one-dimensional wave equation written in terms of the differential pressure across the cochlear partition (see Appendix D for the numerical implementation of frequency domain macromechanics). Note that this is the same wave equation used for implementing the state space method. From the frequency domain numerical implementation the following can be obtained:

$$\mathbf{x}_n = \begin{bmatrix} \dot{x}_{BM}(\omega) \\ x_{BM}(\omega) \\ \dot{x}_{TM}(\omega) \\ x_{TM}(\omega) \end{bmatrix}_n \tag{C.10}$$

From (x_{BM}), ($\dot{x}_{BM}$), (x_{TM}) and ($\dot{x}_{TM}$) it is possible to obtain the difference in displacements and velocities between the BM and the TM:

$$\Delta_{x_{cp}} = x_{TM} - x_{BM} \tag{C.11}$$

$$\Delta_{\dot{x_{cp}}} = \dot{x}_{TM} - \dot{x}_{BM} \tag{C.12}$$

$\mathbf{x}_n$, $\Delta_{x_{cp}}$ and $\Delta_{\dot{x}_{cp}}$ are converted to the time domain where a time vector of Nt samples per period is used to reconstruct the input frequency in the time domain:

$$I_{\mathbf{X}_n}(x,t) = 2 * \Re\{|\mathbf{X}_n| e^{j(\omega t + \phi_{\mathbf{X}_n})}\} \tag{C.13}$$

$$I(x,t)_{\Delta_{x_{cp}}} = 2 * \Re\{|\Delta_{x_{cp}}|e^{j(\omega t+\phi_{\Delta_{x_{cp}}})}\} \tag{C.14}$$

$$I(x,t)_{\Delta_{\dot{x}_{cp}}} = 2 * \Re\{|\Delta_{\dot{x}_{cp}}|e^{j(\omega t+\phi_{\Delta_{\dot{x}_{cp}}})}\} \tag{C.15}$$

$I(x,t)_{\Delta_{x_{cp}}}$ and $I(x,t)_{\Delta_{\dot{x}_{cp}}}$ are passed through the Boltzmann function in order to obtain:

$$\overbrace{I(x,t)_{\Delta_{x_{cp}}}} = Boltz\{I(x,t)_{\Delta_{x_{cp}}}\} \tag{C.16}$$

$$\overbrace{I(x,t)_{\Delta_{\dot{x}_{cp}}}} = Boltz\{I(x,t)_{\Delta_{\dot{x}_{cp}}}\} \tag{C.17}$$

and the ratios between $\overbrace{I(x,t)_{\Delta_{x_{cp}}}}$ and $I(x,t)_{\Delta_{\dot{x}_{cp}}}$, $\overbrace{I(x,t)_{\Delta_{\dot{x}_{cp}}}}$ and $I(x,t)_{\Delta_{\dot{x}_{cp}}}$ are used to obtain the scaling factor κ_x and $\kappa_{\dot{x}}$ to multiply to the displacements and the velocities accordingly in the vector $\mathbf{X}_n$:

$$\kappa_x = \frac{\overbrace{I(x,t)_{\Delta_{x_{cp}}}}}{I(x,t)_{\Delta_{\dot{x}_{cp}}}} \tag{C.18}$$

$$\kappa_{\dot{x}} = \frac{\overbrace{I(x,t)_{\Delta_{\dot{x}_{cp}}}}}{I(x,t)_{\Delta_{\dot{x}_{cp}}}} \tag{C.19}$$

$$\mathbf{x}_{n-scaled-x} = \kappa_x \cdot I_{\mathbf{X}_{n-x}}(x,t) \tag{C.20}$$

$$\mathbf{x}_{n-scaled-\dot{x}} = \kappa_{\dot{x}} \cdot I_{\mathbf{X}_{n-\dot{x}}}(x,t) \tag{C.21}$$

The new values of BM and TM motion $\mathbf{X}_{n-scaled}$ can now be reconverted to the frequency domain and be used to calculate the quasi-linear OHC pressure p_{OHC}.

$$\mathbf{X}_n = \frac{1}{T}\int \mathbf{X}_{n-scaled}dt \tag{C.22}$$

At this point a new impedance of the cochlear partition is obtained from which it is possible to obtain also the vector of γ associated with each micromechanical element:

$$Z_{OHC}^{active}|_{Nt=n} = -\frac{p_{OHC}^{active}}{i\omega\Delta_{x_{cp}}} \tag{C.23}$$

$$\gamma = \Re\left\{ \frac{Z_{OHC}^{active}|_{Nt=n}}{Z_{OHC}^{active}|_{\gamma=0.745}} \right\} \tag{C.24}$$

The new γ obtained can be substituted into Equation C.5 to find the new set of displacements and velocities of the BM and the TM (i.e. $\mathbf{x}_n$); at this point a new iteration starts. Iterations stop when the BM and TM velocities and displacements vary less than 0.1 or when the simulation exceeds 50 iterations.

Note that, initially, the time vector is 24 samples long, as recommended by Kanis and de Boer (1993); however, Young (2011) proposes an alternative method using variable sample length (Nt) in order to reduce numerical integration errors. This is valid mainly for high stimulus levels. Therefore, the value of Nt can increase in a single iteration and will stop increasing only when the estimated pressure, p_{OHC}, is reasonably stable for a given sample rate Nt.

Appendix D

The effect of BM mass on the form of the coupled response

The mass per unit area of the BM used in the model described in Chapter 4 was chosen to be the same as that in the Neely and Kim (1986) model, i.e. $3 \cdot 10^{-2} kgm^{-2}$. This is rather low when compared with the value calculated if fluid loading is accounted for (Neely, 1985; Elliott et al., 2011b; Ni et al., 2011), and so an investigation was undertaken of the effect of the assumed BM on the form of the coupled response.

Simulations were performed using the set of human parameters shown in Table 4.1, but with different assumed BM masses, where all the stiffness and damping were also scaled to ensure that the natural frequencies and damping ratios of the micromechanical model were the same. Rapson et al. (2014) has also demonstrated numerically how changes in mass influence the tuning curves and a similar approach has been taken here, where the results are shown in Figures D.1 and D.2, which show the response of the BM at 1.6 kHz and 6.4 kHz respectively. The curves compare the BM's response when the mass is modified by a factor of 0.5, 1 or 10 to the value shown in Table 4.1. It can be seen that the mass significantly influences the coupled response of the BM in both amplitude and phase. For a given size of fluid chamber, higher masses generate lower sensitivity (sharpness) and a reduced value of the slope of the curve in the apical region. This effect can be explained by picturing the mass as the inertial term associated with the motion of the BM that carries the travelling wave. Incrementing the mass therefore increases the distance the travelling wave travels along the cochlea, and this can be associated with the lower slope of the apical part of the BM response.

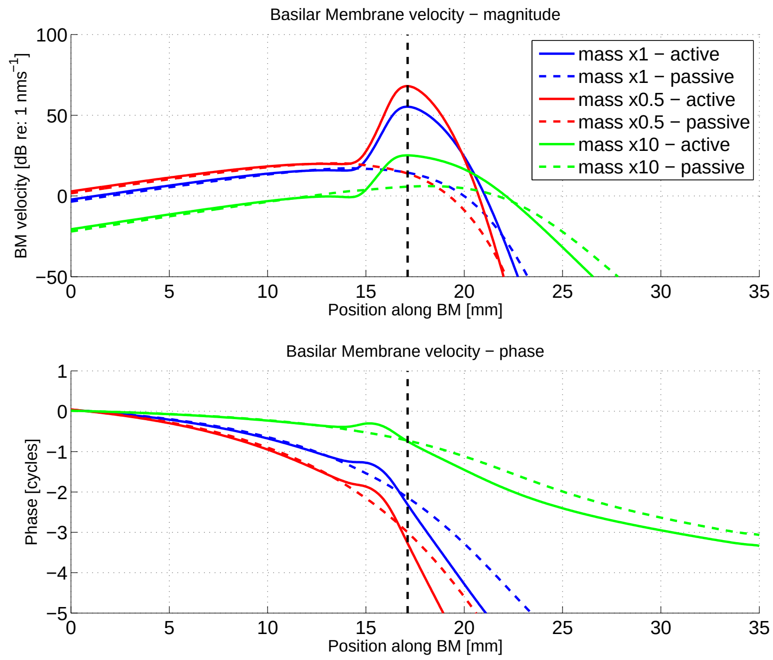

Figure D.1: Frequency response to a 1.6 kHz tone using different fluid inertial loading.

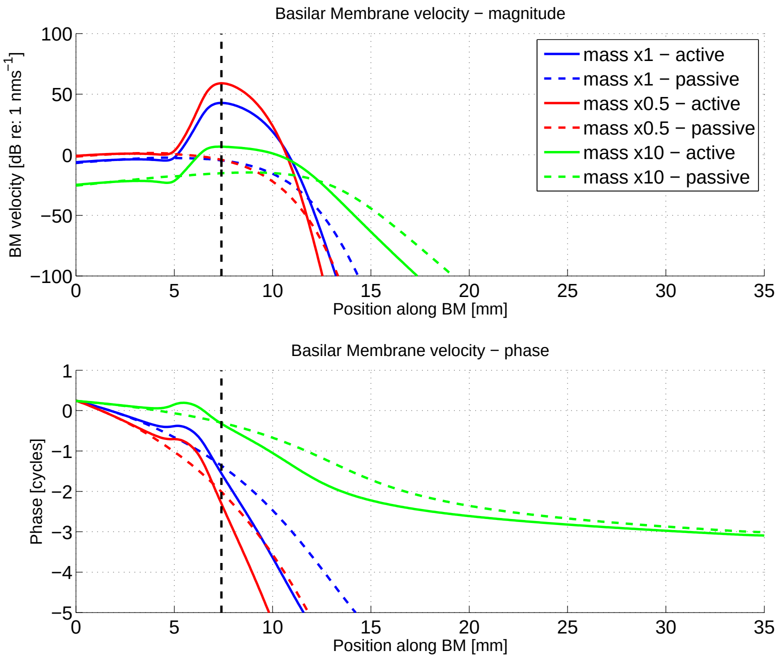

Figure D.2: Frequency response to a 6.4 kHz tone using different fluid inertial loading.

The velocity of the travelling wave can be obtained from its wavenumber, which is given by:

$$k(x,\omega) = \sqrt{\frac{-2i\omega\rho}{H} Y_{BM}(x,\omega)}, \tag{D.1}$$

where $Y_{BM}(x,\omega)$ is the BM admittance, ω is the stimulation frequency (which is kept constant for the cases shown below), ρ is the cochlear fluid density and H is the height of the cochlea chamber. The wave speed is therefore obtained from:

$$c = \frac{\omega}{\Re\{k\}}. \tag{D.2}$$

Figures D.3 and D.4 show plots of the real and imaginary parts of the wavenumber $k(x,\omega)$ against position for the linear model with different assumed values of BM mass at 1.6 kHz and 6.4 kHz, while Figures D.5 and D.6 show the corresponding speed and wavelength of the travelling wave.

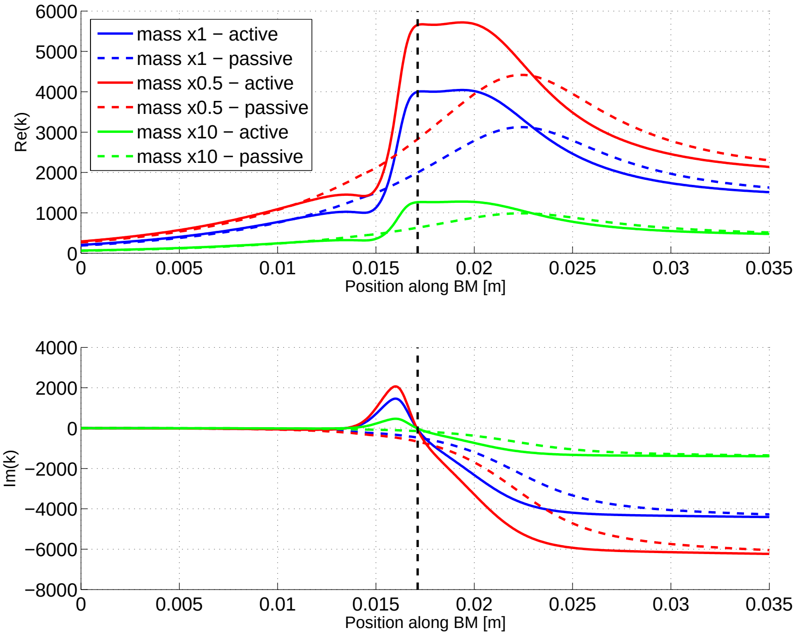

Figure D.3: Real and imaginary parts of the wavenumber k at 1.6 kHz.

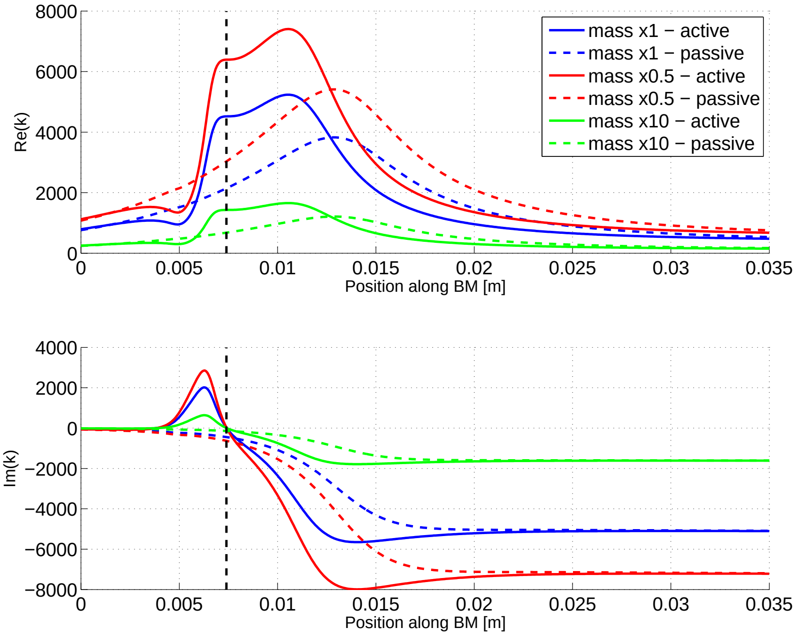

Figure D.4: Real and imaginary parts of the wavenumber k at 6.4 kHz.

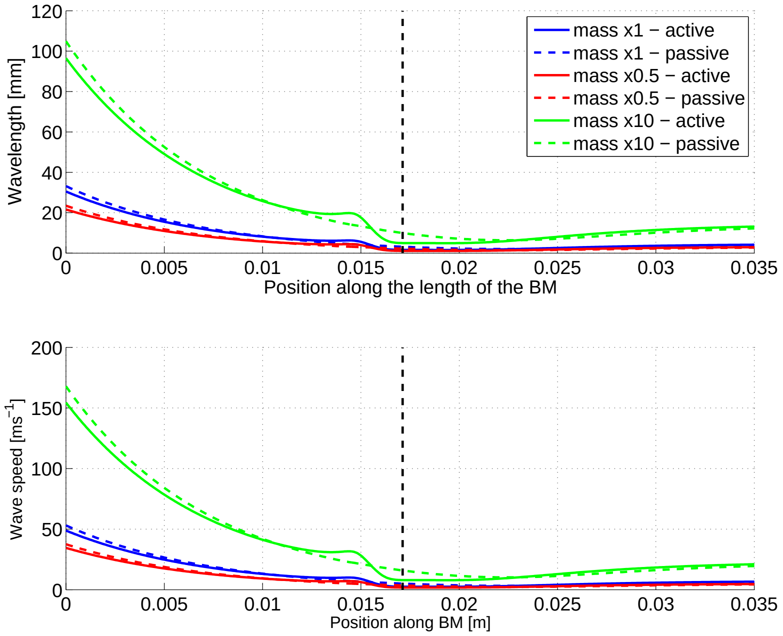

Figure D.5: Properties of the travelling wave at 1.6 kHz. The top plot shows the variation of the wavelength along the length of the BM; the bottom plot shows the wavespeed along the BM.

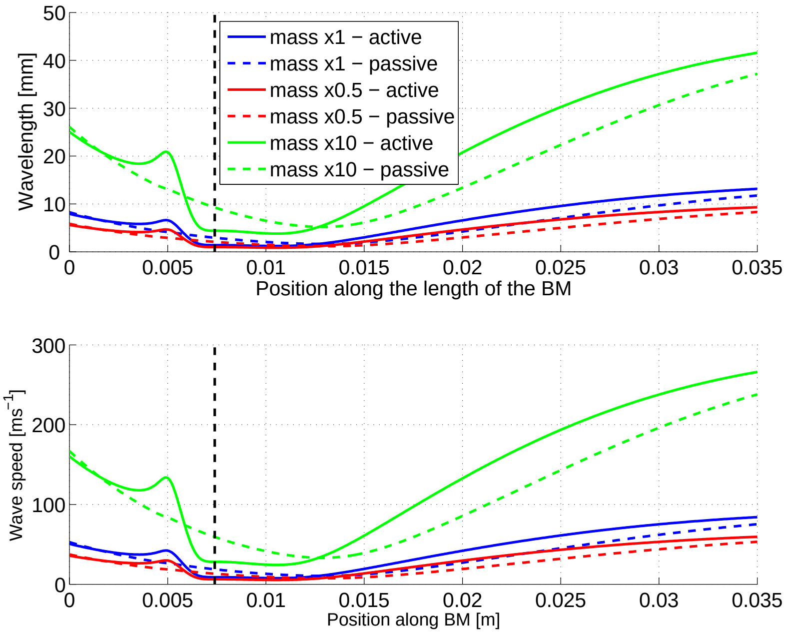

Figure D.6: Properties of the travelling wave at 6.4 kHz. The top plot shows the variation of the wavelength along the length of the BM; the bottom plot shows the wavespeed along the BM.

The wavenumbers plotted as a function of position give valuable information regarding the characteristics of the travelling wave. Before the travelling wave reaches the location of the characteristic frequency, the wavenumber is predominantly real, and therefore carrying energy with very little loss. The wave builds up in amplitude at the location of the CF and stimulates this location most, but when the travelling wave passes this position, the imaginary part of the wavenumber becomes dominant, meaning that the wave decays very fast as the wave becomes evanescent. It can also be seen in Figures D.5 and D.6 that the wave speed decreases slowly until it reaches the place of the CF and then decays rapidly in proximity of this location. The trend of the wave speed varies greatly with different frequencies as the system is dispersive. Also, the change in mass affects the wave speed as high mass allows for greater wave speeds prior to the CF location. Similar considerations can be given to the wavelength of the travelling wave which at first decreases, but then peaks in proximity of the location of the CF allowing that position of the BM to respond with greater selectivity with respect to nearby locations.

The decay of the wave when it is evanescent, can be calculated as the inverse of the imaginary part of the wavenumber. It may also be estimated from the following equation:

$$d = \sqrt{\frac{hm_{BM}}{2\rho}}, \tag{D.3}$$

where m_{BM} is the BM mass for each element, which is constant along the length of the cochlea, ρ is the density of the cochlear fluids and h is defined (Elliott et al., 2011a) as:

$$h = \frac{\pi^2 WH}{8B} \approx H \approx 0.001m, \tag{D.4}$$

where B is the width of the flexible section of the BM and W is the width of the BM, which in this case is assumed to be equal to B. The decay length d is obviously a function of m_{BM}. Table D.1 indicates how the decay length varies when the mass is varied by a factor of 0.5, 1 or 10.

Table D.1: Change in decay length using various BM masses.

$\mathbf{m}_{BM}$ **x factor**	**Decay length [mm] (active)**	**Decay length [mm] (passive)**
m_{BM} x 0.5	0.087	0.087
m_{BM} x 1	0.12	0.12
m_{BM} x 10	0.39	0.39

Figures D.7 and D.8 show the decay against position for the cases of a 1.6 kHz stimulus and a 6.4 kHz stimulus, respectively, where it can be seen that at the most apical end of the BM (35 mm) the decay is in agreement with the values shown in Table D.1. This trend is in accord with Rapson et al. (2014) that shows that if the cochlea with high BM mass is stimulated by an impulse, then the travelling wave covers a large proportion of the partition for each instant in time, although the response decays by three orders of magnitude over a period of 20 ms. On the contrary, in the low mass scenario, narrow bands of the partition are stimulated at subsequent instances in time from base to apex, but the order of magnitude of the decay remains more or less constant over a period of time of 20 ms.

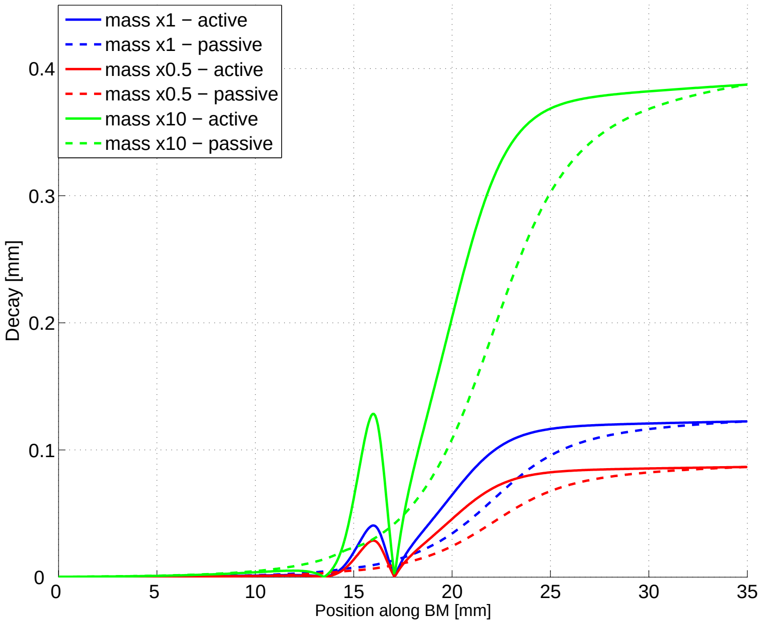

Figure D.7: Wave decay plotted against position along the BM at 1.6 kHz.

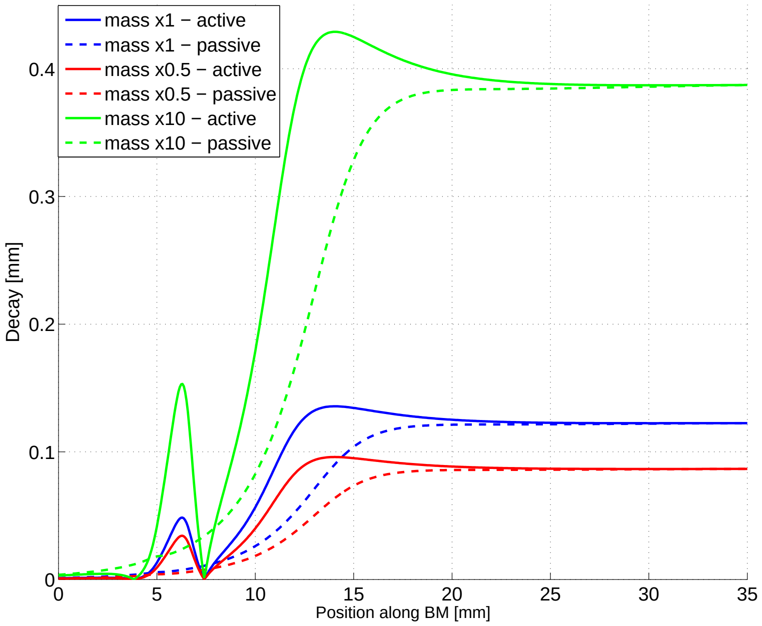

Figure D.8: Wave decay plotted against position along the BM at 6.4 kHz.

By changing the mass of the system there is also a considerable amount of variation in the gain of the system, in particular where the travelling wave peaks (Figures D.1 and D.2). Higher values of mass reduce the gain while lower values of mass tend to increase the gain. The typical gain of the CA is approximately 45 dB at the base to around 20 dB at the apex; with regards to the simulations and results shown above, this is more likely when the mass is multiplied by a factor of 1.

Another aspect to consider in the results is the slope of the wave in the frequency domain after it has peaked at its characteristic place (Figures D.1 and D.2). The blue curve of the plot of the frequency response of the model shows the best slope conditions. In fact the loss of dB per octave can be calculated as follows:

$$slope = 20\log(e^{\frac{-l\cdot\ln(2)}{d}}) \approx 6\frac{l}{d}, \tag{D.5}$$

where d is the decay length previously calculated for different BM masses and l is the cochlear length scale which, as previously mentioned, for the case of the human cochlea is approximately 7 mm. The results shown in Table D.2 demonstrate how the slope decreases for greater values of added mass. Again, the most sensible and realistic value obtained for the slope value is given for values of BM mass multiplied by a factor of 1.

Table D.2: Change in decay length and slope using various BM masses.

$\mathbf{m}_{BM}$ **x factor**	**Decay length [mm]**	**Slope [dB/octave]**
m_{BM} x0.5	0.087	483
m_{BM} x1	0.12	350
m_{BM} x10	0.39	108

In conclusion, it is found that the decay rate at high frequencies and the amplification obtained with the assumed value of BM mass are reasonably representative of those measured in the cochlea (Robles et al., 1986). This is despite its value being somewhat smaller than that which would seem reasonable by taking fluid loading into account. Further work is clearly needed to address this apparent paradox, which is beyond the scope of the present thesis.

Appendix E

The ear canal and middle ear models

The state space model of the cochlea takes into account a boundary condition at its basal end that links the first element of the BM to the stapes of the middle ear. In fact the input to the state space model is the stapes velocity. It is desirable to obtain a transfer function between the external sound pressure level and the stapes velocity. For this reason, models of both the ear canal and the middle ear are necessary that can mimic the behaviour of these sections of the auditory system, i.e. match the low impedance of the air entering the ear canal to the high impedance of the cochlear fluids. It is possible to construct these models by means of two port networks and connect them in cascade so that the input is a sound pressure level and the output is a stapes velocity. The following sections will give details regarding these two models in order to obtain an overall ear canal and middle ear transfer function. The model is based on previous work by Ku (2008) where more details regarding the model can be found.

The two-port network

In general a two-port network may be represented as shown in Figure E.1.

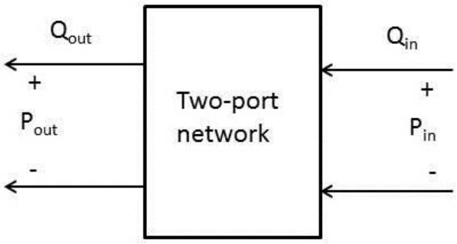

Figure E.1: General representation of a two-port network.

It is possible to calculate the input impedance of the network by loading the output terminal with loading impedance and vice versa. Given the general transmission matrix for two-port networks as follows:

$$\begin{Bmatrix} p_{out} \\ Q_{out} \end{Bmatrix} = \begin{bmatrix} T_{11} & T_{12} \\ T_{21} & T_{22} \end{bmatrix} \begin{bmatrix} p_{in} \\ Q_{in} \end{bmatrix} \tag{E.1}$$

By dividing P_{out} by Q_{out} we can obtain the output impedance (Z_{out}) in relation to the loading input impedance (Z_{in}). The obtained expression is as follows:

$$Z_{out} = \frac{T_{11}Z_{in} + T_{12}}{T_{21}Z_{in} + T_{22}} \tag{E.2}$$

Given that:

$$Z_{in} = \frac{P_{in}}{Q_{in}} \tag{E.3}$$

Same considerations may be made to obtain the expression for the input impedance (Z_{in}) although in this case it is necessary to obtain the inverse of the transmission matrix:

$$\begin{Bmatrix} p_{in} \\ Q_{in} \end{Bmatrix} = \begin{bmatrix} T_{11} & T_{12} \\ T_{21} & T_{22} \end{bmatrix}^{-1} \begin{bmatrix} p_{out} \\ Q_{out} \end{bmatrix} \tag{E.4}$$

Where:

$$\begin{bmatrix} T_{11} & T_{12} \\ T_{21} & T_{22} \end{bmatrix}^{-1} = \frac{\begin{bmatrix} T_{22} & T_{12} \\ T_{21} & T_{11} \end{bmatrix}}{(T_{11}T_{22} - T_{21}T_{12})} \tag{E.5}$$

Hence, if the determinant is equal to 1, i.e.:

$$(T_{11}T_{22} - T_{21}T_{12}) = 1 \tag{E.6}$$

Then the transmission matrix is reciprocal, therefore allowing obtaining an expression for the input impedance (Zin):

$$Z_{in} = \frac{T_{22}Z_{out} + T_{12}}{T_{21}Z_{iout} + T_{11}} \tag{E.7}$$

The two port network ear canal model

A representation of how the ear canal is modelled is shown in Figure E.2 followed by Table E.1, that shows the dimensions assigned to the model.

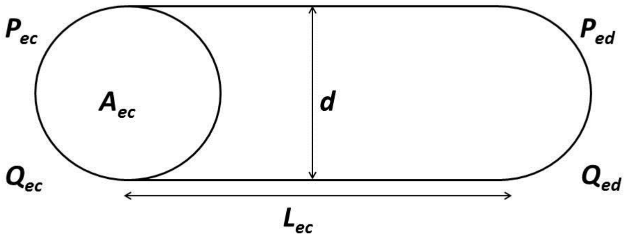

Figure E.2: Dimensions of the modelled ear canal.

Table E.1: Ear canal model parameters

Parameter	**Dimensions**
A_{ec}	$3.85 \cdot 10^{-5}[m^2]$
d	$0.007[m]$
L_{ec}	$0.02[m]$

The two port network used for the ear canal is shown in Figure E.3.

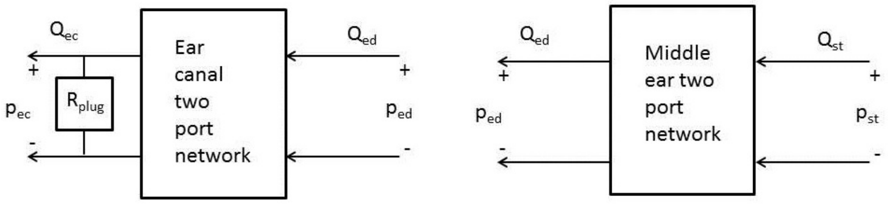

Figure E.3: Two-port network of the ear canal.

The matrix that represents the ear canal two port network contains acoustic variables that are a function of frequency and can be written down as the following:

$$\begin{Bmatrix} p_{ec} \\ Q_{ec} \end{Bmatrix} = \begin{bmatrix} 1 & 0 \\ \frac{1}{R_{plug}} & 1 \end{bmatrix} \begin{bmatrix} T_{11} & T_{12} \\ T_{21} & T_{22} \end{bmatrix} \begin{bmatrix} p_{ed} \\ Q_{ed} \end{bmatrix} \tag{E.8}$$

Equation E.8 can be used to obtain the ear canal transfer function between the ear canal acoustic variables and the ear drum acoustic variables.

The transfer matrix also contains the term R_{plug} which takes account of the loss due to the foam on the ear plug inserted in the ear canal and used for measuring OAEs.

The two port network middle ear model

The set of parameters used for modelling the middle ear are shown in Table E.2 and are taken from Kringlebotn (1988).

The middle ear two port network is shown in Figure E.4.

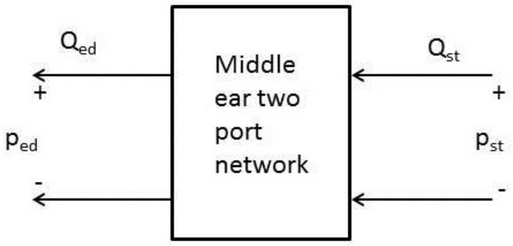

Figure E.4: Middle ear two-port network.

The matrix to represent the middle ear two port network contains acoustic variables that are a function of frequency and can be written down as the following:

Table E.2: Middle ear model parameters

Mechanical element	**Inertia** $[N \cdot s^2/m^5]$	**Compliance** $[m^5/N]$	**Resistance** $[N \cdot s/m^5]$	**Expression for impedance**
Antrum and mastoid cells	$1 \cdot 10^2 (L_a)$	$3.9 \cdot 10^{-11} (C_a)$	$6 \cdot 10^6 (R_a)$	$Z_a = R_a + i\omega L_a + 1/i\omega C_a$
Tympanic cavity	0	$4 \cdot 10^{-12} (C_t)$	0	$Z_t = 1/i\omega C_t$
Eardrum	$7.5 \cdot 10^2 (L_d)$	0	0	$Z_d = i\omega L_d$
Suspensiopn of the eardrum	$6.6 \cdot 10^3 (L_s)$	$3 \cdot 10^{-12} (C_s)$	$2 \cdot 10^6 (R_s)$	$Z_s = R_s + i\omega L_s + 1/i\omega C_s$
Rim of the eardrum	0	$1.3 \cdot 10^{-11} (C_r)$	$1.2 \cdot 10^7 (R_r)$	$Z_r = R_r + 1/i\omega C_r$
Coupling between malleus & incus	0	$3.8 \cdot 10^{-12} (C_m)$	$1.2 \cdot 10^7 (R_m)$	$Z_m = R_m + 1/i\omega C_m$
Ossicles (malleus & incus)	$2.2 \cdot 10^3 (L_o)$	$\inf (C_o)$	$2 \cdot 10^7 (R_o)$	$Z_o = R_o + i\omega L_o + 1/i\omega C_o$
Coupling between incus & stapes	0	$5.6 \cdot 10^{-12} (C_i)$	$6 \cdot 10^8 (R_i)$	$Z_i = R_i + 1/i\omega C_i$
Stapes, stapedius tendon & oval window	$4.6 \cdot 10^3 (L_{st})$	$5.6 \cdot 10^{-12} (C_{st})$	0	$Z_{st} = i\omega L_{st} + 1/i\omega C_{st}$
		Transformer ratios		
	$6 \cdot 10^{-5} (k_1) [m^2]$	$1.3 (k_2) [unitless]$	$3.125 \cdot 10^5 (k_3) [m^{-2}]$	

$$\begin{Bmatrix} p_{ed} \\ Q_{ed} \end{Bmatrix} = \begin{bmatrix} T_{edst11} & T_{edst12} \\ T_{edst21} & T_{edst22} \end{bmatrix} \begin{bmatrix} p_{st} \\ Q_{st} \end{bmatrix} \tag{E.9}$$

Equation E.9 can be used to obtain the middle ear transfer function between the ear drum acoustic variables and the stapes acoustic variables.

The various parameters in Table E.2 are used to obtain the transformer ratios of the middle ear transfer matrix. A detailed derivation is found in Ku (2008).

The ear canal and middle ear transfer function

The two two-port models in cascade allow obtaining a relationship between the external acoustic pressure and the stapes volume velocity. A representation of the overall network is shown in Figure E.5.

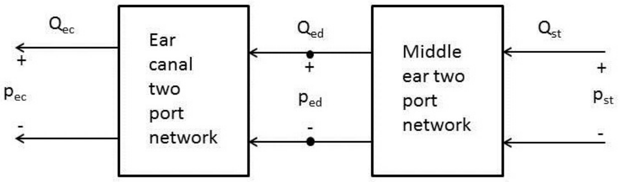

Figure E.5: Two-port network of the ear canal and the middle ear in cascade.

Cascading the networks will give the following transfer matrix.

$$\begin{Bmatrix} p_{ec} \\ Q_{ec} \end{Bmatrix} = \begin{bmatrix} T_{ecst11} & T_{ecst12} \\ T_{ecst21} & T_{ecst22} \end{bmatrix} \begin{bmatrix} p_{st} \\ Q_{st} \end{bmatrix} \tag{E.10}$$

By obtaining the latter transfer matrix a relationship between the input acoustic pressure and volume velocity at the stapes with the output acoustic pressure and volume velocity at the ear canal is obtained. The forward transfer function in the frequency domain is plotted in Figure E.6 while the reverse transfer function is plotted in Figure E.7.

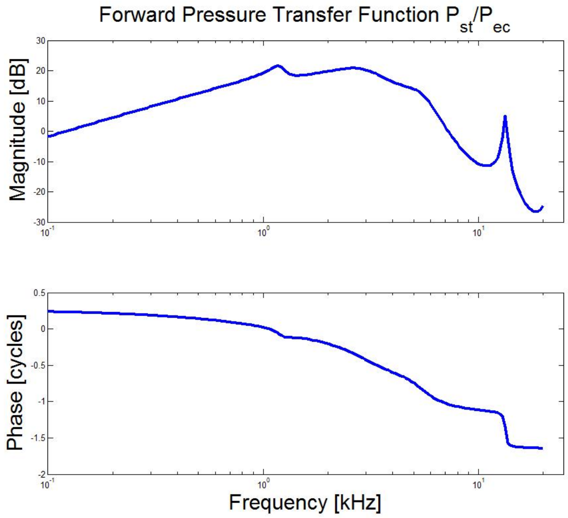

Figure E.6: Forward pressure transfer function between the pressure at the stapes and the pressure at the ear canal.

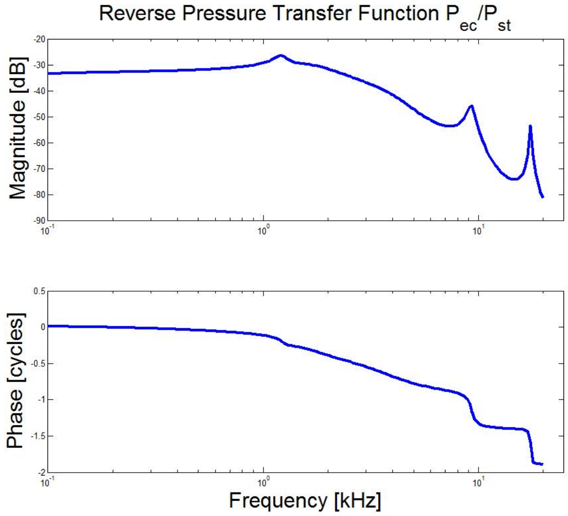

Figure E.7: Reverese pressure transfer function between the pressure at the stapes and the pressure at the ear canal.

Appendix F

Further results from bias tones at different frequencies

A comparison is made between cochlear models using either a tanh function or a 1^{st} order Boltzmann function. The following figures show the results when the input is a low frequency bias tone that changes in frequency for each simulation between 20 Hz and 90 Hz. The velocity in the contour maps shown are plotted with a dB scale with $v_{ref} = 1$ nm, for both positive and negative phases. All the results have been plotted so that the bias tones of different frequencies go through two cycles. Also, the velocity in the 2D plots have had to be scaled differently in each case for clarity; however, each row of plots representing the same locations along the length of the cochlea are scaled equally.

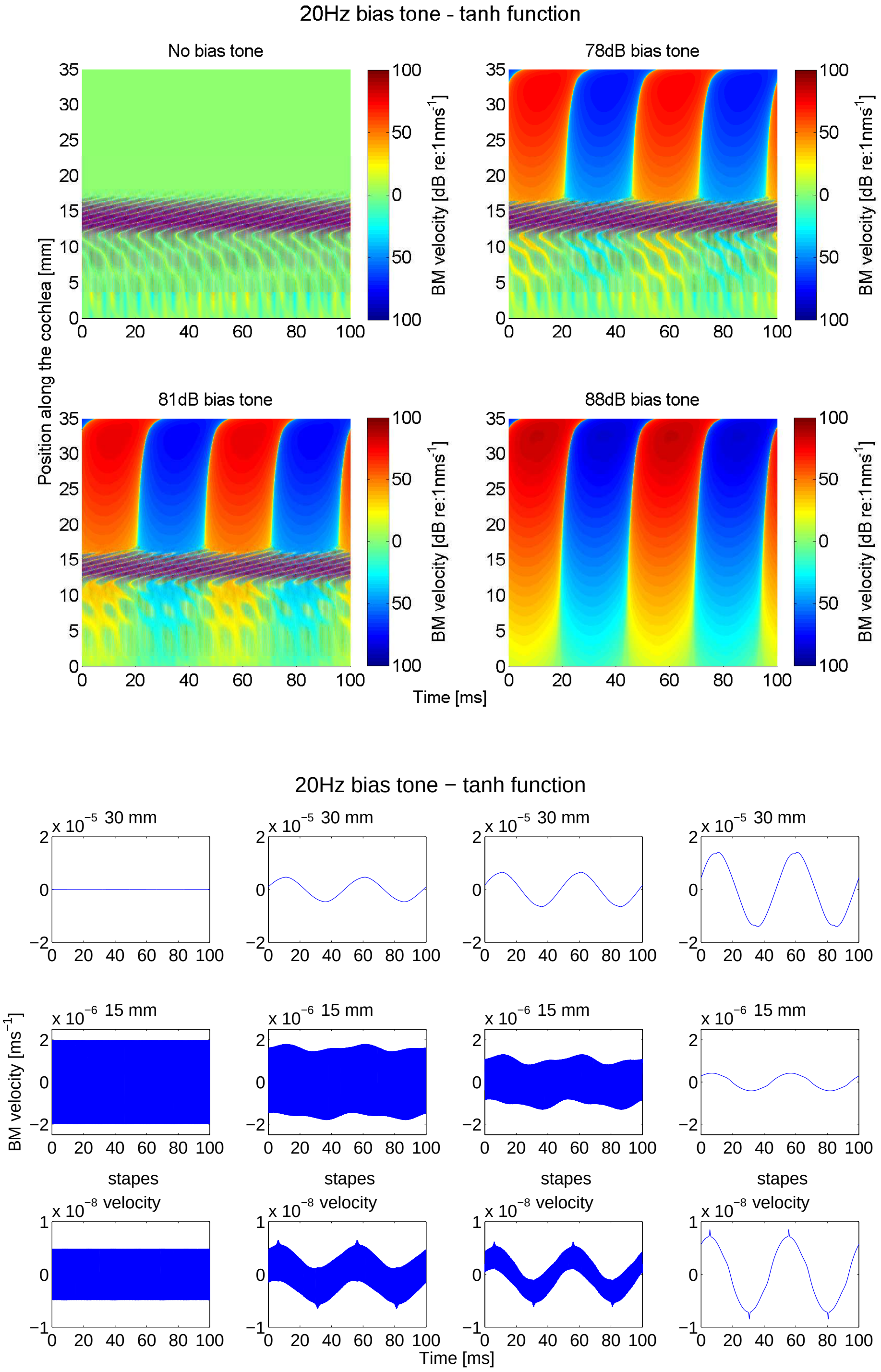

Figure F.1: The results from the time domain simulations in terms of the level of the BM velocity when the model containing tanh nonlinearities is stimulated by a 20 Hz biasing tone of various levels. The contour plots show the response at different positions and times: top left panel, no bias tone present, top right panel, 78 dB, bottom left panel, 81 dB and bottom right panel, 88 dB. The 2D plots show the BM velocity at different times and specific locations: far left panel, no bias tone present, centre-left panel, 78 dB, centre-right panel, 81 dB and far right panel, 88 dB. The plots show how the SOAE is affected by the bias tone at different levels: at first, the emission is unaffected, but higher levels of biasing tone modulate its characteristics until it is suppressed.

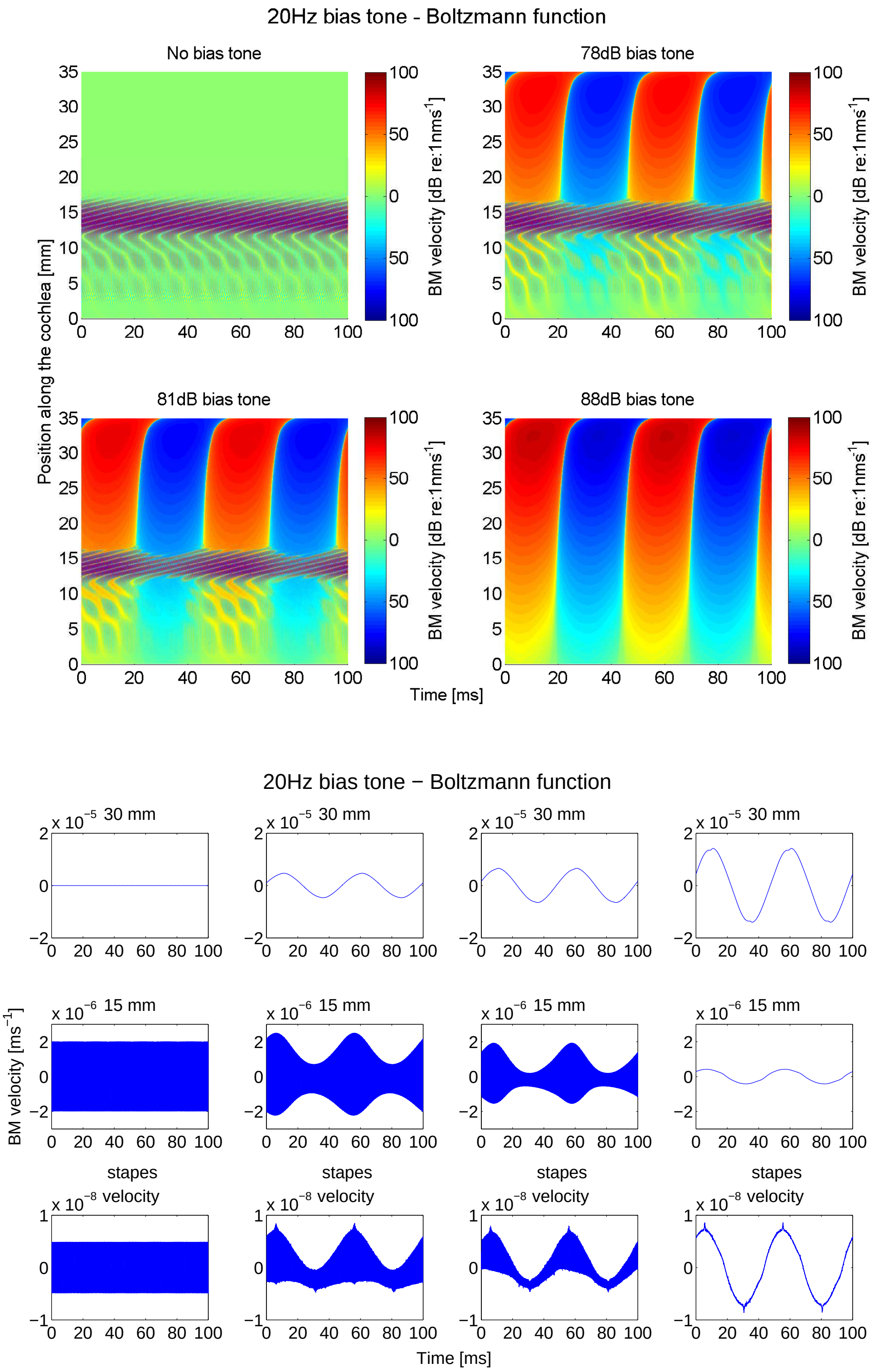

Figure F.2: The results from the time domain simulations in terms of the level of the BM velocity when the model containing Boltzmann nonlinearities is stimulated by a 20 Hz biasing tone of various levels. The contour plots show the response at different positions and times: top left panel, no bias tone present, top right panel, 78 dB, bottom left panel, 81 dB and bottom right panel, 88 dB. The 2D plots show the BM velocity at different times and specific locations: far left panel, no bias tone present, centre-left panel, 78 dB, centre-right panel, 81 dB and far right panel, 88 dB. The plots show how the SOAE is affected by the bias tone at different levels: at first, the emission is unaffected, but higher levels of biasing tone modulate its characteristics until it is suppressed.

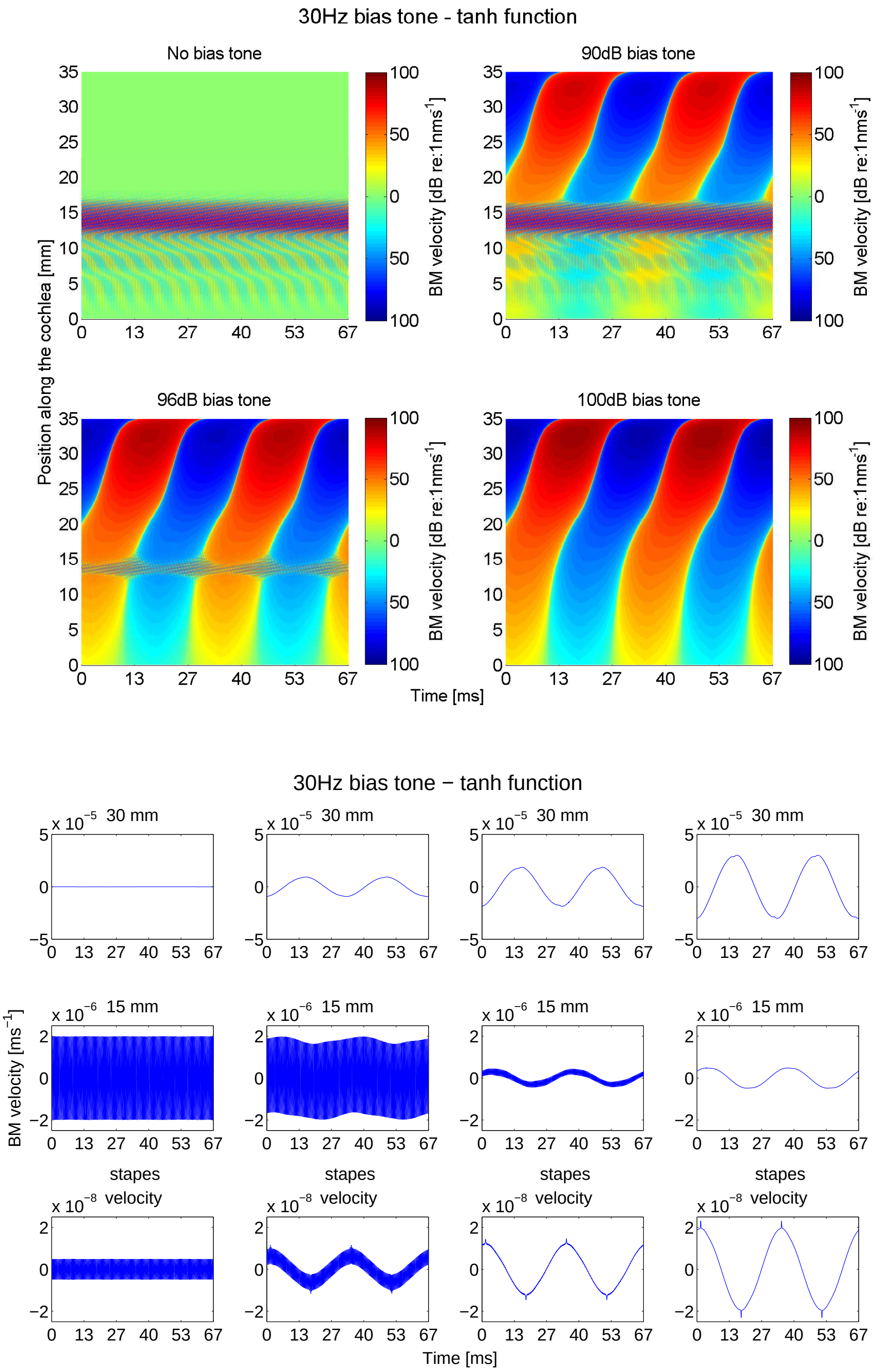

Figure F.3: The results from the time domain simulations in terms of the level of the BM velocity when the model containing tanh nonlinearities is stimulated by a 30 Hz biasing tone of various levels. The contour plots show the response at different positions and times: top left panel, no bias tone present, top right panel, 90 dB, bottom left panel, 96 dB and bottom right panel, 100 dB. The 2D plots show the BM velocity at different times and specific locations: far left panel, no bias tone present, centre-left panel, 90 dB, centre-right panel, 96 dB and far right panel, 100 dB. The plots show how the SOAE is affected by the bias tone at different levels: at first, the emission is unaffected, but higher levels of biasing tone modulate its characteristics until it is suppressed.

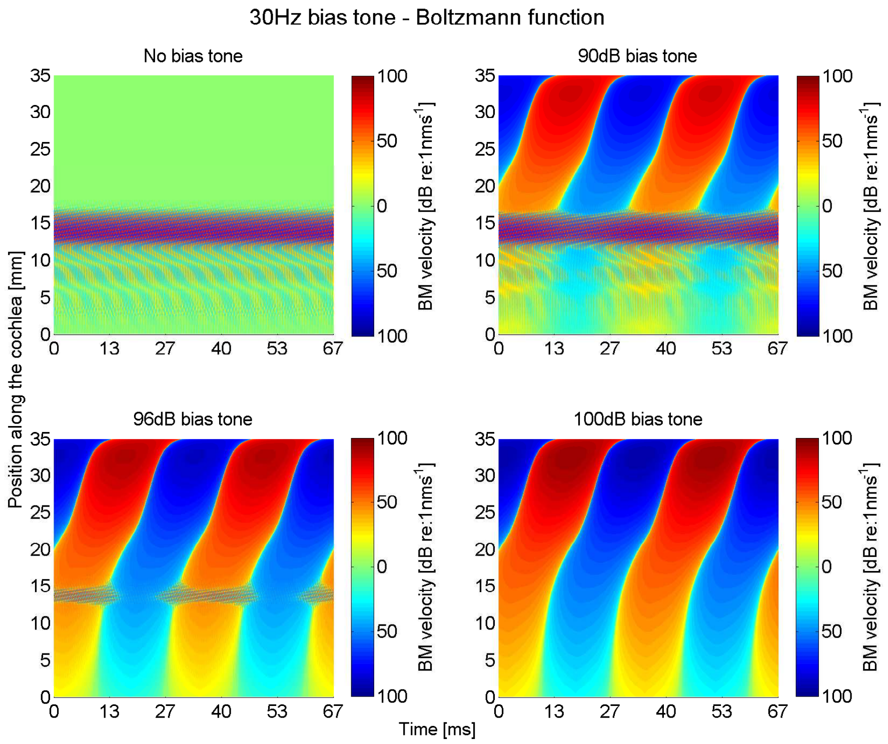

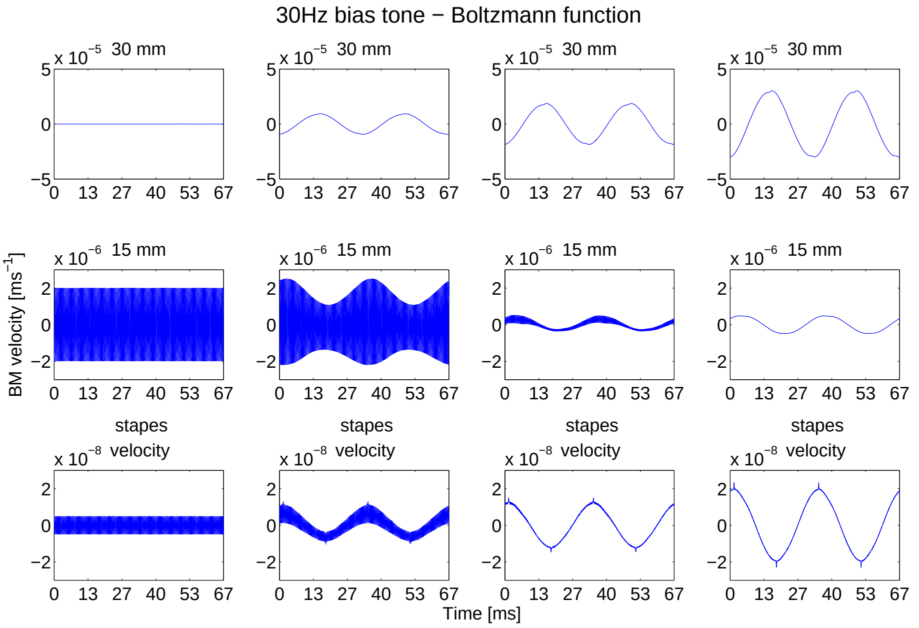

Figure F.4: The results from the time domain simulations in terms of the level of the BM velocity when the model containing Boltzmann nonlinearities is stimulated by a 30 Hz biasing tone of various levels. The contour plots show the response at different positions and times: top left panel, no bias tone present, top right panel, 90 dB, bottom left panel, 96 dB and bottom right panel, 100 dB. The 2D plots show the BM velocity at different times and specific locations: far left panel, no bias tone present, centre-left panel, 90 dB, centre-right panel, 96 dB and far right panel, 100 dB. The plots show how the SOAE is affected by the bias tone at different levels: at first, the emission is unaffected, but higher levels of biasing tone modulate its characteristics until it is suppressed.

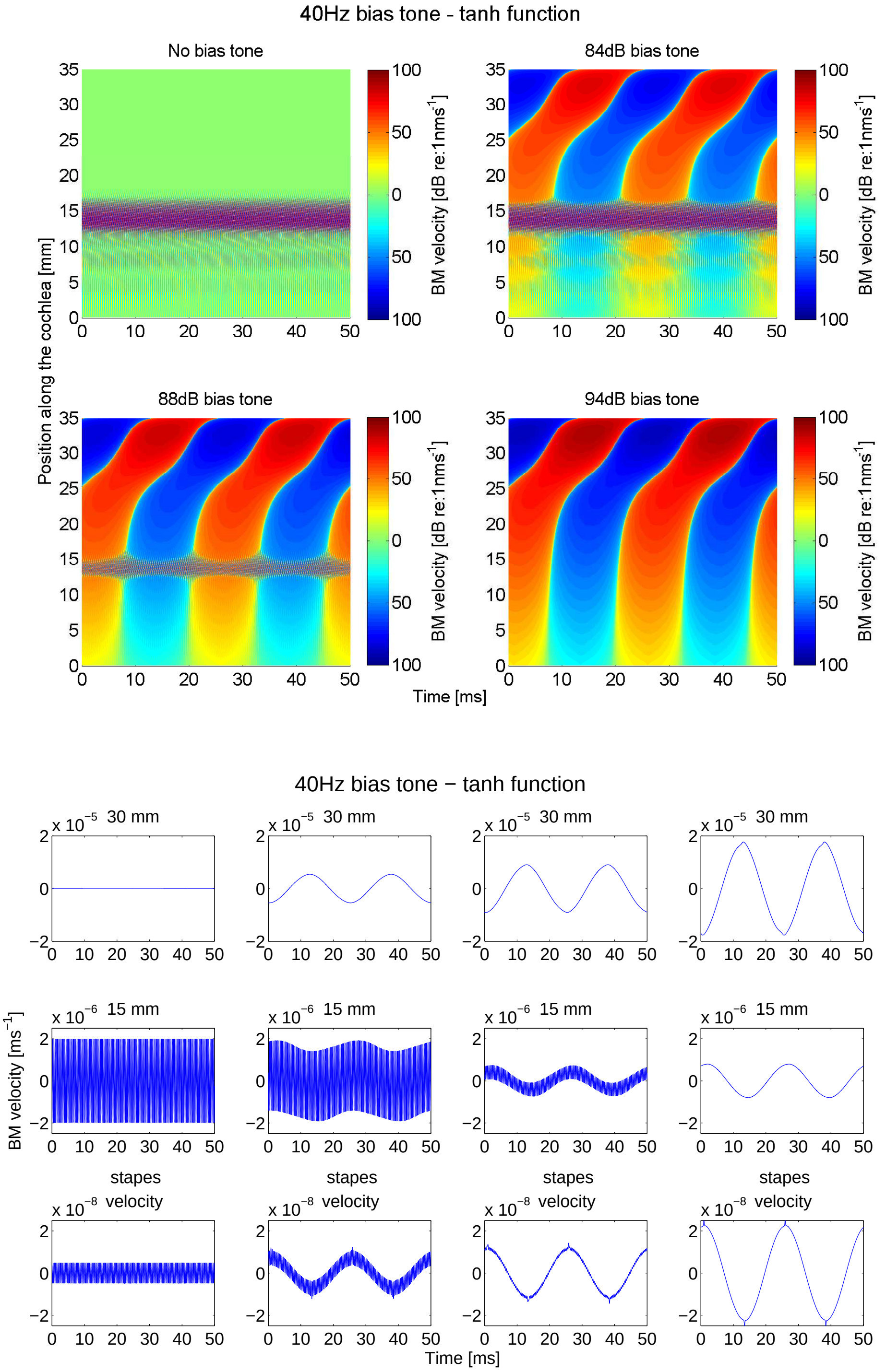

Figure F.5: The results from the time domain simulations in terms of the level of the BM velocity when the model containing tanh nonlinearities is stimulated by a 40 Hz biasing tone of various levels. The contour plots show the response at different positions and times: top left panel, no bias tone present, top right panel, 84 dB, bottom left panel, 88 dB and bottom right panel, 94 dB. The 2D plots show the BM velocity at different times and specific locations: far left panel, no bias tone present, centre-left panel, 84 dB, centre-right panel, 88 dB and far right panel, 94 dB. The plots show how the SOAE is affected by the bias tone at different levels: at first, the emission is unaffected, but higher levels of biasing tone modulate its characteristics until it is suppressed.

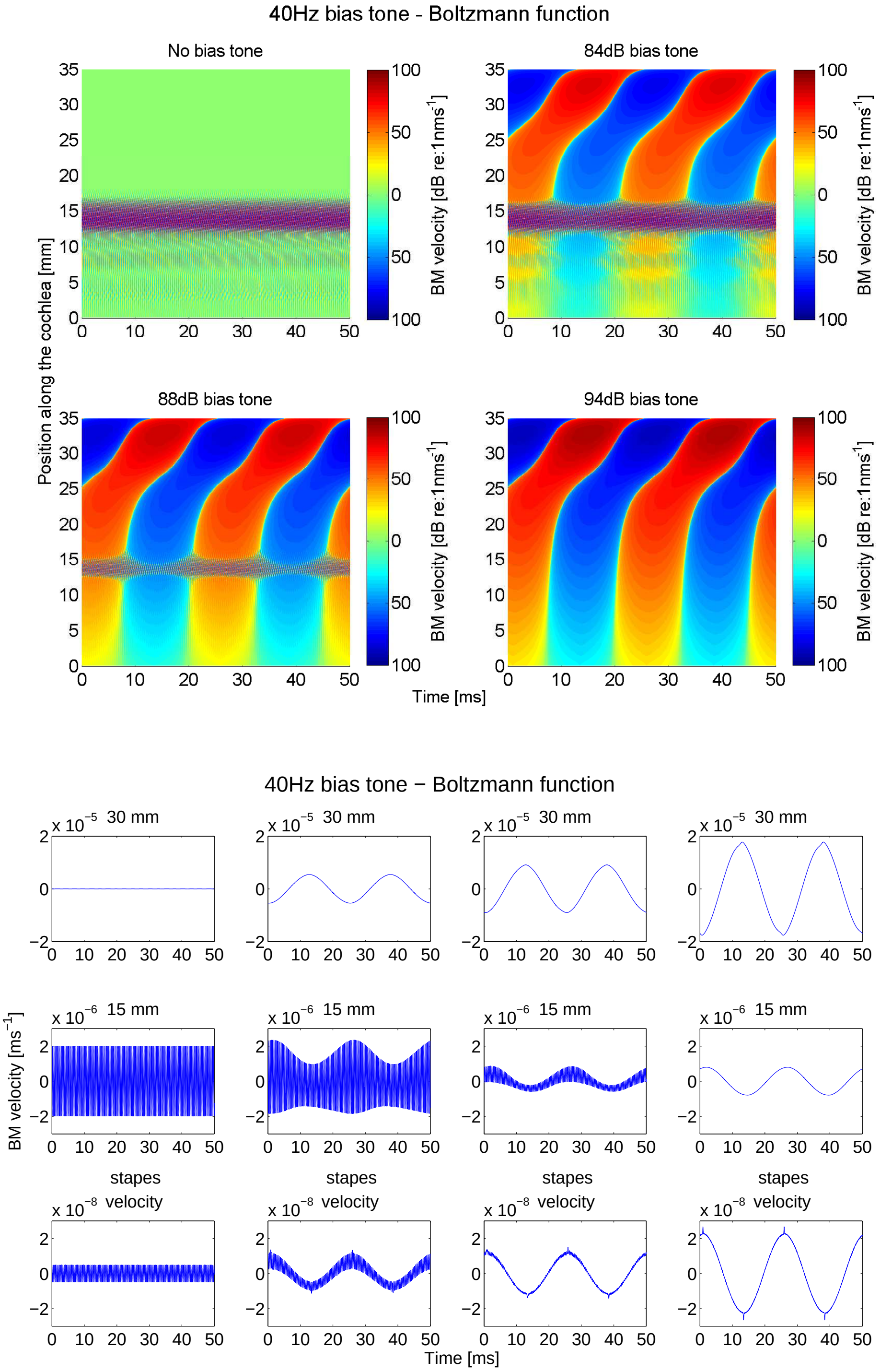

Figure F.6: The results from the time domain simulations in terms of the level of the BM velocity when the model containing Boltzmann nonlinearities is stimulated by a 40 Hz biasing tone of various levels. The contour plots show the response at different positions and times: top left panel, no bias tone present, top right panel, 84 dB, bottom left panel, 88 dB and bottom right panel, 94 dB. The 2D plots show the BM velocity at different times and specific locations: far left panel, no bias tone present, centre-left panel, 84 dB, centre-right panel, 88 dB and far right panel, 94 dB. The plots show how the SOAE is affected by the bias tone at different levels: at first, the emission is unaffected, but higher levels of biasing tone modulate its characteristics until it is suppressed.

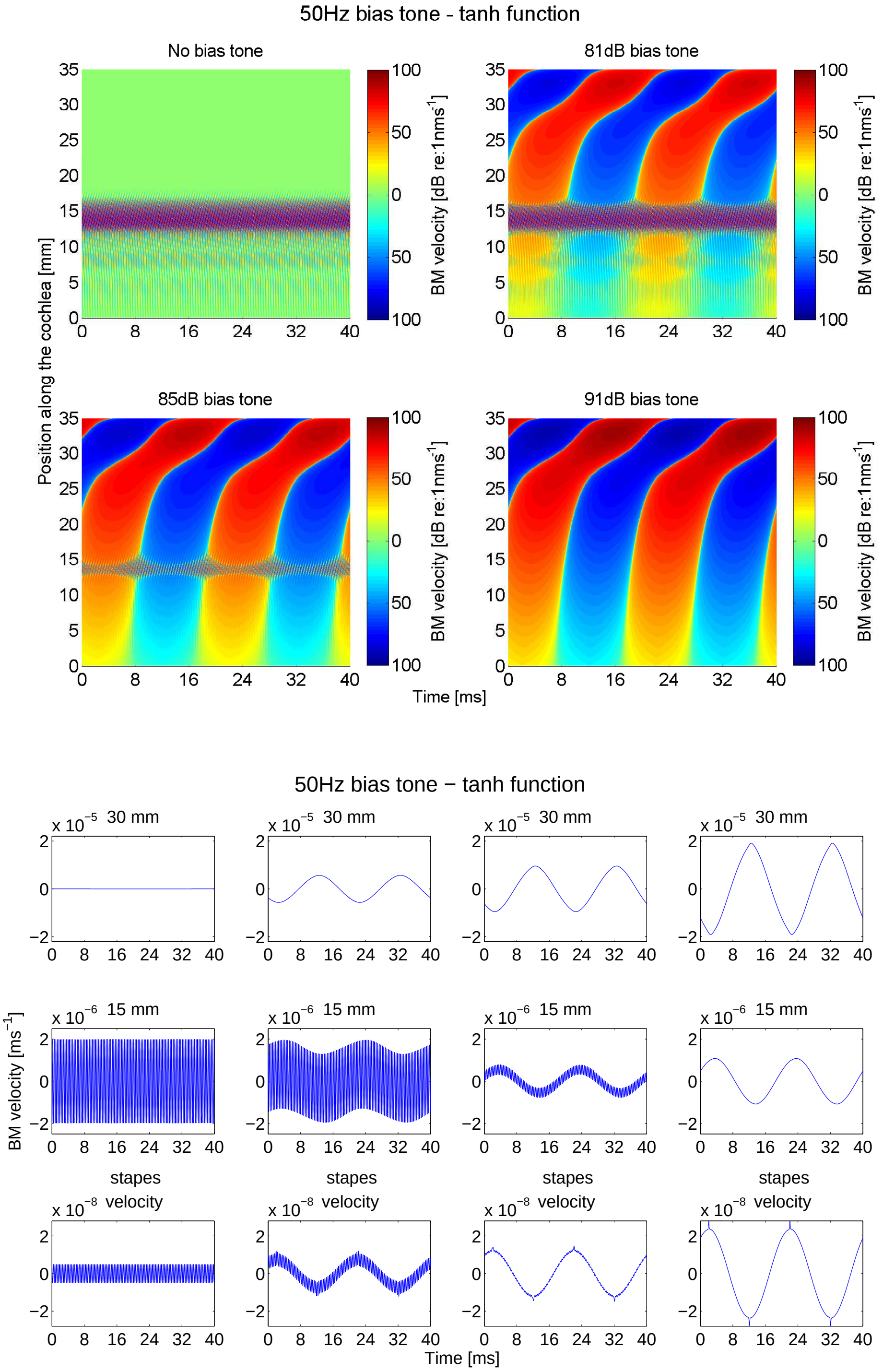

Figure F.7: The results from the time domain simulations in terms of the level of the BM velocity when the model containing tanh nonlinearities is stimulated by a 50 Hz biasing tone of various levels. The contour plots show the response at different positions and times: top left panel, no bias tone present, top right panel, 81 dB, bottom left panel, 85 dB and bottom right panel, 91 dB. The 2D plots show the BM velocity at different times and specific locations: far left panel, no bias tone present, centre-left panel, 81 dB, centre-right panel, 85 dB and far right panel, 91 dB. The plots show how the SOAE is affected by the bias tone at different levels: at first, the emission is unaffected, but higher levels of biasing tone modulate its characteristics until it is suppressed.

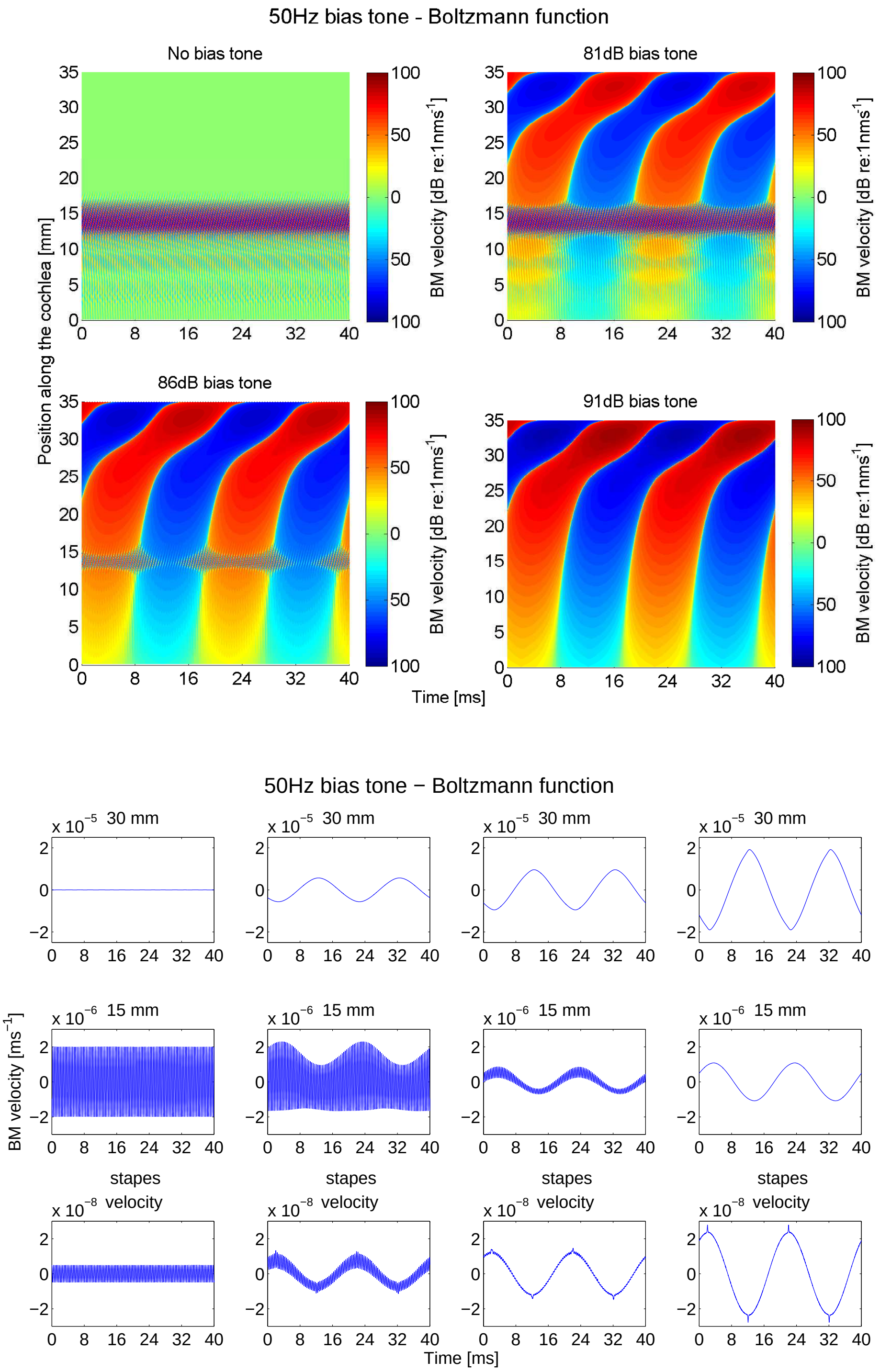

Figure F.8: The results from the time domain simulations in terms of the level of the BM velocity when the model containing Boltzmann nonlinearities is stimulated by a 50 Hz biasing tone of various levels. The contour plots show the response at different positions and times: top left panel, no bias tone present, top right panel, 81 dB, bottom left panel, 85 dB and bottom right panel, 91 dB. The 2D plots show the BM velocity at different times and specific locations: far left panel, no bias tone present, centre-left panel, 81 dB, centre-right panel, 85 dB and far right panel, 91 dB. The plots show how the SOAE is affected by the bias tone at different levels: at first, the emission is unaffected, but higher levels of biasing tone modulate its characteristics until it is suppressed.

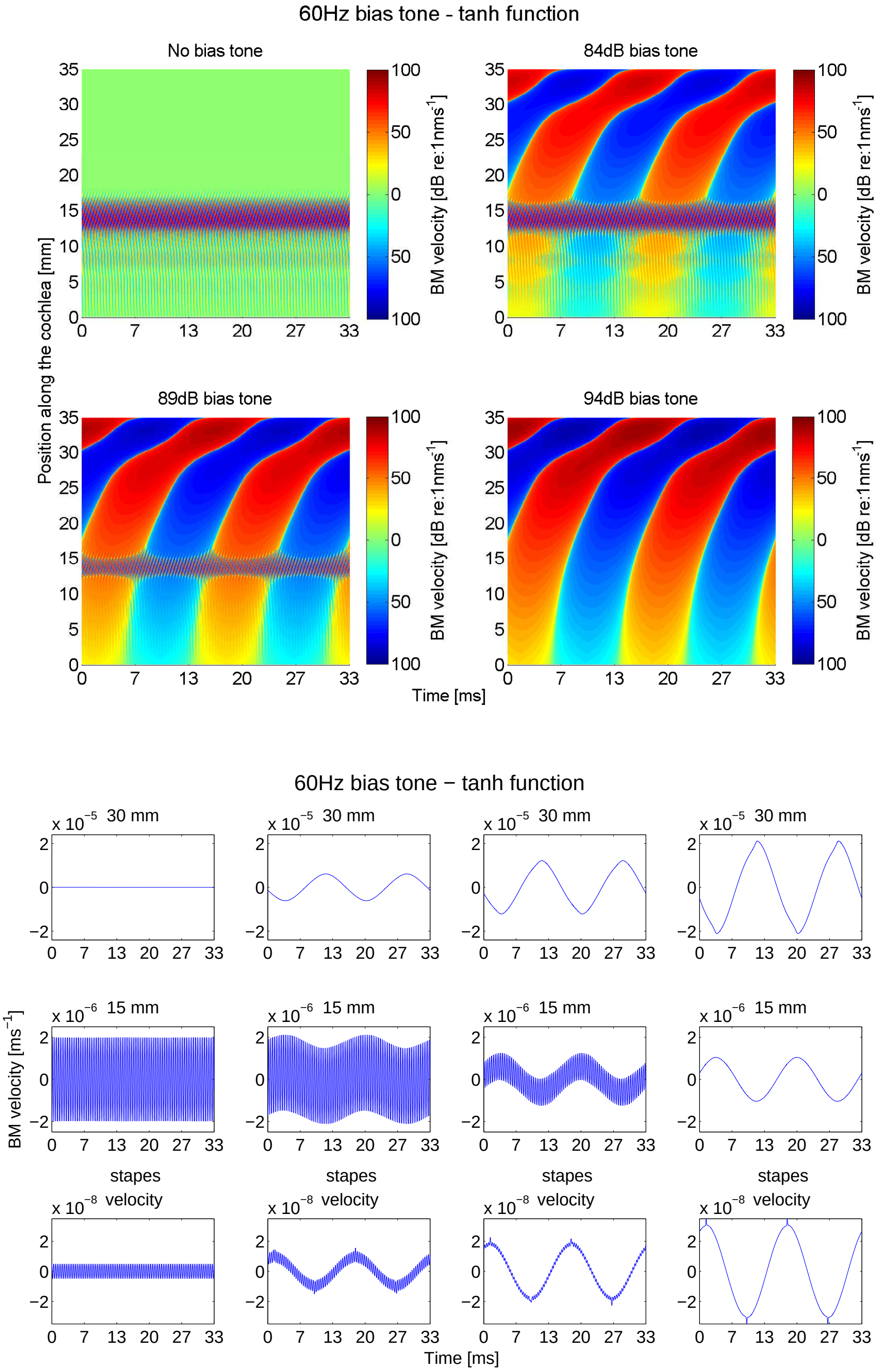

Figure F.9: The results from the time domain simulations in terms of the level of the BM velocity when the model containing tanh nonlinearities is stimulated by a 60 Hz biasing tone of various levels. The contour plots show the response at different positions and times: top left panel, no bias tone present, top right panel, 84 dB, bottom left panel, 89 dB and bottom right panel, 94 dB. The 2D plots show the BM velocity at different times and specific locations: far left panel, no bias tone present, centre-left panel, 84 dB, centre-right panel, 89 dB and far right panel, 94 dB. The plots show how the SOAE is affected by the bias tone at different levels: at first, the emission is unaffected, but higher levels of biasing tone modulate its characteristics until it is suppressed.

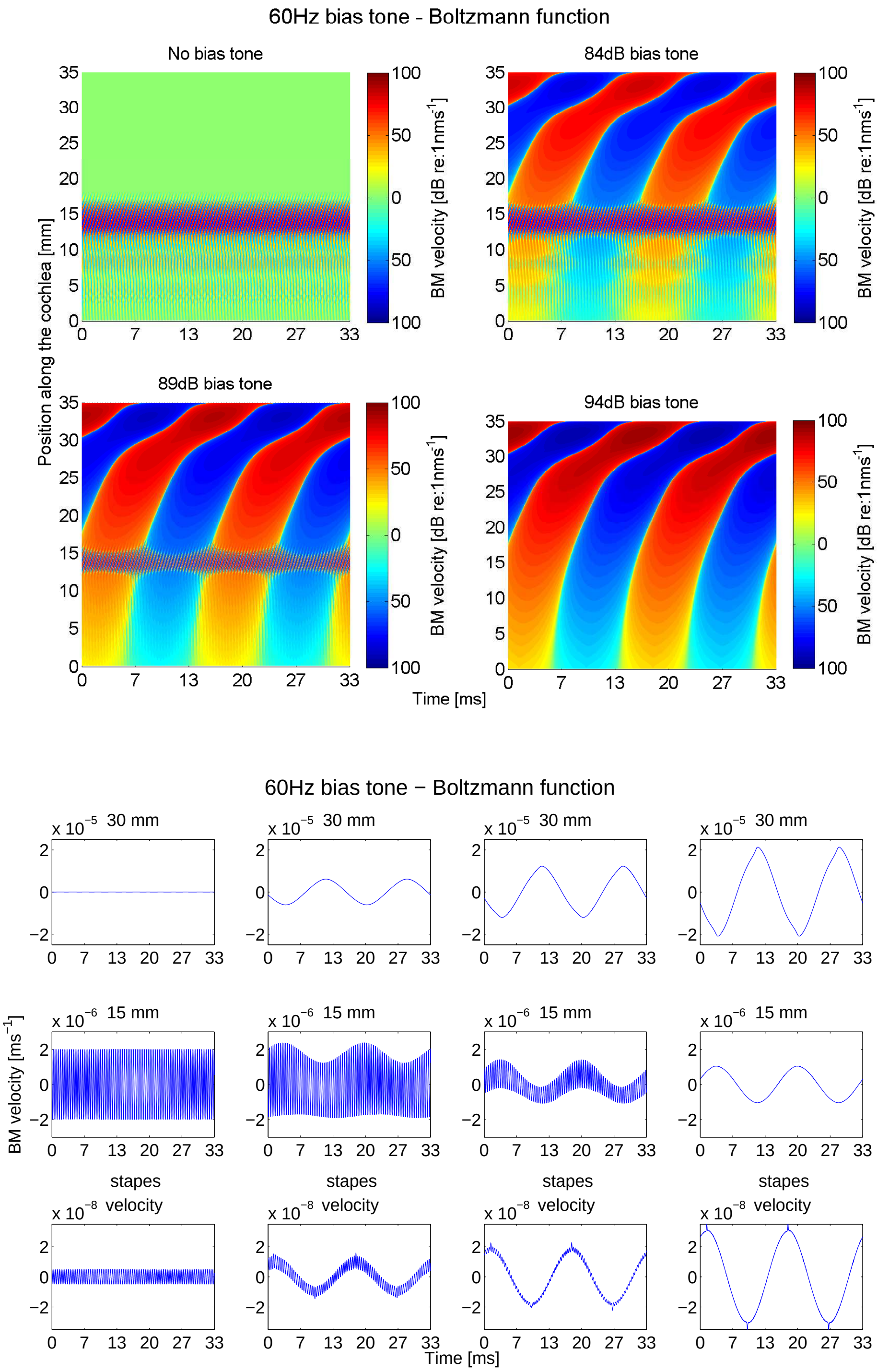

Figure F.10: The results from the time domain simulations in terms of the level of the BM velocity when the model containing Boltzmann nonlinearities is stimulated by a 60 Hz biasing tone of various levels. The contour plots show the response at different positions and times: top left panel, no bias tone present, top right panel, 84 dB, bottom left panel, 89 dB and bottom right panel, 94 dB. The 2D plots show the BM velocity at different times and specific locations: far left panel, no bias tone present, centre-left panel, 84 dB, centre-right panel, 89 dB and far right panel, 94 dB. The plots show how the SOAE is affected by the bias tone at different levels: at first, the emission is unaffected, but higher levels of biasing tone modulate its characteristics until it is suppressed.

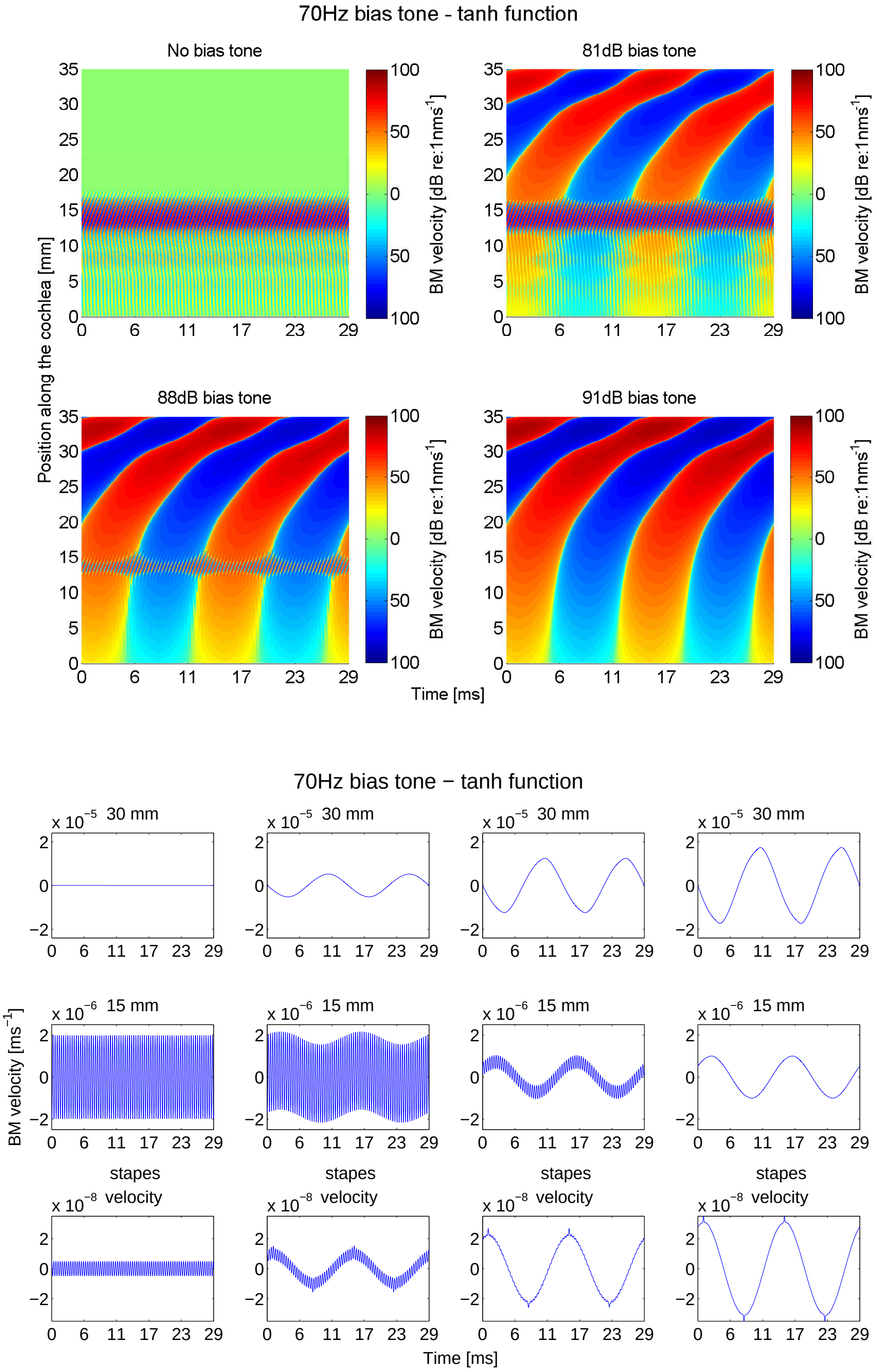

Figure F.11: The results from the time domain simulations in terms of the level of the BM velocity when the model containing tanh nonlinearities is stimulated by a 70 Hz biasing tone of various levels. The contour plots show the response at different positions and times: top left panel, no bias tone present, top right panel, 81 dB, bottom left panel, 88 dB and bottom right panel, 91 dB. The 2D plots show the BM velocity at different times and specific locations: far left panel, no bias tone present, centre-left panel, 81 dB, centre-right panel, 88 dB and far right panel, 91 dB. The plots show how the SOAE is affected by the bias tone at different levels: at first, the emission is unaffected, but higher levels of biasing tone modulate its characteristics until it is suppressed.

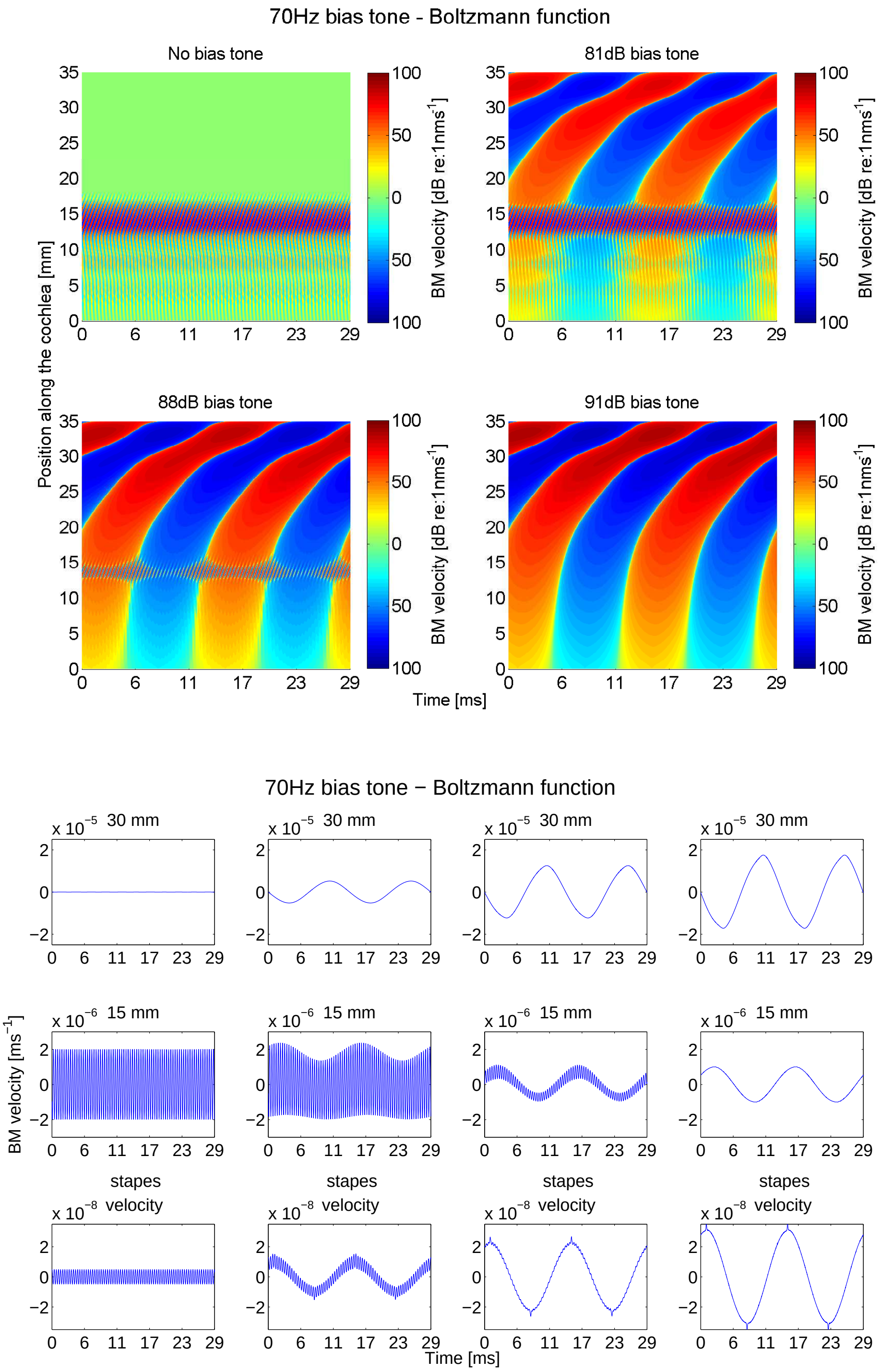

Figure F.12: The results from the time domain simulations in terms of the level of the BM velocity when the model containing Boltzmann nonlinearities is stimulated by a 70 Hz biasing tone of various levels. The contour plots show the response at different positions and times: top left panel, no bias tone present, top right panel, 81 dB, bottom left panel, 88 dB and bottom right panel, 91 dB. The 2D plots show the BM velocity at different times and specific locations: far left panel, no bias tone present, centre-left panel, 81 dB, centre-right panel, 88 dB and far right panel, 91 dB. The plots show how the SOAE is affected by the bias tone at different levels: at first, the emission is unaffected, but higher levels of biasing tone modulate its characteristics until it is suppressed.

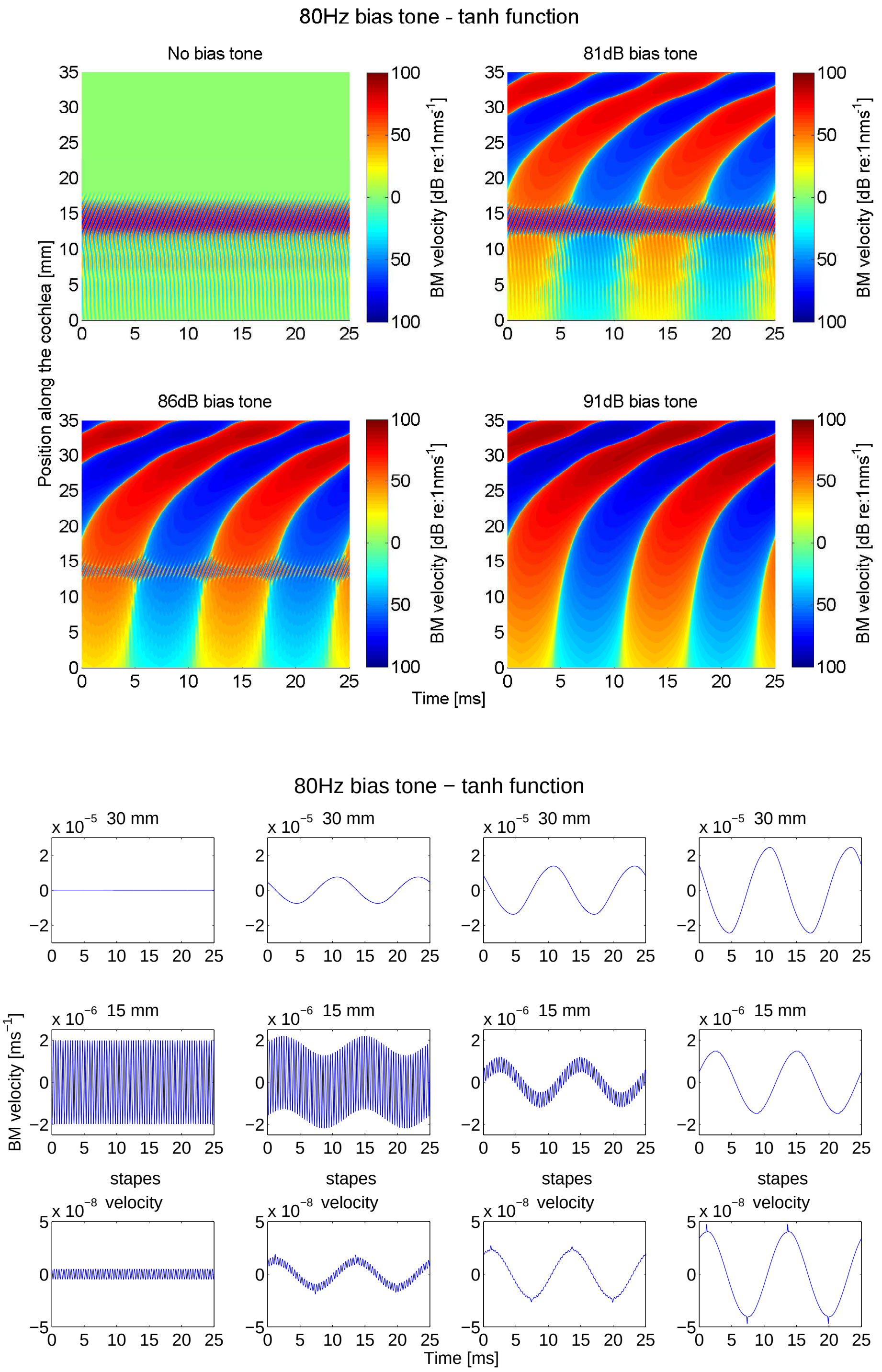

Figure F.13: The results from the time domain simulations in terms of the level of the BM velocity when the model containing tanh nonlinearities is stimulated by a 80 Hz biasing tone of various levels. The contour plots show the response at different positions and times: top left panel, no bias tone present, top right panel, 81 dB, bottom left panel, 86 dB and bottom right panel, 91 dB. The 2D plots show the BM velocity at different times and specific locations: far left panel, no bias tone present, centre-left panel, 81 dB, centre-right panel, 86 dB and far right panel, 91 dB. The plots show how the SOAE is affected by the bias tone at different levels: at first, the emission is unaffected, but higher levels of biasing tone modulate its characteristics until it is suppressed.

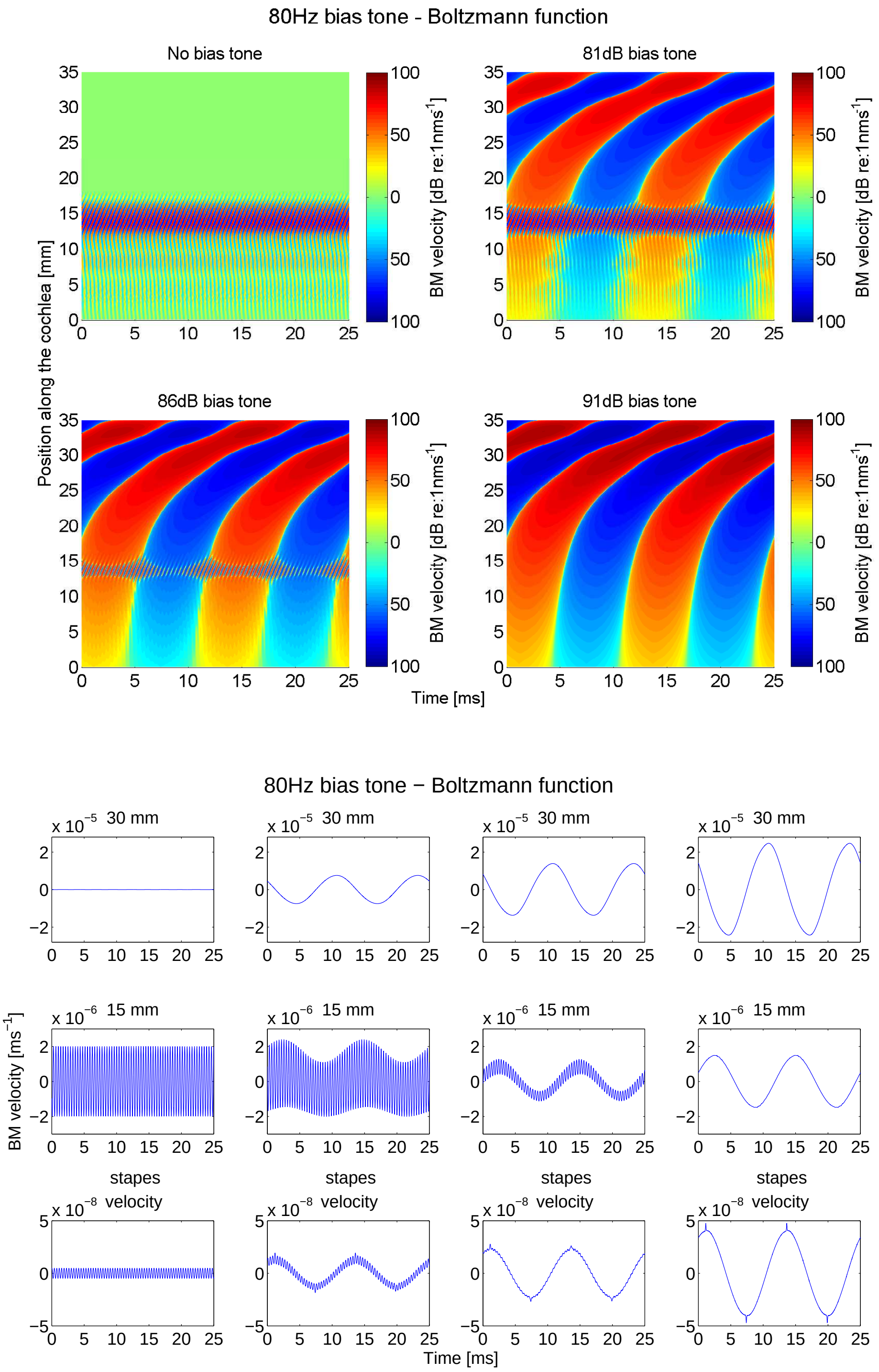

Figure F.14: The results from the time domain simulations in terms of the level of the BM velocity when the model containing Boltzmann nonlinearities is stimulated by a 80 Hz biasing tone of various levels. The contour plots show the response at different positions and times: top left panel, no bias tone present, top right panel, 81 dB, bottom left panel, 86 dB and bottom right panel, 91 dB. The 2D plots show the BM velocity at different times and specific locations: far left panel, no bias tone present, centre-left panel, 81 dB, centre-right panel, 86 dB and far right panel, 91 dB. The plots show how the SOAE is affected by the bias tone at different levels: at first, the emission is unaffected, but higher levels of biasing tone modulate its characteristics until it is suppressed.

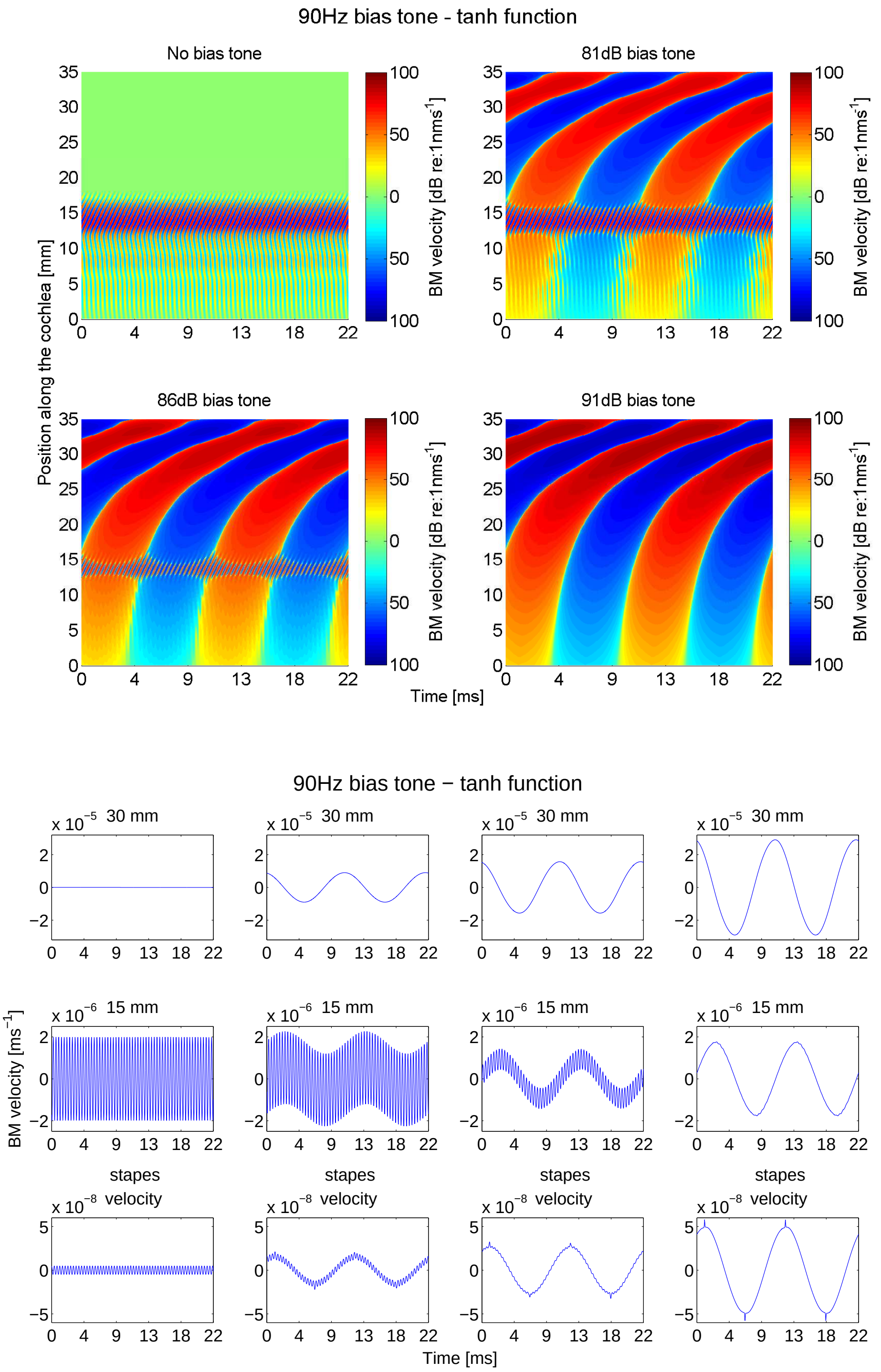

Figure F.15: The results from the time domain simulations in terms of the level of the BM velocity when the model containing tanh nonlinearities is stimulated by a 90 Hz biasing tone of various levels. The contour plots show the response at different positions and times: top left panel, no bias tone present, top right panel, 81 dB, bottom left panel, 86 dB and bottom right panel, 91 dB. The 2D plots show the BM velocity at different times and specific locations: far left panel, no bias tone present, centre-left panel, 81 dB, centre-right panel, 86 dB and far right panel, 91 dB. The plots show how the SOAE is affected by the bias tone at different levels: at first, the emission is unaffected, but higher levels of biasing tone modulate its characteristics until it is suppressed.

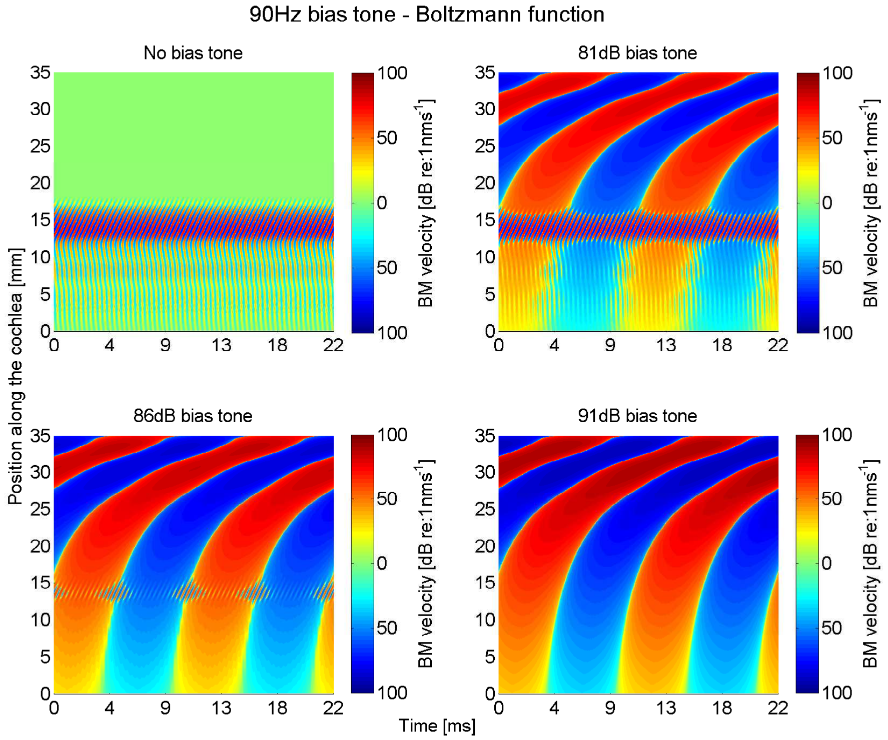

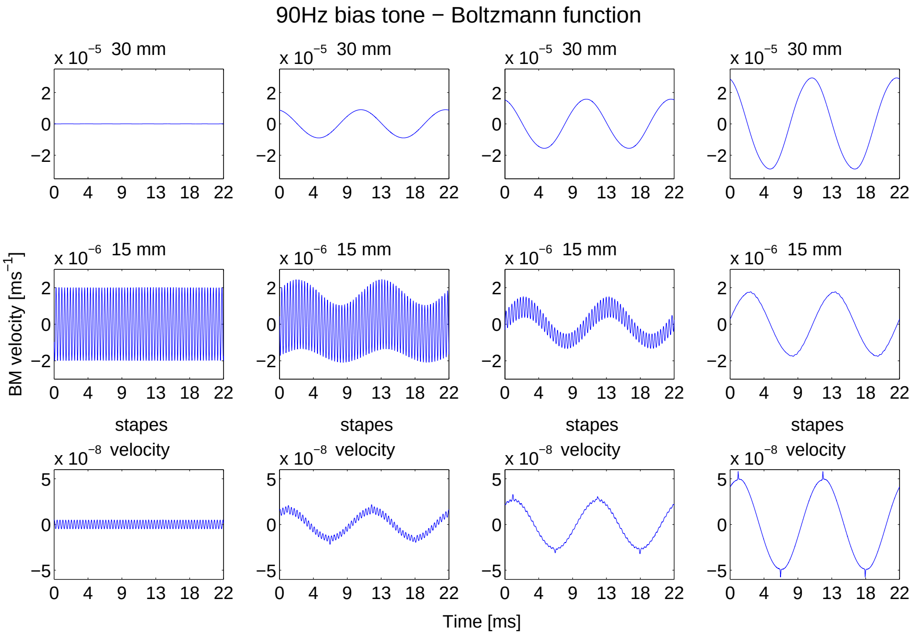

Figure F.16: The results from the time domain simulations in terms of the level of the BM velocity when the model containing Boltzmann nonlinearities is stimulated by a 90 Hz biasing tone of various levels. The contour plots show the response at different positions and times: top left panel, no bias tone present, top right panel, 81 dB, bottom left panel, 86 dB and bottom right panel, 91 dB. The 2D plots show the BM velocity at different times and specific locations: far left panel, no bias tone present, centre-left panel, 81 dB, centre-right panel, 86 dB and far right panel, 91 dB. The plots show how the SOAE is affected by the bias tone at different levels: at first, the emission is unaffected, but higher levels of biasing tone modulate its characteristics until it is suppressed.

Appendix G

Numerical implementation of the wave equation in the frequency domain

This numerical implementation is based on Neely and Kim (1986) formulation for solving the wave Equation describing the dynamics of the cochlea using finite difference approximations cast into a matrix form. The one-dimensional wave equation written in terms of the differential pressure across the cochlear partition can be written as the following:

$$\frac{\partial^2 p_d(x,\omega)}{\partial x^2} + \kappa_{TW}^2(x,\omega) p_d(x,\omega) = 0 \tag{G.1}$$

where the wave number is:

$$\kappa_{TW}^2(x,\omega) = \frac{-2i\omega\rho}{H Z_{cp}(x,\omega)} \tag{G.2}$$

Therefore, the simplified equation becomes:

$$\frac{\partial^2 p(t)}{\partial x^2} - \frac{2\rho}{H}\ddot{w}(t) = 0 \tag{G.3}$$

The boundary condition at the middle ear is:

$$\left.\frac{\partial p(t)}{\partial x}\right|_{x=0} = 2\rho\ddot{w}_S(t) \tag{G.4}$$

where $\ddot{w}_S$ can be divided into its superposing components: $\ddot{w}_{SO}(t)$ is the acceleration due to an external acceleration and $\ddot{w}_{SR}$ is the acceleration due to the loading by the internal pressure response of the cochlea at $x = 0$.

$$\left.\frac{\partial p(t)}{\partial x}\right|_{x=0} - 2\rho\ddot{w}_{SR}(t) = 2\rho\ddot{w}_{SO}(t) \tag{G.5}$$

The boundary condition at the helicotrema is the following:

$$\left.\frac{\partial p(t)}{\partial x}\right|_{x=L} = 2\rho\ddot{w}_N + \frac{1}{H}P_N \tag{G.6}$$

Using finite different approximations, Equations G.3, G.5 and G.6 can be converted such that there formulation is suitable for casting into matrix form. This is done by dividing the length of the cochlea in N section (in this case $N = 512$) having Δ length. The following Equations are therefore obtained:

$$\frac{p_{n-1}(t) - 2p_n(t) + p_{n+1}(t)}{\Delta^2} - \frac{2\rho}{H}\ddot{\xi}_n(t) = 0 \tag{G.7}$$

The boundary condition for the middle ear becomes:

$$\frac{p_2(t) - p_1(t)}{\Delta} - 2\rho\ddot{\xi}_{SR}(t) = 2\rho\ddot{\xi}_{SO}(t) \tag{G.8}$$

The boundary condition for the helicotrema becomes:

$$p_N(t) = p_N(t) = \frac{H}{\Delta^2}[\frac{\Delta}{H}p_{N-1}(t) - (\frac{\Delta}{H} - \frac{\Delta^2}{H^2})p_N(t)] = 2\rho\ddot{\xi}_N \tag{G.9}$$

Equations G.3, G.5 and G.6 are expressed into matrix form:

$$(\mathbf{F} - \mathbf{M})\mathbf{p}_d = \mathbf{q} \tag{G.10}$$

where $\mathbf{F}$ is the fluid coupling matrix:

$$\mathbf{F} = \frac{1}{\Delta^2}\begin{bmatrix} -\Delta & \Delta & & & 0 \\ 1 & -2 & 1 & & \\ & \ddots & \ddots & \ddots & \\ & & 1 & -2 & 1 \\ 0 & & & & \Delta^2 \end{bmatrix} \tag{G.11}$$

M is the mobility matrix:

$$\mathbf{M} = \frac{2i\omega\rho}{H}\begin{bmatrix} Y_m H & & & & 0 \\ & Y_{cp}(2) & & & \\ & & \ddots & & \\ & & & Y_{cp}(N-1) & \\ 0 & & & & Y_H \end{bmatrix} \tag{G.12}$$

$\mathbf{p}_d$ is the matrix of local pressure differences

$$\mathbf{p}_d = \begin{bmatrix} p_d(1) \\ \ddots \\ p_d(n) \\ \ddots \\ p_d(N) \end{bmatrix} \tag{G.13}$$

and **q** is the input matrix

$$\mathbf{q} = \begin{bmatrix} -2i\omega\rho u_{st} \\ 0 \\ \ddots \\ \ddots \\ 0 \end{bmatrix} \tag{G.14}$$

Combining **F** and **M** allows obtaining a tri-diagonal matrix **T**:

$$\mathbf{T} = \mathbf{F} - \mathbf{M} \tag{G.15}$$

Combining Equations G.16 and G.10 gives:

$$\mathbf{T}\mathbf{p}_d = \mathbf{q} \tag{G.16}$$

and by inverting **T**, the distribution of pressure differences is obtained:

$$\mathbf{p}_d = \mathbf{T}^{-1}\mathbf{q} \tag{G.17}$$

BM motion can then be calculated at any position along the BM using the following Equations

$$\dot{\xi}_b(x, /omega) = \frac{p_d(x,\omega)}{Z_{cp}(x,\omega)} \tag{G.18}$$

$$\xi_b(x, /omega) = \frac{\dot{\xi}_b(x,\omega)}{s} \tag{G.19}$$

References

Bacon, S. P. (2006). Auditory compression and hearing loss. *Acoustics today*, 2(2):30–34.

Baiduc, R. R., Lee, J., and Dhar, S. (2014). Spontaneous otoacoustic emissions, threshold microstructure, and psychophysical tuning over a wide frequency range in humans. *Acoustical Society of America*, 135(1):300–314.

Bekesy, G. V. (1947). The variation of phase along the basilar membrane with sinusoidal vibrations. *The Journal of the Acoustical Society of America*, 19(3):452–460.

Bergevin, C., Manley, G. A., and Köppl, C. (2015). Otoacoustic interrelationships of the barn owl. In *Mechanics of hearing: Protein to perception: Proceedings of the 12th International Workshop on the Mechanics of Hearing*, volume 1703, page 090011. AIP Publishing.

Bergevin, C. and Salerno, A. (2015). Dynamics of spontaneous otoacoustic emissions. *AIP Conference Proceedings*, 1703.

Bian, L. (2009). Amplitude and frequency modulations of spontaneous otoacoustic emissions. In N. P. Cooper, D. T. K., editor, *Concepts and Challenges in the Biophysics of Hearing*, pages 183–189. Keele University.

Bian, L., Chertoff, M. E., and Miller, E. (2002). Deriving a cochlear transducer function from low-frequency modulation of distortion product otoacoustic emissions. *The Journal of the Acoustical Society of America*, 112(1):198–210.

Bian, L. and Watts, K. L. (2008). Effects of low-frequency biasing on spontaneous otoacoustic emissions: Amplitude modulation. *The Journal of the Acoustical Society of America*, 123(2):887–898.

Braun, M. (1997). Frequency spacing of multiple spontaneous otoacoustic emissions shows relation to critical bands: a large-scale cumulative study. *Hearing Research*, 114:197–203.

Bright, K. E. (1985). *Microstructure audiograms and psychophysical tuning curves from subjects with spontaneous otoacoustic emissions.* PhD thesis, University of Arizona.

Brownell, W. E. (1990). Outer hair cell electromotility and otoacoustic emissions. *Ear and Hearing*, 11(2):82.

Burns, E. M. (2009). Long-term stability of spontaneous otoacoustic emissions. *Acoustical Society of America*, 125(5):3166–3176.

Burns, E. M., Arehart, K., and Campbell, S. L. (1992). Prevalence of spontaneous otoacoustic emissions in neonates. *Acoustical Society of America*, 91(3):1571–1575.

Cody, A. R. and Russell, I. J. (1987). The response of hair cells in the basal turn of the guinea-pig cochlea to tones. *The Journal of Physiology*, 383(1):551–569.

Cooper, N. and Yates, G. (1994). Nonlinear input-output functions derived from the responses of guinea-pig cochlear nerve fibres: Variations with characteristic frequency. *Hearing Research*, 78(2):221 – 234.

Cooper, N. P. (1996). Two-tone suppression in cochlear mechanics. *The Journal of the Acoustical Society of America*, 99(5):3087–3098.

Cooper, N. P. (1998). Harmonic distortion on the basilar membrane in the basal turn of the guinea-pig cochlea. *The Journal of Physiology*, 509(1):277–288.

Dallos, P. (1996). *Overview: Cochlear Neurobiology*, chapter 1, pages 1–43. 4. Springer, New York.

Davis, H. (1962). Advances in the neurophysiology and neuroanatomy of the cochlea. *The Journal of the Acoustical Society of America*, 34(9B):1377–1385.

de Boer, E. (1996). *Mechanics of the Cochlea: Modelling Efforts*, chapter 5, pages 258–317. 4. Springer, New York.

de Kleine, E., Wit, H. P., Avan, P., and van Dijk, P. (2001). The behavior of evoked otoacoustic emissions during and after postural changes. *Acoustical Society of America*, 110(2):973–980.

de Kleine, E., Wit, H. P., van Dijk, P., and Avan, P. (2000). The behavior of spontaneous otoacoustic emissions during and after postural changes. *The Journal of the Acoustical Society of America*, 107(6):3308–3316.

Elliott, E. (1958). A ripple effect in the audiogram. *Nature*, 181(4615):1076.

Elliott, S., Ku, E., and Lineton, B. (2007). A state space model for cochlear mechanics. *Acoustical Society of America*, 122(2):2759–2771.

Elliott, S. and Shera, C. A. (2012). The cochlea as a smart structure. *Institute of Physics (IOP) Publishing*, 21(6):1–11.

Elliott, S. J., Lineton, B., and Ni, G. (2011a). Fluid coupling in a discrete model of cochlear mechanics. *The Journal of the Acoustical Society of America*, 130(3):1441–1451.

Elliott, S. J., Ni, G., Mace, B. R., and Lineton, B. (2011b). How many waves propagate in the cochlea? *AIP Conference Proceedings*, 1403(1):563–568.

Epp, B., Verhey, J. L., and Mauermann, M. (2010). Modeling cochlear dynamics: Interrelation between cochlea mechanics and psychoacoustics). *The Journal of the Acoustical Society of America*, 128(4):1870–1883.

Fetterman, B. L. (2001). Distortion-product otoacoustic emissions and cochlear microphonics: Relationships in patients with and without endolymphatic hydrops. *The Laryngoscope*, 111(6):946–954.

Friedmand, B. (2005). *Control system desing: an introduction to state-space methods.* Dover Publications, Mineola, New York.

Galvez, M. F. S. and Elliott, S. (2014). Lumped parameter model of the organ of corti. Technical report, Faculty of Engineering and the Environment, Institute of Sound and Vibration Research, Signal Processing & Control Research Group.

Gan, W.-S. and Oo, N. (2010). Analytical and perceptual evaluation of nonlinear devices for virtual bass system. In *Audio Engineering Society Convention 128*.

Gelfand, S. A. and Levitt, H. (1998). *Hearing: An introduction to psychological and physiological acoustics.* Marcel Dekker New York.

Gold, T. (1948). Hearing. ii. the physical basis of the action of the cochlea. *Proceedings of the Royal Society of London B: Biological Sciences*, 135(881):492–498.

Greenwood, D. D. (1990). A cochlear frequency position function for several species29 years later. *The Journal of the Acoustical Society of America*, 87(6):2592–2605.

Guinan Jr., J. J., Salt, A., and Cheatham, M. A. (2012). Progress in cochlear physiology after bksy. *Hearing Research*, 293(12):12–20.

H. Mu, W. S. G. and Tan, E. L. (2015). An objective analysis method for perceptual quality of a virtual bass system. *IEEE/ACM Transactions on Audio, Speech, and Language Processing*, 23(5):840–850.

Hall, J. W. (2000). *Handbook of Otoacoustic Emissions.* Singular Publishing Group, San Diego.

Hanggi, P. and Riseborough, P. (1983). Dynamics of nonlinear dissipative oscillators. *American Journal of Physics*, 51(4):347–352.

Hansen, R., Santurette, S., and Verhulst, S. (2014). Effects of spontaneous otoacoustic emissions on pure-tone frequency difference limensa). *The Journal of the Acoustical Society of America*, 136(6):3147–3158.

He, W. and Ren, T. (2013). Basilar membrane vibration is not involved in the reverse propagation of otoacoustic emissions. *Scientific Reports*, 3(1874):1–7.

Hilger, A. W., Furness, D. N., and Wilson, J. (1995). The possible relationship between transient evoked otoacoustic emissions and organ of corti irregularities in the guinea pig. *Hearing Research*, 84(12):1 – 11.

How, J. A., Elliott, S. J., and Lineton, B. (2010). The influence on predicted harmonic and distortion product generation of the position of the nonlinearity within cochlear micromechanical models. *The Journal of the Acoustical Society of America*, 127(2):652–655.

Johnson, S., Beurg, M., Marcotti, W., and Fettiplace, R. (2011). Prestin-driven cochlear amplification is not limited by the outer hair cell membrane time constant. *Neuron*, 70(6):1143 – 1154.

Johnstone, B. M., Patuzzi, R., and Yates, G. K. (1986). Basilar membrane measurements and the travelling wave. *Hearing Research*, 22(1):147–153.

Joris, P. X., Bergevin, C., Kalluri, R., Mc Laughlin, M., Michelet, P., van der Heijden, M., and Shera, C. A. (2011). Frequency selectivity in old-world monkeys corroborates sharp cochlear tuning in humans. *Proceedings of the National Academy of Sciences*, 108(42):17516–17520.

Kanis, L. J. and de Boer, E. (1993). Self-suppression in a locally active nonlinear model of the cochlea: A quasilinear approach. *The Journal of the Acoustical Society of America*, 94(6):3199–3206.

Kanis, L. J. and de Boer, E. (1994). Two-tone suppression in a locally active nonlinear model of the cochlea. *The Journal of the Acoustical Society of America*, 96(4):2156–2165.

Kemp, D. (1979). The evoked cochlear mechanical response and the auditory microstructure - evidence for a new element in cochlear mechanics. *Scandinavian audiology. Supplementum*, (9):35–47.

Kemp, D. (1980). Towards a model for the origin of cochlear echoes. *Hearing Research*, 2(34):533 – 548.

Kemp, D. T. (1978). Stimulated acoustic emissions from within the human auditory system. *The Journal of the Acoustical Society of America*, 64(5):1386–1391.

Kemp, D. T. (1984). Quantum limits to oscillator stability: Theory and experiments on acoustic emissions from the human ear. *Physics Letters A*, A:173–178.

Kemp, D. T. (2007). *Active Processes and Otoacoustic Emissions in Hearing*, volume 30. Springer Science.

Kemp, D. T. (2009). Otoacoustic emissions. In Squire, L. R., editor, *Encyclopedia of Neuroscience*, pages 317–326. Elsevier.

Kemp, D. T. and Brown, A. M. (1983). *A Comparison of Mechanical Nonlinearities in the Cochleae of Man and Gerbil from Ear Canal Measurements*, pages 82–88. Springer Berlin Heidelberg, Berlin, Heidelberg.

Kringlebotn, M. (1988). Network model for the human middle ear. *Scandinavian Audiology*, 17(2):75–85.

Kros, C. J. (1996). *Physiology of Mammalian Cochlear Hair Cells*, chapter 6, pages 318 – 387. 4. Springer, New York.

Kros, C. J., Rusch, A., and Richardson, G. P. (1992). Mechano-electrical transducer currents in hair cells of the cultured neonatal mouse cochlea. *Proceedings: Biological Sciences*, 249(1325):185–193.

Ku, E. (2008). *Modelling the Human Cochlea.* PhD thesis, University of Southampton, ISVR.

Ku, E., Elliott, E., S., and Lineton, B. (2008a). Periodicity of the spectrum of modelled spontaneous otoacoustic emmisions. *Concepts and Challenges in the Biophysics of Hearing, edited by N. Cooper and D. Kemp*, pages 82–84. World Scientific.

Ku, E. M., Elliott, S. J., and Lineton, B. (2008b). Instabilities in a state space model of the human cochlea. *Korea International Society for Noise and Vibration Engineering Conference No. 1 , 2008*, pages 1767–1774.

Ku, E. M., Elliott, S. J., and Lineton, B. (2008c). Statistics of instabilities in a state space model of the human cochlea. *The Journal of the Acoustical Society of America*, 124(2):1068–1079.

Ku, E. M., Elliott, S. J., and Lineton, B. (2009). Limit cycle oscillations in a nonlinear state space model of the human cochlea. *Acoustical Society of America*, 126(2):739–750.

Kugler, K., Wiegrebe, L., Grothe, B., Kössl, M., Gürkov, R., Krause, E., and Drexl, M. (2014). Low-frequency sound affects active micromechanics in the human inner ear. *Royal Society Open Science*, 1(2):1–11.

Kugler, K., Wiegrebe, L., Gürkov, R., Krause, E., and Drexl, M. (2015). Concurrent acoustic activation of the medial olivocochlear system modifies the after-effects of intense low-frequency sound on the human inner ear. *Journal of the Association for Research in Otolaryngology*, 16(6):713–725.

LeMasurier, M. and Gillespie, P. G. (2005). Hair-cell mechanotransduction and cochlear amplification. *Neuron*, 48(3):403 – 415.

Liberman, M. C. (1982). The cochlear frequency map for the cat: Labeling auditory nerve fibers of known characteristic frequency. *The Journal of the Acoustical Society of America*, 72(5):1441–1449.

Lim, D. J. (1986). Functional structure of the organ of corti: a review. *Hearing Research*, 22(13):117 – 146.

Long, G. (1998). Perceptual consequences of the interactions between spontaneous otoacoustic emissions and external tones. i. monaural diplacusis and aftertones. *Hearing Research*, 119(1):49–60.

Long, G. R. and Tubis, A. (1988a). Investigations into the nature of the association between threshold microstructure and otoacoustic emissions. *Hearing Research*, 36(23):125 – 138.

Long, G. R. and Tubis, A. (1988b). Modification of spontaneous and evoked otoacoustic emissions and associated psychoacoustic microstructure by aspirin consumption. *Acoustical Society of America*, 84(4):1343–1353.

Long, G. R., Tubis, A., and Jones, K. L. (1990). Modeling synchronization and suppression of spontaneous otoacoustic emissions using van der pol oscillators: Effects of aspirin administration. *Acoustical Society of America*, 89(3):1201–1212.

Lonsbury-Martin, B., Martin, G., Probst, R., and Coats, A. (1988). Spontaneous otoacoustic emissions in a nonhuman primate. ii. cochlear anatomy. *Hearing Research*, 33(1):69 – 93.

Manley, G. A. and van Dijk, P. (2016). Frequency selectivity of the human cochlea: Suppression tuning of spontaneous otoacoustic emissions. *Hearing Research*, 336:53 – 62.

Marquardt, T. and Hensel, J. (2013). A simple electrical lumped-element model simulates intra-cochlear sound pressures and cochlear impedance below 2khz. *The Journal of the Acoustical Society of America*, 134(5):3730–3738.

Naidu, R. C. and Mountain, D. C. (2001). Longitudinal coupling in the basilar membrane. *Journal of the Association for Research in Otolaryngology*, 2(3):257–267.

Neely, S. T. (1981). Finite difference solution of a two dimensional mathematical model of the cochlea. *The Journal of the Acoustical Society of America*, 69(5):1386–1393.

Neely, S. T. (1985). Mathematical modeling of cochlear mechanics. *The Journal of the Acoustical Society of America*, 78(1):345–352.

Neely, S. T. and Kim, D. O. (1986). A model for active elements in cochlear biomechanics. *Acoustical Society of America*, 79(5):1472–1480.

Ni, G., Baumgart, J., and Elliott, S. (2015). Modelling motions within the organ of corti. 1703(1).

Ni, G., Elliott, S. J., Lineton, B., and Saba, R. (2011). Finite element modelling of fluid coupling in the coiled cochlea. *AIP Conference Proceedings*, 1403(1):350–355.

Nieder, P. and Nieder, I. (1971). Determination of microphonic generator transfer characteristic from modulation data. *The Journal of the Acoustical Society of America*, 49(2B):478–492.

Nobili, R., Mammano, F., and Ashmore, J. (1998). How well do we understand the cochlea? *Trends in Neurosciences*, 21(4):159 – 167.

Oghalai, J. S. (2004). The cochlear amplifier: augmentation of the traveling wave within the inner ear. *Current opinion in otolaryngology & head and neck surgery*, 12(5):431–438.

Ospeck, M., xia Dong, X., and Iwasa, K. H. (2003). Limiting frequency of the cochlear amplifier based on electromotility of outer hair cells. *Biophysical Journal*, 84(2):739 – 749.

Pan, S., Elliott, S. J., Lineton, B., and Teal, P. D. (2014). Computational efficiency of time domain ssolution to nonlinear cochlear models. (unpublished).

Pan, S., Elliott, S. J., Teal, P. D., and Lineton, B. (2015a). Efficient time-domain simulation of nonlinear, state-space, transmission-line models of the cochlea. *The Journal of the Acoustical Society of America*, 137(6):3559–3562.

Pan, S., Elliott, S. J., and Vignali, D. (2015b). Comparison of the nonlinear responses of a transmission-line and filter cascade model of the human cochlea. *Applications of Signal Processing to Audio and Acoustics (WASPAA)*.

Penner, M., Glotzbach, L., and Huang, T. (1993). Spontaneous otoacoustic emissions: Measurement and data. *Hearing Research*, 68(2):229 – 237.

Penner, M. and Zhang, T. (1997). Prevalence of spontaneous otoacoustic emissions in adults revisited. *Hearing Research*, 103(12):28 – 34.

Pickles, J. O. (2012). *An Introduction to the Physiology of Hearing.* Brill, Leiden.

Probst, R., Lonsbury-Martin, B. L., and Martin, G. K. (1991). A review of otoacoustic emissions. *The Journal of the Acoustical Society of America*, 89(5):2027–2067.

Puria, S. (2003). Measurements of human middle ear forward and reverse acoustics: Implications for otoacoustic emissions. *The Journal of the Acoustical Society of America*, 113(5):2773–2789.

Raphael, Y. and Altschuler, R. A. (2003). Structure and innervation of the cochlea. *Brain Research Bulletin*, 60(56):397 – 422. Functional Anatomy of Ear Connections.

Rapson, M. J., Hamilton, T. J., and Tapson, J. C. (2014). On the fluid-structure interaction in the cochlea. *The Journal of the Acoustical Society of America*, 136(1):284–300.

Reichenbach, T., Stefanovic, A., Nin, F., and Hudspeth, A. (2012). Waves on reissner's membrane: A mechanism for the propagation of otoacoustic emissions from the cochlea. *Cell Reports*, 1(4):374 – 384.

Robles, L. and Ruggero, M. A. (2001). Mechanics of the mammalian cochlea. Technical report.

Robles, L., Ruggero, M. A., and Rich, N. C. (1986). Basilar membrane mechanics at the base of the chinchilla cochlea. i. inputoutput functions, tuning curves, and response phases. *The Journal of the Acoustical Society of America*, 80(5):1364–1374.

Salt, A. N. and Lichtenhan, J. T. (2014). How does wind turbine noise affect people? *Acoustics Today*, 10:20–28.

Sellick, P. M., Patuzzi, R., and Johnstone, B. M. (1982). Measurement of basilar membrane motion in the guinea pig using the mössbauer technique. *Acoustical Society of America*, 72(1):131–141.

Shera, C. A. (2003). Mammalian spontaneous otoacoustic emissions are amplitude stabilized cochlear standing waves. *Acoustical Society of America*, 114(1):244–262.

Shera, C. A. (2004). Mechanisms of mammalian otoacoustic emission and their implications for the clinical utility of otoacoustic emissions. *Ear and Hearing*, 25(2):86–97.

Shera, C. A. and Guinan, J. J. (1999). Evoked otoacoustic emissions arise by two fundamentally different mechanisms: A taxonomy for mammalian oaes. *Acoustical Society of America*, 105(2):782–798.

Shera, C. A. and Guinan, J. J. (2003). Stimulus-frequency-emission group delay: A test of coherent reflection filtering and a window on cochlear tuning. *Acoustical Society of America*, 113(5):2762–2772.

Shera, C. A., Guinan, J. J., and Oxenham, A. J. (2002). Revised estimates of human cochlear tuning from otoacoustic and behavioral measurements. *Proceedings of the National Academy of Sciences*, 99(5):3318–3323.

Shera, C. A. and Zweig, G. (1993). *Biophysics of hair cell sensory systems - Order from chaos: resolving the paradox of periodicity in evoked otoacoustic emission*, chapter 2, pages 54–63.

SIFEM (2011). Seventh framework programme. Technical report.

Slotine, J. J. E. and Li, W. (1991). *Applied Nonlinear Control.* Prentice Hall, Englewood Cliffs, New Jersey.

Talmadge, C., Long, G., Murphy, W., and Tubis, A. (1993). New off-line method for detecting spontaneous otoacoustic emissions in human subjects. *Hearing Research*, 71(1):170 – 182.

Talmadge, C. L., Tubis, A., Long, G. R., and Piskorski, P. (1998). Modeling otoacoustic emission and hearing threshold fine structures. *Acoustical Society of America*, 104(3):1517–1543.

van Dijk, P. and Wit, H. P. (1990). Amplitude and frequency fluctuations of spontaneous otoacoustic emissions. *Acoustical Society of America*, 88(4):1779–1793.

van Dijk, P., Wit, H. P., Tubis, A., Talmadge, C. L., and Long, G. R. (1994). Correlation between amplitude and frequency fluctuations of spontaneous otoacoustic emissions. *The Journal of the Acoustical Society of America*, 96(1):163–169.

Vignali, D., Elliott, S. J., and Lineton, B. (2015). Modelling the effect of low frequency bias tones on spontaneous otoacoustic emissions. In *Proceedings of the 22nd International Congress on Sound and Vibration.*

von Békésy, G. (1949). The vibration of the cochlear partition in anatomical preparations and in models of the inner ear. *The Journal of the Acoustical Society of America*, pages 233–245.

von Békésy, G. (1960). *Experiments in hearing*, volume 8. McGraw-Hill, New York.

Voss, S. E., Horton, N. J., Tabucchi, T. H. P., Folowosele, F. O., and Shera, C. A. (2006). Posture-induced changes in distortion-product otoacoustic emissions and the potential for noninvasive monitoring of changes in intracranial pressure. *Neurocritical Care*, 4(3):251–257.

Whitehead, M. L., Lonsbury-Martin, B. L., Martin, G. K., and McCoy, M. J. (1996). *Experimental and Clinical Studies of Emissions*, chapter 7, pages 199–257. Springer, New York.

Wilson, J. and Sutton, G. (1981). Acoustic correlates of tonal tinnitus. *Tinnitus*, 85(82):107.

Yoon, Y.-J., Steele, C. R., and Puria, S. (2011). Feed-forward and feed-backward amplification model from cochlear cytoarchitecture: An interspecies comparison. *Biophysical Journal*, 100(1):1 – 10.

Young, J. A. (2011). *Modelling the cochlear origins of distortion product otoacoustic emissions.* PhD thesis, University of Southampton, ISVR.

Zha, D., Chen, F., Ramamoorthy, S., Fridberger, A., Choudhury, N., Jacques, S. L., Wang, R. K., and Nuttall, A. L. (2012). In vivo outer hair cell length changes expose the active process in the cochlea. *PLoS ONE*, 7(4):1–9.

Zhang, T. and Penner, M. (1998). A new method for the automated detection of spontaneous otoacoustic emissions embedded in noisy data. *Hearing Research*, 117(12):107 – 113.

Zweig, G. and Shera, C. A. (1995). The origin of periodicity in the spectrum of evoked otoacoustic emissions. *The Journal of the Acoustical Society of America*, 98(4):2018–2047.

Zwicker, E. and Schloth, E. (1984). Interrelation of different oto-acoustic emissions. *The Journal of the Acoustical Society of America*, 75(4):1148–1154.